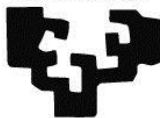eman ta zabal zazu

Universidad
del País Vasco

Euskal Herriko
Unibertsitatea

Modern Rotational Spectroscopy as a Versatile Tool in Chemistry

Ph. D. Thesis

Iciar Uriarte Hernando

2018

Universidad del País Vasco
Euskal Herriko Unibertsitatea

ZIENTZIA
ETA TEKNOLOGIA
FAKULTATEA
FACULTAD
DE CIENCIA
Y TECNOLOGÍA

Modern Rotational Spectroscopy as a Versatile Tool in Chemistry

Ph. D. Thesis

Iciar Uriarte Hernando

Supervised by:

Emilio José Cocinero Pérez
Francisco José Basterretxea Elguezabal

2018

The work in this Thesis would not have been possible without the help and support of many people, scientists and non-scientists. All of them have contributed to this work throughout the years, in one way or another.

I would like to start by expressing my gratitude to my Thesis supervisors, Emilio José Cocinero and Francisco José Basterretxea, for making this work possible. It was a pleasure working with you and I thank you both for your support and wise advice.

I am most grateful to all the members (past and present) of the Spectroscopy Group at the University of the Basque Country (UPV/EHU). Our work frequently required that I had to ask many of you for help, and you were always kind enough to assist me. I cannot stress enough my gratitude to all of you and I wish you the best for the future.

In my Thesis, I have had the chance of working in two foreign laboratories (Walther Caminati's group in Bologna (Italy) and Tim Zwier's group at Purdue University (USA)). Both experiences were amazing and opened my mind in so many ways. I thank all of the people in both groups for making me feel at home. On the Italian side, the microwave group was kind enough to teach me about rotational spectroscopy, but also about food, gelattos or Chinese songs. On the Purdue side, the Zwier group (and Sarah!) showed me the amazes of Indiana and West Lafayette, apart from the spectroscopic work they carry out. I will never forget my stay at Purdue. Overall, it was DOPE!

Finally, I have had the pleasure of meeting a great number of scientists these last few years, at meetings, visitors in our lab, etc. Every one of them has taught me something and I am thankful for that. I firmly believe that interaction with fellow scientists is crucial in the development of science.

I would also like to thank the Ministerio de Educación, Cultura y Deporte for an FPU grant.

Además de toda la gente del ámbito científico que ya he mencionado, este trabajo no hubiera sido posible sin el apoyo de amigos y familia.

Empiezo por dar las gracias a todos l@s Txabatars por todos esos momentos de desahogo que me habéis proporcionado, ya sea al lado de una cerveza, un zumito, una sala de escape, un Ramen, subiendo y bajando la Gran Vía o en mil y una otras ocasiones. Muchas gracias a tod@s por vuestro cariño, apoyo y compañía.

A las componentes de Prototopia y a Roberto, estuvisteis presentes en los años de nuestra Licenciatura y recuerdo aquella época con muchísimo cariño. Me alegro de haber podido contar con vuestra compañía también en estos años de Tesis. Muchas gracias por todo el tiempo que hemos compartido, que me ha ayudado a despejarme cuando más lo necesitaba.

También me gustaría agradecer a los Azpeitia Molina por su cariño y apoyo durante estos años. Gracias de corazón por acogerme y por vuestra compañía.

Mis hermanas Amaia y Nerea, así como sus familias, Asier, Javi, Peru, Irati, Ibon y Oier, me han complementado en todo lo humanamente posible. Muchas gracias por dejar que me auto-invite más de lo que debía y por ayudarme en todo aquello en lo que vuestra hermana pequeña es un poco desastre. Ver nacer y crecer a mis sobrin@s es, sin duda, la
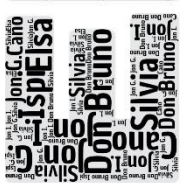
mayor alegría de estos cuatro años de Tesis Doctoral. Tía Lourdes, tío Iñaki, llevadnos a Disneyworld.

Es absolutamente imposible que pueda agradecer lo suficiente a mi madre. No sólo por todo lo que ha hecho por mí estos años de Tesis, sino por todos los sacrificios que ha hecho por mis hermanas y por mí hasta la fecha. Muchas gracias, Amatxu, por haberme ayudado en todos y cada uno de los aspectos de mi vida y de mi trabajo.

Y, por último, tengo una infinidad de motivos por los que agradecer a Sergio; sobre todo, el cariño y apoyo incondicional que me ha demostrado siempre.

A todos vosotros, to all of you,

<div align="right">Eskerrik asko</div>

Index

IV. The conformational landscape of α-ionone, β-ionone, and β-damascone

V. CP-FTMW and FTMW techniques in the structural study of cotinine

The appendices in this Thesis are available in electronic format. The reader can access them online or as pdf files in the CD attached to this Thesis. In the following, we will summarize how to access the appendices of each Chapter (website and name of the pdf file).

-Chapter IV:

- Tables IV.A.1 to IV.A.3 can be found in the pdf file named "IV.appendix.pdf" or in the following link:
https://drive.google.com/open?id=1f6oWsN1IMYySwwEUGoSV_dw4e76FzsP6
- A complete list of all measured rotational transitions is collected in the pdf file named "IV.rotational_transitions.pdf" or in the following link:
https://drive.google.com/open?id=17L6W6T6_Tx5Nfsb9OKb3r-gByLxtGgEP

-Chapter V:
- Tables V.A.1 to V.A.4 can be found in the pdf file named "V.appendix.pdf" or in the following link:
https://drive.google.com/open?id=1EYo3RdXyC6yPaKtwiXoyhEzVr2tLXbUE

-Chapter VI:
- Tables VI.A.1 and VI.A.2 can be found in the pdf file named "VI.appendix.pdf" or in the following link:
  https://drive.google.com/open?id=1l0xrSc7S2WMqynpZNNQMCDl8gIwJlSlZ

-Chapter VII:
- Tables VII.A.1 to VII.A.3 can be found in the pdf file named "VII.appendix.pdf" or in the following link:
  https://drive.google.com/open?id=12lrLGuCZiksC-w_gGJqkXubkkNXth0qt

-Chapter VIII:
- Tables VIII.A.1 to VIII.A.21 can be found in the pdf file named "VIII.appendix.pdf" or in the following link:
  https://drive.google.com/open?id=1t9yGAyfLKWlOjiXL9ltwT9WDtyFjFSvO

Acronyms and symbols

Here we collect some of the acronyms and symbols that we will use throughout this Thesis.

Acronym	Meaning
FTMW	Fourier Transform Microwave (refers to Balle–Flygare's original design)
CP-FTMW	Chirped Pulse Fourier Transform Microwave
FID	Free Induction Decay
DFT	Density Functional Theory
PES	Potential Energy Surface
MD	Molecular Dynamics
MM	Molecular Mechanics
MMFF	Merck Molecular Force Field
WHB	Weak Hydrogen Bond
E, T, C, B, HB, HC, TB	Envelope, Twist, Chair, Boat, Half-Boat, Half-Chair, Twist-Boat (five- and six-membered ring conformations)

Symbol	Meaning
A, B, C	Rotational constants
$D_J, D_{JK}, D_K,$ d_1, d_2	Quartic centrifugal distortion constants
μ_a, μ_b, μ_c	Electric dipole moment components along the principal axes of inertia
μ_{tot}	Total electric dipole moment
ΔE	Difference in electronic energy with respect to the global minimum
$\Delta(E+ZPE)$ or ΔE_0	Difference in electronic energy with respect to the global minimum, taking into account the Zero Point Energy correction (residual energy at vibrational ground state)
ΔG	Difference in Gibbs free energy with respect to the global minimum
σ	Standard deviation of the fit
N	Number of transitions in the fit
V_3	Barrier to internal rotation of a methyl top
$\angle(g, i)$	Orientation of the methyl internal rotor (i) with respect to the axis g ($g=a,b,c$, principal axes of inertia)

Resumen en castellano

La espectroscopía de microondas estudia transiciones entre estados rotacionales de moléculas o complejos intermoleculares en fase gas. En los inicios de esta técnica, se realizaban experimentos de absorción en celdas estáticas, dejando pasar radiación monocromática por una celda con la muestra gaseosa, y detectando la radiación transmitida. Sin embargo, los avances instrumentales en esta técnica han sido notorios y, hoy en día, la mayor parte de los espectros rotacionales se toman con experimentos de emisión. En este tipo de experimentos, se excita la muestra mediante aplicación de un pulso de radiación, se detecta la señal de relajación en el tiempo y se realiza la transformada de Fourier para obtener el espectro en el dominio de frecuencias (el procedimiento es similar a los experimentos de RMN). Además, gran parte de los espectros rotacionales se toman en expansiones supersónicas, donde las diferentes especies moleculares se encuentran aisladas, es decir, libres de interacciones. También cabe destacar que los avances instrumentales en el campo han dado como resultado una mejora de la sensibilidad y de la resolución espectral de estos aparatos. En esta Tesis Doctoral, se analiza el potencial de la espectroscopía rotacional actual como herramienta en la Química moderna.

La principal información que se puede obtener de los espectros de rotación es el valor de las contantes rotacionales. Éstas están relacionadas con los momentos de inercia y, en consecuencia, con la estructura tridimensional de la molécula. Por ello, el campo de la espectroscopía de rotación se ha dedicado tradicionalmente a la determinación estructural de sistemas moleculares en fase gas. Gracias a la elevada resolución espectral de esta técnica (del orden de 0.0000001 cm^{-1}), es posible realizar la determinación de las estructuras con gran precisión y exactitud. Por ello, la espectroscopía de microondas se ha usado (y se sigue usando) para estudiar las diferentes conformaciones que puede adoptar una molécula en fase aislada. Así, se puede evaluar el rol de las fuerzas intermoleculares que determinan la conformación tridimensional de moléculas.

Por otra parte, el empleo de expansiones supersónicas permite aislar complejos intermoleculares (dímeros, trímeros, tetrámeros...) débilmente enlazados. Al realizar la determinación por espectroscopía rotacional de estos complejos, se pueden conocer exactamente el tipo de enlaces que mantienen los monómeros unidos (enlaces de hidrógeno, fuerzas de Van der Waals, etc). Esta técnica se emplea frecuentemente para identificar la naturaleza de los enlaces intermoleculares, por ejemplo, en casos en los que haya competición entre varios tipos de enlaces.

Por último, otro de los campos de aplicación de la espectroscopía de microondas es en el ámbito de la astrofísica. Los espectros de rotación actúan como huellas dactilares de las diferentes especies moleculares, en parte debido a la elevada resolución espectral de esta técnica. La identificación de un conjunto de transiciones rotacionales de una determinada especie confirma sin lugar a duda la presencia de dicha especie. Radiotelescopios como ALMA (Atacama Large Millimeter Array, en Chile) son capaces de recoger información de la región espectral en la que se producen transiciones rotacionales. Por ello, la comparación de datos obtenidos en el laboratorio con datos recogidos mediante radiotelescopios permite confirmar la presencia de determinadas moléculas en el espacio.

El ámbito de la espectroscopía de rotación está en continua evolución, con grandes avances tecnológicos e instrumentales que abren el campo a nuevos retos científicos. A continuación, mencionaremos algunos de los avances recientes más relevantes, teniendo en cuenta que éste no pretende ser un análisis exhaustivo, sino más bien una recopilación de los avances que han tenido un mayor impacto en la consecución de esta Tesis Doctoral. Por una parte, a finales de la década de los noventa, se incorporaron las técnicas de vaporización láser con pulsos ultracortos. Esto permitió la vaporización de muestras termolábiles, es decir, muestras que se descomponen al ser calentadas. La introducción de este tipo de técnicas fue particularmente relevante en el estudio estructural de moléculas de interés biológico ya que éstas son habitualmente sensibles a la temperatura. Por ello, el uso de vaporización láser permitió el estudio rotacional de muchas biomoléculas que antes no eran accesibles con esta técnica.

Por otra parte, uno de los mayores adelantos de la espectroscopía rotacional en los últimos años es la introducción de las técnicas de excitación pulsada de banda ancha por parte del Profesor Brooks H. Pate de la Universidad de Virginia. Este tipo de espectrómetros se denominan habitualmente "CP-FTMW", por sus siglas en inglés (Chirp-Pulsed Fourier Transform Microwave). La principal característica de esta técnica es el empleo de un pulso multifrecuencia como fuente de excitación de la muestra. Gracias a este tipo de pulsos, se pueden registrar simultáneamente rangos espectrales de hasta 12 GHz. A modo ilustrativo, cabe destacar que, en otro tipo de espectrómetros previos al CP-FTMW, el rango espectral era alrededor de 1 MHz, lo cual requería largos barridos para cubrir el rango de frecuencias necesario. Por ello, el empleo de espectrómetros de banda ancha reduce en general el tiempo de adquisición espectral, lo cual ha resultado una importante ventaja en el ámbito de la espectroscopía rotacional.

En esta Tesis Doctoral, ilustramos los diferentes grados de aplicación de la espectroscopía rotacional moderna a diferentes problemáticas en Química. En concreto, se estudian diferentes sistemas moleculares que se han analizado mediante dos espectrómetros de microondas en la Universidad de País Vasco UPV/EHU. Antes de nada, es importante destacar que estos equipos no son comerciales, y por lo tanto su construcción y mantenimiento quedan a cargo del grupo de investigación. Denominamos el primero de los equipos FTMW (Fourier Transform Microwave). Se trata de un equipo basado en el diseño original de Balle y Flygare, y su uso está muy extendido en la comunidad científica internacional. Se construyó en el Departamento de Química Física de la Universidad del País Vasco UPV/EHU en el año 2010. El ancho de banda es aproximadamente 1 MHz, por lo que requiere la realización de barridos en frecuencia para cubrir el rango espectral necesario. Su resolución espectral es aproximadamente 5 kHz. Actualmente, este sistema está acoplado a un sistema de vaporización láser, lo cual permite el estudio de muestras termolábiles. El segundo equipo es un espectrómetro de tipo CP-FTMW, basado en el diseño de Pate. Su incorporación a la Universidad del País Vasco (UPV/EHU) fue más reciente (2014) y en esta Tesis Doctoral se destinó un gran esfuerzo a su construcción y puesta a punto. Permite la adquisición del rango 6-18 GHz en un solo pulso molecular y, además, es posible la acumulación de hasta millones de espectros de forma coherente para alcanzar la relación señal/ruido deseada.

El capítulo I de esta memoria es una introducción tanto a la técnica experimental como al trabajo realizado en esta Tesis Doctoral. En el capítulo II, se resume la teoría de la espectroscopia rotacional necesaria para entender los conceptos básicos del análisis de un espectro rotacional. En el capítulo III, se resume la metodología llevada a cabo en la Tesis Doctoral, desde los cálculos teóricos hasta el equipamiento instrumental empleado.

En el capítulo IV, analizamos la capacidad de la técnica CP-FTMW para explorar espacios conformacionales complejos. En concreto, realizamos el estudio de tres moléculas: α-ionona, β-ionona y β-damascona. Se trata de tres moléculas bastante flexibles y considerablemente grandes en el marco de la espectroscopia de rotación. Los tres sistemas están estructuralmente relacionados entre sí (formula molecular $C_{13}OH_{20}$) y también con el retinal, un biocromóforo muy importante que está involucrado en el proceso de visión. La β-ionona se puede considerar como la unidad reducida prototípica del retinal. Las otras dos especies (α-ionona y β-damascona) son especies "mutantes", en las que hay pequeños cambios estructurales con respecto a la β-ionona. En este capítulo, exploramos el espacio conformacional de las tres moléculas para evaluar las diferencias que existen entre ellas. Primeramente, exploramos las conformaciones de forma teórica, mediante el cálculo de las superficies de energía potencial. En un segundo lugar, identificamos las diferentes conformaciones observadas experimentalmente. Así, detectamos seis conformaciones diferentes para la β-ionona y cuatro para cada una de las especies mutantes. Además, los espectros rotacionales muestran estructura hiperfina debida al movimiento de rotación interna de uno o varios grupos metilo. Los espectros rotacionales poseen una relación señal/ruido muy elevada, lo que permite identificar los espectros de las especies resultantes de sustituciones isotópicas en abundancia natural de ^{13}C (abundancia ~1%) y ^{18}O (~0.2%). Gracias al trabajo realizado en el capítulo IV, podemos observar cómo la β-ionona (es decir, la especie "natural") posee mayor flexibilidad que las dos especies mutantes. Esta mayor flexibilidad podría haber ayudado al retinal a adaptarse mejor a su entorno biológico en la proteína en la que se encuentra albergado.

En el capítulo V, exploramos la complementariedad de las dos técnicas rotacionales disponibles en la Universidad del País Vasco (UPV/EHU), es decir, los espectrómetros FTMW y CP-FTMW, a través del estudio rotacional de la cotinina. Dicha molécula pertenece a la familia de los nicotinoides y está estructuralmente relacionada con la nicotina (la única diferencia entre ambas moléculas es que la cotinina tiene un grupo C=O adicional). El primer paso en el procedimiento experimental de este capítulo es la toma del espectro rotacional en el espectrómetro de banda ancha CP-FTMW. Esto permite tener una idea global de forma rápida de las diferentes conformaciones que adopta esta molécula en fase gas. En concreto, se observa que la cotinina posee dos conformaciones experimentales, que difieren en la rotación de un anillo de piridina. Cabe destacar que los métodos teóricos predicen otros dos confórmeros en un rango de energía bastante bajo; sin embargo, éstos no se observan experimentalmente. En este capítulo demostramos que la ausencia de estas dos conformaciones se debe a que relajan a las conformaciones más estables (observadas experimentalmente). La cotinina tiene una estructura hiperfina muy compleja, debida a la presencia de dos átomos de ^{14}N y un grupo metilo que realiza un movimiento de rotación interna. No es posible resolver esta estructura hiperfina con la resolución del CP-FTMW y, por ello, algunas transiciones de esta molécula se midieron en el espectrómetro FTMW, que dispone de una mayor resolución espectral. La identificación

de los diferentes componentes de la estructura hiperfina confirma la asignación de las dos conformaciones realizada previamente con el CP-FTMW. Por último, el estudio rotacional de la cotinina nos ofrece la posibilidad de comparar con la nicotina, cuyo espectro de microondas había sido analizado anteriormente. Cabe destacar que para ambas moléculas se detectan dos conformaciones en fase gas. Además, se puede considerar que las conformaciones son análogas; tanto en la cotinina como en la nicotina las dos conformaciones observadas difieren en la rotación del anillo de piridina. La principal diferencia entre las dos moléculas es que en la cotinina hay una interacción C-H···O=C, que no puede tener lugar en la nicotina y que, además, provoca una disminución de la barrera de rotación interna del grupo metilo.

En el capítulo VI, usamos la espectroscopía de microondas (en concreto la técnica FTMW) para investigar el equilibrio tautomérico de la purina, una base nitrogenada de gran importancia en el ADN, ya que es la unidad básica de las nucleobases adenina y guanina. La purina existe predominantemente en dos formas tautoméricas, N(9)H y N(7)H. Gracias a la elevada resolución espectral de las técnicas de espectroscopía de microondas, se pueden distinguir e identificar ambas especies tautoméricas. Además, también es posible cuantificar la relación de poblaciones de ambas especies, que en este caso es de N(7)H/N(9)H~1/40. Asimismo, la purina tiene una estructura hiperfina extremadamente compleja debido a la presencia de cuatro ^{14}N en su estructura. Esto produce que cada transición rotacional se desdoble en muchas componentes (entre 4 y 41, dependiendo de cada transición). Gracias a la resolución espectral del espectrómetro FTMW, fue posible resolver la estructura hiperfina de la purina. Así, la información obtenida de este análisis permite confirmar la asignación de los dos tautómeros. Por último, cabe destacar que este análisis de la purina constituye la primera asignación de la estructura hiperfina de una molécula con cuatro átomos de ^{14}N no equivalentes.

En el capítulo VII, ahondamos en otro aspecto clave de la espectroscopía rotacional moderna: la relación entre los cálculos teóricos y los resultados experimentales. Se trata de una relación bilateral. Por una parte, el tamaño de los sistemas moleculares que se pueden determinar espectroscópicamente es cada vez mayor y, por ello, son necesarios cálculos teóricos (sobre todo mecanocuánticos) para predecir las conformaciones y para interpretar los espectros rotacionales. Por otra parte, en el desarrollo de nuevos métodos teóricos, sigue siendo necesario comprobar la capacidad predictiva de éstos frente a resultados experimentales. En este sentido, la espectroscopía de rotación es una técnica idónea como banco de pruebas para los cálculos teóricos. Gracias al empleo de expansiones supersónicas, las moléculas se encuentran en condiciones aisladas, libres de cualquier tipo de interacción. Por ello, los resultados obtenidos experimentalmente son directamente comparables con las estructuras obtenidas con métodos teóricos (en especial *ab initio* y DFT). En esta Tesis Doctoral, ilustramos la relación entre teoría y experimento con el ejemplo de dos moléculas de interés biológico. En primer lugar, estudiamos el caso del metil jasmonato, una fitohormona de gran relevancia en los sistemas de defensa de las plantas, entre otros roles. Estructuralmente, esta molécula posee un anillo de 5 eslabones unido a dos cadenas flexibles. En el capítulo VII, observamos cómo es absolutamente necesario emplear métodos teóricos capaces de describir interacciones dispersivas (en concreto, las interacciones entre los dos brazos flexibles) para poder asignar las conformaciones observadas. Si se emplean métodos que

no incluyen fuerzas dispersivas (como el funcional B3LYP, por ejemplo), no es posible identificar los confórmeros observados. En el caso del B3LYP en concreto, es necesario añadir correcciones dispersivas como D3 o D3BJ para poder reproducir los resultados experimentales. En segundo lugar, presentamos el caso del zingerone, una molécula odorante que consiste en un anillo de benceno sustituido por un hidroxilo y por una cadena lateral flexible. En este caso, la conformación adoptada por la molécula depende de una competición sutil entre dos interacciones débiles: C-H···π y C-H···O. Las dos interacciones no se pueden dar simultáneamente y la estructura tridimensional resultante depende de cuál de las dos tenga lugar. Debido a que se trata de interacciones muy débiles, los métodos teóricos tienen problemas para evaluar la magnitud de cada una de ellas y para determinar cuál es la "ganadora". Gracias a la espectroscopía de rotación, podemos determinar que es la interacción C-H···O la que predomina. Observamos que algunos de los métodos teóricos (entre ellos, MP2, comúnmente empleado en este tipo de experimentos) ni siquiera son capaces de predecir esta estructura.

El capítulo VIII pretende ser un ejemplo del empleo de la espectroscopía de microondas en el análisis conformacional de moléculas de interés biológico en fase gas, así como de la posibilidad de complementar los resultados obtenidos con otras técnicas (por ejemplo, con estudios estructurales en disolución). De esta forma, se puede obtener un conocimiento mayor de las propiedades estructurales de los sistemas moleculares en diferentes medios. En concreto, nos centramos en el monosacárido metil 2-deoxi-ribofuranosa, que es el azúcar presente en el ADN. En este trabajo, se han compatibilizado síntesis química, espectroscopía rotacional en fase gas y estudios conformacionales en disolución acuosa. En primer lugar, el grupo del Profesor Benjamin Davis en la Universidad de Oxford sintetizó el monosacárido. Mediante metilación en el oxígeno en posición 1, fue posible aislar los dos anómeros (α y β) de la forma furanosa (anillo de cinco eslabones). A continuación, en la Universidad del País Vasco UPV/EHU, procedimos a realizar el estudio conformacional de las dos muestras (anómeros α y β) separadamente mediante espectroscopía de microondas CP-FTMW. Detectamos tres confórmeros del anómero β y dos del α. Por último, el grupo del Profesor Francisco Corzana en la Universidad de la Rioja analizó las conformaciones en disolución acuosa combinando Resonancia Magnética Nuclear (RMN) y Dinámica Molecular. Resulta especialmente interesante comparar los resultados obtenidos en fase aislada y en disolución. Así pues, se puede observar que en fase gas predominan las estructuras que favorecen interacciones intramoleculares (por ejemplo, O-H···O). Sin embargo, en disolución, esas conformaciones no están favorecidas, principalmente debido a la solvatación de los grupos más polares de la molécula (por ejemplo, grupos OH).

En el capítulo IX, incluimos un caso de aplicación de la espectroscopía de rotación como técnica analítica. En el pasado, hubo varios intentos de emplear la espectroscopía de microondas como detectores de gases. Sin embargo, esto no tuvo mucho éxito debido a varios factores, como la complejidad de los espectros de rotación o la dificultad de la calibración en intensidades. En la actualidad, con las nuevas mejoras en la técnica, está resurgiendo el interés por aplicar la espectroscopía rotacional a la resolución de problemas analíticos. Recientemente fue creada la empresa Brightspec, como *spin-off* del grupo de investigación de Brooks H. Pate, que comercializa espectrómetros de banda ancha (tipo CP-FTMW) con dos objetivos principales. El primero es la detección de trazas en procesos

químicos, de combustión o petroquímicos y el segundo es el mercado de las empresas farmacéuticas, en especial en el análisis de diastereoisómeros y enantiómeros. En el capítulo IX de esta Tesis Doctoral, presentamos un trabajo en el que detectamos los productos gaseosos de degradación producidos al calentar una muestra de $CH_3NH_3PbI_3$. Esta sustancia es una perovskita híbrida que está siendo estudiada en profundidad para su aplicación en placas fotovoltaicas. En la bibliografía se postulan dos mecanismos de degradación posibles para esta sustancia. Sin embargo, los estudios experimentales realizados hasta la fecha no permiten tener una conclusión clara acerca de qué mecanismo es el predominante. En este trabajo, confirmamos inequívocamente que ambos mecanismos tienen lugar simultáneamente en las condiciones del experimento. Gracias a la elevada resolución espectral de esta técnica, podemos identificar sin lugar a duda los productos de descomposición gaseosos que confirman que ambos mecanismos tienes lugar a la vez.

En conclusión, esta Tesis Doctoral demuestra que los nuevos avances en la espectroscopia de rotación moderna abren un inmenso campo de posibilidades como el análisis de espacios conformacionales complejos, la resolución de equilibrios tautoméricos o incluso como técnica analítica.

Chapter I.

Introduction

In this Thesis, we review the potential of modern rotational spectroscopy to solve problems in different areas such as chemistry, biology and as an analytical tool. Rotational (or microwave) spectroscopy is a high-resolution technique that is carried out in the gas phase. As such, it has traditionally been related to the accurate structural elucidation of molecules or intermolecular complexes under isolation conditions. Virtually all microwave spectrometers used to date are not commercially available, meaning that the research groups are in charge of building and maintaining the devices. This, together with the rather high economical cost of these apparatus may have slowed down the success of the technique. However, thanks to the most recent advances in instrumentation, new theoretical methods to support the experiments and the computational power of large computer clusters, rotational spectroscopy is undergoing a renaissance in the last decades. The field is opening now to tackling new problems; for instance, the structural determination of "larger" biomolecular systems (15-30 heavy atoms), the identification of enantiomers and the determination of enantiomeric excess of mixtures, the detection of molecules in outer space thanks to the use of radiotelescopes or the potential use of this technique as an analytical tool in the pharmaceutical industry, among others. We will consider some of these aspects in this Thesis, with specific cases that we have studied at the Spectroscopy Group at the University of the Basque Country (UPV/EHU).

Rotational spectroscopy studies transitions between rotational energy levels of molecules or intermolecular complexes in the gas phase. Rotational transitions occur in the microwave region. Figure I.1 summarizes the frequency ranges in the microwave region. In this Thesis, we will exclusively work in the centimeter wave (cm wave) range.
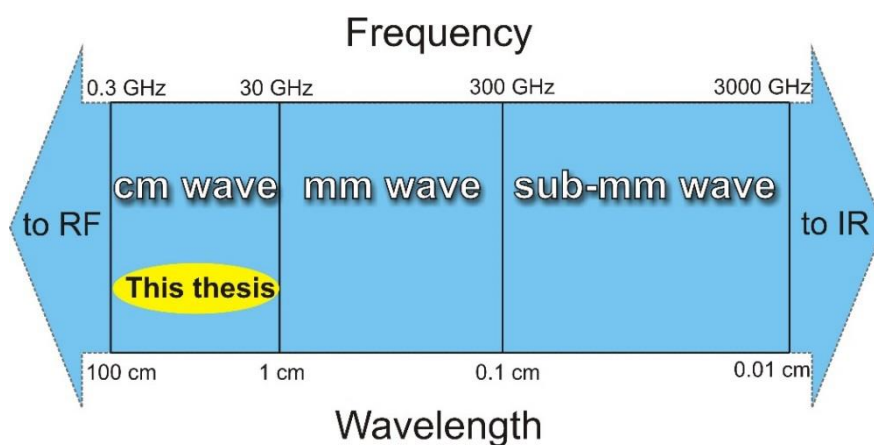

Figure I.1 Microwave region of the electromagnetic spectrum.

I.1 Microwave spectroscopy: past and present

The first microwave spectroscopy study dates back to 1934.[1] It investigated the ammonia rotational spectrum, with special focus on the *umbrella* inversion motion of this molecule. It was an absorption experiment, carried out in a static gas cell. Briefly, monochromatic microwave radiation was passed through a sample cell and the transmitted intensity was monitored. We can also refer to this kind of experiments as *frequency-domain*. In the following decades, spectroscopists studied a myriad of small molecular systems (up to ~10 heavy atoms) using the same basic experimental design. However, important improvements in spectral resolution and sensitivity were achieved, partly due to the instrumental advances in microwave radiation sources and detectors resulting from the development of radars in World War II. A major breakthrough in the field was the introduction of *time-domain* rotational spectroscopy techniques.[2,3,4] These can be viewed as Fourier Transform experiments analogous to pulsed NMR spectroscopy. Briefly, a relatively high power (up to 20W) monochromatic microwave pulse is used to excite the molecular sample. After the excitation pulse has dissipated, the molecular emission in the time domain (Free Induction Decay, FID) is detected and later Fourier transformed to obtain the rotational spectrum in the frequency domain. It was proved that better sensitivity and resolution were achieved compared to *frequency-domain* rotational spectroscopy. Finally, in 1981, Balle and Flygare designed a new spectrometer combining FTMW (Fourier Transform Microwave) spectroscopy and supersonic expansions.[5] They achieved better resolution and sensitivity and rotational spectroscopists have extensively used this technique in the last 40 years.

More recently, other developments in the field of rotational spectroscopy have also had an impact on the work of microwave spectroscopists. In 1996, a new improvement in FTMW techniques was achieved with the introduction of the Coaxially Oriented Beam Resonator Arrangement (COBRA).[6] In this set-up, the supersonic expansion is coaxial with the microwave resonator and one can obtain higher spectral resolution and sensitivity compared to a perpendicular arrangement. Very importantly, the instrument was fully automated for scanning operations and remotely controlled by a computer. Many microwave spectrometers around the world are based on the COBRA design, including one of the two microwave spectrometers available at the University of the Basque Country (UPV/EHU).

The incorporation of laser ablation techniques was a major breakthrough in the field. Two pioneering set-ups were independently created that used laser ablation techniques mostly to study metallic oxides and halides in the gas phase.[7,8] Later, in 1995, laser vaporization techniques were incorporated to FTMW spectrometers to bring thermally unstable molecules into the gas phase to be later probed with rotational spectroscopy.[9] This opened the field to the study of biologically relevant molecules such as amino acids[10] or sugars.[11] Furthermore, the use of shorter picosecond laser pulses (rather than nanosecond) was a major advancement in laser vaporization techniques, resulting in greater signal-to-noise ratios, less decomposition of the sample and a longer duration of the latter.

Later, in 2008, Brooks H. Pate introduced the novel technique Chirped Pulse Fourier Transform Microwave (CP-FTMW) spectroscopy.[12] By using broadband excitation pulses,

this spectrometer allows, in general, for shorter spectral acquisition times compared to FTMW spectrometers based on Balle-Flygare's design. The CP-FTMW machine has had a tremendous success in the microwave community in recent years.

The spectroscopic community has also devoted some efforts to the development of conformer specific microwave techniques. In rotational spectra, transitions belonging to different conformers appear interspersed amongst one another, which can be a source of difficulty in the subsequent analysis. To facilitate this task, several approaches have been devised to identify the rotational transitions belonging to the same conformation by using microwave-microwave double resonance techniques.[13,14]

Finally, the most recent development is probably the application of double quantum coherence to phase-discriminate the enantiomeric pair of chiral molecules, thanks to three-wave mixing techniques.[15,16,17] Enantiomers can be discriminated spectroscopically in this way, and it is possible to estimate enantiomeric excess. However, a reference of a pure enantiomer must be used in order to identify the nature (R or S) of a given chiral molecule.

Apart from the instrumental developments abovementioned, it is worth mentioning the tremendous impact that theoretical calculations and large computing facilities have had on rotational spectroscopy, and, in particular, on the use of this technique in structural elucidation. As the size of the molecular systems targeted increases, it becomes more necessary to rely on theoretical calculations to have an idea of the conformations that the molecule may adopt. This is particularly relevant in flexible molecules or intermolecular complexes, for which chemical intuition may be insufficient to predict the preferred conformations. The advancements in theoretical methods such as Molecular Mechanics (to perform fast conformational searches) or *ab initio* and Density Functional Theory (DFT) methods (to obtain accurate structural predictions) are key in the success of modern structural studies. Nowadays, it is possible to obtain very accurate predictions of molecular conformations in a rapid way and this is most helpful in the interpretation of rotational spectra.

I.2 Uses of rotational spectroscopy

The most important piece of information that one can extract from a rotational spectrum of a given molecular species is the value of the rotational constants (A, B and C). With a spectral resolution of ~3-100 kHz (in the order of 10^{-7}-10^{-6} cm^{-1}) in modern microwave spectrometers, the experimental values of A, B and C are obtained to a very high precision (not achievable with other techniques). Rotational constants are inversely proportional to the moments of inertia along the principal axes of the molecule (I_a, I_b and I_c). Therefore, they are directly related to the three-dimensional structure of that molecule. Small structural/conformational changes lead to large changes in the rotational constants. Therefore, different conformers give rise to different rotational spectra that can be unambiguously identified. Even isotopologues are identified routinely in rotational spectra. With all this, rotational spectroscopy is a very powerful tool to perform structural studies under isolation conditions.

In fact, most rotational studies focus on the structural study of molecules or molecular aggregates in one way or another. For example, the conformational landscapes of flexible molecules are very often probed with microwave spectroscopy. Up to fifteen different conformers were identified for citronellal.[18] In this way, we can study the intrinsic structural preferences of a molecule without the interference of interactions such as crystal packing or solvent. The presence of intramolecular interactions can be detected and its effect on the overall conformation of the molecule can be assessed. Furthermore, microwave spectroscopy can also be used to study tautomeric equilibria. In the case of keto-enol tautomerism, for example, the two tautomeric forms can be independently and unambiguously identified in rotational spectra. By estimating the population ratio of the two species, we can have an overall idea of the balance between keto and enol forms.

The study of intermolecular complexes is another field in which the power of rotational spectroscopy as a structure elucidation tool becomes clear. Supersonic expansions allow for the isolation of intermolecular complexes (dimers, trimers, tetramers, and up to decamers, such as the water decamer[19]) that can be probed with microwave spectroscopy. Spectroscopists use this technique for the investigation of the nature of the intermolecular interactions that hold molecules together. Several research groups, such as the groups of Professor Walther Caminati at the University of Bologna or Professor Anthony Legon at University of Bristol devote a lot of effort to the identification of weak intermolecular interactions and the competition between them. They have studied a great number of short-lived intermolecular complexes (mostly dimers) by confronting small monomers (for example, substituted alkanes, small carboxylic acids or alcohols) and analyzing the interactions between them. The nature of the interactions under study ranges from strong and moderate hydrogen bonds (O-H···O, O-H···N, etc) to weak hydrogen bonds and other kind of interactions (C-H···F weak hydrogen bond,[20] Cl···C halogen bond[21] and others[22,23]) Moreover, microwave studies on intermolecular complexes are also used to model the interactions between biomolecules and their biological receptors. For example, the study on the sevoflurane-benzene heterodimer[24] mimics the interaction between the anesthetic (sevoflurane) and aromatic residues at the protein's binding site.

In some cases, rotational transitions display fine and hyperfine splittings from which one can extract structural information. For instance, molecules with one or several nuclei with spin (I) equal to or greater than 1 will give rise to rotational spectra with hyperfine structure, due to the effect of nuclear quadrupole coupling. The analysis of this hyperfine structure renders information about the electronic surrounding of the atom. In addition, some rotational spectra may also display fine structure arising from large amplitude motions, from which one can extract dynamical information. A recurring example is the case of molecules with a methyl group. The internal rotation of the methyl top couples with the overall rotation of the molecule and produces splittings in rotational transitions. By analyzing those splittings, we can estimate the barrier to internal rotation of the methyl top. This, in turn, yields structural information; for example, about the sterical hindrance around the methyl group. Moreover, microwave spectroscopy is also a useful tool in the determination of experimental permanent dipole moments, thanks to Stark effect experiments.[25]

Furthermore, microwave spectroscopy studies serve as a perfect benchmark for testing the performance of quantum chemical methods. Rotational spectroscopy in supersonic expansions yields the structures of molecular systems under isolation conditions (*in vacuo*). Therefore, the results are directly comparable to the theoretical structures obtained with *ab initio* or DFT methods. For example, in the cases where there is a subtle competition between two intra- or intermolecular interactions in a molecule (or intermolecular complex), theoretical methods may struggle to find the dominant one. In those cases, rotational spectroscopy experiments will find the solution by unambiguously identifying the experimental molecular structure. This interplay between experiment and theory is even more important nowadays, because the size of the molecular systems targeted in structural studies (by either microwave spectroscopy or any other technique) is increasing and, therefore, it becomes necessary to support the experiments with accurate theoretical predictions.

Because of the inherently high spectral resolution of microwave spectroscopy experiments, rotational spectra serve as fingerprints of molecules. That is, the observation of several rotational lines belonging to a given molecular species unambiguously confirms the presence of that species. Indeed, the microwave spectroscopy community devotes a great effort to the detection of molecules in outer space. By comparing laboratory rotational frequencies with data obtained from radiotelescopes such as ALMA (Atacama Large Millimeter Array, in Chile), it is possible to confirm the presence of molecules in space. For this purpose, the millimeter wave (mm wave) and sub-mm wave frequency regions are most useful, since that is the frequency range that radiotelescopes cover. For instance, CH_3NCO was detected in Orion Clouds.[26]

The fact that rotational spectra act as fingerprints of molecular species implies that this technique may be used as an analytical tool for the detection of chemical species. Since the 1990s, there have been several attempts to commercialize trace gas sensors based on FTMW spectrometers. However, the complexity of rotational spectra and the problems with intensity calibrations, amongst other issues, have prevented the success of these techniques. Nowadays, with the new developments in instrumentation, there is a renewed interest in commercializing microwave spectrometers. The company Brightspec was founded in 2012 as a spin-off from Brooks H. Pate's laboratory. It commercializes broadband spectrometers that serve two main purposes. On the one hand, some of their instruments are designed for the determination of trace level process contaminants in chemical, petrochemical, combustion, and semiconductor industries. On the other hand, they focus on the pharmaceutical industry, in particular, chiral process monitoring. The unambiguous identification of molecular species, including diastereoisomers and, to some extent, enantiomers, is the major strength of rotational spectroscopy that could transform it into an analytical tool.

I.3 Aim and objectives of this Thesis

The Spectroscopy Group at the University of the Basque Country (UPV/EHU) (Department of Physical Chemistry) currently possesses two microwave spectrometers. The first one (built in 2010) is an FTMW machine based on Balle-Flygare's original design, covering the 5-18 GHz frequency region, with a spectral resolution of ~5 kHz. It is coupled to an ultrafast laser vaporization set-up, allowing for the vaporization of thermally unstable samples. The second one is a CP-FTMW machine based on Pate's design, working on the frequency range 6-18 GHz, with a spectral resolution of ~20 kHz. A major part of the work in this Thesis was devoted to the construction, implementation and optimization of the CP-FTMW spectrometer and, therefore, we will mainly focus on this machine.

The objectives of this Thesis are:

- Implementation of a CP-FTMW spectrometer at the Spectroscopy Group at the University of the Basque Country (UPV/EHU)

- Investigation of the potential of rotational spectroscopy in conformational elucidation, the determination of biomolecular structures, the study of tautomeric equilibria and as a potential analytical tool

In Chapter II, we will review the basic concepts about the theory behind rotational spectra. This chapter is not meant as a thorough explanation of rotational spectroscopy, but rather as an overview of the basic tools to understand the analysis of rotational spectra.

In Chapter III, we will summarize the methodology employed in rotational studies. In particular, we will review the basic concepts about experimental set-ups, computational methods, and some other concepts that will be needed throughout this Thesis.

Chapter IV focuses on α- and β-ionone and β-damascone, three structurally related biomolecules. We use these molecular systems to explore the power of microwave spectroscopy to probe rich conformational landscapes of moderately large flexible molecules.

In Chapter V, we unravel the conformations of the nicotinoid cotinine in the gas phase. The rotational study of this molecule needed the use of the two spectrometers at the University of the Basque Country (UPV/EHU) (FTMW and CP-FTMW). This chapter serves as an example of the complementarity of both techniques: the CP-FTMW machine provided an overview of the conformational landscape of cotinine in a rapid way, while the FTMW device was used to solve the hyperfine structure of rotational transitions.

Chapter VI deals with purine, a nucleobase that presents a very complex hyperfine pattern due to the presence of four ^{14}N nuclei. The goal of this study is to address the tautomeric equilibrium of purine. For doing so, we take advantage of the unequalled spectral resolution of FTMW spectroscopy to solve the hyperfine pattern of rotational transitions.

In Chapter VII, the cases of methyl jasmonate and zingerone stress the importance of the interplay between theory and experiment and show how the results from microwave spectroscopy serve as a benchmark for theoretical methods.

Chapter VIII presents the structural study of methyl 2-deoxy-D-ribofuranoside, the monosaccharide present in the DNA, as an example of the potential of microwave spectroscopy in the study of biomolecular systems. We combine the results of rotational spectroscopy with further data in solution (Molecular Dynamics calculations and NMR spectroscopy). Thus, in this work, we probe the conformational landscape of this sugar under isolation conditions, and we compare it with data on aqueous solution. In this way, we can differentiate the intrinsic properties of this sugar from the ones coming from interactions with the solvent.

Finally, Chapter IX serves as an example of rotational spectroscopy as an analytical tool. Thanks to this technique, we can monitor the gaseous degradation products of a hybrid perovskite that is a prototype material for solar cells. The goal is to determine the degradation mechanism of this substance.

I.4 References

[1] C. E. Cleeton, N. H. Williams, *Phys. Rev.* **1934**, *45*, 234-237.

[2] R. H. Dicke, R.H. Romer, *Rev. Sci. Instrum.* **1955**, *26*, 915-928.

[3] J. Ekkers, W. H. Flygare, *Rev. Sci. Instrum.* **1976**, *47*, 448-454.

[4] R. M. Somers, T. O. Poehler, P. E. Wagner, *Rev. Sci. Instrum.* **1975**, *46*, 719-725.

[5] T. J. Balle, W. H. Flygare, *Rev. Sci. Instrum.* **1981**, *52*, 33-45.

[6] J.-U. Grabow, W. Stahl, H. Dreizler, *Rev. Sci. Instrum.* **1996**, *67*, 4072-4084.

[7] R. D. Suenram, F. J. Lovas, G. T. Fraser, K. Matsumura, *J. Chem. Phys.* **1990**, *92*, 4724-4733.

[8] K. D. Hensel, C. Styger, W. Jäger, A. J. Merer, M. C. L. Gerry, *J. Chem. Phys.* **1993**, *99*, 3320-3328.

[9] F. J. Lovas, Y. Kawashima, J.-U. Grabow, R. D. Suenram, G. T. Fraser, E. Hirota, *Astrophys. J.* **1995**, *455*, L201-L204.

[10] A. Lesarri, S. Mata, E. J. Cocinero, S. Blanco, J. C. López, J. L. Alonso, *Angew. Chem. Int. Ed.* **2002**, *41*, 4673-4676.

[11] E. J. Cocinero, A. Lesarri, P. Écija, F. J. Basterretxea, J.-U. Grabow, J. A. Fernández, F. Castaño, *Angew. Chem. Int. Ed.* **2012**, *51*, 3119-3124.

[12] G. G. Brown, B. C. Dian, K. O. Douglass, S. M. Geyer, S. T. Shipman, B. H. Pate, *Rev. Sci. Instrum.* **2008**, *79*, 053103-1 – 053103-13.

[13] M.-A. Martin-Drumel, M. C. McCarthy, D. Patterson, B. A. McGuire, K. N. Crabtree, *J. Chem. Phys.* **2016**, *144*, 124202.

[14] A. O. Hernandez-Castillo, C. Abeysekera, B. M. Hays, T. S. Zwier, *J. Chem. Phys.* **2016**, *145*, 114203.

[15] D. Patterson, M. Schnell, J. M. Doyle, *Nature* **2013**, *497*, 475-477.

[16] D. Patterson, J. M. Doyle, *Phys. Rev. Lett.* **2013**, *111*, 023008.

[17] S. Lobsiger, C. Pérez, L. Evangelisti, K. K. Lehmann, B. H. Pate, *J. Phys. Chem. Lett.* **2015**, *6*, 196-200.

[18] S. R. Domingos, C. Pérez, C. Medcraft, P. Pinacho, M. Schnell, *Phys. Chem. Chem. Phys.* **2016**, *18*, 16682-16689.

[19] C. Pérez, D. P. Zaleski, N. A. Seifert, B. Temelso, G. C. Shields, Z. Kisiel, B. H. Pate, *Angew. Chem. Int. Ed.* **2014**, 53, 14368-14372.

[20] L. Spada, Q. Gou, S. Tang, W. Caminati, *New J. Chem.* **2015**, *39*, 2296-2299.

[21] W. Caminati, L. Evangelisti, G. Feng, B. M. Giuliano, Q. Gou, S. Melandri, J.-U. Grabow, *Phys. Chem. Chem. Phys.* **2016**, *18*, 17851-17855.

[22] J. G. Hill, A. C. Legon, *Phys. Chem. Chem. Phys.* **2015**, *17*, 858-867.

[23] A. C. Legon, *Phys. Chem. Chem. Phys.* **2017**, *19*, 14884-14896.

[24] N. A. Seifert, D. P. Zaleski, C. Pérez, J. L. Neill, B. H. Pate, M. Vallejo-López, A. Lesarri, E. J. Cocinero, F. Castaño, I. Kleiner, *Angew. Chem.* **2014**, *126*, 3274-3277.

[25] P. D. Godfrey, S. Firth, L. D. Hatherley, R. D. Brown, A. P. Pierlot, *J. Am. Chem. Soc.* **1993**, *115*, 9687-9691.

[26] J. Cernicharo, Z. kisiel, B. Tercero, L. Kolesniková, I. R. Medvedev, A. López, S. Fortman, M. Winnewisser, F. C. de Lucia, J. L. Alonso, J.-C. Guillemin, *Astron. Astrophys.* **2016**, *587*, L4 1-44.

Chapter II.

Theory of rotational spectroscopy

This chapter reviews the basic theory about molecular rotation necessary to understand the analysis of rotational spectra. The aim of the following sections is not to give a full and detailed description of the theory and the underlying mathematics, but rather a general overview presenting the basic tools to understand rotational analysis. Thorough analysis of molecular rotation theory and subsequent mathematical developments can be found in the literature.[1,2,3]

II.1 Hamiltonian for rotation

The first approach to molecular rotation is to assume the rigid rotor model, in which bond angles and distances adopt constant values. In that case, the Hamiltonian for molecular rotation can be written as:

$$H_{rot} = AJ_a^2 + BJ_b^2 + CJ_c^2$$

where J_g ($g = a, b, c$) are the operators corresponding to the angular momenta along the principal axes of inertia a, b and c. A, B and C are the rotational constants, which are inversely proportional to the moments of inertia along a, b and c:

$$A = \frac{h^2}{8\pi^2 I_a} \qquad B = \frac{h^2}{8\pi^2 I_b} \qquad C = \frac{h^2}{8\pi^2 I_c}$$

where I_g ($g = a, b, c$) is the moment of inertia along the g axis ($I_g = \sum_i m_i r_{g,i}^2$) ($m_i$ and $r_{g,i}$ are the mass of atom i and its distance to the g axis, respectively).

The principal axes of inertia are defined as follows. The a axis is the one that yields the minimum value for I_a and the c axis is chosen to give the maximum value to I_c. It can be proved that a and c are always perpendicular to each other. Finally, b is the axis orthogonal to a and c. Depending on the values of I_a, I_b and I_c, the molecules can be divided in the following groups:

-Linear: I_a=0 ‹ I_b=I_c

-Spherical top: I_a=I_b=I_c

-Prolate symmetric top: I_a ‹ I_b=I_c

-Oblate symmetric top: I_a=I_b ‹ I_c

-Asymmetric top: I_a ‹ I_b ‹ I_c

Most of the biomolecules targeted in microwave studies in the gas phase belong to the last group (asymmetric tops), and to the C_1 symmetry group. However, in some cases, their structure may be close to that of a symmetric top (prolate or oblate). Ray's asymmetry parameter (κ)[4] is a measure of how much a conformation deviates from the symmetric top limits:

$$\kappa = \frac{2B - A - C}{A - C}$$

The values of κ lie between +1 and -1. In the prolate limit κ=-1 while for an oblate top κ=+1.

For linear and symmetric top molecules, the energy levels can be expressed in a closed form, as follows:[5,6]

$$E(J) = BJ(J + 1) \text{ linear}$$

$$E(J,K) = BJ(J + 1) + (A - B)K^2 \text{ Prolate}$$

$$E(J,K) = BJ(J + 1) + (C - B)K^2 \text{ Oblate}$$

where J=0, 1 ,2 , 3... is the quantum number associated to total angular momentum (J, with $J^2 = J_a{}^2 + J_b{}^2 + J_c{}^2$) and K=0, ±1, ±2,..., ±J is the quantum number associated to the projection of the angular momentum along one of the symmetry axes (J_g with g = a for prolate and c for oblate).

In the case of asymmetric rotors, the theoretical treatment of molecular rotation is more complex and the energy levels cannot be expressed in convenient equations. None of the J_g operators commutes with H_{rot} and therefore K is no longer a good quantum number. An important difference with the symmetric case is that, while in the symmetric case the energy levels corresponding to +K and −K are degenerate (E(J,K) depends on the square of K), this is not the case for the asymmetric rotor. Hence, each J level gives rise to J+1 distinct energy sublevels in a symmetric top, while it generates 2J+1 sublevels in an asymmetric top. The approach to label the rotational energy levels in an asymmetric top is to extrapolate to the prolate and oblate symmetric top limits. Therefore, for asymmetric tops rotational energy levels are expressed as J,K$_{-1}$, K$_{+1}$, where K$_{-1}$ represents the K value corresponding to the limiting prolate top and K$_{+1}$ the one for the oblate top.

It is important to note that K$_{-1}$ y K$_{+1}$ are not *good* quantum numbers, but rather numbers used to design the sequence of sublevels for a given J value. They are often referred to as *pseudo-quantum numbers*.

II.2 Selection rules

In this section, we will summarize the selection rules for rotational transitions. In particular, the focus is on asymmetric rotors, which encompasses all the molecular systems studied in this thesis.

Given two rotational levels defined by the wavefunctions ψ(J, K$_{-1}$, K$_{+1}$) and ψ(J′,K′$_{-1}$,K′$_{+1}$), the transition dipole moment is the following magnitude:

$$R = \int \psi^*(J, K_{-1}, K_{+1}) \, \boldsymbol{\mu} \, \psi(J', K'_{-1}, K'_{+1})$$

where $\boldsymbol{\mu}$ is the electric dipole moment operator. The intensity of a rotational transition is proportional to the square of the transition dipole moment and hence, the condition for allowed transitions between rotational energy levels is that R adopts non-zero values. This imposes a suite of restrictions on the values of J, K$_{-1}$ and K$_{+1}$ of the two energy levels that we will discuss in the following paragraphs.

First, for asymmetric rotors the conditions on J are that ΔJ=0, ±1 (this is also the case for symmetric rotors). Q-branches correspond to ΔJ=0, P-branches to ΔJ=-1 and R branches to ΔJ=+1.

Second, regarding the pseudo-quantum numbers K_{-1} and K_{+1}, the selection rules derived from the condition $\boldsymbol{R} \neq 0$ are summarized in Table II.1.

Table II.1 Selection rule for the pseudo quantum numbers K_{-1} y K_{+1} for an asymmetric rotor. Larger variations in the indices (in parentheses) produce weaker transitions.

Type of transition	ΔK_{-1}	ΔK_{+1}
a	$0\,(\pm even)$	$\pm 1\,(\pm odd)$
b	$\pm 1\,(\pm odd)$	$\pm 1\,(\pm odd)$
c	$\pm 1\,(\pm odd)$	$0\,(\pm even)$

At this point, it is important to note that only molecules with non-zero permanent dipole moment (μ) can be studied with microwave spectroscopy. Molecules with $\mu = 0$ (molecules with inversion center always have $\mu=0$ by symmetry requirements) do not possess allowed rotational transitions and therefore it is not possible to record their rotational spectra. In the case of molecules with non-zero μ, it is necessary to know the orientation of the electric dipole moment in order to identify the type of transitions in the spectrum. For example, if the only component of μ is along the a axis, then $\mu_a \neq 0$ and $\mu_b=\mu_c=0$ and the only transitions expected in the rotational spectrum are a-type. The molecules of biological interest analyzed in this Thesis normally present at least two non-zero components of the permanent dipole moment and therefore different types of transitions are found simultaneously in the spectra.

II.3 Centrifugal distortion

So far, we have assumed the rigid rotor model for the treatment of molecular rotation. In this approximation, the atoms are punctual masses connected by a rigid bond of constant length. However, a more realistic picture would be to consider bonds as springs with finite restoring forces. As the molecule rotates, the nuclei tend to be thrown outwards by centrifugal forces, the spring stretches and the intermolecular distance increases. This phenomenon is known as *centrifugal distortion effect*. Since centrifugal distortion has the effect of increasing bond lengths, there is an effective increase in the moment of inertia, which translates into an effective decrease in rotational constants. The rotational transitions appear then at lower frequencies than in a perfect rigid rotor. Therefore, it becomes important to account for centrifugal distortion in the analysis of rotational spectra. This is particularly so for small and/or flexible molecules (the latter being the case for most of the molecules in this Thesis) and weakly bound intermolecular complexes for which the effect of centrifugal distortion is more dramatic. One of the methods employed to account for this effect is to use Watson's Hamiltonian.[7] In particular, we present it here in its symmetric (S) reduction, which is particularly appropriate for asymmetric tops that approach the symmetric limit:

$$H_{Watson}^{(S)} = H_{rot}^{(S)} + H_{cd}^{(S)}$$

$$H_{rot}^{(S)} = A^{(S)}J_a^2 + B^{(S)}J_b^2 + C^{(S)}J_c^2$$

$$H_{cd}^{(S)} = -D_J J^4 - D_{JK}J^2J_c^2 - D_K J_c^4 + d_1 J^2(J_+^2 + J_-^2) + d_2(J_+^4 + J_-^4)$$

$$+H_J J^6 + H_{JK}J^4J_c^2 + H_{KJ}J^2J_c^4 + H_K J_c^6 + h_1 J^4(J_+^2 + J_-^2) + h_2 J^2(J_+^4 + J_-^4) + h_3(J_+^6 + J_-^6)$$

where $J_{\pm} = (J_a \pm i\, J_b)$, D_J, D_K, D_{JK}, d_1 and d_2 are centrifugal distortion constants (quartic terms) and H_J, H_K, H_{JK}, H_{KJ}, h_1, h_2 and h_3 are sextic terms.

II.4 Nuclear quadrupole coupling

Often, pure rotational spectra display complex patterns of fine and hyperfine structures, in which rotational transitions split into several components. This is the case for some of the molecules presented in this Thesis. Among the phenomena that cause those splittings is nuclear quadrupole coupling, which we will discuss in the following.

If we consider a specific atom in a molecule, two conditions must be fulfilled for nuclear quadrupole coupling to take place:

  a. Non-spherical distribution of nuclear charge about the nucleus

  b. Non-spherical distribution of electronic charge about the nucleus

Condition (b) can be taken for granted in virtually all molecules targeted by rotational spectroscopy. Condition (a) requires that the nucleus has a nuclear spin $I \geq 1$. In the case of organic molecules, the most common atoms with $I \geq 1$ are ^{14}N ($I=1$), ^2H ($I=1$), ^{35}Cl ($I=3/2$), ^{37}Cl ($I=3/2$) and ^{127}I ($I=5/2$). When condition (a) is fulfilled, it gives rise to a nuclear quadrupole moment while the fulfilment of condition (b) gives rise to an electric field gradient about the nucleus. The interaction between these two magnitudes (quadrupole moment and electric field gradient) results in a coupling between the nuclear spin momentum I and the rotational angular momentum J, such that the total angular momentum F is now:

$$F = I + J$$

The quantum number F is introduced such that:

$$F = J+I,\ J+I-1,\ J+I-2,\ \dots,\ |J-I|$$

The selection rules that govern transitions between these rotational states are $\Delta I=0$, $\Delta J=0, \pm 1$ and $\Delta F=0, \pm 1$. Each rotational transition is therefore split into additional components compared to a case with no quadrupole coupling. For example, in the case of the rotational transition 4 0 4 ← 3 0 3 and an atom with I=1 (for example, ^{14}N), the allowed quantum numbers are summarized in Table II.2.

Table II.2 Allowed quantum numbers for the 4 0 4 and 3 0 3 states of an asymmetric rotor with a quadrupolar nucleus (I=1)

	J, K$_{-1}$, K$_{+1}$=4 0 4	J, K$_{-1}$, K$_{+1}$=3 0 3
J	4	3
I	1	1
F	5; 4; 3	4; 3; 2

The allowed transitions in this case would be the ones with ΔF=0 (4←4; 3←3), ΔF=+1 (5←4; 4←3; 3←2) and ΔF=-1 (3←4), although in most cases only the transitions with ΔF=+1 are intense enough to be observed experimentally.

In molecules with a single nucleus with I≥1, the Hamiltonian takes on the following form:

$$H = H^{(S)}_{Watson} + H_Q$$

where H_Q accounts for the interaction with the quadrupolar moment. The derivation of H_Q can be found in detail in the literature,[1,2,3] resulting in:

$$H_Q = \frac{eQq_J}{2J(2J-1)I(2I-1)}[(I \cdot J)^2 + \frac{3}{2}I \cdot J - I^2J^2]$$

where I and J are the operators associated with spin and rotational angular momentum, respectively, eQ is the nuclear quadrupole moment and q_J is the coupling constant, defined as the mean value of the field gradient in the direction of the maximum projection of J along a space-fixed axis:

$$q_J = \langle\frac{\partial^2 V}{\partial Z^2}\rangle_{M_J=J}$$

where V is the potential and Z is the laboratory-fixed axis. q_J can be transformed into the principal axis of inertia coordinate system resulting in:

$$q_{g,g'} = \frac{\partial^2 V}{\partial g \partial g'}$$

with g,g'=a, b, c. The magnitude $q_{g,g'}$ can be related to the elements of the nuclear quadrupole coupling tensor:

$$\chi_{g,g'} = eQq_{g,g'}$$

The nuclear quadrupole coupling tensor is symmetric and takes on the following form:

$$\chi = \begin{pmatrix} \chi_{aa} & \chi_{ab} & \chi_{ac} \\ \chi_{ba} & \chi_{bb} & \chi_{bc} \\ \chi_{ca} & \chi_{cb} & \chi_{cc} \end{pmatrix}$$

The diagonal elements of the quadrupole coupling tensor fulfill the requirement:

$$\chi_{aa} + \chi_{bb} + \chi_{cc} = 0$$

Experimental values of χ_{aa}, χ_{bb} and χ_{cc} are often inferred from the analysis of hyperfine structure in rotational spectra. Since they represent the electric field gradient along the principal axes of inertia, they are very sensitive to local electronic environment and, therefore to chemical structure. That is the reason why these magnitudes are very helpful in structural elucidation. In those cases where rotational constants do not provide enough proof to identify molecular conformations, χ_{aa}, χ_{bb} and χ_{cc} may be extremely helpful in discerning different species. [8] Furthermore, the determination of the off-diagonal components of the nuclear quadrupole coupling tensor allows for its diagonalization.

Finally, it is worth mentioning that, in this Thesis, we have mostly used Pickett's SPFIT/SPCAT program suite[9] for the spectral fitting of experimental rotational spectra in order to obtain the experimental values of rotational constants, centrifugal distortion constants and nuclear quadrupole coupling parameters. In many cases, we have also used Kisiel's AABS program package[10] as a graphical aid for spectral fitting.

II.5 Large amplitude motions: internal rotation of methyl tops

In some cases, rotational spectra are affected by large amplitude motions that need to be taken into account when performing the rotational analysis. In this section, we will review the fundamentals of a specific kind of motion: internal rotation of a methyl top. This situation occurs when a methyl group is able to rotate about a single bond by which it is attached to the rest of the molecule. Under certain conditions, internal rotation of methyl tops can produce splittings in rotational transitions and therefore make their analysis more complicated. However, it is possible to obtain more information about the molecule or intermolecular complex from the effects of internal rotation. Other large amplitude motions often encountered in rotational spectra include ring puckering or inversion motions.[11,12,13]

In methyl tops, rotation about the single bond gives rise to three equivalent minima (C_{3v} symmetry). We encounter three different situations depending on the height of the potential energy barrier (V_3) separating the minima.

a. $V_3 \rightarrow \infty$: the barrier to internal rotation is very high. Internal motions are restricted to small, harmonic oscillations around the single bond.

b. V_3 has a finite, intermediate value.

c. $V_3 \rightarrow 0$: the barrier is very low, negligible and the methyl top is treated as a free rotor.

For the very high barrier case (a), the system can be described as three harmonic isolated oscillators each located at a minimum. Tunneling between the different minima is forbidden and each torsional energy level is threefold degenerated (because the three hydrogens are equivalent). For finite barriers (b), on the other hand, there is a probability of tunneling between the minima since the wave functions extend through the classically forbidden regions and the potential energy takes the shape of a periodic function (see Figure II.1). Because of tunneling, the degeneracy is partially lifted. Each torsional energy

level splits into two sub-levels: A (non-degenerate) and E (doubly degenerate). For the free rotor case (c), the energy levels are normally labeled with the quantum number m. The degeneracy is also partially lifted (as with the case of intermediate barriers) except for the cases where m is a multiple of 3. Figure II.2 displays the correlation between the energy levels in the three cases.
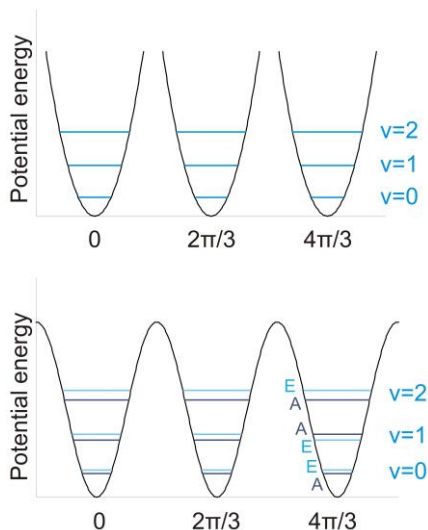
Figure II.1 Shape of the potential energy function for a methyl rotor in the high barrier limit (top) and in the intermediate barrier situation (bottom)
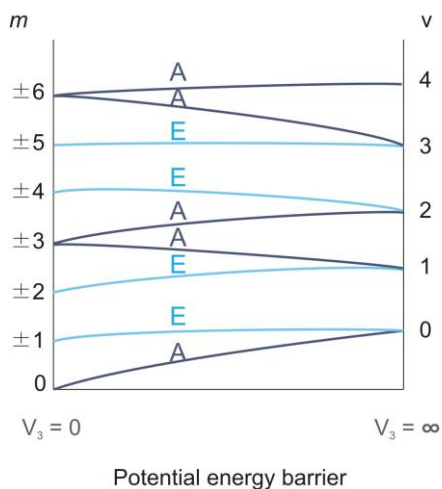
Figure II.2 Correlation between the torsional energy levels of the two limiting cases. For very high V_3 values, the energy levels are denoted with the v quantum number. For the free rotor case (V_3=0), we use the m quantum number to label energy levels. For the intermediate cases, the lifting of the degeneracy results in A/E sublevels.

Each A or E torsional sub-level hosts rotational energy levels. Rotational transitions follow the selection rules A←→A and E←→E. Hence, direct transitions between A and E torsional states are forbidden. Moreover, rotational levels in A and E states are slightly different and therefore rotational transitions have slightly different frequencies (A←→A compared to E←→E). That is the reason why rotational transitions appear as doublets (A and E) in the case of molecules with a methyl top with finite V_3 barrier. In general, high V_3 barriers yield small splittings (of the order of a few kHz), which can be unresolvable with the resolution of the spectrometer if the barrier is very high. On the other limit, low V_3 barriers can result in A-E splittings of several GHz.

One can derive structural information from the analysis of the A-E splittings. In particular, it is possible to estimate the height of the potential energy barrier (V_3), but also the orientation of the methyl top with respect to the principal axes of inertia of the molecule. In order to do so, the following Hamiltonian is used:

$$H = H_R + H_T + H_{RT}$$

where H_R refers to the rotation of the molecule, H_T to the torsions of the methyl top and H_{RT} to the coupling between both of them. In general, there are two main approaches to solving this Hamiltonian; they differ mostly in the choice of the coordinate system. The Principal-axis method (PAM)[14,15] uses the principal axes of the molecule as the coordinate system. The axis of internal rotation may or may not be coincident with one of the principal axes. Alternatively, the Internal-axis method (IAM)[16,17,18] uses a coordinate system in which the symmetry axis of the top is one of the coordinate axes. In this Thesis, we mostly used the XIAM program,[19] which is based on the IAM method, to carry out the fits with methyl internal rotation.

II.6 Determination of molecular structures

As we have mentioned in Chapter I, one of the most common applications of rotational spectroscopy is the precise and unambiguous determination of gas phase conformations of molecular systems with atomic resolution. From rotational spectroscopy experiments, we can determine the values of the rotational constants A, B, C (inversely proportional to the moments of inertia I_a, I_b and I_c) to an accuracy not achievable with other experimental techniques. Rotational constants are extremely sensitive to the overall conformation of the molecule or intermolecular complex. That is the reason why rotational spectroscopy is probably the most accurate tool for elucidating conformations of small-medium sized molecules in the gas phase.

Apart from the overall conformation of the system under study, detailed structural information can also be obtained from the moments of inertia derived from rotational studies. Accurate determination of bond distances and angles provide useful data about the forces that govern molecular structures. In particular, the magnitude of intra- and inter- molecular interactions may be assessed by the values of inter-atomic distances and angles. However, there is an uncertainty in the determination of structural parameters from experimental values of moments of inertia because the dimensions of the molecule are affected by vibrational energy. Even in its ground vibrational state, the molecule possesses residual vibrational energy. Different strategies exist for dealing with vibrational

effects. Each one of these procedures gives rise to a different kind of structure. We will review some of them in the following subsections.

It is worth mentioning that, in most cases, these structure calculations require the experimental determination of a large set of rotational constants. Hence, it is necessary to obtain the rotational constants of several isotopologues of a given molecule. In favorable cases where the rotational spectrum is intense, isotopologue species in natural abundance are detectable in the rotational spectra and their rotational constants can be experimentally obtained. The most common isotopologues arise from ^{13}C substitution (~1% natural abundance), ^{18}O (~0.2%), ^{15}N (~0.4%) and ^{37}Cl (~24%). Alternatively, isotopically enriched samples can be purchased or obtained with chemical synthesis.

In the following, we will review four different strategies to calculate molecular structures (r_e, r_s, r_0 and r_e^{SE}). These are probably the most commonly used and that is the reason why we are only focusing on them. Several other strategies for structural calculations exist, such as $r_m^{(1)}$, $r_m^{(2)}$, $r_m^{(1L)}$, $r_m^{(2L)}$ (see reference 20) or r_z among others.

II.6.1   Equilibrium structure, r_e

The equilibrium structure is the one adopted by the molecule at the minimum of the potential energy well. It is not possible to reach this structure physically because the molecule will always have residual zero-point energy (energy at the vibrational ground state). However, the structures obtained by theoretical calculations approach r_e, since they estimate the energy at the bottom of the potential energy well (and not at the vibrational ground state). Therefore, it is common to find in the literature that the structures coming from theoretical calculations are referred to as r_e.

It is possible to determine r_e experimentally (through the rotational constants at equilibrium B_e) by extrapolation to the excited vibrational states. This procedure is summarized in Figure II.3 for a diatomic molecule (for the sake of simplicity). The potential energy curve with the different vibrational states is displayed. It can be observed how, once the experimental values of r_0, r_1, r_2, etc are known, it is possible to extrapolate to r_e. Therefore, for this procedure it is necessary to know the shape of the potential energy surface and the rotational constants in several excited vibrational states. In practice, rotational spectra of excited vibrational states of larger molecules have low intensity because these states have lower population in the supersonic expansion. In consequence, it becomes hard to obtain rotational constants in excited vibrational states for the extrapolation. Therefore, it is not common to carry out this procedure in rotational studies of larger molecular systems and the experimental determination of r_e is mostly restricted to small molecular systems.

It is important to remember that rotational constants obtained from microwave studies correspond to structures in the vibrational ground state (B_0) and not in the minimum of the potential energy well (B_e). When a thorough comparison between experimental and B_e rotational constants is desired (for example, to compare the performance of different theoretical methods), it becomes necessary to add a correction to the experimental values to account for the structural differences between the minimum in potential energy and the vibrational ground state. Anharmonic calculations

(in suitable level of theory and basis set) yield the values of B_e-B_0 corrections. Therefore, by correcting the experimental rotational constants with those corrections, it is possible to perform a systematic comparison between experimental results and equilibrium structures. This strategy has been applied to large biological molecules in order to assess the performance of different theoretical methods in accounting for dispersion interactions.[21]
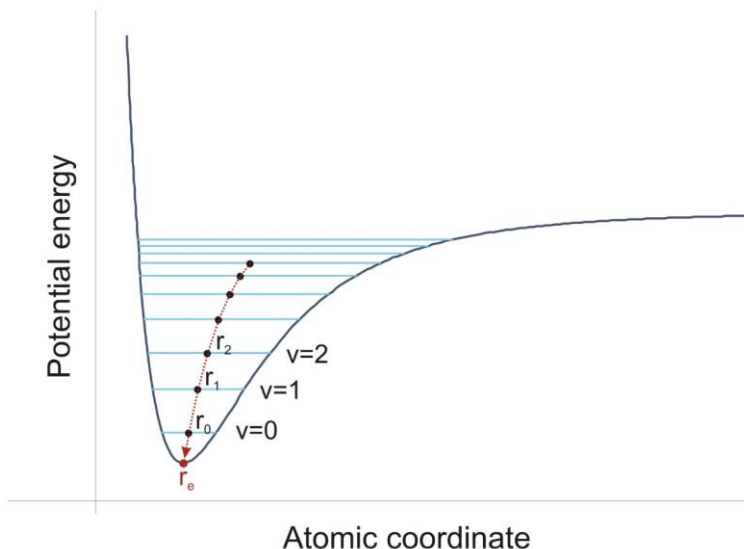
Figure II.3 Potential energy curve for a diatomic molecule, indicating the equilibrium geometry (r_e) and the extrapolation technique to attain it from the structures of excited vibrational states (r_0, r_1, r_2, ...).

II.6.2   Substitution structure, r_s

The substitution structure derives from the analysis of a molecule's changes in its own moments of inertia upon isotopic substitution of one of its atoms. Kraitchman's method[22] yields the coordinates of an atom with respect to the molecule's center of mass from the variation of the moments of inertia upon isotopic substitution of that specific atom. It implies that we can only obtain the coordinates of those atoms for which data on isotopic substitution are available. The same applies for structural parameters, meaning that bond distances, angles and dihedral angles are only attainable if there are data on isotopic substitutions of the atoms involved. Moreover, it is assumed that bond distances and angles remain unchanged upon isotopic substitution. For non-planar asymmetric tops, atomic coordinates according to Kraitchman's equations can be written as:

$$|x| = \left[\frac{\Delta P_x}{\mu} \left(1 + \frac{\Delta P_y}{I_x - I_y}\right)\left(1 + \frac{\Delta P_z}{I_x - I_z}\right)\right]^{1/2}$$

$$|y| = \left[\frac{\Delta P_y}{\mu}\left(1 + \frac{\Delta P_z}{I_y - I_z}\right)\left(1 + \frac{\Delta P_x}{I_y - I_x}\right)\right]^{1/2}$$

$$|z| = \left[\frac{\Delta P_z}{\mu}\left(1 + \frac{\Delta P_x}{I_z - I_x}\right)\left(1 + \frac{\Delta P_y}{I_z - I_y}\right)\right]^{1/2}$$

where:

$$\Delta P_x = \frac{1}{2}(\Delta I_y + \Delta I_z - \Delta I_x)$$

$$\Delta P_y = \frac{1}{2}(\Delta I_x + \Delta I_z - \Delta I_y)$$

$$\Delta P_z = \frac{1}{2}(\Delta I_x + \Delta I_y - \Delta I_z)$$

The x, y, z axes correspond to the three principal axes a, b, c and μ is the reduced mass defined as $\mu = \frac{M\Delta m}{M + \Delta m}$, where M is the total mass of the parent molecule and Δm is the difference in mass between the isotopically substituted molecule and the parent molecule.

Finally, one of the major drawbacks of r_s structures is that vibrational effects are very acute when the substituted atom lies close to a principal axis of inertia. In fact, the uncertainty in the atomic coordinate is inversely proportional to the atomic coordinate itself. Therefore, for very small atomic coordinates (< 0.1 Å) r_s coordinates may be inaccurate. There are other effects that may jeopardize the accuracy of r_s structures, such as H/D substitutions (due to the large change in atomic mass) and the existence of large amplitude motions.

II.6.3   Effective structure, r_v

The effective structure r_v is the one that best reproduces the observed moments of inertia (I_v) and the subsequent rotational constants (B_v) in a given vibrational state. Most rotational studies in supersonic expansions are restricted to the vibrational ground state and therefore refer to r_0, I_0 and B_0. In practice, r_0 is calculated by performing a least-squares fit of structural parameters (bonds distances, angles and dihedral angles) to reproduce experimental values of rotational constants in the vibrational ground state. A large number of rotational constants (from the parent species and isotopologues) is desirable in order to obtain the best possible fit and to calculate the maximum number of structural parameters. The approximation that bond distances and angles remain unchanged upon isotopic substitution also holds in the case of effective structures. Contrary to r_s, structural parameters involving non-substituted atoms may be obtained in r_0 structures, at least in very favorable cases in which there is a large number of rotational constants of isotopologues available.

II.6.4   Semi-experimental structure r_e^{SE}

Finally, the r_e^{SE} structure approximates the equilibrium structure at the non-physical minimum of the potential energy by a least-squares fit of experimental rotational constants of different isotopologues corrected by computed vibrational contributions.[23,24] These vibrational contributions take on the following form: $\Delta B = B_0 - B_e$ and they are

calculated through anharmonic frequency calculations. The latter are normally very costly and require a lot of computing time when performed at an acceptable level of theory. This is currently the major bottleneck of the r_e^{SE} molecular structure.

II.7 References

[1] W. Gordy, L. R. Cook, 'Microwave Molecular Spectra', *John Wiley & Sons Inc.*, New York, **1975**.

[2] C. H. Townes, A. L. Schawlow, 'Microwave Spectroscopy', *Dover Publication Inc.*, New York, **1975**.

[3] H. W. Kroto, 'Molecular Rotation Spectra', *Dover Publications Inc.*, New York, **1992**.

[4] B. S. Ray, *Z. Physik* **1932**, *78*, 74-91.

[5] R. L. Kronig, I. I. Rabi, *Phys. Rev.* **1927**, *29*, 262-269.

[6] F. Reiche, H. Rademacher, *Z. Physik* **1927**, *39*, 444-464.

[7] J. K. G. Watson, 'Vibrational spectra and structure', Vol. 6, *Elsevier*, Amsterdam, Oxford and New York, **1977.**

[8] P. Écija, E. J. Cocinero, A. Lesarri, J. Millán, F. Basterretxea, J. A. Fernández, F. Castaño, *J. Chem. Phys.* **2011**, *134*, 164311.

[9] H. M. Pickett, *J. Mol. Spectrosc.* **1991**, *148*, 371-377.

[10] Z. Kisiel, L. Pszczolkowski, I. R. Medvedev, M. Winnewisser, F. C. De Lucia, E. Herbst, *J. Mol. Spectrosc.* **2005**, *233*, 231-243.

[11] B. E. Long, E. A. Arsenault, D. A. Oberchain, Y. J. Choi, E. J. Ocola, J. Laane, W. C. Pringle, S. A. Cooke, *J. Phys. Chem. A* **2016**, *120*, 8686-8690.

[12] L. B. Favero, W. Li, G. Spadini, W. Caminati, *J. Mol. Spectrosc.* **2015**, *316*, 45-48.

[13] J. W. I. Van Bladel, A. Van der Avoird, P. E. S. Wormer, *Chem. Phys.* **1992**, *165*, 47-55.

[14] E. B. Wilson, Jr, *Chem. Rev.* **1940**, *27*, 17-38.

[15] B. L. Crawford, Jr, *J. Chem. Phys.* **1940**, *8*, 273-282.

[16] H. H. Nielsen, *Phys. Rev.* **1932**, 445-456.

[17] D. G. Burkhard, D. M. Dennison, *Phys. Rev.* **1951**, *94*, 408-417.

[18] K. T. Hecht, D. M. Dennison, *J. Chem. Phys.* **1957**, *26*, 31-47.

[19] H. Hartwig, H. Dreizler, *Z. Naturforsch* **1996**, *51a*, 923-932.

[20] J. K. G. Watson, A. Roytburg, W. Ulrich, *J. Mol. Spectrosc.* **1999**, *196*, 102-119.

[21] S. Grimme, M. Steinmetz, *Phys. Chem. Chem. Phys.* **2013**, *15*, 16031-16042.

[22] J. Kraitchman, *Am. J. Phys.* **1953**, *21*, 17-24.

[23] P. Pulay, W. Meyer, J. E. Boggs, *J. Chem. Phys.* **1978**, *68*, 5077-5085.

[24] M. Piccardo, E. Penocchio, C. Puzzarini, M. Biczysko, V. Barone, *J. Phys. Chem. A* **2015**, *119*, 2058-2082.

Chapter III.

Methodology

III.1   General approach in MW studies

Rotational spectroscopy has been traditionally used for the structural/conformational/dynamical analysis of molecules or intermolecular complexes under isolation conditions. In this Thesis, we mostly work on the structural elucidation of molecular systems in the gas phase, with the exception of Chapter IX. The methodology used in these structural studies is mostly the same. Figure III.1 summarizes the steps in the methodology, which we explain in the following:

- First, a fast conformational search (using Molecular Mechanics (MM)) yields the approximate structures that the system under study may adopt in the gas phase, by performing a complete and unrestricted scan of the Potential Energy Surface.

- Second, these structures are further re-optimized with quantum chemistry methods. We obtain more accurate and precise structural predictions of the lowest-lying conformers, as well as more realistic values for their relative energies. This allows us, on the one hand, to identify which may be the most populated conformations (normally, the lowest lying in energy) and, on the other hand, to predict the most relevant spectroscopic parameters (rotational and centrifugal distortion constants, permanent electric dipole moments, nuclear quadrupole coupling constants, barriers to internal rotation in methyl tops, etc) of those conformations. Thanks to this information, we can make a simulation of the rotational spectrum, which is the sum of the rotational transitions arising from all populated conformations.

- Third, we record the experimental rotational spectrum and we identify the rotational lines belonging to the different conformations. The subsequent fit yields the experimental values of the rotational and centrifugal distortion constants, etc. Furthermore, hyperfine structure arising from nuclear quadrupole coupling may be analyzed at this point, as well as features of dynamical motions such as the internal rotation of a methyl top. Moreover, if the signal-to-noise ratio allows for it, we can look for rotational lines arising from isotopologues in natural abundance (^{13}C, ^{15}N, etc). It is important to note that the theoretical predictions (second step) are very important to guide the analysis of the spectrum and to assign each set of rotational constants to a molecular structure.

- Fourth, the experimental values of the spectroscopic parameters serve as a benchmark to validate the predictive capabilities of the different theoretical methods.

In the following sections, we will give more details about the different steps in the methodology.
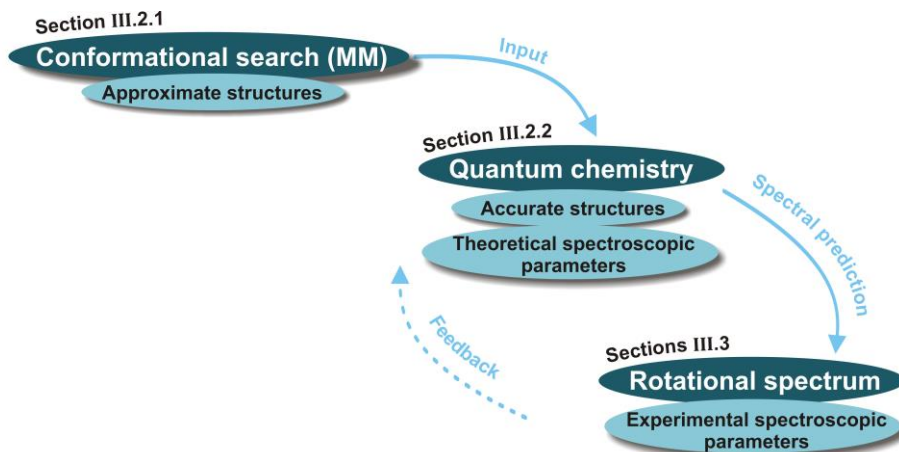
Figure III.1 Summary of the methodology in rotational spectroscopy structural studies.

III.2   Theoretical calculations

The first studies in microwave spectroscopy were limited to small molecules consisting of 2-10 heavy atoms.[1,2,3] With the development of new techniques and instrumentation, larger molecular systems are nowadays available for microwave studies, the largest molecule studied to date being covalent oxadiamantyl dimer with 28 heavy atoms.[4] In the quest for larger molecules and intermolecular complexes through microwave spectroscopy, the advances in computational methods play a pivotal role, at the same level as the developments in instrumentation. These larger molecules are often very flexible systems, with several degrees of freedom defining their conformation. Hence, chemical intuition is sometimes not enough to predict the most stable conformations that these systems may adopt in the gas phase. That is why computational calculations have become nowadays an essential tool for spectroscopists in general and for rotational spectroscopists in particular. *Ab initio* and DFT calculations are routinely used for predicting the most favored conformations of molecular systems in the gas phase as well as for the prediction and interpretation of rotational spectra. The field of rotational spectroscopy owes many of its recent successes to the development of new theoretical methods. Furthermore, researchers have very often access to large computational resources (computer clusters) that allow them to perform costly calculations. In this Thesis, we have used the IZO-SGI Scientific Computing Service (SGIker) at the University of the Basque Country (UPV/EHU).

III.2.1   Conformational search

The first step in the methodology is an exhaustive conformational search to estimate the structures and relative energies of the lowest lying conformers. A scan of the Potential Energy Surface (PES) of the molecule (or intermolecular complex) is carried out in the vibrational ground state. For that purpose, we use MM,[5] which allows for a fast and unrestricted scan of the PES. MM uses classical mechanics to calculate the energy of a

molecule in a given conformation. The atoms in the molecule are considered as spheres and bonds as springs. The potential energy of a given conformation is calculated by application of classical mechanics as a sum of *stretching, bending, torsional* and *non-bonded interaction* terms. There are many different force fields to calculate the potential energy, each of them accounting for different effects and types of molecular systems. One of the greatest advantages of MM is that it remains a cheap method in terms of computational cost. This means that the complete Potential Energy Surface of relatively large molecular systems can be sampled without any kind of restriction in the molecule's degrees of freedom, and it gives us an overall idea of the conformational landscape. Hence, local minima can be found at a low computational cost. Of course, this is in detriment of the accuracy of the structure and potential energy of the different local minima. That is why more thorough and time-consuming *ab initio* and DFT calculations are carried out starting from the conformational search structures, in order to perform a proper geometry optimization of the local minima.

In this Thesis, we have mainly used the *Merck Molecular Force Field* (MMFF) [6] in the conformational searches. This force field is specifically designed to deal with bio-organic and pharmaceutical related molecular systems. In particular, one of the goals of this technique is the 'study of receptor-ligand interactions involving proteins or nucleic acids as receptor'.[6] Conformational geometries and energies are crucial to fulfill that task and that is the reason why MMFF is specifically parametrized to carefully assess molecular conformations and conformational energies. This characteristic makes it a good choice for the conformational search purposes of this Thesis. Other force fields include OPLS[7] (*Optimized Potentials for Liquid Simulations*), AMBER[8] (*Assisted Model Building with Energy Refinement*) or GLYCAM,[9] the last being originally parameterized for carbohydrates, although it can be used for other biomolecules.

Finally, it is worth mentioning that the algorithm used to sample the conformational landscape is a combination of Monte Carlo (MC) and *large-scale low-mode sampling* (LLMOD)[10]. MC performs random changes to dihedral angles in rotatable bonds to create new conformations while LLMOD calculates the molecules normal modes of vibration and amplifies them to create a very different structure. Finally, the energy window typically used in the conformational search is 20-30 kJ/mol, although it is adjusted to each molecular system.

III.2.2   Quantum mechanical calculations

As was mentioned before, MM provides a means of rapidly scanning the conformational space of a given molecule or intermolecular complex and predict the structures of the most stable conformations. However, the low computational cost of MM is in detriment of the accuracy of the structures and potential energy of the different conformations. Therefore, in order to obtain more accurate structures and energies, the conformations obtained in the conformational search are further re-optimized using quantum mechanics. The structures resulting from this step can then be used to accurately predict relative energies, rotational constants and any other spectroscopic parameter necessary for the interpretation and analysis of the rotational spectra.

Different quantum mechanical methods are routinely used in rotational spectroscopy analysis. In this work, we make use of several methods, depending on the characteristics of the molecule under study (size, dispersive interactions, etc). On the one hand, we use *ab initio* methods, in particular second-order Møller–Plesset perturbation theory (MP2).[11] This method provides very accurate values of rotational constants and can take into account dispersive interactions, although it may overestimate their strength in some cases. This makes it one of the most common choices of quantum mechanical methods in the rotational spectroscopy community. However, it has the disadvantage of a high computational cost. As the size of the molecules measurable by microwave spectroscopy increases, MP2 calculations may no longer be affordable. On the other hand, we also use quantum mechanical methods based on Density Functional Theory (DFT). In general, the DFT methods used in this work are less time-consuming than MP2 calculations. A common choice among the rotational spectroscopy community is hybrid functionals, in which the exchange-correlation energy functional incorporates a part of the exact exchange from HF and the rest from other sources. One of the methods used in this work is M06-2X.[12] Although it does not explicitly include dispersion corrections, it accounts for part of them thanks to a flexible functional and extensive parametrization.[13] Another common method is B3LYP, which includes Becke's form of the exchange correlation functional[14] with the non-local correlation provided by the LYP expression.[15] Although B3LYP is a very common functional in the spectroscopic community, it has the major drawback that it does not account for dispersion interactions. However, the quantum chemistry community is making a great effort to design dispersion corrections to these functionals. In this work we consider Grimme's dispersion correction D3[16] and also D3BJ,[17] which includes Becke-Johnson damping. Regarding the basis sets, in this work we use mostly the split valence 6-311G basis set by Pople,[18] augmented with polarization functions and diffuse functions (6-311++G(d,p)).

Geometry optimizations with the above mentioned quantum chemistry methods lead to better and more accurate *in vacuo* structures than those obtained in the conformational search. These calculations yield theoretical values for rotational constants, dipole moments along the principal axes of inertia, nuclear quadrupole coupling constants, relative energies, etc that can be used to predict and analyze rotational spectra.

The next step in the computational work is to perform calculations on vibrational frequencies for each optimized geometry. These serve three purposes. First, frequency calculations allow the identification of *real* minima. Geometry optimizations by quantum chemistry methods sometimes lead to structures that are transition states (instead of the desirable local minima). These transition states are easily spotted in harmonic frequency calculations since they contain one imaginary frequency value in the vibrational modes. Second, thanks to these calculations we can estimate the Zero Point Energy Correction, and therefore the energy of the molecule in the vibrational ground state ($v=0$) (rather than at the minimum of the potential energy well). Third, vibrational calculations yield the values of the centrifugal distortion constants. The experimental values of the latter can be obtained from the fits of the rotational spectra and hence we can make a comparison theoretical vs. experimental.

Using the theoretical (*ab initio* or DFT) values of the rotational constants of the lowest-lying conformations, we predict the rotational spectrum of the molecule under study. This simulation guides the interpretation and analysis of the experimental rotational spectrum. Comparison of experimental and theoretical rotational constants allows for the identification of each species to a given conformation. It is also important to note that the results obtained from rotational spectroscopy (i.e. experimental values of *A*, *B* and *C*) serve as a benchmark to validate theoretical methods *in vacuo*. For example, the ability of different methods to account for dispersion interactions may be put to the test by comparing calculated rotational constants with experimental results from rotational spectroscopy.[13] In Chapter VII, we perform this test with two molecular systems: methyl jasmonate and zingerone.

III.3   Experimental rotational spectroscopy set-ups

III.3.1   Vaporization methods

The first step in any high-resolution structural study in the gas phase is, precisely, to bring the sample into a gaseous state. There are several methods for doing so. In order to choose the most appropriate vaporization method, one has to carefully analyze the characteristics of the sample (such as state of matter, vapor pressure or thermal (in)stability). In this Thesis, we have worked with either solid or liquid samples. We have used two vaporization methods, conventional heating techniques and ultrafast laser vaporization, which will be further explained in the following.

a.   *Conventional heating techniques*

We use this method in the cases of samples (either solid or liquid) that are at the same time not very volatile and not thermally unstable. In those cases, we can increase the vapor pressure (and, subsequently, the amount of molecules in the gas phase) by increasing the temperature of the sample, which is located in a customized heating nozzle. In this Thesis, we have optimized the vaporization method in order to obtain maximum signal-to-noise ratio in the rotational spectra. The conventional heating vaporization set-up currently consists of:

- Customized heating nozzle. It features a reservoir where the sample (either a solid or a liquid impregnated in glass wool) is placed. The nozzle is attached to a pulsed solenoid valve and a carrier gas is flown through it. The heating nozzle has a "crown" shape on the outside with four holes so that it can be fixed to a support and we can adjust the opening of the valve in the optimization process. Figure III.2 displays a picture of the nozzle.

- Resistance heating wire. We have designed a piece consisting of two metallic concentric tubes with a resistance heating wire coiled between the two of them. Its shape is specifically designed so that it adapts to the customized heating nozzle. With this design, we ensure that the process of heating is homogeneous throughout the heating nozzle. Moreover, we are able to reach temperatures of 220°C under vacuum.

- Temperature controller. We use a digital temperature controller Fuji Electric PXR4. In its auto-tuning mode, the temperature controller automatically adjusts its own settings (duration and frequency of the current pulse, etc.) to provide constant temperature.
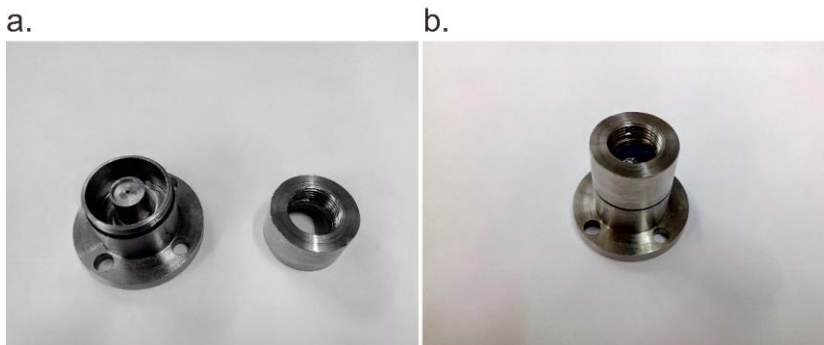

Figure III.2 a. The customized heating nozzle consists of two pieces: the one on the left hosts the sample reservoir while the one on the right serves as the attachment to the pulsed valve. b. The two pieces are screwed to each other.

b.   Ultrafast laser vaporization

When using conventional heating techniques, some samples may decompose before they are transferred into the gas phase; that is, they are thermally unstable. This is the case of many biomolecules. For example, molecules with a carboxylic acid group (such as amino-acids) tend to decompose by releasing CO_2 when they are heated. Sugars also tend to decompose easily, for example with ring opening at the anomeric carbon. In those cases, we cannot use conventional heating techniques to bring the intact molecules into the gas phase. Instead, one can use ultrafast laser vaporization. In this strategy, a mixture of the sample and a commercial binder is mechanically pressed to get cylinder-type solid samples ("rods"). The rod is then attached to a stepper motor that sits immediately before a customized ablation nozzle. The vaporization process goes as follows. A picosecond pulse coming from a Nd-YAG laser in the third harmonic (355 nm) hits the rod in the presence of a carrier gas (Neon, ~6 bar). The sample is vaporized due to the action of the laser pulse and supersonically expanded (with the carrier gas) through a 1.0 mm ablation nozzle. The motor translates and rotates the sample rod after every pulse so that the next laser pulse hits "fresh" surface of the sample rod.

By using ultrafast laser vaporization, a fraction of the sample is brought intact into the gas phase. This strategy opened the field of rotational spectroscopy to the study of biomolecular systems that could not be studied with other vaporization techniques, such as amino acids,[19,20] monosaccharides,[21,22] and even small peptides.[23]

III.3.2   Supersonic expansions

Supersonic expansions are very often combined with spectroscopic techniques (rotational, vibrational) to identify and characterize the different conformations that a molecule or intermolecular complex may adopt in the gas phase.

A supersonic expansion occurs when a gas expands from a high-pressure region (2-10 bar) into a low-pressure region (10^{-5}-10^{-7} mbar) through a small orifice (~1 mm diameter). In spectroscopic studies, the gas is typically a mixture of the vaporized sample diluted in an inert carrier gas (usually helium, neon or argon). During the expansion, the gas reaches very high speed, greater than the speed of sound. Since a high-pressure gas expands through a very small orifice, the sample molecules undergo many collisions with the carrier gas (and with other molecules of the sample to a lesser extent). These collisions result in an effective cooling of the molecules and the rotational and vibrational temperatures decrease dramatically. In particular, the rotational temperature attained in the experiments carried out in this Thesis is ~0.5-5 K. The consequence of this rotational cooling is that only the lowest rotational levels are populated and this results in a simplification of rotational spectra.

Even though the molecules are cooled vibrationally and rotationally, the conformational distribution corresponds to a situation of equilibrium. This is so because, prior to the small orifice, the distribution of conformations corresponds to an equilibrium situation (at room temperature or at the temperature of the nozzle). Later, in the supersonic expansion, those conformations are trapped in their corresponding potential energy wells. Therefore, provided that the barrier for interconversion between conformers is high enough, the different conformations can be identified separately in an equilibrium distribution within the supersonic expansion.
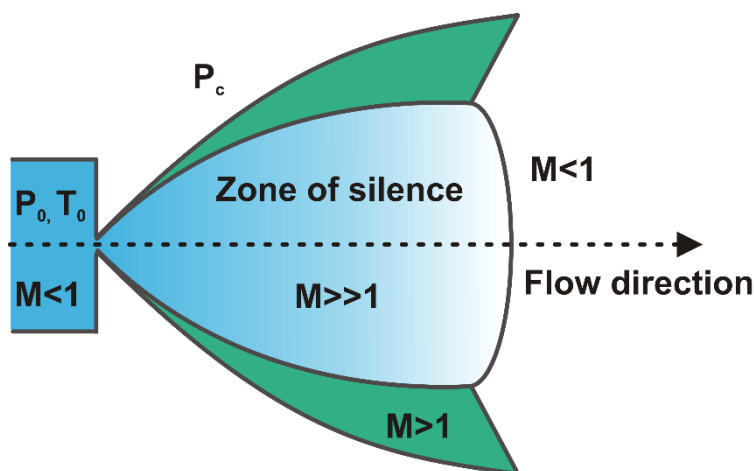
Figure III.3 Schematic diagram of a supersonic expansion. M is the Mach number (ratio between the speed of the gas and the speed of sound). P_0 and T_0 are the pressure and temperature of the gas before the expansion (in our case, in the following ranges: 298-498 K and 2-6 bar). P_c is the pressure of the region where the expansion takes place (vacuum chamber). In our case P_c ~ 10^{-6} mbar.

The lowest pressures and temperatures of the supersonic expansions lie in the so-called 'zone of silence', (see Figure III.3) which makes it the most appropriate region of the supersonic expansion to probe with spectroscopic techniques. Most importantly, the

'zone of silence' is virtually a non-interaction zone, where the molecules are free from collisions or interactions.

Finally, a key feature of supersonic expansions is that it makes it possible to isolate weakly bound intermolecular complexes. They are formed in the vecinity if the orifice and later trapped in the supersonic expansion. Then, it is possible to probe them with spectroscopic techniques.

To sum up, the combination of supersonic expansions with spectroscopic techniques (in this Thesis, rotational spectroscopy) presents the following advantages:

- Molecules are under isolation conditions, allowing for the analysis of their intrinsic properties, as opposed to the properties arising from the interactions with the surrounding (solvent, crystal packing, etc).

- We can isolate and identify separately each conformation of a given molecular system.

- Supersonic expansions allow for the generation and later characterization of weakly bound intermolecular complexes (dimers, trimers, tetramers, etc).

- There is a considerable simplification of rotational spectra because only the lowest vibrational and rotational states are populated. This results in a larger molecular density in the populated states and, consequently, in an increase of the intensity of rotational signals in the frequency region in which we are working (in this case, mostly 6-18 GHz).

III.3.3   FTMW spectrometer

Fourier Transform Microwave (FTMW) spectroscopy allows for the measurement of the resonant frequencies of rotational transitions of a given molecular system. This technique is based on the excitation of the rotational energy levels in the microwave region, followed by the detection of the emission in the time domain (Free Induction Decay, FID) and the Fourier transformation to the frequency domain to obtain the rotational spectrum. The combination of FTMW spectroscopy with supersonic expansions is a very powerful tool to identify the different species in the jet. It benefits from a very high spectral resolution (~5 kHz, ~10^{-7} cm^{-1}), hardly achievable with other spectroscopic techniques. Therefore, the different conformations of a given molecular system can be unambiguously identified and we can infer their structures with great precision. Also tautomers and isotopologues can be clearly identified with the spectral resolution of this technique.

In 2010, a FTMW spectrometer was built at the Department of Physical Chemistry of the University of the Basque Country (UPV/EHU),[24] see Figure III.4 for a picture of the device. It is based on Balle-Flygare's original design[25] and features a COBRA arrangement,[26] as many other FTMW spectrometers used nowadays by other research groups. This spectrometer is coupled to an ultrafast laser vaporization set-up, which makes it possible to analyze thermally unstable samples. In this Thesis, we have used the Balle-Flygare device for two molecular systems (see Chapters V and VI), either because we needed very high spectral resolution or because we needed the laser vaporization set-up.

The apparatus is not commercially available and it has been described in detail elsewhere.[24] It is not the objective of this Thesis to give a detailed description of the experimental set-up (we will do it for the CP-FTMW machine). We will rather review the most important features of the Balle-Flygare's FTMW spectrometer.

In this kind of spectrometer, the supersonic expansion is generated inside a Fabry-Pérot resonator located in a vacuum chamber. The resonator consists of two concentric mirrors (radius=33 cm), at the center of which are located two L-shaped antennas. The microwave radiation is introduced in the chamber by one of the antennas and is reflected in the resonator. This radiation interacts with the supersonic expansion and produces a molecular excitation. After a few microseconds, the molecular emission FID is collected with the second antenna and Fourier transformed to obtain the rotational spectrum in the frequency domain.

The main disadvantage of this kind of spectrometers is that its bandwidth is quite narrow (~1 MHz). This means that portions of only 1 MHz of the rotational spectrum can be collected at a time. Therefore, we need to perform a mechanical tuning for each different frequency, consisting in changing the distance between the two mirrors (one of them is attached to a motor and, therefore, mobile). This results in long spectral acquisition times.

Figure III.4 Picture of the FTMW spectrometer at the University of the Basque Country (UPV/EHU), with numbering of the main components (1: Electronic tower with the electronic equipment, 2: Vacuum chamber, 3: Ultrafast laser vaporization set-up).

III.3.4   CP-FTMW spectrometer

In 2008, Professor Brooks H. Pate revolutionized the field of microwave spectroscopy with the introduction of the Chirped Pulse Fourier Transform Microwave (CP-FTMW) spectrometer.[27] The novelty of this technique is the use of short (~1μs duration) broadband

(~12 GHz) pulses to excite the molecules. This means that a wide fraction of the rotational spectrum (12 GHz in our case) can be collected in a single acquisition. Moreover, millions of spectra can be averaged coherently over time in order to increase signal-to-noise ratio. In general, the use of CP-FTMW spectrometers results in shorter spectral acquisition times compared to FTMW machines based on Fabry-Pérot resonators. As a reminder, the typical bandwith of a Fabry-Pérot FTMW spectrometer is around 1MHz (requiring mechanical tuning to measure each rotational transition), while it can be 12GHz for the CP-FTMW spectrometer. One of the goals of this Thesis was to build and optimize a CP-FTMW device at the Spectroscopy Group at the University of the Basque Country (UPV/EHU). In the following, we will describe the main characteristics of the apparatus.

Figure III.5 shows a picture of the CP-FTMW apparatus as it was initially built, with the labelling of the main components of the set-up. Briefly, a broadband pulse is generated in the Arbitrary Waveform Generator (AWG, 1 in Figure III.5) and later amplified in a Travelling Wave Tube Amplifier (TWTA, 2 in Figure III.5). The pulse is broadcast into the vacuum chamber (3 in Figure III.5) through a horn antenna where it interacts with the supersonic expansion. The time-domain signal of the molecular emission is collected in a digital 20 GHz oscilloscope (4 in Figure III.5) and Fourier-transformed to obtain the rotational spectrum.
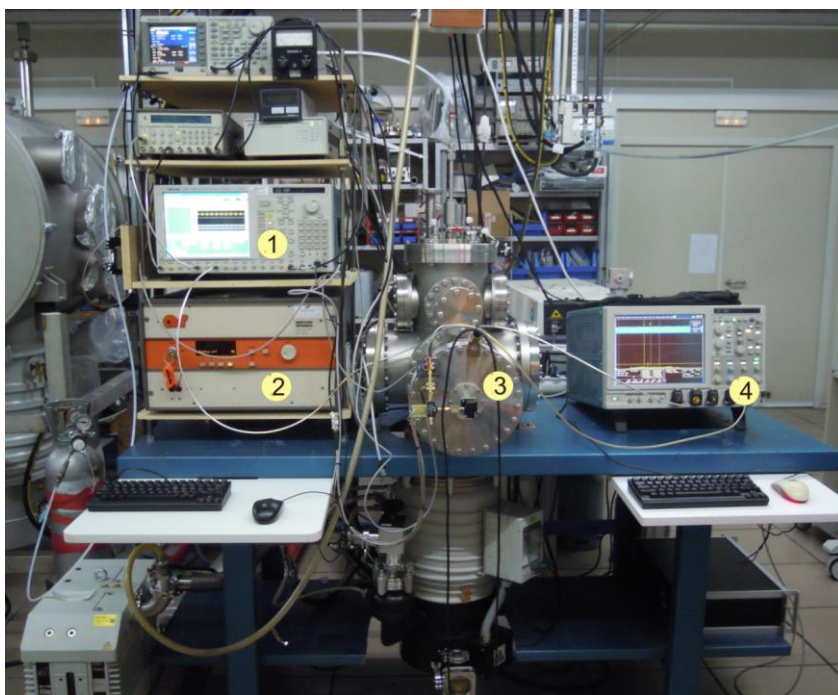
Figure III.5 Picture of the CP-FTMW spectrometer at the University of the Basque Country (UPV/EHU), with numbering of the main components (1: Arbitrary Waveform Generator, 2: Travelling Wavetube Amplifier, 3: Vacuum chamber, 4: Oscilloscope).

In 2016, we incorporated a larger vacuum chamber that could host three pulsed solenoid valves that can run simultaneously in order to increase signal-to-noise ratio. Moreover, we incorporated a new set of Q-par horn antennas. Figure III.6 displays a picture of the new, larger vacuum chamber and Figure III.7 shows one of the two identical Q-par antennas.
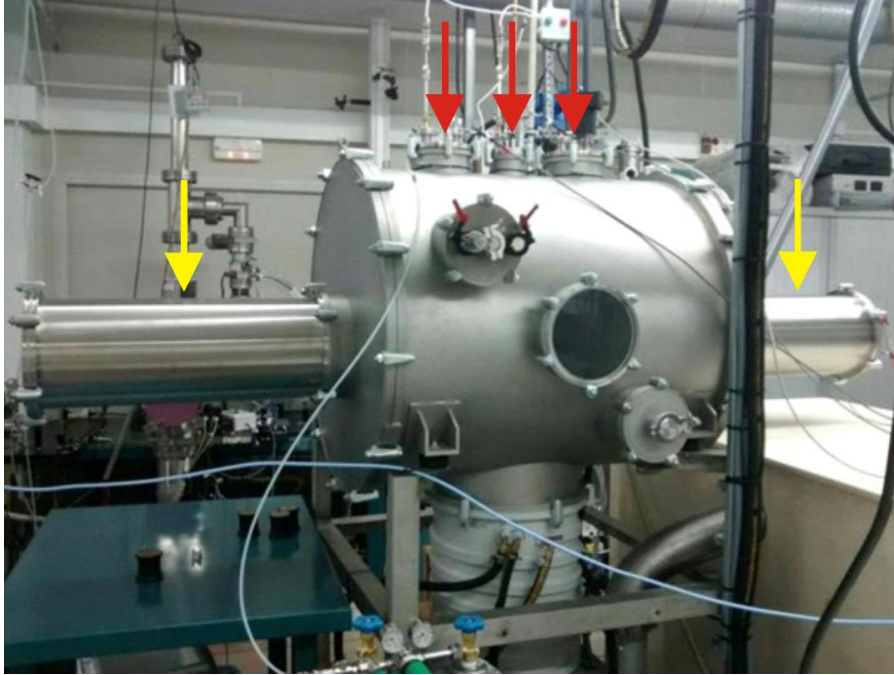
Figure III.6 Picture of the larger vacuum chamber installed in the CP-FTMW device. Red arrows mark the positions of the gas inlets leading to the three pulsed valves. Yellow arrows mark the locations of the two extenders that host the new horn antennas.

Figure III.7 Q-par horn antenna.

Finally, a detailed scheme of the electronic components of the spectrometer is presented in Figure III.8.
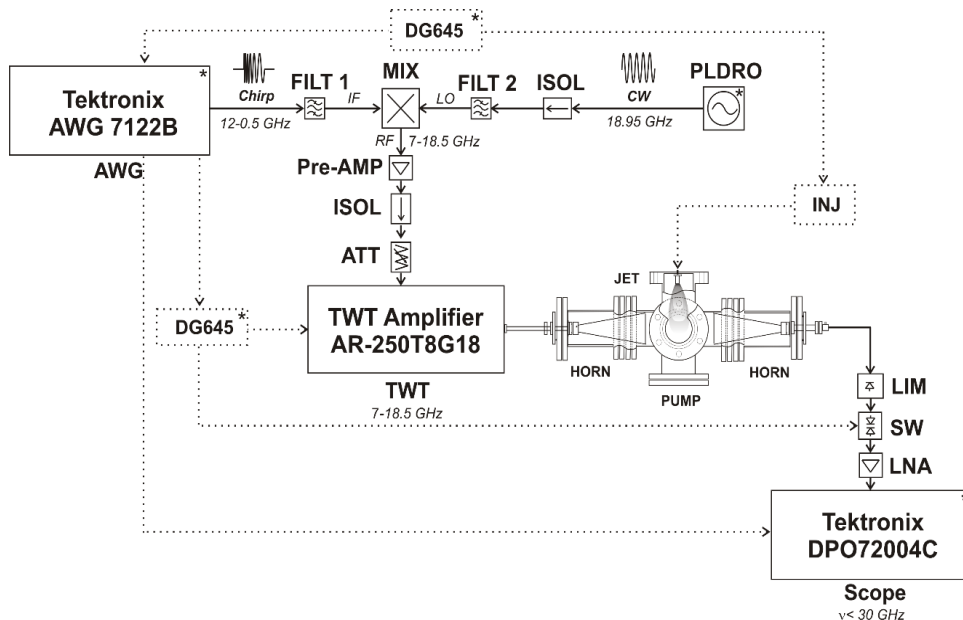
Figure III.8 Detail of the electronics of the CP-FTMW spectrometer at the UPV/EHU. A chirped pulse created by an arbitrary waveform generator (AWG) covering a base band of 12 GHz is filtered (FILT 1) and upconverted to the operating region 7-18.5 GHz with a broadband mixer (MIX). The local radiation originates from a stabilized oscillator (PLDRO, 18.95 GHz), followed by an isolator (ISOL) and a filter (FILT 2). The polarizing radiation is preamplified (Pre-AMP), leveled (ATT) and power amplified with a travelling wave tube amplifier (TWT), to be finally radiated through a horn antenna (HORN). The jet propagates perpendicular to the exciting emission. The molecular free-induced-decay captured by a second horn passes a power limiter (LIM) and a protection switch (SW), and is amplified (Low Noise Amplifier, LNA) and digitized in the time domain. The components marked with an asterisk are frequency-referenced to a 10 MHz Rb standard. Solid arrows indicate the propagation of the microwave signal, while dotted arrows represent the electric signals that trigger the different electronic devices. DG-645 is a digital delay/pulse generator and INJ is the pulsed valve driver (iota one).

We will briefly review the main characteristics of the most relevant electronic components of this apparatus.

-Arbitrary Waveform Generator (AWG)

The AWG creates a short microwave pulse (1-2 µs duration in all the experiments carried out in this Thesis) covering a 12 GHz frequency region. The pulse is a linear chirp, meaning that the frequency increases linearly with time. Figure III.9 shows the shape of a linear frequency sweep such as the one we are using in this Thesis. That microwave signal will later be mixed with a fixed frequency signal in order to convert it to the desired working

range (7.5 to 18 GHz in this case). In practice, the AWG creates a sequence of chirped pulses (from 10 to 30) separated by a 25 μs buffer time. In this way, we can record multiple (from 10 to 30) spectra per molecular pulse and reduce even further the spectral acquisition time. In Figure III.10, we can see a front view of the AWG, with a sequence of 10 chirped pulses

Figure III.9 Shape of a 1μs long chirped pulse.

Figure III.10 Front view of the Arbitrary Waveform Generator (AWG) used in this Thesis. A sequence of 10 chirped pulses (1 μs duration) with a buffer time of 25 μs between them can be seen on the screen of the AWG.

-Traveling-Wave Tube Amplifier

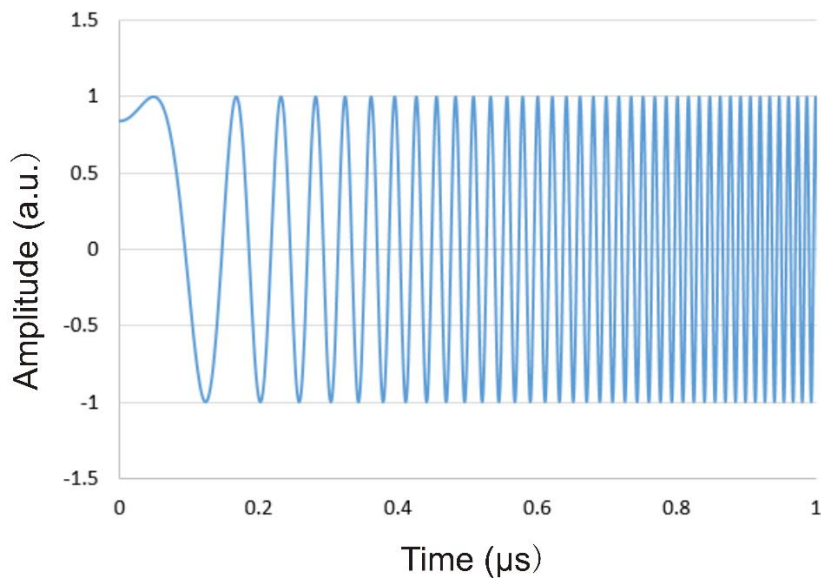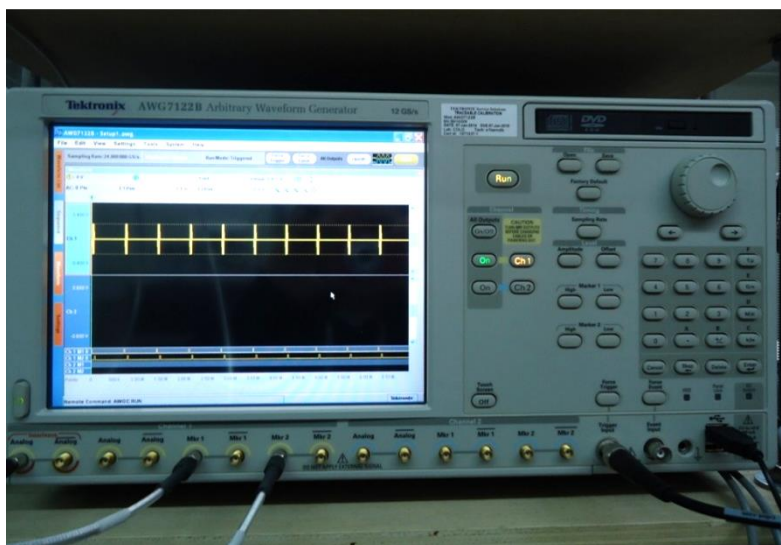This device amplifies (200 W power amplification) the microwave signal generated by the AWG (and later up-converted). In the current set-up, the TWTA covers the 7.5 to 18 GHz region.

-Vacuum chamber

This is where the interaction between microwave radiation and the supersonic expansion takes place. The vacuum chamber (made of stainless steel) has a cylindrical form, it is 90 cm long and the diameter is 85 cm. Moreover, the two side extensors that host the horn antennas are 65 cm long and the diameter is 25 cm. The vacuum system consists of an oil diffusion pump (pumping speed 5000 L/s) backed with a rotatory (20 L/s) and a roots pump (180 L/s). With this system, the pressure can be as low as 10^{-6} mbar, which ensures that the supersonic expansion is cold enough to carry out the experiment. The vacuum chamber sits on a metallic support, as it can be observed in Figure III.6.

The gas mixture is introduced into the chamber (through a 1 mm circular orifice) thanks to a pulsed solenoid valve at the top. The valve runs at 1 or 2 Hz. The output of the TWTA is broadcast into the chamber through a horn antenna, while a second antenna collects the signal emitted a few microseconds later and drives it to the oscilloscope. Inside the vacuum chamber, the supersonic expansion and the microwave radiation are arranged perpendicular to each other.

-Detection system

The oscilloscope collects the molecular signal, which has been previously driven through the horn antenna and amplified with a Low Noise Amplifier. The oscilloscope we use in this Thesis covers the 0 to 20 GHz frequency span, which allows us to collect the molecular signal directly, without having to convert the signal to another region. We collect a 20 µs-long time-domain FID (Free Induction Decay) signal for every molecular pulse. The oscilloscope offers the chance to perform the Fourier transformation (Fast Fourier Transform, FFT) to obtain the rotational spectrum in the frequency domain in real time. However, we select a 0.6 µs section of the FID for the FFT because the oscilloscope cannot process a longer signal in real time. Thanks to the FFT in real time, we can optimize the conditions of the experiment (opening of the valve, delay of the MW pulse) by looking at the microwave signal directly on the oscilloscope. Finally, it is worth mentioning that we developed an application (using LabVIEW) that controls the oscilloscope remotely and saves the FIDs at regular intervals. This allows us to monitor the evolution of the microwave signal with time.

All frequency signals in the CP-FTMW spectrometer are frequency-referenced to a 10 MHz rubidium standard. This allows the averaging of rotational spectra coherently.

Figure III.11 summarizes the operating sequence of the CP-FTMW spectrometer.

1. Formation of the supersonic expansion

Pulsed valve driver

Molecular pulse, τ = 0.8 - 1.2 ms

Supersonic expansion

~1 ms

2. Polarization

AWG

TWT Amplifier

MW sequence

25μs

1 μs
MW Pulse
Amplification

Polarization

3. Molecular emission and cavity relaxation

2 μs

4. Time-domain detection and Fourier Transformation

Detection

25μs

Rotational spectrum (frequency domain)

Oscilloscope

FID (time domain)

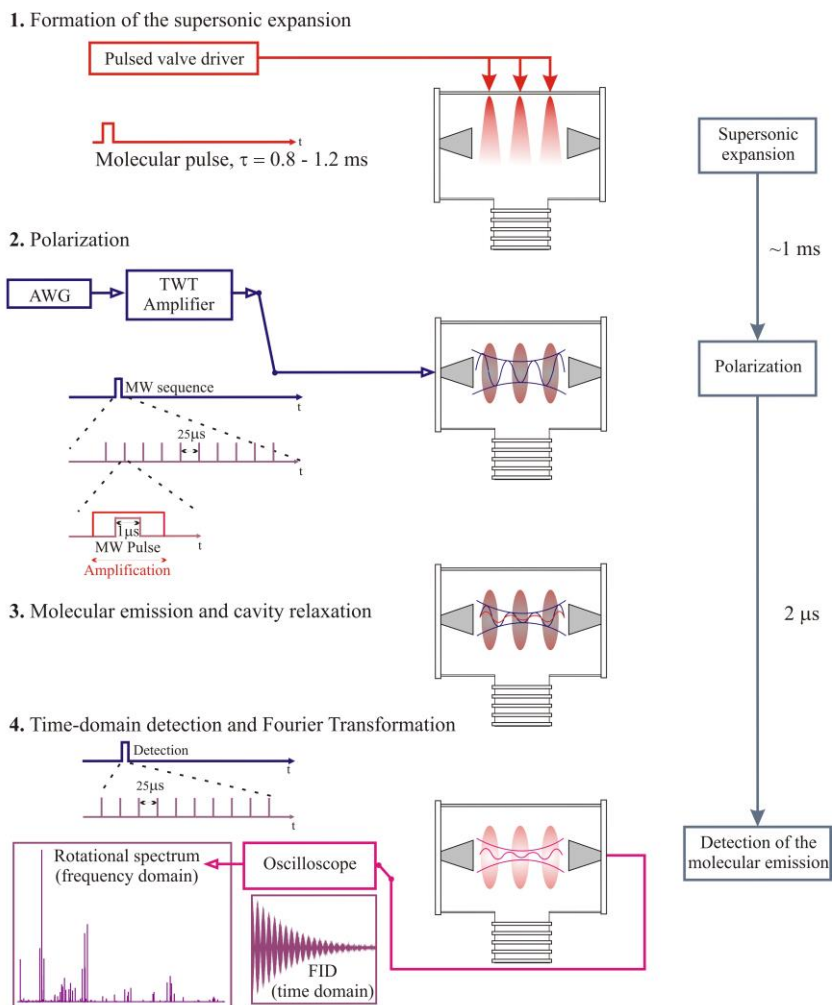Detection of the molecular emission

Figure III.11 Operating sequence of the CP-FTMW spectrometer.

The steps in the operation of the apparatus are:

1. Molecular pulse

The duration of the opening of the valve is around 500-1200 μs. During that period, the quasi-adabiatic expansion of the gas mixture originates a supersonic expansion inside the vacuum chamber.

2. Polarization: microwave pulse

In this step, we induce the polarization (excitation in the microwave region) of all the species in the supersonic expansion. The excitation sequence generated in the AWG is amplified in the TWTA and broadcast into the vacuum chamber through a horn antenna. This step is delayed about 600-1300 μs with respect to the opening of the valve.

3. Molecular emission

The molecular species in the supersonic expansion spontaneously emit coherent radiation at the resonant frequencies of rotational transitions.

4. Detection

After a few microseconds, the molecular emission is collected thanks to a horn antenna, later amplified with a Low Noise Amplifier and driven to the oscilloscope.

To sum up, we will briefly compare the two microwave spectrometers available at the University of the Basque Country (UPV/EHU). The Fabry-Pérot cavity based FTMW spectrometer was the first rotational spectroscopy machine installed at the University of the Basque Country (in 2010). It was built and fully operating before the work of this Thesis started. Currently, it is coupled to an ultrafast laser vaporization set-up, which allows for the analysis of thermally unstable samples. It features a very high spectral resolution (~5 kHz), which makes it an ideal tool to study subtle hyperfine interactions. The main disadvantage of the technique is that its short bandwith (~1 MHz) results in long spectral acquisition times.

More recently, in 2014, a CP-FTMW spectrometer was built at the University of the Basque Country (UPV/EHU). A large part of the work in this Thesis focused on the building, conditioning and optimising of this machine. With a bandwidth of 12 GHz, spectral acquisition times are normally shorter than the Fabry-Pérot machine for the recording of a rotational spectrum with similar signal-to-noise ratio. The spectral resolution of this apparatus is ~20 kHz. Therefore, it might not be enough to resolve the hyperfine structure in cases with very small splittings (see sections II.4 and II.5 for nuclear quadrupole coupling and internal rotation effects, respectively). This spectrometer is not currently coupled to a laser vaporization set-up, although there are plans to do it in the future. At present, we use the CP-FTMW device for gaseous samples or for solid or liquid samples that can be vaporized with conventional heating techniques.

III.4 Population distribution of the different conformations

Many molecules may exist under different conformations, because they possess one or more degrees of freedom. These conformations can be identified separately in microwave spectra. It is possible to derive the relative population of the individual conformations from the values of the intensities of rotational lines. In general, we assume that, before the supersonic expansion, there is a situation of thermodynamical equilibrium, and the population of the different conformations corresponds to a Boltzmann distribution at the pressure and temperature conditions prior to the expansion (room temperature, or temperature at which the sample is being heated). During the expansion, this distribution "freezes" and, therefore, the population distribution in the supersonic expansion corresponds to the one prior to the expansion, that is, an equilibrium distribution. The intensity of rotational lines depends both on the dipole moment and on the population of the given conformation. Therefore, by comparing the intensities of rotational lines (weighted with the dipole moments) between different conformers, we can infer the population ratio between the different conformations. Finally, by assuming an equilibrium distribution, we can estimate the energy difference between conformations.

In some cases, an effect called the "missing conformer" may occur. Let us suppose that there are two conformations that can interconvert to one another (for example, by a rotation about a single bond). If the interconversion energy barrier between the two conformations is low enough (tentatively, under 4-5 kJ/mol), collisions with the carrier gas may have enough energy to overcome the barrier. In that case, the high-energy conformer relaxes into the low-energy one. Therefore, the high-energy conformer is not detected in the microwave spectrum and we call it the "missing conformer".[28] The extent of the relaxation process is very dependent on the nature of the carrier gas. Heavier gases (such as Ar or Kr) result in more conformational relaxation than lighter gases (such as He or Ne).[29]

III.5 Cremer–Pople analysis

Some of the molecules that we have analyzed in this Thesis possess a ring in their structure (all of them are five or six membered rings). In order to analyze quantitatively the conformations of the rings, we can perform a Cremer-Pople analysis;[30] we have done that for the ionones and damascone, cotinine and methyl 2-deoxy-D-ribofuranoside. In this section, we will briefly review the basic concepts of the Cremer-Pople analysis necessary to understand the contents of this Thesis.

The atoms in an N-membered ring arrange in different conformations in order to reduce ring strain. We can describe these conformations with N-3 parameters called the Cremer-Pople coordinates. In the following, we will focus on two cases: five and six membered rings.

In five-membered cycles (N=5), we can describe the conformation of the ring with two coordinates, the amplitude (q) and the phase angle (φ). A five-membered ring adopts preferably two conformations: envelope (E) and twist (T). When the ring adopts an E form, four atoms lie in the same plane, and the fifth stands either above or below that plane. The nomenclature is ^{x}E or E_x, where x is the atom that stands above (superscript) or below

(subscript) the plane formed by the other four. In a T conformation, there are three atoms in the same plane, the fourth stands above that plane and the fifth stands below. In this case, the nomenclature is $^{x}T_{y}$ (x is the atom above and y is the atom below). Figure III.12 shows two examples of an E and a T conformation.
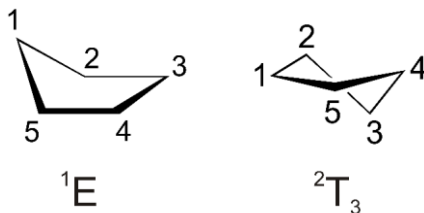
Figure III.12 Example of E and T conformations for a prototypical cyclopentane unit.

There are only two coordinates (q and φ) to define a five-membered ring. Briefly, the angle φ defines what kind of T or E conformation the system adopts (for example E_3, ^{2}E, $^{1}T_2$, $^{5}T_4$, etc...). Meanwhile, the amplitude q is a measure of how far the atom(s) stand out of the plane formed by the other four (three) atoms in the ring. The visual representation of the Cremer-Pople analysis for a five-membered ring is a disc, such as the one presented in Figure III.13.
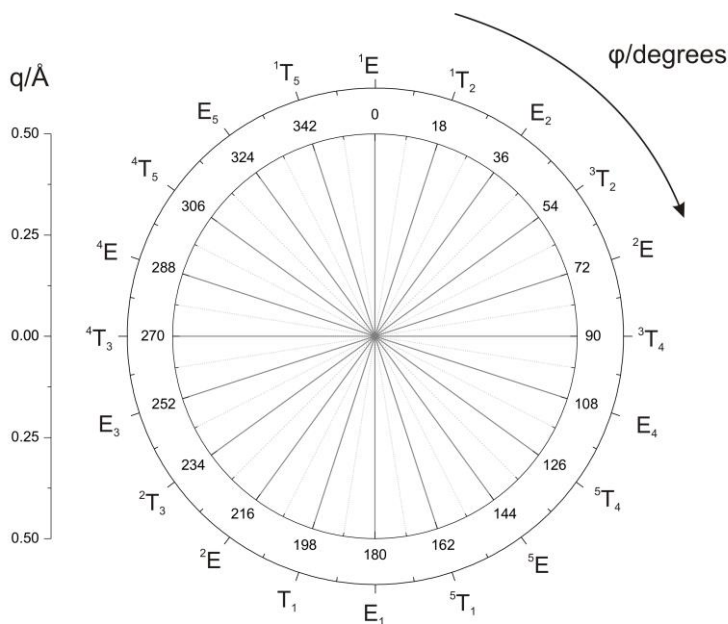
Figure III.13 Cremer-Pople wheel for a five-membered ring.

In the case of six-membered cycle (N=6), we can describe the configuration of the ring with three coordinates; an amplitude (q) and two phase angles (φ and θ). There is a wider range of possible conformations for a six-membered ring than for a five-membered one. Perhaps the most common is the Chair (C) conformation, where four atoms lie in a plane, the fifth lies above the plane, and the sixth below. The nomenclature is ^xC_y, where x is the atom above and y the one below the plane. The Boat (B) conformation is also quite common, in this case, two atoms (standing opposite to each other in the ring) are either above ($^{x,y}B$) or below ($B_{x,y}$) the plane formed by the other 4 atoms. Furthermore, there are other conformations such as Half-Boat (HB), Half Chair (HC) or Twist-Boat (TB).

Since there are three polar Cremer-Pople coordinates to describe a six-membered ring (q, φ and θ), the visual representation is a sphere. Figure III.14 features the Cremer-Pople sphere for a six-membered ring, and displays examples of C, B, HB, HC and TB conformations.
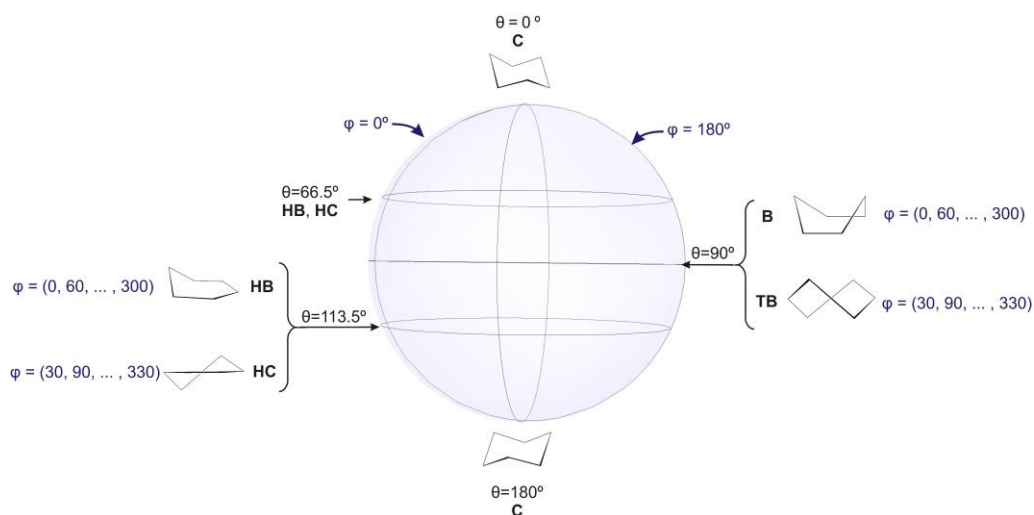
Figure III.14 Cremer-Pople sphere for a cyclohexane prototype ring. The shapes of the C, B, HB, HC and TB conformations are detailed.

Furanoses and pyranoses are specific cases of five- and six-membered rings, respectively. These terms refer to the cyclic units present in saccharides, in which one of the atoms in the ring is an oxygen atom and the rest are carbon atoms. We will refer to furanoses in Chapter VIII and we will review the conformations adopted by this kind of cycles.

III.6 References

[1] J. R. Rusk, W. Gordy, *Phys. Rev.* **1962**, *127*, 817–830.

[2] W. Caminati, P. Forti, *Chem. Phys. Lett.* **1974**, *29*, 239-241.

[3] J. L. Alonso, A. Lesarri, S. Mata, J. C. López, J.-U. Grabow, H. Dreizler, *Chem. Phys.* **1996**, *208*, 391-401.

[4] A. A. Fokin, T. S. Zhuk, S. Blomeyer, C. Pérez, L. V. Chernish, A. E. Pashenko, J. Antony, Y. V. Vishnevskiy, R. J. F. Berger, S. Grimme, C. Logemann, M. Schnell, N. W. Mitzel, P. R. Schreiner, *J. Am. Chem. Soc.* **2017**, *139*, 16696-16707.

[5] F. Jensen, 'Introduction to Computational Chemistry', *John Wiley & Sons Inc.*, New York, **2007**.

[6] T. A. Halgren, *J. Comput. Chem.* **1996**, *17*, 490-519.

[7] W. L. Jorgensen, J. Tirado-Rives, *J. Am. Chem. Soc.* **1988**, *110*, 1657-1666.

[8] P. K. Weiner, P. A. Kollman, *J. Comput. Chem.* **1981**, *2*, 287-303.

[9] K. N. Kirschner, A. B. Yongye, S. M. Tschampel, J. González-Outeiriño, C. R. Daniels, B. L. Foley, R. J. Woods, *J. Comput. Chem.* **2007**, *29*, 622-655.

[10] I. Kolossváry, G. M. Keserü, *J. Comput. Chem.* **2000**, *22*, 21-30.

[11] C. Moller, M. S. Plesset, *Phys. Rev.* **1934**, *46*, 618-622.

[12] Y. Zhao, D. G. Truhlar, *Theor. Chem. Acc.* **2008**, *120*, 215-241.

[13] S. Grimme, M. Steinmetz, *Phys. Chem. Chem. Phys.* **2013**, *15*, 16031-16042.

[14] A. D. Becke, *J. Chem. Phys.* **1993**, *98*, 5648-5652.

[15] C. T. Lee, W. T. Yang, R. G. Parr, *Phys. Rev. B* **1988**, *37*, 785-789.

[16] S. Grimme, J. Antony, S. Ehrlich, H. Krieg, *J. Chem. Phys.* **2010**, *132*, 154104-1 – 154104-19.

[17] S. Grimme, S. Ehrlich, L. Goerigk, *J. Comput. Chem.* **2011**, *32*, 1456-1465.

[18] W. J. Hehre, R. Ditchfield, J. A. Pople, *J. Chem. Phys.* **1972**, *56*, 2257.

[19] A. Lesarri, S. Mata, E. J. Cocinero, S. Blanco, J. C. López, J. L. Alonso, *Angew. Chem. Int. Ed.* **2002**, *41*, 4673-4676.

[20] A. Lesarri, R. Sánchez, E. J. Cocinero, J. C. López, J. L. Alonso, *J. Am. Chem. Soc.* **2005**, *127*, 12952-12956.

[21] E. J. Cocinero, A. Lesarri, P. Écija, F. J. Basterretxea, J.-U. Grabow, J. A. Fernández, F. Castaño, *Angew. Chem Int. Ed.* **2012**, *51*, 3119-3124.

[22] P. Écija, I. Uriarte, L. Spada, B. G. Davis, W. Caminati, F. J. Basterretxea, A. Lesarri, E. J. Cocinero, *Chem. Commun.* **2016**, *52*, 6241-6244.

[23] C. Cabezas, M. Varela, J. L. Alonso, *Angew. Chem. Int. Ed.* **2017**, *56*, 6420-6425.

[24] E. J. Cocinero, A. Lesarri, P. Écija, J.-U. Grabow, J. A. Fernández, F. Castaño, *Phys. Chem. Chem. Phys.* **2010**, *12*, 12486-12493.

[25] T. J. Balle, W. H. Flygare, *Rev. Sci. Instrum.* **1981**, *52*, 33-45.

[26] J.-U. Grabow, W. Stahl, H. Dreizler, *Rev. Sci. Instrum.* **1996**, *67*, 4072-4084.

[27] G. G. Brown, B. C. Dian, K. O. Douglass, S. M. Geyer, S. T. Shipman, B. H. Pate, *Rev. Sci. Instrum.* **2008**, *79*, 053103-1 – 053103-13.

[28] P. D. Godfrey, R. D. Brown, F. M. Rodgers, *J. Mol. Spectrosc.* **1996**, *376*, 65-81.

[29] R. S. Ruoff, T. D. Klots, T. Emilsson, H. S. Gutowsky, *J. Chem. Phys.* **1990**, *93*, 3142-3150.

[30] D. Cremer, J. A. Pople, *J. Am. Chem. Soc.* **1975**, *97*, 1354-1358.

Chapter IV.

The conformational landscapes of α-ionone, β-ionone, and β-damascone

IV.1 Introduction

In this Chapter, we explore the potential of CP-FTMW spectroscopy to study complex and rich conformational landscapes of flexible molecules. One of the goals in modern rotational spectroscopy is to extend the technique to molecular systems of increasing size and flexibility. The study we present here represents a step in that direction and unveils the potential of CP-FTMW spectroscopy to probe the conformational landscape of flexible molecules of biological interest. For doing that, we present the conformational analysis of three biomolecules (α- and β–ionone and β-damascone) that are structurally related. We will study how the structural differences between the three of them affect their preferred conformations (and their dynamics) and the possible implications in biological activity.

Retinal is a very important biocromophore involved in vision processes. It interacts with rhodopsin receptor protein in the form of retinal protonated Schiff-base (RPSB).[1] The position of the absorption maximum is strongly affected by a subtle interplay of interactions between the protein and the chromophore, but the details of these interactions are not clear and are still debated in a variety of studies.[2,3,4,5,6,7] In general, there is a common agreement that the interactions between the different protein's amino acids residues and the chromophore induce conformational changes in retinal that vary the wavelength absorption maximum position.[8]

In this work, we study the structural preferences of this biocromophore by addressing the conformational space of β-ionone (β-i), which can be considered as the basic structural motif of retinal. Moreover, we also study two "mutant" species: α-ionone (α-i) and β-damascone (β-d). These two molecules allow us to explore the consequences of performing structural changes in the cyclohexene ring (change in the position of the double bond in α-i) and in the lateral chain (interchange between the double bond and the C=O group in β-d). See Scheme IV.1 for the chemical structures of β-i, α-i and β-d.
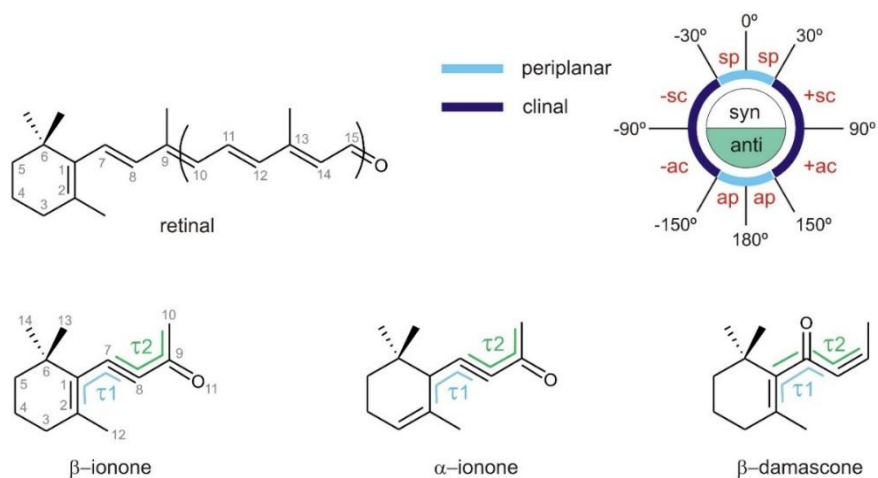
Scheme IV.1 Sketch of the structures of retinal, α-i, β-i and β-d, including the corresponding torsions (τ_1, τ_2), and the atom numbering used in the text. IUPAC nomenclature was used: sp (syn-periplanar), sc (synclinal), ac (anticlinal) and ap (anti-periplanar) for τ_1 and C, T (cis /trans~0°/180°) for τ_2. A conformer labelled as -sc/C would indicate that τ_1 is between -30° and -90° and τ_2 has a cis configuration.

Supersonic expansions provide an interaction-free medium where we can investigate, by means of CP-FTMW spectroscopy, the main forces governing the conformations of β-i and its two mutants. There are previous rotational spectroscopy studies in the gas phase reported in the literature about α-i and β-i. In particular, a Low Resolution MicroWave (LRMW) study in 1974[9] estimated the values of B+C for the two molecules. However, these data are not very precise and, moreover, only one conformation was reported. More recently, in 2016, Martin-Drumel et al. reported the experimental rotational constants of one conformation of α-i and one of β-i.[10] However, that work focused on introducing a novel automated microwave double resonance spectroscopic technique and did not present a full description of the conformational landscape of these systems, as we intend in this work. Furthermore, Legani et al. performed a theoretical study on α-i and β-i (among other related molecules) at the B3LYP/6-31G(d) level of theory.[11]

IV.2 Experimental section

Commercial samples of α-i (90%, b.p. 260°C), β-i (96%, b.p. 271°C), and β-d (95%, b.p. 200°C) were purchased from Sigma Aldrich and used without any further purification. All samples appear as colorless to pale yellow clear liquids with a sweet-floral odor. In order to vaporize the samples, we used conventional heating techniques. In particular, we used customized heating nozzles as explained in Chapter III. Table IV.1 summarizes the experimental conditions used for the rotational study of the three molecules.

Table IV.1 Experimental conditions for the rotational spectra of the three molecules.

Experimental conditions	α-i	β-i	β-d
Number of nozzles	2	3	2
Nozzle temperature	210ºC	200ºC	135ºC
Carrier gas	Ne/He (80/20)	Ne/He (80/20)	Ne/He (80/20)
Number of chirps/molecular pulse	10	10	10
Total number of cycles	22.50 millions	16.25 millions	15.10 millions

IV.3   Results

IV.3.1   Theoretical calculations

a.   *Potential Energy Surfaces and predicted conformations*

The common structural motif of the three molecules is a six-membered cyclohexene ring with a lateral chain containing double bonds and a C=O group. The conformational landscape of α-i, β-i, and β-d can be analyzed grouping the three main torsions that rule their structural arrangements (see Scheme IV.1):

- τ_1: orientation of the alkyl chain with respect to the ring.

- τ_2: orientation of the double bond of the alkyl chain with respect to C_{10} ($\tau_2 \sim 0°$ or 180°)

- Ring puckering of the cyclohexene ring.

These three torsions enable the description of the conformational panorama that characterizes the three compounds.

In order to predict the most stable conformations, we calculated the Potential Energy Surfaces (PES) of each molecule by scanning τ_1 and τ_2 in steps of 15º at the B3LYP-D3/6-31+G(d) level of theory. Due to the presence of a double bond, the ring can only adopt two conformations. Both of them are distorted HC configurations (see section III.5 about the Cremer-Pople analysis). The difference between the two HC configurations is an interchange between the atom that is standing above the plane and the one that is below (in general, it would be ^aHC_b and ^bHC_a). The inversion barrier between them is close to 20 kJ/mol, in agreement with data reported in literature.[12] For this reason, the ring can be treated as independent of the other two torsions (τ_1 and τ_2). For β-i and β-d, the two positions are equivalent by symmetry ($^aHC_b = ^bHC_a$). Only for α-i does the puckering give rise to non-equivalent species and hence, two PESs were calculated for α-i. The PESs are depicted in Figure IV.1 for the three systems in the form of two-dimensional contour plots. Eight different minima are predicted for α-i (four $^5HC_6$ and four $^6HC_5$), six for β-i and four for β-d, the latest with $^5HC_4$ ring configuration (see the Cremer-Pople analysis later for details of the HC configurations). The labelling chosen for the identification of the conformers

refers to the IUPAC nomenclature (see Scheme IV.1). The geometries at these minima were optimized at MP2 and B3LYP-D3 levels of theory with the 6-311++G(d,p) basis set. The most relevant spectroscopic parameters of the different predicted conformations are summarized in the appendix (Tables IV.A.1 to IV.A.3 in the appendix).
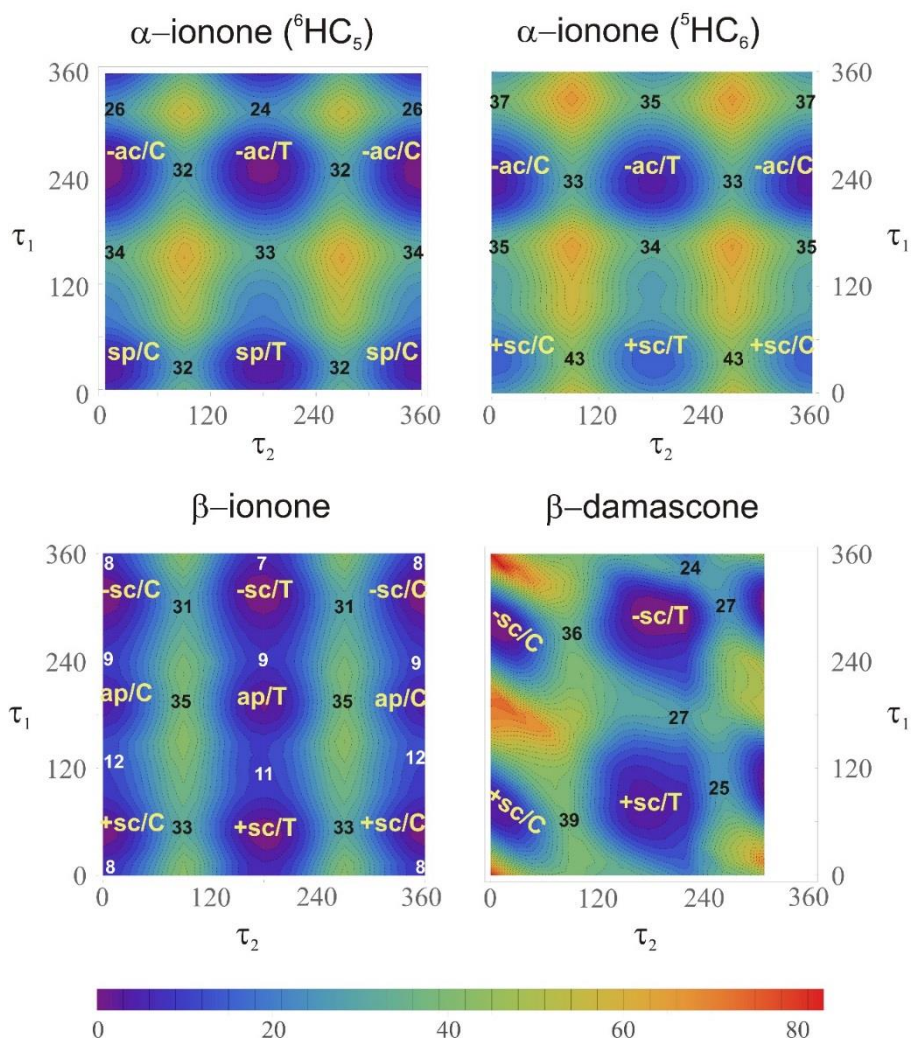
Figure IV.1 Theoretical 2D conformational PESs (kJ/mol) of α-i, β-i and β-d, exploring the τ_1 and τ_2 torsions at the B3LYP-D3/6-31+G(d) level of theory. The numbers reported on the graphics refer to the barrier heights separating the minima. Regarding β-d, it was not possible to calculate a section of the surface ($\tau_2 > 315°$) because of the steric hindrance due to the closeness of the carbonyl group and the cyclohexene ring. The energy scale is common to the four PESs. However, it is woth noting that the 0 kJ/mol energy point refers to the energy minimum of each molecule separately. That is, the 0 kJ/mol energy point for β-i is different than the 0 kJ/mol energy point for α-i, and β-d.

In addition to this, we used Molecular Mechanics (MM) to perform a conformational search on the three molecules. In particular, we used the MMFFs force field with a 20 kJ/mol energy window. As expected, the conformers obtained in the conformational search correspond to the ones arising from the 2D scans.

b. *Barriers to internal rotation of the methyl tops*

Each of the three molecules possesses four non-equivalent methyl tops that are subject to produce splittings in the rotational spectra due to coupling of the internal rotation with the overall rotation of the molecule. We estimate the barriers for internal rotation of the different methyl tops for the observed conformers (see later) by performing a relaxed scan at MP2/6-311++G(d,p) in steps of 10º. The results are shown in Tables IV.2, IV.3 and IV.4.

Table IV.2 Calculated methyl internal rotation barriers of the different methyl tops of α-i at the MP2/6-311++G(d,p) level of theory.

α-i	-ac/T $^6HC_5$	-ac/C $^6HC_5$	sp/T $^6HC_5$	sp/C $^6HC_5$	-ac/T $^5HC_6$	-ac/C $^5HC_6$
$V_3(C10)$/kJ/mol	3.8	4.6	3.7	4.7	3.9	4.6
$V_3(C12)$/kJ/mol	8.1	8.3	7.9	7.7	9.7	9.2
$V_3(C13)$/kJ/mol	14.4	14.4	14.3	14.2	16.0	15.9
$V_3(C14)$/kJ/mol	16.3	16.1	18.9	18.8	16.3	16.7

Table IV.3 Calculated methyl internal rotation barriers of the different methyl tops of β-i at the MP2/6-311++G(d,p) level of theory.

β-i	-sc/T	-sc/C	+sc/T	+sc/C
$V_3(C10)$/kJ/mol	3.6	4.3	3.6	4.5
$V_3(C12)$/kJ/mol	7.4	7.0	6.9	6.8
$V_3(C13)$/kJ/mol	14.7	14.5	12.5	12.5
$V_3(C14)$/kJ/mol	16.1	16.1	17.3	16.8

Table IV.4 Calculated methyl internal rotation barriers of the different methyl tops of β-d at the MP2/6-311++G(d,p) level of theory.

β-d	–sc/T	–sc/C	+sc/T	+sc/C
V_3(C10)/kJ/mol	7.9	7.7	7.9	7.7
V_3(C12)/kJ/mol	5.3	5.8	6.0	7.2
V_3(C13)/kJ/mol	17.6	17.6	14.0	14.7
V_3(C14)/kJ/mol	16.2	18.0	18.2	19.1

IV.3.2   Spectroscopic analysis

The rotational spectra (6-18 GHz) of the three samples (β-i, α-i, and β-d) were collected in three different experiments using the CP-FTMW available at the University of the Basque Country (UPV/EHU). In general, the three rotational spectra were very complex and dense, as shown in Figures IV.2, IV.3 and IV.4. In the spectrum of α-i, six different sets of rotational transitions were identified and fitted to a semi-rigid asymmetric rotor Hamiltonian in the Watson's *S*-reduction. The experimental values of the rotational constants A, B and C (see Table IV.5) were obtained and compared to the calculated values for the predicted conformations. This comparison proves that the six different sets of transitions observed correspond to conformers ac/C, ac/T with both [5]HC[6] and [6]HC[5] configurations of the ring, and sp/C and sp/T with an arrangement [6]HC[5] of the cyclohexene. Most rotational transitions displayed splittings due to tunneling effects from internal rotation of a methyl top. These splittings were included in the fit and we could estimate the value of the barrier to internal rotation (V_3) and the angles between the axis of internal rotation and the principal axes of inertia of the molecule. Once all the lines arising from the six assigned conformations were removed from the spectrum, several lines remained unassigned. Some of those lines were assigned to the isotopic species arising from ^{13}C substitution in natural abundance (~1%, 13 different species) and also [18]O (~0.2%, one species) for the most stable conformation of α-i (-ac/C [6]HC[5]). Table IV.6 collects the values of the experimental rotational constants of all observed isotopologues of α-i. A similar procedure was used for β-i and β-d, where four conformers were identified (sc/C, sc/T, sc/C and sc/T) (see Tables IV.7 and IV.9 for experimental rotational constants of the parent species). In the case of β-i, the lines appeared as doublets, proof of the internal rotation from one single methyl top (analogous to α-i). However, for β-d the situation was slightly different. Rotational transitions appeared as quintuplets, coming from the internal rotation of two non-equivalent methyl tops. The signal-to-noise ratio in the spectra of β-i and β-d allowed for the detection of isotopic species arising from ^{13}C substitution in natural abundance, the results of the corresponding fits are summarized in Tables IV.8 and IV.10.

The calculated values of the rotational constants at MP2/6-311++G(d,p) and B3LYP-D3/6-311++G(d,p) levels of theory are in very good agreement with the experimental values. Both methods are able to characterize the structures with very high

accuracy, giving an average percent relative error in the rotational constants of $\delta_{MP2} = 0.2/0.4/0.8$ and $\delta_{B3LYP-D3} = 0.5/0.4/0.4$ for β-i, α-i, β-d, respectively.

Furthermore, each molecule possesses four methyl tops that may potentially induce splittings in the rotational transitions. In order to know which methyl top is the one responsible for the splittings, it is necessary to compare the theoretical values of V_3 with the experimental ones that result from the fits (that is, comparing the values in Tables IV.2, IV.3 and IV.4 and the ones in Tables IV.5, IV.7 and IV.9). By doing that, we can easily conclude that in the case of α-i and β-i, the methyl top responsible for the internal rotation is the terminal methyl group in the chain (C10) while in β-d it is C10 and C12 (the one that stands alone in the ring) the ones that induce splittings in the rotational transitions.

All measured rotational transitions of the three molecules and their isotopologues are collected here.

Figure IV.2 Experimental rotational spectrum of α-i, with a zoomed view around the 10350 MHz region where the splittings due to internal rotation are observable. The spectrum contains approximatively 3600 lines with a signal-to-noise ratio greater than 2/1. Signal-to-noise ratio of the most intense line assigned (11 2 9 ← 10 2 8) is about 3200.

Figure IV.3 Experimental rotational spectrum of β-i, with a zoomed view around the 9750 MHz region where the splittings due to internal rotation are observable. The spectrum contains approximatively 2800 lines with a signal-to-noise ratio greater than 2/1. Signal-to-noise ratio of the most intense line assigned (10 2 8 ← 9 2 7) is about 950.
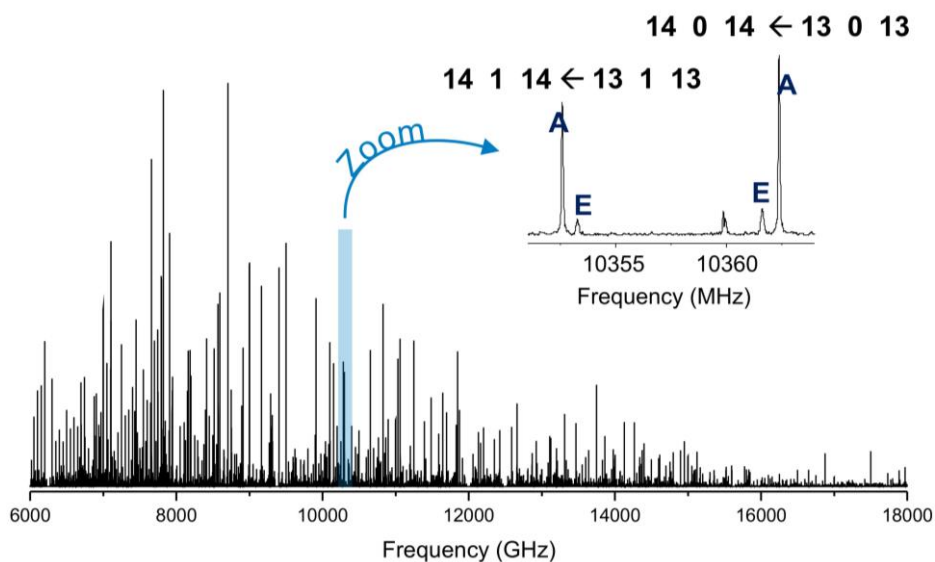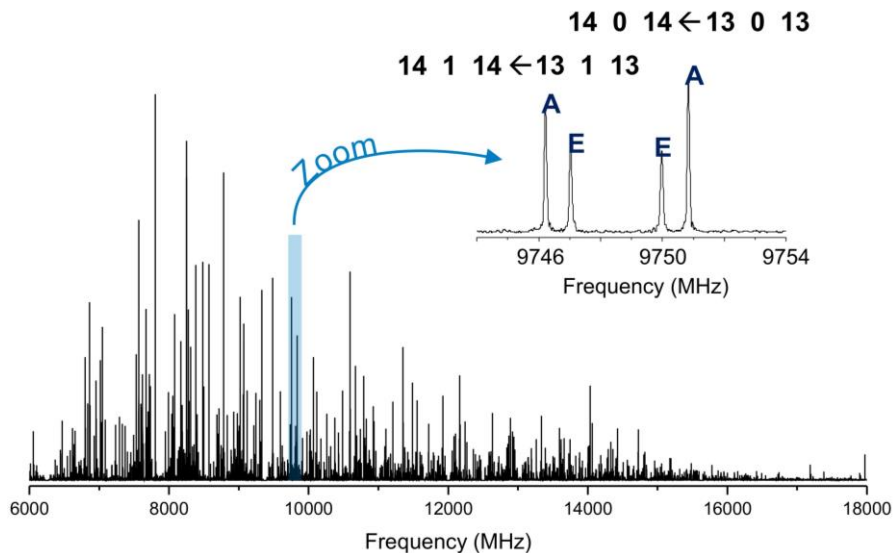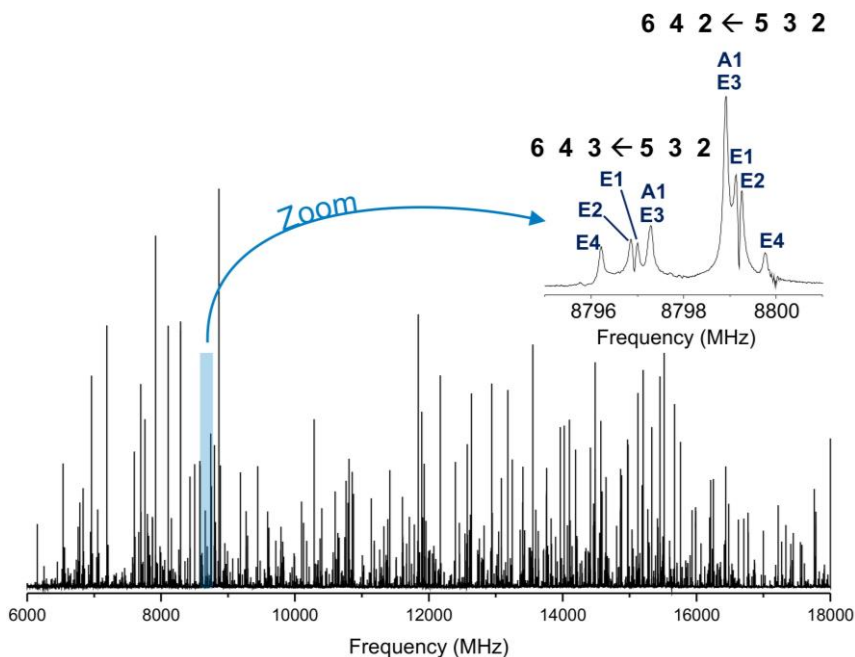

Figure IV.4 Experimental rotational spectrum of β-d, with a zoomed view around the 8800 MHz region where the splittings due to internal rotation are observable. The spectrum contains approximatively 1000 lines with a signal-to-noise ratio greater than 2/1. Signal-to-noise ratio of the most intense line assigned (7 3 4 ← 6 2 4) is about 700.

Table IV.5 Experimental spectroscopic parameters of α-i and comparison with theoretical predictions at MP2/6-311++G(d,p) level.

	-ac/T $^6HC_5$		-ac/C $^6HC_5$		sp/T $^6HC_5$	
	Exp.	Theory	Exp.	Theory	Exp.	Theory
A/MHz	1059.1769(7)	1061	1041.5530(5)	1044	980.8933(9)	978
B/MHz	405.7415(1)	406	408.06351(7)	409	450.4025(2)	454
C/MHz	359.6409(1)	360	363.66898(8)	365	392.9703(2)	398
D_J/kHz	0.0067(3)	0.0068	0.00564(8)	0.0068	0.0151(3)	0.0167
D_{JK}/kHz	0.178(2)	0.1889	0.1803(2)	0.1780	0.071(3)	0.0791
D_K/kHz	−0.16(1)	−0.1257	−0.087(7)	−0.1236		
d_1/Hz			0.13(6)	−0.04		
d_2/Hz	−0.34(5)	−0.05	−0.20(4)	−0.15	−0.7(2)	−1.3
V_3/kJ mol^{-1}	4.3070(9)	3.78	5.254(3)	4.56	4.30(2)	3.71
$\angle(a,i)$/deg	145.28(6)	146.96	97.0(1)	92.35	128.5(9)	125.47
$\angle(b,i)$/deg	89.180(1)	89.22	86.851(1)	86.83	58.5(4)	57.06
$\angle(c,i)$/deg	124.71(6)	123.03	172.4(1)	176.05	54.4(5)	52.67
N	290		954		142	
σ/kHz	18		19		16	
	sp/C $^6HC_5$		-ac/T $^5HC_6$		-ac/C $^5HC_6$	
	Exp.	Theory	Exp.	Theory	Exp.	Theory
A/MHz	977.6680(6)	974	1156.413(1)	1159	1137.4744(9)	1140
B/MHz	452.9156(1)	457	399.7992(1)	400	402.3243(1)	403
C/MHz	393.5871(1)	399	341.2269(2)	342	344.53064(9)	346
D_J/kHz	0.0144(2)	0.0159			0.00442(8)	0.0055
D_{JK}/kHz	0.073(1)	0.0741	0.208(6)	0.1930	0.1701(5)	0.1842
D_K/kHz					−0.13(4)	−0.1237
d_1/Hz	0.8(1)	0.4			−0.87(6)	−1.0
d_2/Hz	−1.10(8)	−0.8			−0.23(4)	−0.3
V_3/kJ mol^{-1}	5.446(7)	4.69	4.26(2)	3.85	5.276(3)	4.62
$\angle(a,i)$/deg	120.9(3)	113.57	34(2)	37.24	79.2(1)	83.65
$\angle(b,i)$/deg	46.2(2)	42.27	81.7(4)	80.97	80.222(5)	80.10
$\angle(c,i)$/deg	59.6(1)	57.26	122(2)	125.76	165.3(1)	168.21
N	455		102		689	
σ/kHz	18		14		17	

Table IV.6 Experimental spectroscopic parameters of the observed isotopologues of α-i.

	13C(1)	13C(2)	13C(3)	13C(4)	13C(5)	13C(6)	13C(7)
A/MHz	1040.753 (8)	1037.061 (9)	1035.57 (1)	1037.465 (8)	1036.914 (7)	1038.892 (8)	1041.540 (9)
B/MHz	407.8626 (1)	407.6155 (1)	406.3951 (1)	404.8913 (1)	406.2871 (1)	407.3069 (1)	407.8753 (1)
$C‹$/MHz	363.6107 (1)	362.7895 (1)	361.8522 (2)	361.5769 (1)	362.3641 (1)	362.7861 (1)	363.5213 (1)
N	60	58	53	58	76	60	57
σ σ/kHz	9	10	10	8	10	9	9
	13C(8)	13C(9)	13C(10)	18O(11)	13C(12)	13C(13)	13C(14)
A/MHz	1040.863 (6)	1041.546 (7)	1036.151 (8)	1040.01 (2)	1025.125 (9)	1035.53 (1)	1028.781 (9)
B/MHz	406.69360 (8)	404.5240 (1)	403.5347 (1)	396.0581 (3)	407.7227 (1)	405.2094 (1)	407.8199 (1)
C/MHz	362.66659 (8)	360.8544 (1)	360.6930 (1)	354.2730 (4)	361.7532 (1)	361.5333 (1)	361.9954 (1)
N	64	57	55	16	54	60	63
σ/kHz	6	8	9	9	10	9	10

Table IV.7 Experimental spectroscopic parameters of β-i and comparison with theoretical predictions at MP2/6-311++G(d,p) level.

	-sc/T		-sc/C		+sc/T		+sc/C	
	Exp.	Theory	Exp.	Theory	Exp.	Theory	Exp.	Theory
A /MHz	1109.0046 (3)	1108	1100.5066 (2)	1100.2	1134.5209 (6)	1135	1121.9807 (4)	1123
B /MHz	406.02837 (8)	407	408.99572 (6)	410.5	402.9824 (1)	404	405.98131 (9)	407
C /MHz	338.45550 (7)	339	339.93901 (6)	340.4	333.3748 (1)	334	335.12030 (7)	336
D_J /kHz	0.0060 (1)	0.0059	0.00456 (7)	0.0055	0.0051 (2)	0.0044	0.00453 (9)	0.0042
D_{JK} /kHz	0.0988 (9)	0.0901	0.0997 (5)	0.0878	0.077 (2)	0.0900	0.0821 (6)	0.0892
D_K /kHz	-0.050(2)	-0.033	-0.053(2)	-0.040			-0.048(5)	-0.059
d_1/Hz	-0.34(6)	-0.3	-0.12(5)	-0.4	-0.49(9)	-0.5	-0.57(6)	-0.6
d_2/Hz	-0.48(4)	-0.8	-0.70(4)	-0.7	-0.44(6)	-0.6	-0.55(4)	-0.6
V_3 /kJ mol^{-1}	4.1064(5)	3.5836	5.107(2)	4.34	4.074(3)	3.56	5.231(3)	4.45
$\angle(a,i)$ /deg	45.61(3)	47.22	69.72(7)	73.30	41.7(2)	44.21	71.9(2)	76.07
$\angle(b,i)$ /deg	62.97(2)	62.17	46.55(2)	45.39	64.8(1)	63.44	46.09(5)	44.92
$\angle(c,i)$ /deg	56.54(2)	55.51	50.36(2)	49.35	120.7(1)	122.35	130.55(4)	131.59
N	710		802		227		550	
σ /kHz	15		15		12		13	

Table IV.8 Experimental spectroscopic parameters of the observed isotopologues of β-i.

	13C(1)	13C(2)	13C(3)	13C(4)	13C(5)	13C(6)	13C(7)
A/MHz	1084.128 (9)	1095.94 (1)	1093.827 (9)	1098.94 (1)	1099.101 (8)	1097.436 (9)	1100.031 (8)
B/MHz	408.8616 (2)	408.6215 (2)	406.9550 (2)	405.3739 (2)	406.1545 (1)	408.3047 (2)	408.7095 (1)
C/MHz	338.4334 (2)	339.2877 (2)	337.8931 (1)	337.4493 (2)	337.8504 (2)	339.1716 (1)	339.7721 (2)
N	32	31	26	24	29	28	38
σ/kHz	11	9	8	9	8	8	9

	13C(8)	13C(9)	13C(10)	13C(12)	13C(13)	13C(14)
A/MHz	1099.92 (1)	1100.417 (7)	1096.60 (1)	1100.361 (8)	1088.852 (9)	1086.26 (1)
B/MHz	407.8293 (2)	405.4211 (1)	404.1882 (2)	408.8903 (1)	407.9011 (1)	408.1980 (2)
C/MHz	339.1283 (2)	337.4749 (1)	336.5480 (2)	339.8888 (2)	338.9608 (1)	338.4916 (3)
N	28	31	26	32	31	27
σ/kHz	13	7	10	9	9	10

Table IV.9 Experimental spectroscopic parameters of β-d and comparison with theoretical predictions at MP2/6-311++G(d,p) level.

	-sc/T		-sc/C		+sc/T		+sc/C	
	Exp.	Theory	Exp.	Theory	Exp.	Theory	Exp.	Theory
A/MHz	1014.172 (2)	1008	860.9633 (5)	854	1059.0938 (5)	1052	897.2905 (3)	889
B/MHz	466.4507 (6)	468	541.9859 (2)	549	462.8105 (1)	464	536.2615 (1)	541
C/MHz	401.7351 (9)	404	489.0367 (2)	495	389.8836 (2)	393	472.7732 (1)	480
D_J/kHz	0.018 (3)	0.026	0.0281 (6)	0.0298	0.0085 (3)	0.0092	0.0237 (3)	0.0239
D_{JK}/kHz	0.326 (7)	0.206	0.069 (2)	0.088	0.195 (2)	0.201	0.0255 (8)	0.0321
D_K/kHz	-0.244 (6)	-0.075	-0.046 (2)	-0.061	-0.114 (3)	-0.124	0.0076 (9)	0.0031
d_1/Hz	6(1)	-5					1.2(1)	1.4
d_2/Hz			-0.4(1)	0.01	-0.42 (9)	-0.5	-0.23(5)	0.1
V_3(C10) /kJ mol^{-1}	6.948 (7)	7.89	6.950 (9)	7.71	6.92 (8)	7.88	7.040 (6)	7.66
V_3(C12) /kJ mol^{-1}	5.419 (2)	5.29	6.54(1)	5.82	6.49 (7)	5.96	6.60(1)	7.16
∠(a,i)(C10) /deg			33.1(6)	30.64	39(5)	40.19	157.6(7)	152.3
∠(b,i)(C10) /deg			80.7(2)	81.33	78(1)	78.04	84.8(2)	83.63
∠(c,i)(C10) /deg			121.4(6)	119.1	127(4)	127.7	111.7(7)	116.9
∠(a,i)(C12) /deg			53.7(4)	51.84	48(3)	55.46	124.4(5)	126.9
∠(b,i)(C12) /deg			54.3(2)	55.34	45(3)	38.31	49.0(3)	50.57
∠(c,i)(C12) /deg			56.2(2)	57.12	76.8(6)	75.48	59.9(2)	60.89
N	198		602		227		793	
σ/kHz	20		20		12		19	

Table IV.10 Experimental spectroscopic parameters of the observed isotopologues of β-d.

	13C(1)	13C(2)	13C(3)	13C(4)	13C(5)	13C(6)	13C(7)
A/MHz	897.144 (1)	894.172 (2)	891.086 (3)	895.297 (2)	894.679 (2)	895.615 (2)	895.273 (3)
B/MHz	536.1 (4)	536.7 (5)	533.6 (7)	530.8 (5)	533.7 (7)	536.7 (5)	537.3 (8)
C/MHz	472.8 (4)	471.0 (6)	470.7 (8)	469.7 (6)	469.4 (8)	470.2 (6)	469.8 (9)
N	36	32	36	36	32	40	32
σ/kHz	24	32	25	34	39	37	49
	13C(8)	13C(9)	13C(10)	13C(12)	13C(13)	13C(14)	
A/MHz	896.847(3)	896.183(3)	893.770(2)	886.936(2)	888.876(2)	891.550 (2)	
B/MHz	535.2(7)	531.5(8)	527.8(5)	534.0(5)	535.4(6)	533.9(5)	
C/MHz	468.2(8)	470.8(9)	465.0(6)	471.9(6)	470.9(7)	469.5(6)	
N	32	32	32	36	36	32	
σ/kHz	42	44	33	34	38	31	

IV.3.3   Cremer–Pople analysis

We performed a Cremer-Pople analysis (see section III.5) on the cyclohexene ring of β-i, α-i, and β-d to assess quantitatively what conformations the six-membered ring adopts in the gas phase. The results are summarized in Figure IV.5, which shows the Cremer-Pople sphere for the observed conformers of the three molecular systems. According to this, all observed conformations share a distorted Half-Chair conformation, where four atoms in the ring lie in the same plane and two stand out of that plane (one up and one down). The two atoms that are not in the plane are the ones located opposite from the double bond.
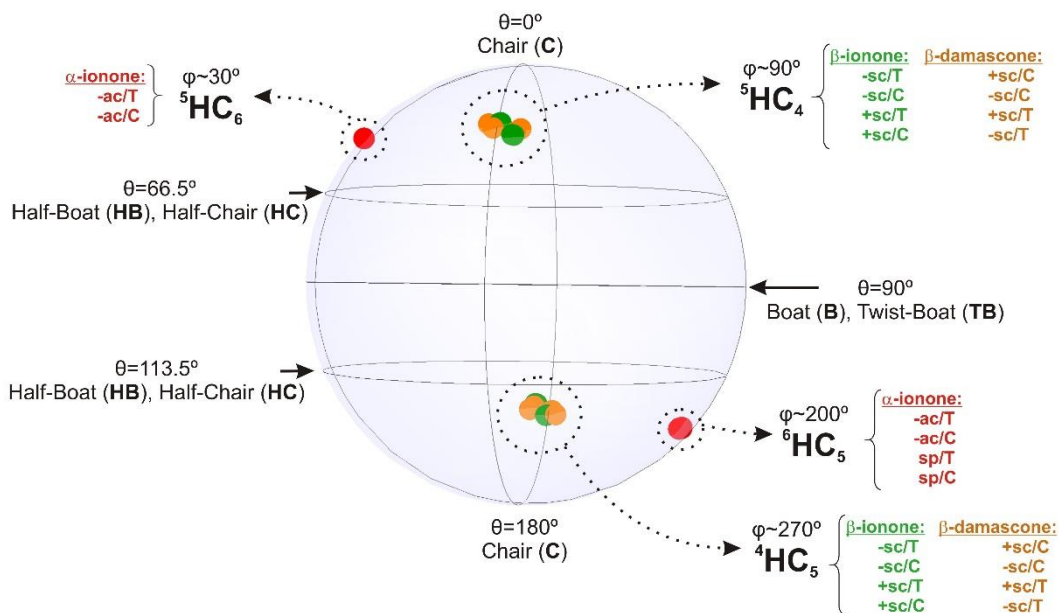
Figure IV.5 Cremer-Pople sphere for the observed conformers of β-i, α-i, and β-d. All amplitudes (q, distance to the center of the sphere) have been given the same value for the sake of clarity.

IV.4   Discussion

In this work, we have reported on the conformational landscape of the three structurally related biomolecules β-i, α-i, and β-d by means of a combination of rotational spectroscopy and theoretical calculations. These systems appear as flexible structures, each of them giving rise to several conformations (six for α-i and four for β-i and β-d). The rotational transitions displayed splittings due to the internal rotation of methyl tops. The signal-to-noise ratio of the different spectra was high enough to allow for the detection of isotopologues arising from isotopic substitution in natural abundance of ^{13}C and ^{18}O (the latter only for α-i) for the global minima.

In order to evaluate the changes in the ring puckering properties among the three molecules, we performed a Cremer-Pople analysis, which allows the description of a six-membered ring with three polar coordinates. Each conformation with its corresponding coordinates is located in the spherical visual representation of the Cremer-Pople study in Figure IV.5. As mentioned above, all three systems share the same structure of the ring: a distorted HC conformation. We can clearly observe that, within a given molecule, conformations with different ring configurations are diametrically opposed. All β-i and β-d conformations are located in the same region of the sphere, corresponding to a distorted $^5HC_4$ conformation equivalent to $^4HC_5$ by symmetry. α-i has a different behavior. In this case, the position of the double bond is different from the other two molecules. Consequently, the symmetry is lost and the two HC configurations are no

longer equivalent. Hence, α-i adopts two non-equivalent $^5HC_6$ and $^6HC_5$ configurations, where atoms 5 and 6 are the ones that stand out of the plane, as opposed to the case of β-i and β-d, where the out-of-plane atoms are 4 and 5.

In the rotational spectra of β-i, α-i, and β-d, rotational transitions displayed splittings due to the internal motions of methyl tops. Hence, it was possible to calculate the corresponding barriers to internal rotation (V_3). In the case of β-i and α-i, rotational lines appear as doublets due to the methyl top at the end of the flexible chain (C10). V_3 is sensitive to the electronic surrounding of the methyl group, so it acts as a probe of the local environment of the given internal top. In fact, in the case of β-i and α-i, V_3 tells us about the configuration of τ_2. When $\tau_2 \sim 0°$ (*cis*, C conformers), V_3 is around 5 kJ/mol, and when $\tau_2 \sim 180°$ (*trans*, T conformers), V_3 takes on values around 4 kJ/mol. The rest of the methyl tops (C12, C13 and C14) in the molecules possess V_3 barriers greater than ~7 kJ/mol for all conformers and do not produce splittings in the rotational spectrum. Steric effects might be the cause of this dependence of V_3 on τ_2. When $\tau_2 \sim 0°$, the lateral chain adopts a more compact, folded structure, and the CH_3 group is closer to the hydrogen in the double bond, which may cause sterical hindrance and, hence, increase the potential energy barrier. β-d has a different behavior than the other two molecules. Its rotational transitions appear as quintuplets, due to the internal rotation of both the terminal methyl top (C10) and the methyl group in the ring (C12). The value of V_3 of the terminal chain methyl top is higher than in the cases of β-i and α-i (~7 kJ/mol compared to 4-5 kJ/mol). In the latter, there is a C=O adjacent to the CH_3 while this is not the case for β-d (where the C=O group is moved two positions toward the ring). Therefore, a CH···O attractive interaction in the case of β-i and α-i might be responsible for the decreasing in V_3 compared to β-d. Finally, the barrier for internal rotation of the CH_3 in the ring (C12) is lower in the case of β-d, probably due to a combination of electronic (proximity of the C=O group) and steric effects.

Rotational spectroscopy studies such as the one presented here allow for the estimation of the relative populations of the different conformations in the supersonic expansion, and their relative energies (see section III.4). We have performed this task for the three molecules under study and the estimations of the relative energies are presented in Table IV.11. For doing that, we have selected rotational transitions that are close in frequency (maximum 1 GHz span) to avoid problems caused by the instrument having slightly different responses in different frequency regions. We can observe that, for β-d and α-i, a single conformation dominates the conformational landscape (-ac/C $^6HC_5$ for α-i and +sc/C for β-d), with the next conformer lying around 4 kJ/mol higher in energy. β-i, on the other hand, has a slightly different behavior. Two conformers are almost isoenergetic (-sc/C and -sc/T), and the next conformer lies only 2.0(9) kJ/mol higher in energy.

Table IV.11 Experimental relative energies of the different observed conformers of α-i, β-i and β-d.

α-i	-ac/C $^6HC_5$	-ac/T $^6HC_5$	-ac/C $^5HC_6$	sp/T $^6HC_5$	-ac/T $^5HC_6$	sp/C $^6HC_5$
$\Delta E_{0.0}$ / kJ*mol^{-1}	0	4.1(8)	6.0(1.1)	7.0(8)	8.2(3)	9.8(7)

β-i	-sc/C	-sc/T	+sc/T	+sc/C
$\Delta E_{0.0}$ / kJ*mol^{-1}	0	0	2.0 (9)	3.9(9)

β-d	+sc/C	-sc/C	+sc/T	-sc/T
$\Delta E_{0.0}$ / kJ*mol^{-1}	0	3.8(8)	6.7(6)	12.4(5)

In general, we have demonstrated that the PES of β-i is flatter than its two mutants, β-d and α-i. From a theoretical point of view, it is clear from the two-dimensional PESs that the energy barriers to interconvert between conformers along τ_1 (that is, up to down or down to up in Figure IV.1) are the lowest of all molecules (8-12 kJ/mol, while any other interconversion in the two other molecules requires more than 25 kJ/mol). While this interconversion in β-i does not seem to occur in our supersonic expansion, it could be the case in other media. From the experimental point of view, we have demonstrated that two conformations dominate in β-i (-sc/C and –sc/T) that share the same configuration of $\tau_1 \sim \pm 52°$ (corresponding $^5HC_4$ and $^4HC_5$ configurations (equivalent by symmetry)), but differ in *cis /trans* conformation of τ_2. For β-d and α-i, on the other hand, there is only one dominant conformation for each molecule, the rest of the conformers being more than 4 kJ/mol higher in energy. Moreover, one could think that resonance in β-i should induce a planarity of the $C_2=C_1-C_7=C_8$ dihedral angle. However, the two conformers that approach planarity (ap/T and ap/C) are predicted higher in energy and hence they are not observed in our rotational spectra. The steric effects between the hydrogen atom attached to C8 and the hydrogen atoms of the methyl group (C12) prevent these arrangements. With all this, we can say that β-i possesses more structural flexibility than its two mutants. The ability to interconvert between different conformers may help this molecule adapt to the biological medium (for instance, in the interaction with the protein), in comparison with β-d and α-i, which display a more rigid structure.

IV.5   References

[1] G. Wald, *Science* **1968**, *162*, 230–239.

[2] N. Ferré, M. Olivucci, *J. Am. Chem. Soc.* **2003**, *125*, 6868–6869.

[3] L. H. Andersen, I. B. Nielsen, M. B. Kristensen, M. O. A. El Ghazaly, S. Haacke, M. B. Nielsen, M. Å. Petersen, *J. Am. Chem. Soc.* **2005**, *127*, 12347–12350.

[4] M. B. Nielsen, *Chem. Soc. Rev.* **2009**, *38*, 913–924.

[5] J. Rajput, D. B. Rahbek, L. H. Andersen, A. Hirshfeld, M. Sheves, P. Altoè, G. Orlandi, M. Garavelli, *Angew. Chemie - Int. Ed.* **2010**, *49*, 1790–1793.

[6] E. Nango, A. Royant, M. Kubo, T. Nakane, C. Wickstrand, T. Kimura, T. Tanaka, K. Tono, C. Song, R. Tanaka, et al., *Science* **2016**, *354*, 1552 LP-1557.

[7] C. M. Suomivuori, L. Lang, D. Sundholm, A. P. Gamiz-Hernandez, V. R. I. Kaila, *Chem. - A Eur. J.* **2016**, *22*, 8254–8261.

[8] W. Wang, Z. Nossoni, T. Berbasova, C. T. Watson, I. Yapici, K. S. S. Lee, C. Vasileiou, J. H. Geiger, B. Borhan, *Science* **2012**, *338*, 1340 LP-1343.

[9] W. E. Steinmetz, *J. Am. Chem. Soc.* **1974**, *96(3)*, 685-692.

[10] M.-A. Martin-Drumel, M. C. McCarthy, D. Patterson, B. A. McGuire, K. N. Crabtree, *J. Chem. Phys.* **2016**, *144*, 124202-1-124202-7.

[11] L. Legnani, M. Luparia, G. Zanoni, L. Toma, G. Vidari, *Eur. J. Org. Chem.* **2008**, *28*, 4755-4762.

[12] F. A. L. Anet, D. I. Freedberg, J. W. Storer, K. N. Houk, *J. Am. Chem. Soc.* **1992**, *114*, 10969–10971.

Chapter V.

CP-FTMW and FTMW techniques in the structural study of cotinine

V.1 Introduction

In this Chapter, we prove the complementarity of the CP-FTMW and FTMW techniques in the rotational study of the nicotinoid cotinine. First, the broadband spectrometer allows for the acquisition of the rotational spectrum of this nicotinoid in the 7 to 18 GHz frequency region in a rapid way. A first analysis of the rotational spectrum obtained with the CP-FTMW device yields the overall picture of the conformational landscape of the molecule. However, the complicated fine and hyperfine structure arising from internal rotation of the methyl top and the presence of two quadrupolar nuclei is not completely discernible at the resolution of the broadband spectrometer. Therefore, in a second step, some rotational transitions of cotinine are measured in the FTMW, whose spectral resolution allows for the identification of the hyperfine components separately.

Nicotinoids are agonists of specific acetylcholine receptors (nAChRs)[1,2,3] inducing a wide range of natural and pharmacological responses in the central and peripheral nervous system. The structural prototype of this family of biomolecules is nicotine (see **1**, Scheme V.1). The search for a nicotine pharmacophore and alternative nAChRs receptors has been active in the last decades, calling for additional attention on other nicotinoids. Cotinine (1-methyl-5-(3-pyrinidyl)-2-pyrrolidinone, **2** in Scheme V.1) is the predominant oxidative metabolite of nicotine,[4] differing only in the addition of a carbonyl group to the pyrrolidine ring. However, cotinine shows a reduced desensitizing effect on nAChRs. Xiu and co-workers explained the interaction between nicotine and nAChR in terms of a strong cation···π interaction between the protonated nicotine and an aromatic residue of a tryptophan residue.[5] Several reasons have been postulated to explain the lower affinity of other nicotinoids (such as cotinine) to the nAChRs receptors. First, the N···N distance could modulate the intensity of their biological activity. Second, the partial charge on the pyrrole N atom might influence the tendency to protonation and hence the biological activity. Third, a possible C-H···O=C intramolecular interaction is also suggested as an explanation for the lower affinity of cotinine to the receptor.[6] Accurate structural information on nicotinoids is thus required to model binding to receptor proteins and to define structure-activity biochemical relationships.
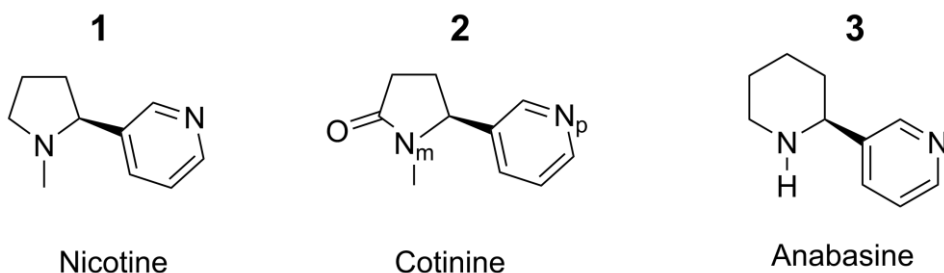
Scheme V.1 Chemical structure of three nicotinoids.

There are no previous high-resolution spectroscopic studies of cotinine reported in the literature. A recent vibrational circular dichroism (VCD) analysis in solution and in solid phase suggested that four conformations could be responsible for the vibrational spectra.[7]

However, intra- and intermolecular interactions can be masked by solvent and crystal-packing forces, so these data are not always conclusive for the free molecule. A gas phase electron diffraction (GED)[6] also pointed to the coexistence of four different conformations, but the spectral resolution of this technique is not enough to resolve small structural differences in conformationally complex mixtures. Here, we apply the unique power of rotational spectroscopy as a structural elucidation tool to solve the problem of conformational analysis of cotinine. Other nicotinoids such as nicotine[8] or anabasine[9] (**3**, Scheme V.1) have been previously studied with this method. From the spectroscopic point of view, cotinine presents a challenge since its rotational spectrum is expected to display a very complicated hyperfine structure arising from the two ^{14}N nuclei and the methyl top. In this work, we pursue two goals. The first one is the identification of the dominant conformations of cotinine under isolation conditions. The second one is the unraveling of the complex hyperfine structure. We use here the two microwave spectrometers available at the University of the Basque Country (UPV/EHU) and demonstrate the complementarity of the two machines. While the CP-FTMW spectrometer provides a rapid means of surveying the conformational preferences of cotinine, the higher spectral resolution of the FTMW cavity device allows for the assignment of subtle fine and hyperfine patterns.

V.2 Experimental section

Cotinine samples (solid at room temperature, m. p. 40ºC) take on a wet appearance, with small crystals sticking together. The consistency of the sample made it impossible to use laser vaporization techniques, which are more suitable for samples with low volatility. Therefore, we used conventional heating techniques to bring cotinine into the gas phase. Table V.1 summarizes the experimental conditions used for the rotational study of cotinine in the CP-FTMW and FTMW spectrometers.

Table V.1 Experimental conditions for CP-FTMW and FTMW spectra of cotinine.

Experimental conditions	CP-FTMW	FTMW
Number of nozzles	1	1
Nozzle temperature	200ºC	200ºC
Carrier gas	Ne/He (80/20)	Ne/He (80/20)
Number of chirps/molecular pulse	10	2
Total number of cycles	5 millions	20000-200000*

*The exact value depends on the required number of cycles to obtain a good signal-to-noise ratio of a given rotational transition.

V.3 Results

V.3.1 Theoretical calculations

a. Predicted conformations

Cotinine is an assembly of pyrrolidinone and pyridine rings linked by a single C–C bond. This two-ring assembly structure is a common motif among nicotinoids. Cotinine's conformational landscape can be rationalized attending to two factors:

- The first one is the pyrrolidinone conformation. The five-membered ring may preferably adopt two distorted twist conformations, distinguishable by the equatorial/axial (*eq/ax*) position of the pyridine substituent.

- The second one is the internal rotation around the single bond connecting the two rings. Two rotamers (denoted *a* and *b*) arise by a ~180º rotation of the pyridine moiety.

We used Molecular Mechanics (MM) to perform a conformational search on cotinine. In particular, we used the MMFFs force field with a 25 kJ/mol energy window and it yielded the four conformations expected from the two abovementioned structural factors. Then, those conformations were optimized by quantum mechanical methods to yield accurate structures. The structures were labeled *eq-a*, *ax-a*, *eq-b* and *ax-b* according to the two structural factors. The results from MP2, M06-2X, B3LYP and B3LYP-D3 theoretical calculations are summarized in Table V.2.

Table V.2 Computed spectroscopic parameters for the lowest lying conformers of cotinine (MP2/M06-2X/B3LYP/B3LYP-D3)

	eq-a	*ax-a*	*eq-b*	*ax-b*
A/MHz	1914/1916/1900/1903	1625/1646/1686/1658	1893/1900/1882/1884	1606/1631/1668/1640
B/MHz	478/483/474/478	535/536/508/522	482/487/478/482	541/541/513/528
C/MHz	449/452/447/449	514/511/490/500	453/454/450/452	518/514/493/503
D_J/kHz	0.014/0.014/0.014/0.011	0.040/0.042/0.036/0.034	0.015/0.014/0.016/0.007	0.041/0.045/0.040/0.023
$^{14}N_p$				
χ_{aa}/MHz	-1.7/-2.1/-1.8/-1.9	-2.8/-3.1/-2.8/-2.9	1.3/1.2/1.4/1.4	1.5/1.5/1.6/1.6
χ_{bb}/MHz	2.7/2.8/3.0/2.9	1.0/1.0/2.0/1.3	1.6/1.3/1.9/1.5	-2.2/-2.1/-0.5/-1.6
χ_{cc}/MHz	-1.0/-0.7/-1.2/-1.0	1.9/2.1/0.8/1.6	-2.9/-2.5/-3.3/-2.9	0.7/0.6/-1.1/-0.0
$^{14}N_m$				
χ_{aa}/MHz	1.0/1.0/1.1/1.1	-0.3/-0.3/0.1/-0.1	0.9/1.0/1.0/1.0	-0.4/-0.3/-0.0/-0.2
χ_{bb}/MHz	2.1/2.1/2.3/2.2	0.0/0.3/0.8/0.4	2.1/2.0/2.2/2.1	-0.1/0.2/0.6/0.3
χ_{cc}/MHz	-3.1/-3.1/-3.4/-3.3	0.3/0.0/-0.9/-0.3	-3.0/-3.0/-3.2/-3.2	0.4/0.1/-0.6/-0.1
$\|\mu_b\|$/D	1.5/1.6/1.7/1.7	1.0/1.1/1.3/1.2	2.7/2.8/2.8/2.9	2.8/2.9/2.9/2.9
$\|\mu_b\|$/D	1.0/1.1/1.2/1.1	1.0/1.1/1.1/1.0	2.7/3.0/2.7/2.9	4.0/4.0/3.5/3.8
$\|\mu_c\|$/D	0.6/0.5/0.5/0.5	0.4/0.6/0.3/0.5	2.9/2.8/3.0/2.9	2.5/2.6/3.0/2.8
$\|\mu_{tot}\|$/D	1.9/2.0/2.2/2.1	1.5/1.7/1.7/1.7	4.8/5.0/4.9/5.0	5.5/5.5/5.4/5.5
$\Delta E+ZPE$ /kJ mol^{-1}	0.0/0.0/0.0/0.0	0.1/0.4/2.1/0.8	2.3/2.4/2.0/2.0	2.7/2.8/4.2/3.0
$\Delta G(473$ K) /kJ mol^{-1}	0.0/0.0/0.0/0.0	0.4/0.1/0.8/1.0	2.3/2.8/1.7/2.1	3.0/2.5/2.3/3.3

b. Barriers to interconversion among conformers

Conformers *a* (*eq-a* and *ax-a*) differ from conformers *b* (*eq-b* and *ax-b*) in a ~180° rotation along the bond connecting the two rings. Therefore, it is possible to estimate the barrier for interconversion *a*→*b* by scanning the rotation along the bond connecting the two rings. To do that, we scan the dihedral angle N1-C2-C6-C7 in steps of 10° at the MP2/6-311++G(d,p) level of theory (see Figure V.1 for atom numbering). The barrier for interconversion *eq-b*→*eq-a* is estimated at 29.9 kJ/mol while the barrier *ax-b*→*ax-a* is 22.7

kJ/mol. Both barriers are too high to be surmounted in the environment of a supersonic expansion. Figure V.1 shows a graphical display of the barriers.
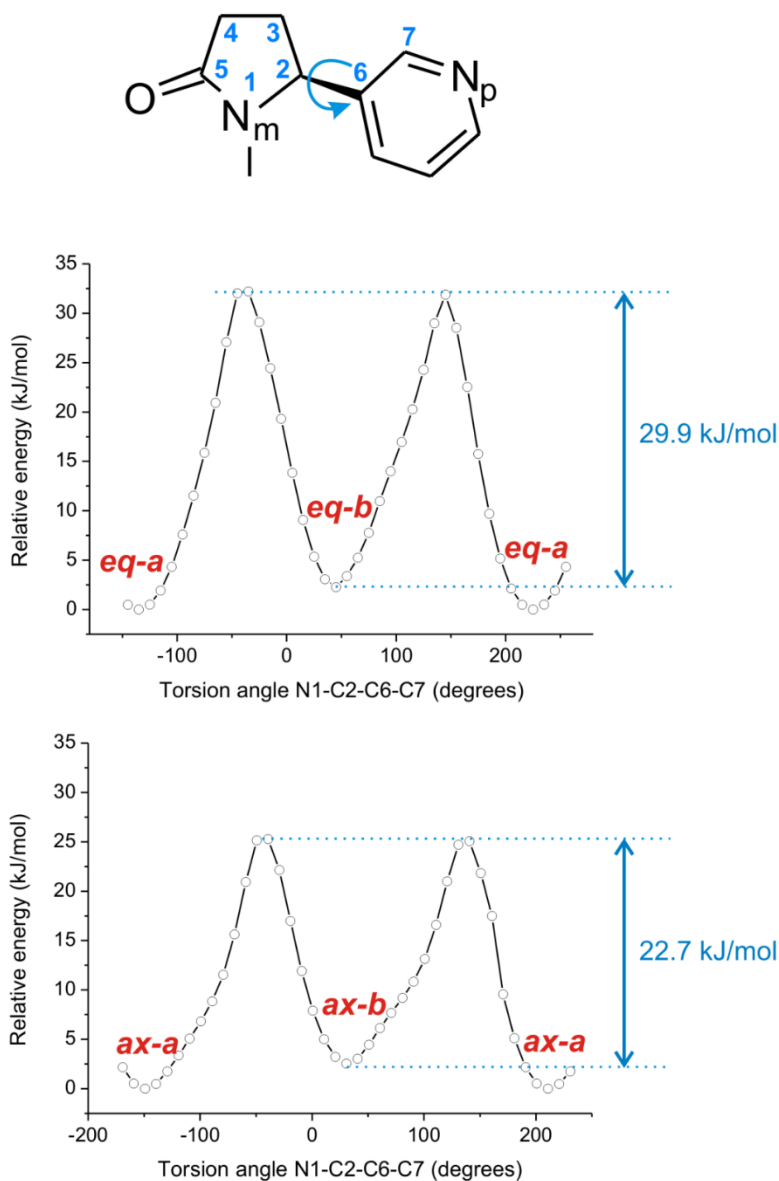

Figure V.1 *Ab initio* potential curve (MP2/6-311++G(d,p)) for the rotation along the bond connecting the two rings of cotinine. The barrier height for the *eq-b→eq-a* and the *ax-b→ax-a* conversions are marked in blue. At the top of the figure, atom numbering of cotinine.

Moreover, conformers *eq* (*eq-a* and *eq-b*) are different from conformers *ax* (*ax-a* and *ax-b*) in that they possess different twist conformations of the ring. We can estimate an interconversion path between these structures by scanning one of the dihedral angles defining the configuration of the pyrrolidinone ring. Therefore, we performed a relaxed potential energy scan of the N1-C2-C3-C4 angle at the B3LYP-D3/6-311++G(d,p) level of theory in steps of 2° (see Figure V.1 for atom numbering). We estimated both barriers (*ax-a→eq-a* and *ax-b→eq-b*) to be around 3.6 kJ/mol. Figure V.2 shows the steps of the above mentioned scans along with the variation of the unidimensional potential energy. It is important to note that the interconversion between conformers *ax* and *eq* could proceed through a different path than the one suggested here. For example, a concerted movement of the atoms in the ring could have a lower potential energy barrier than the one calculated here. Therefore, our result (3.6 kJ/mol) should be taken as an upper limit to the barrier for *ax→eq* interconversion.
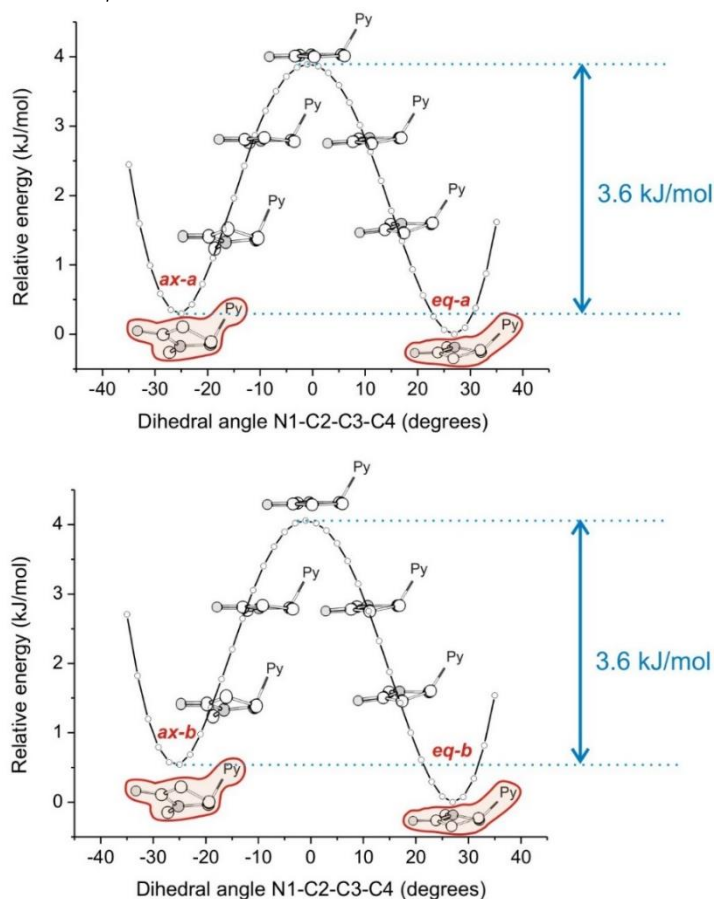

Figure V.2 A possible relaxation path between conformers *ax-b* and *eq-b*. Different steps of the scan are shown as well as the variation in potential energy (using B3LYP-D3 method and 6-311++G(d,p) basis set). Hydrogen atoms and the pyridine ring have been removed from the molecular structures for the sake of clarity.

Finally, Figure V.3 displays the four predicted MP2 conformations and summarizes the potential energy barriers for interconversion among conformers.

22.7 kJ/mol

ax-a
0.1 kJ/mol

ax-b
2.7 kJ/mol

3.6 kJ/mol

3.6 kJ/mol

eq-a
0.0 kJ/mol

eq-b
2.3 kJ/mol

29.9 kJ/mol
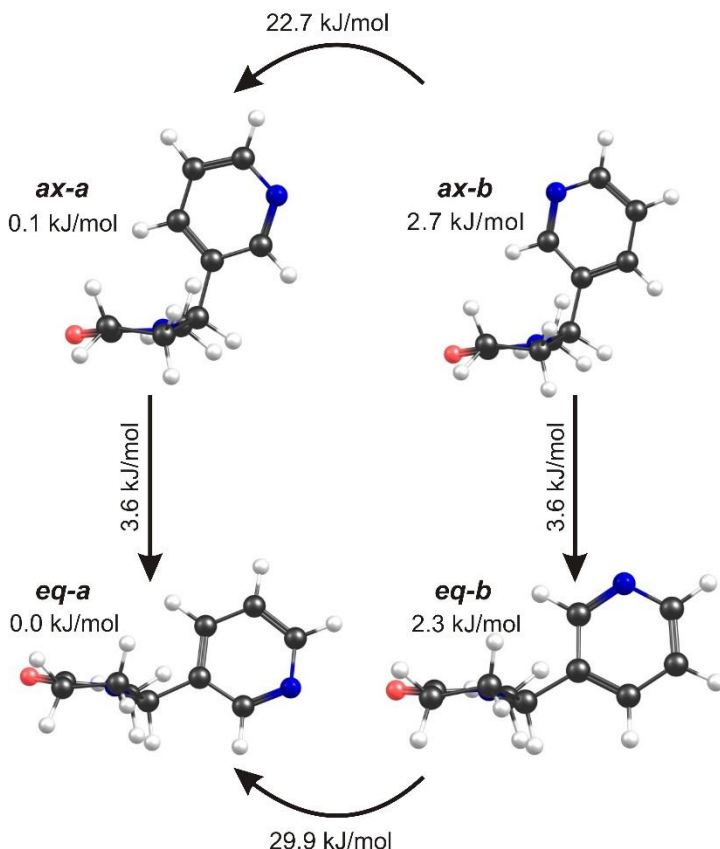
Figure V.3 The four MP2 lowest-lying conformations of cotinine in the gas phase. Zero-point corrected relative energy values are shown (Δ(E+ZPE)), as well as the barriers for interconversion between conformers.

c.   Barriers to internal rotation of the methyl top

Cotinine possesses a methyl top that is subject to produce splittings in its rotational spectrum due to coupling of the internal rotation with the overall rotation of the molecule. We estimate the barriers for internal rotation of the methyl top by performing a relaxed scan at MP2/6-311++G(d,p) in steps of 10º. The results are shown in Table V.3.

Table V.3 Calculated methyl internal rotation barriers at MP2/6-311++G(d, p) level.

	eq-a	*eq-b*	*ax-a*	*ax-b*
V_3/kJ mol^{-1}	4.3	4.3	4.0	4.0

V.3.2   Spectroscopic analysis

a.   CP-FTMW spectrum

First, we recorded the rotational spectrum of cotinine in the CP-FTMW spectrometer, which allows us to obtain a wide spectral range in a rapid way. The experimental spectrum of cotinine in the 7 to 18 GHz region displays a pattern of μ_a R-branches with a regular spacing of ~1000 MHz, characteristic of near-prolate asymmetric rotors. Figure V.4a shows an overview of the spectrum, where several branches can be observed. Figure V.4b displays the branch in the 7500 MHz region with J=8. Due mainly to the low vapor pressure of this nicotinoid,[10] the spectrum is very weak. Some lines in the spectrum appear as doublets (splitting~100 kHz), evidencing the effects of internal rotation of the methyl top. At first glance, this behavior seems anomalous since other nicotinoids like nicotine[8] or anabasine[9] do not show any internal rotation patterns in their rotational spectrum. No hyperfine structure due to nuclear quadrupole coupling interactions seemed noticeable at the spectral resolution of the CP-FTMW. In a first step, we assigned a series of μ_a transitions to an asymmetric rotor (labeled as I). After removal of the assigned lines, a series of slightly weaker transitions remained in the spectrum, also displaying a regular pattern of μ_a R-branches. These were assigned to a different asymmetric rotor (labeled as II). All the transitions measured in the CP-FTMW spectrometer are collected in Tables V.A.1 and V.A.2 of the Appendix. The observed transitions were fitted to a standard semi-rigid Watson Hamiltonian including centrifugal distortion, as discussed in Chapter II. Comparison of the derived rotational constants with the values predicted by theoretical calculations (see Table V.4) allowed us to propose a preliminary assignment of the detected species I and II to the *eq-a* and *eq-b* conformers of cotinine, respectively. A later fit was carried out considering internal rotation terms according to the Internal Axis Method (IAM) (see section II.5). The results of the internal rotation fit, in particular the barrier heights and the orientation of the CH_3 group relative to the molecule frame, are collected in Table V.5. The barrier height for internal rotation of the methyl top was determined to be nearly equal for both conformers (ca. 4.6 kJ/mol), indicating a similar chemical environment around the methyl top. After removal of the lines corresponding to *eq-a* and *eq-b*, no other lines attributable to higher-energy conformations remained in the spectrum. The absence of *ax-a* and *ax-b* species is remarkable and will be discussed in the following section.
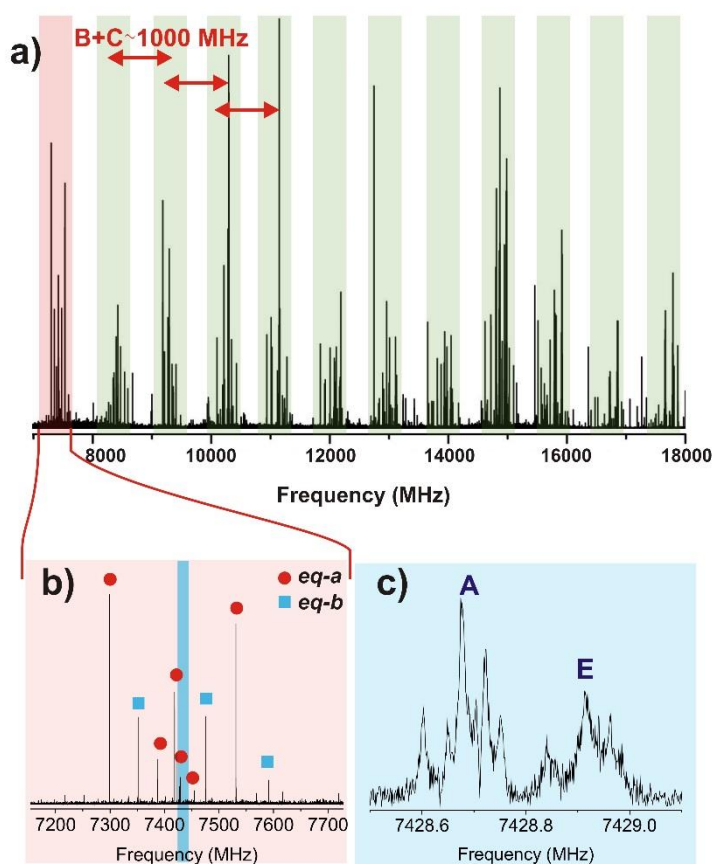
Figure V.4 a) Overview of the CP-FTMW rotational spectrum of cotinine in the 7-18 GHz region, where the regularly spaced μ_a R-branches can be observed. b) Expanded view of J=8 μ_a R-branch transitions corresponding to *eq-a* and *eq-b* conformers. c) Narrow-band FTMW measurement of the 8 3 6←7 3 5 transition of conformer *eq-a* (blue-shaded in b)).

Table V.4 Experimental spectroscopic parameters of cotinine (global fit including CP-FTMW and FTMW measured lines) and comparison with theoretical predictions at MP2/6-311++G(d,p) level.

	Experimental		Calculated (MP2)			
	Conformer I	Conformer II	eq-a	ax-a	eq-b	ax-b
A/MHz	1911.19(12)	1893.66(11)	1914.0	1624.8	1892.7	1605.6
B/MHz	478.56272(41)	482.65540(38)	477.7	534.5	482.0	541.0
C/MHz	449.43077(45)	452.49336(39)	449.4	514.4	453.0	518.2
D_J/kHz	0.01408(50)	0.01606(26)	0.014	0.040	0.015	0.041
$^{14}N_p$						
χ_{aa}/MHz	-1.76(11)	1.215(65)	-1.73	-2.81	1.25	1.50
χ_{bb}/MHz	2.31(25)		2.70	0.96	1.60	-2.16
χ_{cc}/MHz	-0.55(25)		-0.97	1.85	-2.85	0.66
$^{14}N_m$						
χ_{aa}/MHz	1.09(11)	0.747(73)	0.95	-0.27	0.87	-0.37
χ_{bb}/MHz	2.09(25)	1.45(28)	2.1	0.02	2.06	-0.06
χ_{cc}/MHz	-3.17(25)	-2.19(28)	-3.05	0.25	-2.93	0.43
$\lvert\mu_b\rvert$/D			1.53	0.97	2.69	2.77
$\lvert\mu_b\rvert$/D			1.01	1.04	2.70	4.01
$\lvert\mu_c\rvert$/D			0.59	0.40	2.93	2.48
$\lvert\mu_{tot}\rvert$/D			1.93	1.48	4.81	5.47
ΔE+ZPE /kJ mol^{-1}			0.0	0.1	2.3	2.7
ΔG(473K) /kJ mol^{-1}			0.0	0.4	2.3	3.0
$N_{CP-FTMW}$	56					
$\sigma_{CP-FTMW}$/kHz	20.0					
N_{FTMW}	34					
σ_{FTMW}/kHz	5.7					

Table V.5 Internal rotation parameters for the observed conformers of cotinine.

	Conformer I (exp.)	eq-a (MP2)	Conformer II (exp)	eq-b (MP2)
V_3/kJ mol^{-1}	4.55(4)	4.26	4.64(3)	4.32
$\angle$(a, i)/deg	85.4(2)	82.4	84.8(2)	82.4
$\angle$(b, i)/deg	24.64(4)	25.3	26.36(4)	26.9
$\angle$(c, i)/deg	65.854(7)	66.0	64.23(1)	64.4
I_α/u Å^2	[3.18]*	3.18	[3.27]	3.27
N	128		126	
σ_{FTMW}/kHz	18.2		16.6	

*values in brackets were fixed to *ab initio* values

b. FTMW spectrum

The two ^{14}N atoms in cotinine induce splittings in the rotational transitions due to the nuclear quadrupolar effect (see Chapter II). Since two quadrupolar nuclei are present, we define the coupling scheme as $I = I_1 + I_2$, $F = I + J$. These splittings are predicted to be only a few kHz and therefore not resolvable with the CP-FTMW instrument (~20 kHz resolution). That is the reason why some transitions of both conformers were re-measured in the narrow band FTMW instrument, which achieves a higher spectral resolution (~5 kHz). This allowed us to perform the separate identification of each hyperfine component. We chose a set of transitions with a compromise between spread of hyperfine components (greater at higher K_{-1} values) and line intensities (greater at lower K_{-1} and J values). As an example, Figure V.4c displays the 8 3 6 ← 7 3 5 transition, in which the A-E splitting due to the internal rotation of the methyl top can be observed, as well as the hyperfine structure arising from the two ^{14}N atoms. Tables V.A.3 and V.A.4 in the appendix collect all measured transitions.

The analysis of the hyperfine structure rendered the values of the nuclear quadrupole coupling tensor elements in Table V.4. Comparison between theoretical and fitted $\chi_{\alpha\alpha}$ values in Table V.4 provides unambiguous identification of Conformer I in Table V.4 to conformer *eq-a* and Conformer II to *eq-b*. This is the most conclusive evidence for conformer identification, as the rotational constants of both species are remarkably similar. It should be noticed that conformers I and II differ only in the location of the nitrogen atom in the pyridine ring. This leads to different values of the nuclear quadrupole coupling tensor elements for the N_p atom (see Scheme V.1).

c. Cremer-Pople analysis

We performed a Cremer-Pople analysis (see section III.5) on the pyrrolidinone ring of cotinine to assess quantitatively what kind of twist or envelope conformation the five-membered ring adopts in the gas phase. The results are summarized in Figure V.5, which shows the Cremer-Pople wheel for cotinine (all four predicted conformations) and for the observed conformations of nicotine.[8] According to this, conformers *eq-a* and *eq-b* (i.e. the observed conformers of cotinine) adopt a distorted twist $^3T_2$ ring conformation in the gas phase.
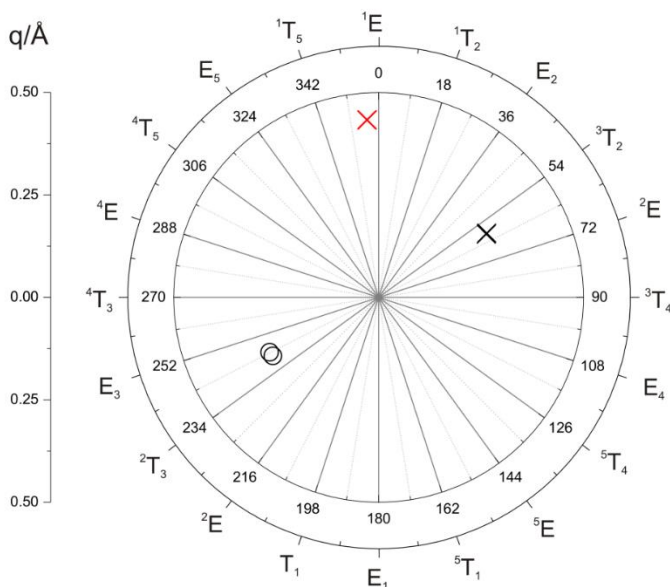
Figure V.5 Cremer-Pople wheel for cotinine and nicotine. The stable conformations are indicated by polar coordinates q (the magnitude of ring puckering) and the angle of pseudorotation φ. Values φ = 0, 36, 72°, . . . correspond to *envelope* (E) conformations with C_s symmetry, and φ = 18, 54, 90°, . . . give *twist* (T) conformations of C_2 symmetry. Black symbols show the position of cotinine conformations (crosses for *eq-a* and *eq-b* and circles for *ax-a* and *ax-b*) and red crosses correspond to the observed conformations of nicotine in reference 8.

V.4 Discussion

The conformational landscape of the nicotinoid cotinine was successfully probed under isolation conditions. The two structures observed (*eq-a* and *eq-b*) share the same conformation of the five-membered ring, demonstrating a preference of the pyridine substituent for the equatorial position. The difference between both structures is a ~180° rotation around the bond connecting the two rings. The barrier for interconversion between both species is estimated at 29.9 kJ/mol. This high value excludes conformer relaxation and supports the observation of *eq-a* and *eq-b* simultaneously in the seeded expansion. Microwave studies also allow one to estimate the relative populations of the observed conformers. The intensity of a given rotational transition in the jet is proportional to the population difference between the rotational levels involved in the transition and to the molecule's dipole moment. An estimate of the relative population is $N_{eq-a}/N_{eq-b} \approx 4.0(2.8)$, corresponding to a relative energy (ΔG) of 2.2(1.4) kJ/mol at 473 K, indicating that conformer *eq-a* is the dominant species. These values are approximate as the intensity of a given transition is spread into many hyperfine components and many lines overlap. Surprisingly and pleasantly this value is in excellent agreement with the predicted theoretically (2.3 kJ/mol at 473 K).

The relative stabilities (Δ(E+ZPE)) of *ax-a* and *ax-b* conformations were estimated to be 0.1 and 2.7 kJ/mol respectively above the global minimum at MP2/6-311++G(d,p) level. Although these values imply that the axial conformers should have enough population to be detected, none of them was observed in our experiment. In fact, *ax-a* was predicted to be more stable than one of the observed conformations (*eq-b*). These facts suggest a relaxation of the five-membered ring into its most stable conformation, with the pyridine substituent in an equatorial position. The barriers for the *ax-a*→*eq-a* and the *ax-b*→*eq-b* relaxations were both estimated to be 3.6 kJ/mol. Both potential energy barriers are low enough to be overcome in our supersonic expansion. Although the relaxation process could occur through a concerted motion different from the one suggested in this work, our calculations set an upper limit to the energy barrier that can be surmounted in the conditions of our experiment. A similar behavior was observed for anabasine[9] and nicotine[8] in the gas phase, where two conformations were also found, sharing the same conformation of the five membered ring and differing in a rotamerization around the bond connecting the cycles. However, for nicotine, the two "non-observed" conformers were predicted to be much higher in energy (~25 kJ/mol) and their absence from the rotational spectrum was rationalized in terms of non-population of the high-energy conformers. We have also performed a conformational search and *ab initio* calculations on nicotine. These calculations yielded two additional conformers that are analogues to *ax-a* and *ax-b* of cotinine and which were not reported in reference 8. These lie at ~14 kJ/mol above the global minimum.

As mentioned above, cotinine differs from nicotine in the addition of a C=O moiety to the non-aromatic ring. The results presented here offer the chance to study the effect of this modification on the behavior of this nicotinoid. The five-membered ring adopts a distorted twist $^3T_2$ configuration, while nicotine was found to display an envelope ^1E structure, as shown in the Cremer-Pople diagram in Figure V.5. The cotinine five-membered ring takes on a more planar configuration than that in nicotine (shown by a lower value of the puckering amplitude in Figure V.5). This can be explained in terms of the presence of an amide moiety in which the carbonyl group adopts a planar geometry reducing ring's strain. This fact can also explain why predicted relative energies of the non-observed conformers are much higher in nicotine than cotinine. In nicotine, the five-membered ring takes on a very stable structure, and the energy cost of placing the pyridine ring in an axial position is very high. On the other hand, the more planar configuration of cotinine reduces the energy difference between axial and equatorial conformations. Finally, it is noteworthy that in previous studies about cotinine,[6,7] the same four conformations as calculated here were described as envelope-type structures. In our work, we have determined quantitatively that the pyrrolidinone ring adopts a distorted twist $^3T_2$ configuration thanks to the Cremer-Pople diagram. This result stresses the need for quantitative analysis of distorted ring configurations in cases such as cotinine where visual inspection may be misleading.

The analysis of the hyperfine structure of cotinine allowed us to calculate the internal rotation barrier of the methyl top. Values for both observed conformers are almost identical (4.55(4) and 4.64(3) kJ/mol for *eq-a* and *eq-b* respectively) and prove no dependence of the methyl internal rotation with the position of the N_p atom. These values are in agreement with the theoretically estimated values of ~4.3 kJ/mol at

MP2/6-311++G(d,p) level for both conformers (see Table V.3). However, no internal rotation splittings were observed for nicotine,[8] and the barrier for internal rotation was estimated to be at a substantially higher value than in cotinine (MP2/6-311++G(d,p): ~16.5 kJ/mol). This result seems surprising, since both molecules are structurally similar. The different behavior may be explained by differences in the electronic distribution in the N-CH₃ bond and weak intramolecular interactions. First, the internal rotor bond is adjacent to the amide N-C=O, with partial double bond character, which could influence the methyl internal rotation. Second, Figure V.6 shows the computed (MP2/6-311++G(d,p)) energy variation for the internal rotation of the C-CH₃ group for cotinine (conformer *eq-a*) and nicotine (conformer *trans-a*). In cotinine, the shortest interatomic distance between non-covalently bonded atoms involving the CH₃ top corresponds to a weak C-H···O=C attractive interaction. This stabilization results in a low barrier for internal rotation. Conversely, in nicotine such stabilizing C-H···O=C interaction cannot take place. The shortest distances correspond to highly energetic C-H···H-C repulsions and the barrier is much higher. In addition, a phase shift of ~30° can be observed between both profiles, due to the fact that in the C-H···O=C interaction (cotinine) the four atoms are coplanar, whereas for the C-H···H-C interaction (nicotine) they are not. It is worth mentioning that a similar behavior was observed for the N-methylpyrrolidine/N-methylpyrrolidone system, which is closely related to the nicotine/cotinine pair in the sense that they also differ only in the addition of a C=O group. An internal rotation barrier of 16.1(2)kJ/mol was observed for N-methylpyrrolidine in a microwave study.[11] On the contrary, the N-methylpyrrolidone displays a nearly free internal rotation of the methyl top,[12] which was attributed to an attractive interaction C-H···O=C.
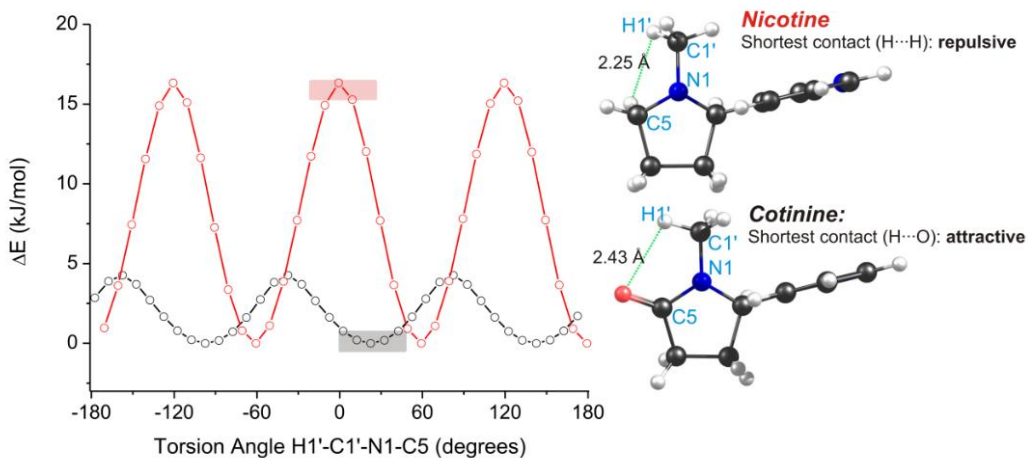

Figure V.6 *Ab initio* potential curve (MP2/6-311++G(d,p)) for the internal rotation of the C-CH₃ group for cotinine (black, conformer *eq-a*) and nicotine (red, conformer *trans-a*). The torsion angles with the shortest C-H···X distances are highlighted.

The molecule-receptor activity of cotinine has been suggested to arise from various factors,[6] including the N···N distance, the charge distribution on the N_m atom and a possible intramolecular hydrogen bond C-H···O=C. In Table V.6, we present the calculated N···N distances for the observed conformers of cotinine and nicotine. It is apparent that this distance is quite different for the two conformations of each sample (i.e. *eq-a* (4.79 Å) vs. *eq-b* (4.25 Å) in cotinine), but there is no significant difference between similar conformations of cotinine and nicotine (i.e. *eq-a* of cotinine (4.79 Å) vs. *trans-a* of nicotine (4.80 Å)). This may rule out the first factor. The internal rotation analysis presented in this work suggests that the methyl rotation in cotinine is favored by the existence of a weak intramolecular hydrogen bond C-H···O=C. Such interaction corresponds to the third factor that is suggested in reference 6 as responsible for the lower affinity of cotinine to its receptor.

Table V.6 N···N distance (in Å) for the lowest lying conformers of cotinine (this work) and the observed conformers of nicotine (reference 8). Values are calculated in both cases at MP2 level using the 6-311++G(d,p) basis set.

Cotinine				Nicotine	
eq-a	*ax-a*	*eq-b*	*ax-b*	*trans-a*	*trans-b*
4.79	4.86	4.25	4.24	4.80	4.24

V.5 References

[1] K. Brejc, W. J. van Dijk, R. V. Klaassen, M. Schuurmans, J. van der Oost, A. B. Smit, T. K. Sixma, *Nature* **2001**, *411*, 269-276.

[2] V. Tsetlin, F. Hucho, *Curr.Opin. Pharmacol.* **2009**, *9*, 306-310.

[3] I. Yamamoto, G. Yabuta, M. Tomizawa, T. Saito, T. Miyamoto, S. Kagabu, *J. Pesticide Sci.* **1995**, *20*, 33-40.

[4] L.P. Dwoskin, L. Teng, S.T. Buxton, P.A. Crooks, *J. Pharmacol. Exp. Ther.* **1999**, *288*, 905-911.

[5] X. Xiu, N. L. Puskar, J. A. P. Shanata, H. A. Lester, D. A. Dougherty, *Nature* **2009**, *458*, 534-538.

[6] T. Takeshima, H. Takeuchi, T. Egawa, S. Konaka, *J. Mol. Struct.* **2007**, *841*, 13-21.

[7] P. G. Rodríguez Ortega, M. Montejo, F. Márquez, J. J. López González, *ChemPhysChem* **2015**, *16*, 1416-1427.

[8] J.-U. Grabow, S. Mata, J. L. Alonso, I. Peña, S. Blanco, J. C. López, C. Cabezas, *Phys. Chem. Chem. Phys.* **2011**, *13*, 21063-21069.

[9] A. Lesarri, E. J. Cocinero, L. Evangelisti, R. D. Suenram, W. Caminati, J.-U. Grabow, *Chem. Eur. J.* **2010**, *16*, 10214-10219.

[10] C. Siitsman, I. Kamenev, V. Oja, *Thermochim. Acta.* **2014**, *595*, 35-42.

[11] W. Caminati, F. Scappini, *J. Mol. Spectrosc.* **1986**, *117*, 184-194.

[12] D. P. MacDermott, H. L. Strauss, *J. Am. Chem. Soc.* **1972**, *94*, 5124-5125.

Chapter VI.

- -

Tautomeric equilibrium and complex hyperfine structure of purine
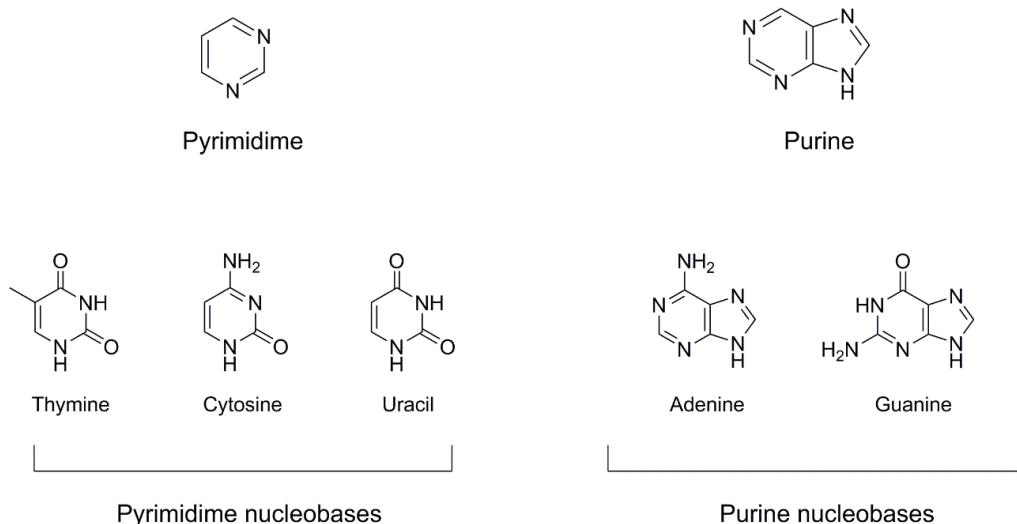
VI.1   Introduction

In this Chapter, we solve the tautomeric equilibrium of purine in the gas phase. This molecule exists in the form of two main tautomers and has a very complex hyperfine structure arising from the presence of four ^{14}N nuclei. Thanks to the spectral resolution achievable by the FTMW spectrometer, we are able to solve the hyperfine structure of both tautomers and provide unambiguous identification of each of them. This work represents an example of the power of rotational spectroscopy in the analysis of subtle hyperfine structures. Moreover, purine is the first case of a molecule with four non-equivalent quadrupolar nuclei whose hyperfine structure has been fully resolved.

Conformational/tautomeric equilibria of isolated biomolecules in the gas phase have been investigated in the past years, partly due to the development of techniques based on laser spectroscopy. Resonant-enhanced multiphoton ionization (REMPI), laser-induced fluorescence excitation (LIF), and IR and/or UV double/triple resonance methods[1,2,3,4] are some examples of techniques that are applied to the structural study of biomolecules in the gas phase. Conformational or tautomeric assignments require, within the above-mentioned techniques, the support of accurate theoretical calculations. Even so, the assignments are not always unambiguous.

Due to its inherent spectral resolution (5 kHz in the present case), rotational spectroscopy provides the most accurate vision of the molecular structure in the ground electronic state. It was initially restricted to the investigation of small molecules but, with the advent of pulsed jet Fourier transform microwave (FTMW) spectroscopy first[5,6] and, more recently, broadband (chirped pulse) CP-FTMW spectroscopy,[7] it has turned into a very competitive technique in the study of moderate-size biomolecules. It can indeed provide many fine details (tunneling splitting, quadrupole hyperfine structures, interaction energies, etc.), which supply chemical information difficult to be achieved otherwise. More recently, laser vaporization techniques have been combined with microwave spectroscopy,[8,9] to unravel conformational equilibria of several amino acids,[10,11] to study the conformational/tautomeric forms of some nucleobases,[12,13] and to resolve the conformational/tautomeric landscape of some sugars.[14,15,16,17]

Nucleobases (nitrogenous bases or bases in genetics) are organic compounds with two or more nitrogen atoms (see Scheme VI.1). These biological compounds are found linked to a sugar within nucleosides, the building blocks of DNA or RNA. The rotational spectra of nucleobases are complicated because of the nuclear quadrupole coupling effects. The ^{14}N nuclei possess a nuclear spin I = 1, and each one produces a splitting of the rotational transitions into several hyperfine components. Nucleobases have 2–5 nitrogen atoms that indeed generate a very complex hyperfine pattern. Occasionally, this hyperfine structure of the ^{14}N nuclei has been eliminated (or simplified) by replacing one or several ^{14}N with ^{15}N nuclei, which have a nuclear spin I=1/2. So far, it has been possible to analyze the quadrupolar effect of up to three ^{14}N nuclei (e.g., in cytosine[13]). But this hyperfine analysis was not possible for guanine,[12] which contains five ^{14}N nuclei. In this case, no attempt was made to assign the quadrupole hyperfine components and the rotational frequencies were measured as the intensity-weighted mean of the line clusters. In this way, a provisional set of rotational constants was estimated for four tautomers of this species. It is important to note that the analysis of hyperfine structure in nucleobases may provide

important information in the assignment of tautomeric species. The rotational constants of tautomers are very similar and additional information on quadrupole coupling constants may be crucial in the identification of tautomeric species.

Pyrimidime

Purine

Thymine   Cytosine   Uracil

Adenine   Guanine

Pyrimidime nucleobases

Purine nucleobases

Scheme VI.1 Molecular structure of pyrimidine and purine and the five primary nucleobases.

Purine belongs to a series of molecules characterized by two aromatic rings, one six- and one five-membered, fused together to give a planar aromatic bicycle. There are two main tautomers of purine, N(9)H and N(7)H, drawn in Figure VI.1. The physicochemical properties of purine (which is the mainframe of the nucleobases adenine and guanine, see Scheme VI.1) are useful for the interpretation of several biochemical processes. The understanding of the N(9)H⇌N(7)H tautomeric equilibrium is particularly relevant in this respect. This kind of tautomerisms can play a role in chemical mutagenesis.[18,19] In the solid state, purine exists as the N(7)H tautomer,[20,21] although small amounts of the N(9)H tautomer have also been postulated.[22,23] Several studies in solution conclude that purine exists as a mixture of N(7)H and N(9)H tautomeric forms in several solvents.[24,25] A gas-phase UV photoelectron spectroscopy study suggests (rather indirectly) the dominance of the N(9)H species,[26] while contradictory results have been obtained with matrix isolation techniques.[27,28] Several DFT and *ab initio* calculations predict the N(9)H form to be more stable by 15–40 kJ·mol^{-1}.[27,29,30] The only previous rotational study of purine is a free jet absorption millimeter wave (mmw) spectrum, obtained by heating the sample to 140 °C in a preexpansion furnace.[31] In that case, only the N(9)H tautomer was detected.
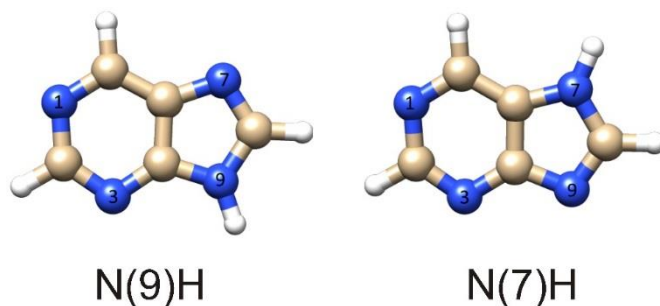
Figure VI.1 Two main tautomers of purine

Our interest in studying purine was fueled mainly by two factors. First, purine has a high energy tautomer (N(7)H), not observed previously in the gas phase. Second, it has a very complicated hyperfine structure due, similarly to adenine and guanine, to four quadrupolar nuclei. Our goal is to unravel these two challenging tasks.

VI.2   Experimental section

Purine is a white powder with a high melting point (214-217 °C). In order to bring it into the gas phase, we used laser vaporization techniques. About 0.8 g of the sample were mixed with a commercial binder and mechanically pressed to form a solid rod. Later, we performed the experiment using the set-up for laser vaporization described in Chapter III. The experiment conditions used in this study are summarized in Table VI.1.

Table VI.1 Experimental conditions for the recording of the FTMW spectra of purine.

Experimental conditions	FTMW
Number of nozzles	1
Nozzle temperature	NA (Laser desorption)
Carrier gas	Ne
Number of chirps/molecular pulse	2
Total number of cycles	9000-84000*

*The exact value depends on the required number of cycles to obtain a good signal-to-noise ratio of a given rotational transition.

VI.3   Results

VI.3.1   Theoretical calculations

Although several theoretical works (mentioned above) have been published on purine, no theoretical predictions of the spectroscopic parameters (rotational and quadrupole coupling constants, and electric dipole moment components) were available in the literature. For this reason, we performed several new calculations. The structures of the N(9)H and N(7)H species of purine have been optimized at the MP2/6-311++G(d,p) level using the GAUSSIAN09 package.[32] Tautomer N(9)H has been predicted to be more stable than the N(7)H by 16.9 kJ·mol⁻¹, a value that is reduced to 15.9 kJ·mol⁻¹ when including zero point energy corrections. These data, together with the calculated spectroscopic parameters, are reported in Table VI.1.

Table VI.1 MP2/6-311++G(d,p) calculated spectroscopic parameters of the N(9)H and N(7)H tautomers of purine

	N(9)H	N(7)H
A, B, C / MHz	4099, 1750, 1227	4101, 1745, 1224
N1: $\chi_{aa}, \chi_{bb}, \chi_{cc}$/MHz	$-3.502, 0.381, 3.121$	$-3.553, 0.367, 3.187$
N3: $\chi_{aa}, \chi_{bb}, \chi_{cc}$/MHz	$1.659, -4.663, 2.630$	$1.427, -4.633, 3.207$
N7: $\chi_{aa}, \chi_{bb}, \chi_{cc}$/MHz	$1.567, -3.171, 1.605$	$1.680, 1.488, -3.168$
N9: $\chi_{aa}, \chi_{bb}, \chi_{cc}$/MHz	$1.432, 1.508, -2.940$	$1.373, -3.379, 2.005$
$|\mu_a|, |\mu_b|$/D	3.0, 2.3	3.1, 5.0
$\Delta E, \Delta E_0$/kJ mol⁻¹	0.0, 0.0	16.9, 15.9

VI.3.2   Spectroscopic analysis

The rotational and centrifugal distortion constants of the N(9)H tautomer were available from the mmw study mentioned above.[31] Based on these data, we could easily locate the 303←202 transition. It appeared as a ~ 3.5 MHz wide band, centered at about 8660.7 MHz. Several other μ$_a$-type R-branch and four μ$_b$-type R-branch transitions were identified. Transitions with J = 1 to 5 and with K−1 = 0 to 2 could be measured. All measured rotational transitions of conformer N(7)H are collected in in the appendix. Once the N(9)H tautomer was measured, we performed the search of the rotational spectrum of the high energy N(7)H tautomer. First we empirically corrected the *ab initio* rotational constants by the "observed minus calculated" values determined for the N(9)H species. We could detect in this way the 404←303 transition. Later on, one additional μ$_a$ and some stronger μ$_b$-type R-branch transitions were measured, to a total of nine transitions. All measured rotational transitions of conformer N(9)H are collected in in the appendix. For each transition we could measure many hyperfine component lines (from

4 to 41, depending on the transition and on the tautomer). An example of the complexity of hyperfine structure is shown in Figure VI.2 for the 221 ← 110 transition of the N(9)H tautomer, for which up to 21 different components were individually identified. In that figure, the experimental spectrum (positive values, black) is compared to the calculated one (negative values, red).
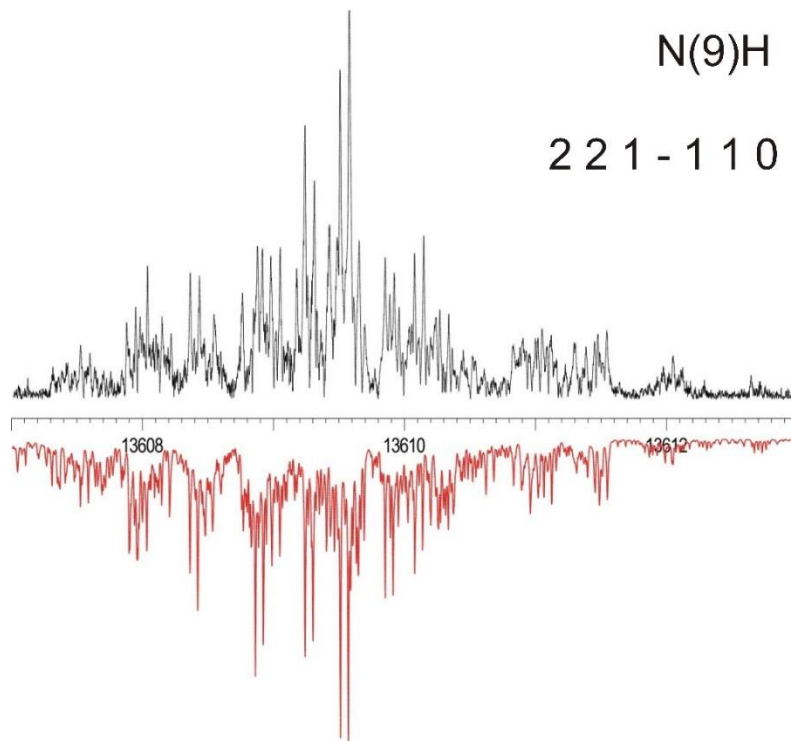

Figure VI.2 Recorded (positive values, black) 2 2 1 ← 1 1 0 transition of the N(9)H tautomer is compared to its simulated pattern (negative values, red) (frequency in MHz). Up to 21 different hyperfine components were identified for this transition.

All measured hyperfine component lines could be fit independently for each tautomer according to the following Hamiltonian (Watson S-reduction, I^r representation):

$$H = H_R + H_Q(^{14}N1) + H_Q(^{14}N3) + H_Q(^{14}N7) + H_Q(^{14}N9)$$

H_R represents the rigid-rotor Hamiltonian (no centrifugal distortion parameters were required) and H_Q are the operators associated with the quadrupolar interactions of the four ^{14}N nuclei with end-over-end rotation. The hyperfine correction calculations follow the coupling schemes $F_3 = J + I(^{14}N1)$, $F_2 = F_3 + I(^{14}N3)$, $F_1 = F_2 + I(^{14}N7)$, and $F = F_1 + I(^{14}N9)$. The obtained spectroscopic constants are reported in Table VI.2, as well as the defects of inertia ($\Delta c = I_a + I_b - I_c$), whose values are very close to zero, indicating the planarity of both tautomers.

VI.4   Discussion

Comparison of theoretical and experimental values of the rotational constants already outline the tautomeric assignment reported in Table VI.2 (there is a perfect agreement between the calculated and experimental differences of the rotational constants of the two tautomers).

Table VI.2 Experimental spectroscopic parameters of the observed N(9)H and N(7)H tautomers of purine

		N(9)H	N(7)H
	A / MHz	4125.8895(2)	4127.3813(3)
	B / MHz	1755.1720(1)	1749.7594(3)
	C / MHz	1231.55819(6)	1229.42760(7)
N1	χ_{aa} / MHz	-3.343(5)	-3.560(15)
	χ_{bb} / MHz	0.440(6)	0.566(17)
	χ_{cc} / MHz	2.904(6)	2.994(17)
N3	χ_{aa} / MHz	1.673(7)	0.695(11)
	χ_{bb} / MHz	-4.229(9)	-2.744(20)
	χ_{cc} / MHz	2.555(9)	2.049(20)
N7	χ_{aa} / MHz	1.547(7)	1.254(11)
	χ_{bb} / MHz	-3.379(9)	1.532(16)
	χ_{cc} / MHz	1.833(9)	-2.786(16)
N9	χ_{aa} / MHz	1.489(5)	1.541(11)
	χ_{bb} / MHz	1.495(7)	-3.239(18)
	χ_{cc} / MHz	-2.985(7)	1.699(18)
	Δc / uÅ^2	-0.069(78)	-0.20(15)
	σ / kHz	4.8	4.9
	N	251	95

However, definitive proof of the assignment can be obtained from the values of the quadrupole coupling constants of the four ^{14}N nuclei, which act as a fingerprint for the correct assignment of the two spectra to the right tautomers. These parameters are very sensitive to small structural changes around of the ^{14}N nucleus. Hence, they serve as a

powerful tool to discriminate between different conformers or tautomers.[33] In particular, the χ_{gg} (g = a, b, c) parameters of nuclei N9 and N7, which interchange their values in going from N(9)H to N(7)H, are very significant in this sense. The quadrupole coupling constants are related to the gradient of the electric field at the quadrupolar nucleus (see Chapter II) within the inertia principal axes system, through the relation $\chi_{gg} = eQ \left(\frac{\partial^2 V}{\partial g^2} \right)$ (g = a, b, c) and are less adequate to distinguish between different bonding situations of N atoms. These parameters only have a physical meaning if the quadrupole tensor is expressed within its principal axes system of nuclear coupling, generally labeled as χ_x, χ_y and χ_z. Then, iminic and pyrimidinic nitrogen atoms have quite different values from each other. In our case, purine being planar, $\chi_{cc} \equiv \chi_y$. For this reason, we can use these values to discriminate between the different kinds of N nuclei. We list the eight experimental χ_{cc} values in Table VI.3. From the χ_{cc} values of Table VI.3 one can note that N1 and N3 are pyrimidine-like nuclei for both tautomers. Instead, N7 is pyrimidine-like in tautomer N(9)H and pyrrole-like in N(7)H; the contrary is true for N9, providing a doubtless identification of the two tautomers. The pyrimidinic χ_{cc} values of N1 and N3 are on the average 30% smaller than χ_{cc} in isolated pyrimidine. A similar decrease is observed in the pyrimidine-like imidazolic ^{14}N (N7 or N9) nucleus with respect to isolated imidazole, while an increase in the absolute value is observed in χ_{cc} values (which are negative) in the pyrrole-like N7 or N9 nucleus. This effect is probably related to the higher π-electron delocalization in purine with respect to isolated pyrimidine and imidazole rings.

Table VI.3 χ_{cc} values of the four ^{14}N nuclei of the N(9)H and N(7)H tautomers and comparison to some prototype molecules

	Purine N(9)H	Purine N(7)H	Related molecules
χ_{cc}[N1] / MHz	2.904(6)	2.994(17)	Pyrimidine N: 3.5584(7)[34]
χ_{cc}[N3] / MHz	2.555(9)	2.049(20)	Pyrrole N: -2.704(9)[35]
χ_{cc}[N7] / MHz	1.833(9)	-2.786(16)	Imidazole N1 (pyrrole-like): -2.559(9)[36]
χ_{cc}[N9] / MHz	-2.985(7)	1.699(18)	Imidazole N3 (pyrimidine-like): 2.228(8)[36]

Relative intensity measurements of some pairs of nearby transitions allowed the estimation of the relative population of the two tautomers. μ_a-type and μ_b-type rotational transitions were used for this task. We obtained $N_{N(9)H}/N_{N(7)H} \approx 40(15)/1$. It is worth noting that the observed relative abundances of tautomers in the jet plume is the consequence of a series of processes that include the laser vaporization, a complex process that could alter the thermodynamic equilibrium situation. In addition, the relative concentration of the two species could also be related to their molecular fractions in the solid state sample.[15] Despite this, our study clearly demonstrates the high dominance of the N(9)H tautomer, a fact that generated controversy in previous studies.[26,27] In the case of a Boltzmann distribution in the pre-expansion (but this is not certain), this ratio would correspond to $\Delta E = 9(1)$ kJ·mol^{-1} in favor of N(9)H, against the 15.9 kJ·mol^{-1} predicted

theoretically. However, the calculated value is also very dependent on the method used.[27,29,30]

In summary, with the combination of Fourier transform microwave technique and ultrafast laser vaporization, we unambiguously confirmed the N(9)H tautomer and extended the previously reported measurements to the centimeter region. We also assigned the rotational spectrum of the very high energy N(7)H tautomer and for both species we unraveled the very complex hyperfine structure due to interaction of the angular momenta generated by the end-over-end rotation with the spins of the four ^{14}N quadrupolar nuclei. The full sets of diagonal quadrupole coupling constants allow for a definitive tautomeric assignment, which is difficult to achieve with other techniques.

VI.5 <u>References</u>

[1] A. M. Rijs, J. Oomens, *Gas-Phase IR Spectroscopy and Structure of Biological Molecules*, EdSpringer: Cham, Switzerland, **2015**.

[2] P. Çarçabal, R. A. Jockusch, I. Hünig, L. C. Snoek, R. T. Kroemer, B. G. Davis, D. P. Gamblin, I. Compagnon, J. Oomens, J. P. Simons, *J. Am. Chem. Soc.* **2005**, *127*, 11414-11425.

[3] W. Chin, F. Piuzzi, J.-P. Dognon, I. Dimicoli, B. Tardivel, M. Mons, *J. Am. Chem. Soc.* **2005**, *127*, 11900-11901.

[4] E. J. Cocinero, P. Çarçabal, T. D. Vaden, J. P. Simons, *Nature* **2011**, *469*, 76-79.

[5] T. J. Balle, W. H. Flygare, *Rev. Sci. Instrum.* **1981**, *52*, 33-45.

[6] J.-U. Grabow, W. Stahl, H. Dreizler, *Rev. Sci. Instrum.* **1996**, *67*, 4072-4084.

[7] G. G. Brown, B. C. Dian, K. O. Douglass, S. M. Geyer, S. T. Shipman, B. H. Pate, *Rev. Sci. Instrum.* **2008**, *79*, 053103/1-053103/13.

[8] A. Lesarri, S. Mata, J. C. López, J. L. Alonso, *Rev. Sci. Instrum.* **2003**, *74*, 4799-4804.

[9] F. J. Lovas, Y. Kawashima, J.-U. Grabow, R. D. Suenram, G. T. Fraser, E. Hirota, *Astrophys. J.* **1995**, *455*, L201-L204.

[10] A. Lesarri, S. Mata, E. J. Cocinero, S. Blanco, J. C. López, J. L. Alonso, *Angew. Chem. Int. Ed.* **2002**, *41*, 4673-4676.

[11] A. Lesarri, R. Sánchez, E. J. Cocinero, J. C. López, J. L. Alonso, *J. Am. Chem. Soc.* **2005**, *127*, 12952-12956.

[12] J. L. Alonso, I. Peña, J. C. López, V. Vaquero, *Angew. Chem. Int. Ed.* **2009**, *48*, 6141-6143.

[13] J. L. Alonso, V. Vaquero, I. Peña, J. C. López, S. Mata, W. Caminati, *Angew. Chem. Int. Ed.* **2013**, *52*, 2331-2334.

[14] E. J. Cocinero, A. Lesarri, P. Écija, F. J. Basterretxea, J.-U. Grabow, J. A. Fernández, F. Castaño, *Angew. Chem. Int. Ed.* **2012**, *51*, 3119-3124.

[15] I. Peña, E. J. Cocinero, C. Cabezas, A. Lesarri, S. Mata, P. Écija, A. M. Daly, A. Cimas, C. Bermúdez, F. J. Basterretxea, S. Blanco, J. A. Fernández, J. C. López, F. Castaño, J. L. Alonso, *Angew. Chem. Int. Ed.* **2013**, *52*, 11840-11845.

[16] E. J. Cocinero, A. Lesarri, P. Écija, A. Cimas, B. G. Davis, F. J. Basterretxea, J. A. Fernández, F. Castaño, *J. Am. Chem. Soc.* **2013**, *135*, 2845-2852.

[17] P. Écija, I. Uriarte, L. Spada, B. G. Davis, W. Caminati, F. J. Basterretxea, A. Lesarri, E. J. Cocinero, *Chem. Commun.* **2016**, *52*, 6241-6244.

[18] J. P. Cerón-Carrasco, D. Jacquemin, E. Caüet, *Phys. Chem. Chem. Phys.* **2012**, *14*, 12457-12464.

[19] A. Pérez, M. E. Tuckerman, H. P. Hjalmarson, O. A. Von Lilienfeld, *J. Am. Chem. Soc.* **2010**, *132*, 11510-11515.

[20] D. G. Watson, R. M. Sweet, R. E. Marsh, *Acta Crystallogr.* **1965**, *19*, 573-580.

[21] S. F. Parker, R. Jeans, R. Devonshire, *Vib. Spectrosc.* **2004**, *35*, 173-177.

[22] M. Majoube, M. Henry, G. Vergoten, *J. Raman Spectrosc.* **2005**, *25*, 233-243.

[23] X. Cao, G. Fischer, *Spectrochim. Acta A* **1999**, *55*, 2329-2342.

[24] M. T. Chenon, R. J. Pugmire, D. M. Grant, R. P. Panzica, L. B. Townsend, *J. Am. Chem. Soc.* **1975**, *97*, 4636-4642.

[25] T. Bartl, Z. Zacharová, P. Seckárová, E. Kolehmainen, R. Marek, *Eur. J. Org. Chem.* **2009**, 1377-1383.

[26] J. Lin, C. Yu, S. Peng, I. Akiyama, K. Li, L. K. Lee, P. R. LeBreton, *J. Am. Chem. Soc.* **1980**, *102*, 4627-4631.

[27] S. G. Stepanian, G. G. Sheina, E. D. Radchenko, Y. P. Blagoi, *J. Mol. Struct.* **1985**, *131*, 333-346.

[28] L. Houben, K. Schoone, J. Smets, L. Adamowicz, G. Maes, *J. Mol. Struct.* **1997**, *410-411*, 397-401.

[29] M. J. Nowak, H. Rostkowska, L. Lapinski, J. S. Kwiatkowski, J. Leszczynski, *J. Phys. Chem.* **1994**, *98*, 2813-2816.

[30] J. S. Kwiatkowski, J. Leszczynski, *J. Mol. Struct.: THEOCHEM* **1990**, *208*, 35-44.

[31] W. Caminati, G. Maccaferi, P. G. Favero, L. B. Favero, *Chem. Phys. Lett.* **1996**, *251*, 189-192.

[32] M. J. Frisch, G. W. Trucks, H. B. Schlegel, G. E. Scuseria, M. A. Robb, J. R. Cheeseman, G. Scalmani, V. Barone, B. Mennucci, G. A. Petersson, H. Nakatsuji, M. Caricato, X. Li, H. P. Hratchian, A. F. Izmaylov, J. Bloino, G. Zheng, J. L. Sonnenberg, M. Hada, M. Ehara, K. Toyota, R. Fukuda, J. Hasegawa, M. Ishida, T. Nakajima, Y. Honda, O. Kitao, H. Nakai, T. Vreven, J. A. Montgomery, Jr., J. E. Peralta, F. Ogliaro, M. Bearpark, J. J. Heyd, E. Brothers, K. N. Kudin, V. N. Staroverov, T. Keith, R. Kobayashi, J. Normand, K. Raghavachari, A. Rendell, J. C. Burant, S. S. Iyengar, J. Tomasi, M. Cossi, N. Rega, J. M. Millam, M. Klene, J. E. Knox, J. B. Cross, V. Bakken, C. Adamo, J. Jaramillo, R. Gomperts, R. E. Stratmann, O. Yazyev, A. J. Austin, R. Cammi, C. Pomelli, J. W. Ochterski, R. L. Martin, K. Morokuma, V. G. Zakrzewski, G. A. Voth, P. Salvador,

J. J. Dannenberg, S. Dapprich, A. D. Daniels, O. Farkas, J. B. Foresman, J. V. Ortiz, J. Cioslowski, and D. J. Fox, Gaussian 09, revision B.01; Gaussian, Inc.: Wallingford, CT, **2009**.

[33] P. Écija, E. J. Cocinero, A. Lesarri, J. Millán, F. Basterretxea, J. A. Fernández, F. Castaño, *J. Chem. Phys.* **2011**, *134*, 164311-1 – 164311–8.

[34] Z. Kisiel, L. Pszczolkowski, J. C. López, J. L. Alonso, A. Maris, W. Caminati, *J. Mol. Spectrosc.* **1999**, *195*, 332-339.

[35] R. K. Bohn, K. W. Hillig, II, R. L. Kuczkowski, *J. Phys. Chem.* **1989**, *93*, 3456-3459.

[36] M. Stolze, D. H. Sutter, *Z. Naturforsch.* **1987**, *42a*, 49-56.

Chapter VII.

Interplay of theory and experiment in methyl jasmonate and zingerone

Manuscript for publication in preparation.

VII.1   Introduction

In this Chapter, we stress the importance of the interplay between theory and experiment in rotational spectroscopy applied to structural determination. We use the specific cases of two biomolecules, methyl jasmonate and zingerone. These molecules represent two examples where a poor choice of the theoretical method can lead to a misinterpretation of experimental results. Furthermore, this chapter serves as an illustration of the power of rotational spectroscopy as a benchmark for evaluating the performance of quantum chemistry theoretical calculations.

In the past decade, structural studies on large, flexible organic molecules of biological interest moved increasingly into the focus of interest. The three-dimensional conformation that a given biomolecule adopts is intimately related to its function in the biological medium. Hence, a lot of effort is devoted to the structural determination of biomolecules of increasing size. Structural studies carried out in condensed media provide a good environment to compare with biological surroundings, but the solvent or crystal packing forces may mask some key interactions. High-resolution structural studies in the gas phase benefit from an interaction-free environment where biomolecules can be probed without any kind of interference. The intrinsic properties of the molecule under study can be analyzed and separated from the effects arising from solvent or crystal packing.

Chapter III of this Thesis reviews the general methodology employed in structural studies in the gas phase using microwave spectroscopy. However, regardless of the high-resolution spectroscopic technique (laser spectroscopy, microwave, etc...), the general strategy in these studies includes an interplay between experimental results and theoretical calculations (molecular mechanics, molecular dynamics, quantum chemistry). This symbiosis between theory and experiment is nowadays a cornerstone in structural studies. Because of the increasing size and degrees of freedom of the molecular systems targeted, there is a need for good theoretical models that support the interpretation of experimental results. On the other hand, theoretical methods still require a reliable experimental counterpart to guarantee the accuracy of any implemented model. In this sense, a combination of rotational spectroscopy with highly accurate quantum chemistry is a powerful tool to study the molecular structures of large and flexible organic molecules. The efficiency of this strategy was previously shown in biologically relevant cases such as amino acids,[1,2] sugars,[3,4,5,6] nucleobases,[7,8,9] odorants,[10,11,12] and some drugs[13,14,15]

Recently, the unprecedented speed of rotational spectra acquisition obtained with broadband chirped-pulse Fourier transform microwave (CP-FTMW) spectrometers has opened new perspectives in structural chemistry.[16,17,18] Hence, it is possible to study larger molecular systems (15-25 heavy atoms) such as biomolecules[19,] or large organic compounds,[20,21] and their weakly bound intermolecular complexes.[22,23,24] In addition, the implementation of laser vaporization sources allows one to study thermally unstable systems, avoiding the undesirable thermal decomposition processes that occur when using conventional heating techniques.[1,5] The experimental progress brought by CP-FTMW spectroscopy now requires the development of more accurate, faster and efficient theoretical methods to analyze the experimental data.

One of the crucial points in the predictive value of the key parameters (structure, energy, dipole and quadrupole moments...) of larger biomolecular systems is the choice of the theoretical method. There is a large array of quantum chemical methods for that purpose. For instance, B3LYP[25,26] was historically very important, its cost-effectiveness making it very commonly used. However, the need to account for dispersive interactions (for instance, in weakly bound systems) led to the appearance of empirical corrections such as Grimme's[27,28,29,30] (D, D2, D3, D4 and its subvariants). Minnesota functionals[31] are more modern and highly parameterized, and Møller-Plesset perturbation theory[32] is very reasonable for small-medium size systems but not without limitations. In rotational studies, MP2 is probably the most common among the Møller-Plesset theory; however, its computational cost is quite high for medium sized systems. Hence, the choice of the method is usually subject to a compromise between accuracy and computational cost.

Molecular systems with only covalent interactions or relatively strong hydrogen bonds (e. g. O-H···O, O-H···N, N-H···O) can be described at almost any level of theory. However, systems stabilized by O-H···halogen, C-H···O, C-H···N, C-H···π, halogen-halogen, π···π, lone-pair···π, Van der Waals or London dispersive interactions require specific approaches to be modelled properly. In many cases, when performing a high-resolution structural study, the choice of the theoretical method is done routinely without taking into account the key interactions of the system. In addition, it is well-known that some methods are able to describe very well some weak interactions but fail at characterizing others.

In this Chapter, we prove that the choice of the appropriate quantum chemical method can be vital in the structural determination of biomolecules. In order to do so, we use the case studies of methyl jasmonate and zingerone, two of the main flavor components of jasmine and ginger, respectively (see Scheme VII.1 for chemical formulae).[33] The results reported in this work may serve as a gentle reminder to the spectroscopy community that choosing a theoretical method that is not appropriate for the molecular system under study could compromise the interpretation of the experimental results.
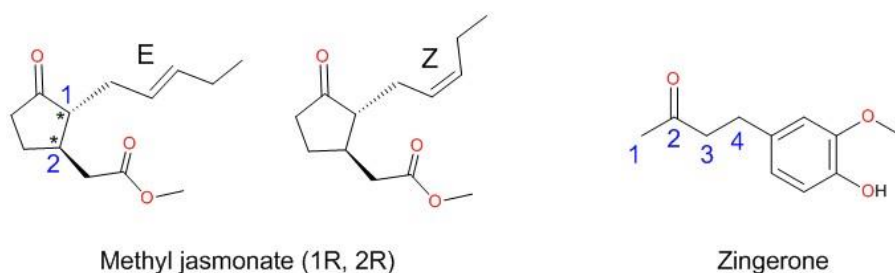
Scheme VII.1 Structures and atom numbering of methyl jasmonate and zingerone.

Both substances are widely present in plants. Methyl jasmonate is a vital lipidic phytohormone produced by many plants in response to biotic (pathogens, pests) and abiotic stress (heat, cold, wind, precipitation). It is an important signaling molecule and it plays an important role in the communication of plants. [34] Zingerone is the main component of ginger responsible for its pungency. It has been shown that it exhibits diuretic and neuroprotective functions, which are still not fully understood at a molecular scale. [35] Besides their interesting biological effects, these molecules represent limiting cases with respect to their size and molecular weights, for both the theoretical and the experimental studies presented in this work.

VII.2   Experimental section

Methyl jasmonate and zingerone are liquids with an oily consistency. Both of them have a low vapor pressure and need to be heated to be brought into the gas phase. Table VII.1 shows the relevant experimental parameters to record rotational spectra of these substances in the pulsed jet.

Table VII.1 Experimental conditions for the CP-FTMW spectrum of methyl jasmonate.

Experimental conditions	CP-FTMW
Number of nozzles	1
Nozzle temperature	200ºC
Carrier gas	He
Number of chirps/molecular pulse	10
Total number of cycles	3.9 millions

Table VII.2 Experimental conditions for the CP-FTMW and FTMW spectra of zingerone.

Experimental conditions	CP-FTMW	FTMW
Number of nozzles	1	1
Nozzle temperature	200ºC	200ºC
Carrier gas	Ne/He (80/20)	Ne
Number of chirps/molecular pulse	10	5
Total number of cycles	1.5 millions	1000-20000*

*The exact value depends on the required number of cycles to obtain a good signal-to-noise ratio of a given rotational transition.

VII.3   Case study 1: Methyl jasmonate

Methyl jasmonate consists of a cyclopentanone ring with two large flexible side chains. Each of them may adopt different conformations arising from rotations along single bonds. Apart from that, both chains could interact with each other. Moreover, the double bond in one of the side chains may adopt Z or E configurations. Finally, there are two chiral centers in the molecule, meaning that there are two diastereoisomers to consider (RR and RS). The corresponding enantiomers, SS and SR, would give rise to the same rotational spectra as RR and RS, respectively. Because of the flexibility of the molecule and the possible diastereoisomers to consider, the conformational casuistry is very broad and complex. Following the methodology explained in Chapter III, we used molecular mechanics (MM) as a first step in the conformational search. About 100 plausible structures for each system were found in an energy window of 20 kJ/mol. Hence, ≈ near 400 structures (4 x ~100) had to be re-optimized with more accurate theoretical calculations to predict the relevant rotational parameters (structures, energies, dipole moments...). We chose the B3LYP method, a fast and reasonably accurate method, to guide the experiment and re-optimized all the geometries.

Once we performed the calculations, the rotational spectrum of methyl jasmonate in the 6-18 GHz frequency region was collected in the CP-FTMW spectrometer available at the University of the Basque Country (UPV/EHU) (see Figure VII.1 for an overview of the spectrum). The sample was heated to 200ºC in a customized heating nozzle in order to build up enough concentration of methyl jasmonate in the gas phase. We spotted two sets of rotational transitions in the spectrum, although they were very far from the theoretical predictions and the process of fitting was a hard task. The two sets were fitted separately to two semirigid asymmetric rotor Hamiltonians in the Watson S-reduction. The rotational transitions in the spectrum displayed splittings due to tunneling effects from internal rotation of a methyl top. These splittings were also accounted for in the fit, allowing for the estimation of the barrier for internal rotation of the methyl top (V_3). Table VII.3 summarizes the results of the fits. All measured rotational transitions are collected in Tables VII.A.1 and VII.A.2 in the appendix.
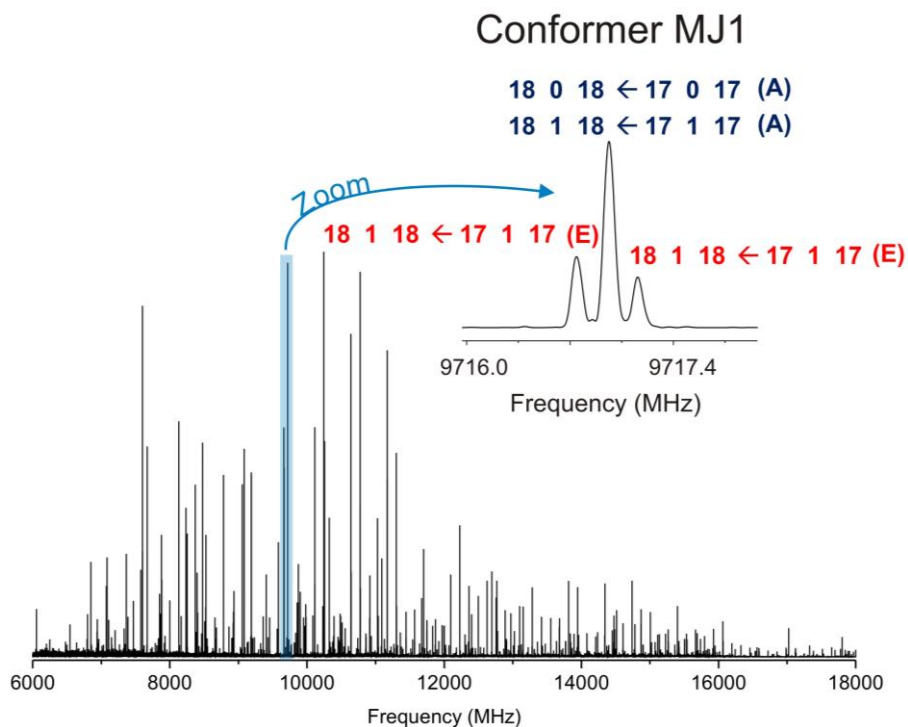
Figure VII.1 CP-FTMW experimental rotational spectrum of methyl jasmonate, with a zoomed view around the 9716 MHz frequency region, where two rotational transitions from conformer MJ1 can be observed, as well as the splitting arising from methyl internal rotation. The A components overlap, while the E do not, and the lines take the shape of a triplet.

Table VII.3 Microwave spectroscopic results of methyl jasmonate

	Conf. MJ1	Conf. MJ2
A_0/MHz	634.08650(61)	562.012(25)
B_0/MHz	370.027243(69)	382.88673(91)
C_0/MHz	264.431586(64)	260.374(23)
D_J/kHz	-0.001843(75)	0.147(11)
D_{JK}/kHz	0.4011(16)	-0.739(68)
d_1/kHz		0.0676(55)
d_2/kHz	-0.005797(39)	
V_3/cm^{-1}	437.3(2.5)	427.32(82)
σ/kHz	18.3	19.8
N_{tot}	679	215
N_A/N_E	372/307	114/101

As we have seen in previous chapters of this Thesis, the common strategy used in the microwave spectroscopy community to assign a molecular conformation to a given set of experimental rotational constants is to compare with the values arising from quantum chemical calculations. However, all attempts to assign the spectrum based on the calculated molecular structures of methyl jasmonate failed. This spectrum did not correspond to any of the predicted conformations for methyl jasmonate with the B3LYP method. We considered the possibility of sample fragmentation resulting in decomposition products or internal reactions, but these solutions did not match the spectrum either. By this point, we had carried out more than 1000 calculations but none of them reproduced the experiment. Finally (and fortunately), we decided to re-do the optimizations of methyl jasmonate with the MP2 ab initio method and to our surprise it led to very different results. The new lowest lying energy conformers (Conf. MJ1 and Conf.MJ2) had not been detected by the B3LYP method and these structures reproduced the experimental data. The B3LYP method had led us to erroneous results, causing us to waste considerable time.

Finally, we carried out numerous calculations with different methods to compare their performance at reproducing experimental values. We always used the same basis set (6-311++G(d,p)), which we have used with other molecular systems. Theoretical methods yield the rotational constants at the nonphysical bottom of the potential well (commonly known as B_e *equilibrium structure*) while the experimental rotational constants refer to the structure at the vibrational ground state v=0 (B_0). We estimated $B_{vib}=B_0-B_e$ with anharmonic calculations at the B97-D3/def2-SVP level of theory and subtracted it from the experimental rotational constants in order to obtain the "experimental" values of B_e. The latter are directly comparable to the rotational constants obtained from quantum chemical calculations.[20,36] The results are summarized in Tables **VII.4** and **VII.5** for the two observed conformers of methyl jasmonate. It is noteworthy that the B3LYP method, which does not account for dispersion effects, fails at reproducing the experimental structure (relative errors in A around 15%). This is also the case for other methods such as PBE, TPSS or B2PLYP (although B2PLYP provides significantly better results, with ~6% error in the *A* rotational constant). Only *ab initio* and DFT methods that considered dispersion effects (either intrinsically or by adding a correction) were successful at reproducing experimental values.

Table VII.4 Values of A_e, B_e and C_e based on experimental measurements are compared to theoretical values calculated with different methods (basis set: 6-311++G(d,p)) for Conf MJ1 of methyl jasmonate. Note that the experimental values of B_e are calculated such that $B_e = B_0 - B_{vib}$, and the anharmonic correction B_{vib} is estimated at the B97D3/def2-SVP level of theory.

	Exp.	B3LYP	TPSS	PBE	B2PLYP
A_e/MHz	641.37750	549.8	550.7	572.6	600.9
%error A_e		**14.3**	**14.1**	**10.7**	**6.3**
B_e/MHz	371.505243	366.1	366.5	368.2	369.2
%error B_e		**1.4**	**1.3**	**0.9**	**0.6**
C_e/MHz	267.381586	245.1	245.1	250.4	257.4
%error C_e		**8.3**	**8.3**	**6.3**	**3.7**
CPU time (h) /opt cycle		‹1	3.2	2.3	15.8

	Exp.	B3LYP -D3	B3LYP -D3BJ	B2PLYP -D3BJ	MP2	M06-2X	B97 -D3	B97 -D3BJ
A_e/MHz	641.37750	643.1	644.3	633.9	642.0	662.8	637.1	623.3
%error A_e		**-0.3**	**-0.5**	**1.2**	**-0.1**	**-3.3**	**0.7**	**2.8**
B_e/MHz	371.505243	368.1	367.7	369.3	370.8	373.9	365.7	366.7
%error B_e		**0.9**	**1.0**	**0.6**	**0.2**	**-0.7**	**1.6**	**1.3**
C_e/MHz	267.381586	265.1	265.7	264.3	266.7	269.6	263.1	260.9
%error C_e		**0.9**	**0.6**	**1.2**	**0.3**	**-0.8**	**1.6**	**2.4**
CPU time (h) /opt cycle		‹1	‹1	13.8	5.1	1.0	1.7	0.9

Table VII.5 Values of A_e, B_e and C_e based on experimental measurements are compared to theoretical values calculated with different methods (basis set: 6-311++G(d,p)) for Conf MJ2 of methyl jasmonate. Note that the experimental values of B_e are calculated such that $B_e=B_0-B_{vib}$, and the anharmonic correction B_{vib} is estimated at the B97D3/def2-SVP level of theory.

	Exp.	B3LYP	TPSS	PBE	B2PLYP
A_e/MHz	560.758	477.2	488.0	501.2	532.2
%error A_e		**14.9**	**13.0**	**10.6**	**5.1**
B_e/MHz	388.22373	382.5	381.2	382.0	382.4
%error B_e		**1.5**	**1.8**	**1.6**	**1.5**
C_e/MHz	261.010	237.4	240.5	243.9	253.8
%error C_e		**9.1**	**7.9**	**6.6**	**2.8**
CPU time (h) /opt cycle		**1.0**	**2.6**	**2.0**	**16.0**

	Exp.	B3LYP -D3	B3LYP -D3BJ	B2PLYP -D3BJ	MP2	M06-2X	B97 -D3	B97 -D3BJ
A_e/MHz	560.758	573.1	568.6	564.9	572.9	588.2	567.9	556.6
%error A_e		**-2.2**	**-1.4**	**-0.7**	**-2.2**	**-4.9**	**-1.3**	**0.7**
B_e/MHz	388.22373	380.0	380.9	381.6	382.5	382.5	378.0	379.3
%error B_e		**2.1**	**1.9**	**1.7**	**1.5**	**1.5**	**2.6**	**2.3**
C_e/MHz	261.010	261.5	261.1	262.2	266.7	267.6	259.7	258.3
%error C_e		**-0.2**	**0.0**	**-0.5**	**-2.2**	**-2.5**	**0.5**	**1.0**
CPU time (h) /opt cycle		**1.0**	**1.3**	**14.8**	**5.8**	**2.2**	**‹1**	**2.0**

Figure VII.2 displays the steps of the optimization of Conf. MJ2 with the B3LYP and B3LYP-D3BJ methods starting from the same geometry. We can clearly see that with B3LYP, as the optimization progresses, the two arms get further from each other, the final distance CH···O being 4.1 Å (conformer Conf. MJ2'). Hence, the CH···O interaction is not contemplated by this B3LYP method. On the contrary, in B3LYP-D3BJ, the two arms remain close to each other, held together by the CH···O weak interaction (final distance 2.8 Å, Conf.MJ2). We infer that the dispersion correction D3BJ has a dramatic effect on the rotational constants. In particular, the rotational constant A is most influenced by dispersion in the case of methyl jasmonate because the principal axis a lies along the two side chains. Hence, the moment of inertia I_a (to which A is inversely proportional) is very sensitive to the coordinates of the atoms in the side chains (see Figure VII.3 for display of the principal axes of inertia). The effect of dispersion is so great in this molecule that the assignment to the molecular conformation could not be possible with the B3LYP methodology.
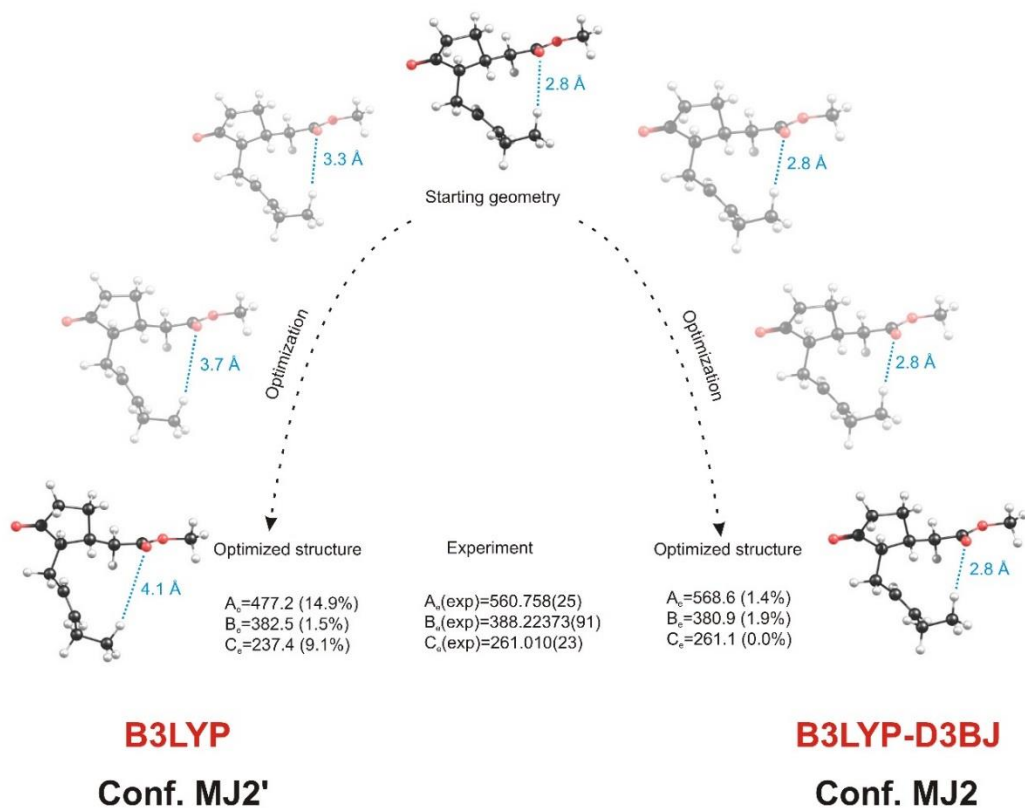
Figure VII.2 Steps of the optimization of Conf. MJ2' and Conf. MJ2 of methyl jasmonate (RR, Z conformation of the double bond) using the B3LYP and B3LYP-D3BJ DFT methods, respectively, from the same starting geometry (basis set: 6-311++G(d,p)).
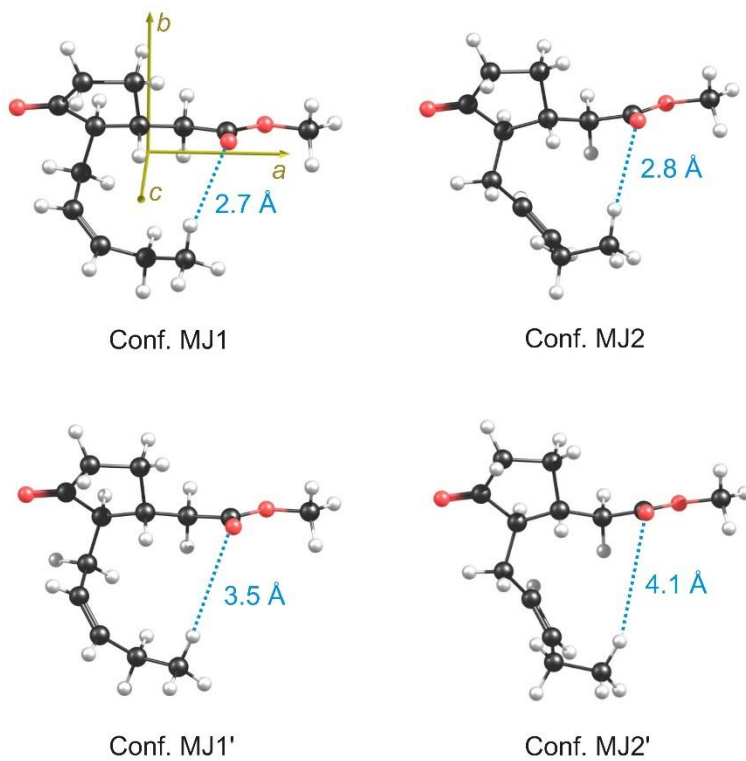
Conf. MJ1   Conf. MJ2

Conf. MJ1'   Conf. MJ2'

Figure VII.3 The two experimentally observed conformations of methyl jasmonate (RR, Z conformation of the double bond) (Conf. MJ1 and Conf. MJ2) as optimized at the B3LYP-D3BJ/6-311++G(d,p) level of theory, as well as the corresponding conformations Conf. MJ1' and Conf. MJ2' calculated at the B3LYP/6-311++G(d,p) level of theory. For Conf. MJ1, we also show the principal axes of inertia *a*, *b*, and *c*.

To sum up, the two experimental conformations are assigned to Conf. MJ1 and Conf. MJ2. Both of them are RR diastereaoisomers (or SS), the configuration of the double bond in the side chain is Z and both conformations are stabilized by a C-H⋯O Weak Hydrogen Bond (WHB). The corresponding 3D-structures are depicted in Figure VII.3, along with the structures of Conf. MJ1' and Conf. MJ2', that is, the resulting conformations when no dispersion is included.

VII.4   Case study 2: Zingerone

Zingerone (4-(4-hydroxy-3-methoxyphenyl)-2-butanone), see Scheme **VII**.1) consists of an *o*-methoxyphenol moiety with a flexible chain in *para* with respect to the hydroxy group. In order to guide the spectral search, we predicted the most favorable structures employing the strategy summarized in Chapter **III**. We performed MM calculations to have an initial screening of the conformational landscape (14 structures were found in 15kJmol^{-1}) and then we re-optimized all of them with the MP2 method, a very common level of theory in rotational studies.

Later, the rotational spectrum of zingerone in the 6-18 GHz frequency region was collected in the Balle-Flygare's FTMW and in the CP-FTMW spectrometers at the University of the Basque Country (UPV/EHU) (see Figure **VII**.4). The sample was heated to 200ºC in a customized heating nozzle in order to bring it into the gas phase. A set of rotational transitions corresponding to one rotor of the molecule was detected and fitted to a semirigid asymmetric rotor Hamiltonian in the Watson S-reduction. Rotational transitions displayed splittings due to tunneling effects from internal rotation of a methyl top that were accounted for in the fit. The results of the fit are summarized in Table **VII**.6. All measured rotational transitions are collected in in the appendix.
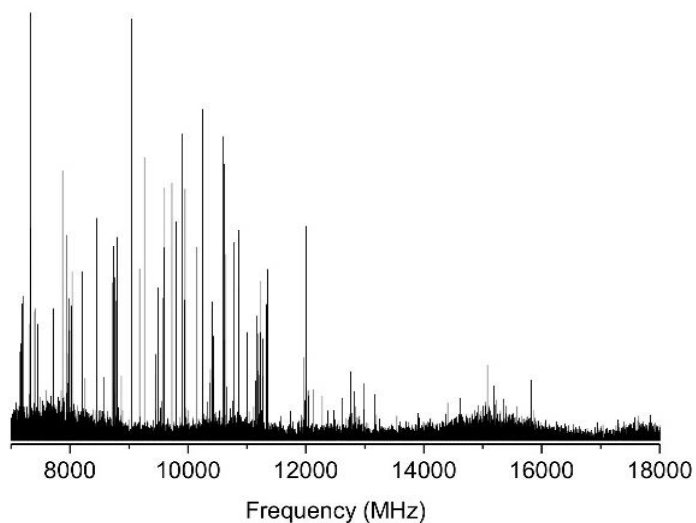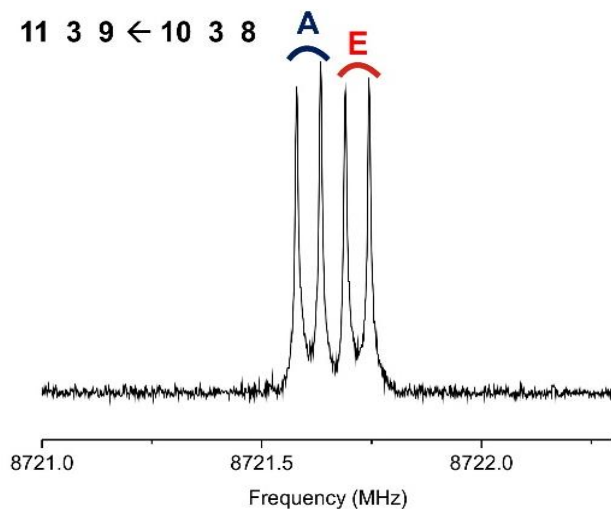
Figure VII.4 Experimental rotational spectra of zingerone. Top, CP-FTMW spectrum. Down, section of the FTMW spectrum with the 11 3 9 ← 10 3 8 rotational transition (the A/E splitting due to internal rotation can be observed). In the FTMW spectrum, rotational lines display Doppler splittings due to the coaxial disposition of the supersonic expansion and the MW radiation.

Table VII.6 Microwave spectroscopic results of zingerone

	Conf. Z2
A_0/MHz	1025.0726(22)
B_0/MHz	436.1622(40)
C_0/MHz	354.21908(24)
D_J/kHz	0.06605(65)
D_{JK}/kHz	0.1049(65)
d_1/kHz	-0.00489(37)
V_3/cm^{-1}	336.748(88)
σ/kHz	24.2
N_{tot}[d]	198
N_A/N_E[e]	114/84

Surprisingly, there was no correspondence between experiment and theory. The discrepancy in the rotational constants was remarkable. Errors of ~17 % indicated that the predicted structure was not the experimentally observed structure, despite having used a method as trusted as MP2.

In this case, we decided to re-optimize all the structures using DFT theory, in particular B3LYP-D3BJ. We were surprised to see that the results generated with this functional were not comparable to those obtained with the MP2 method. With both methods, all the lowest lying conformations were stabilized by an OH···O interaction between the hydroxy and the methoxy group. However, the global minimum was different for the MP2 and B3LYP-D3BJ calculations. Not only that, but the lowest lying structure predicted by B3LYP-D3BJ was not even predicted by MP2. The two conformations predicted as global minima in zingerone are shown in Figure VII.5. The first one (Conf. Z1, MP2 structure) corresponds to the situation where there is an attractive CH···π interaction between the terminal CH$_3$ in the flexible chain and the π cloud in the aromatic ring. This interaction forces the side chain to tilt towards the ring. It is worth noting that this structure is not predicted by B3LYP (or TPSS, PBE and B2PLYP, that is, methods that do not account for dispersive interactions). In the second conformation (Conf. Z2, B3LYP-D3BJ structure), no such interaction occurs and the side chain is perpendicular to the ring. This conformer exhibits a C=O···H-C attractive interaction. In this case, this conformation was not predicted by MP2 method. To sum up, we have two possible global minima, one of which was not predicted by the MP2 method.
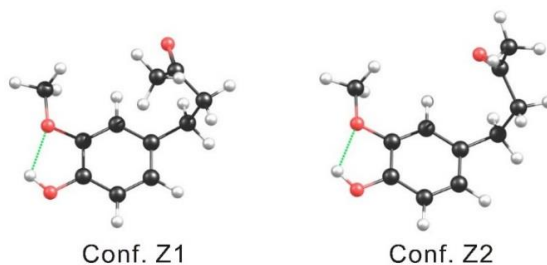

Conf. Z1   Conf. Z2

Figure VII.5 The conformations of zingerone predicted as global minima with the MP2 (Conf. Z1) and B3LYP-D3BJ methods (Conf. Z2).

In addition, we extended the predictions to other theoretical models. Tables **VII.6** and VII.7 summarize the results of those calculations. Clearly, not every theoretical method is able to predict the two conformations. The balance between the CH···π interaction (Conf. Z1) and the CH···O interaction (Conf. Z2) is very subtle. It is a challenging task for theoretical models to weigh the strength of these interactions, since both are weak hydrogen bonds (WHB) with very similar stabilization energies. Regarding the theoretical methods, three different trends are observed. They are summarized in Figure VII.6 with the three prototype methods MP2, B3LYP and M06-2X. We can observe that M06-2X is capable of reproducing both conformations if the correct starting geometry is chosen. B3LYP always yields Conf. Z2 stabilized by CH···O interaction, that is, with the lateral chain perpendicular to the plane of the aromatic ring. Finally, MP2 calculations result always in Conf. Z1 with a CH···π interaction, where the chain is bent towards the benzene ring. Tables **VII.6** and **VII.7** show the difference in the rotational constants. Therefore, the choice of the theoretical method is crucial to success. The rotational constants are very sensitive to both conformers and we will only be able to discern unambiguously the structure of the zingerone through microwave spectroscopy.
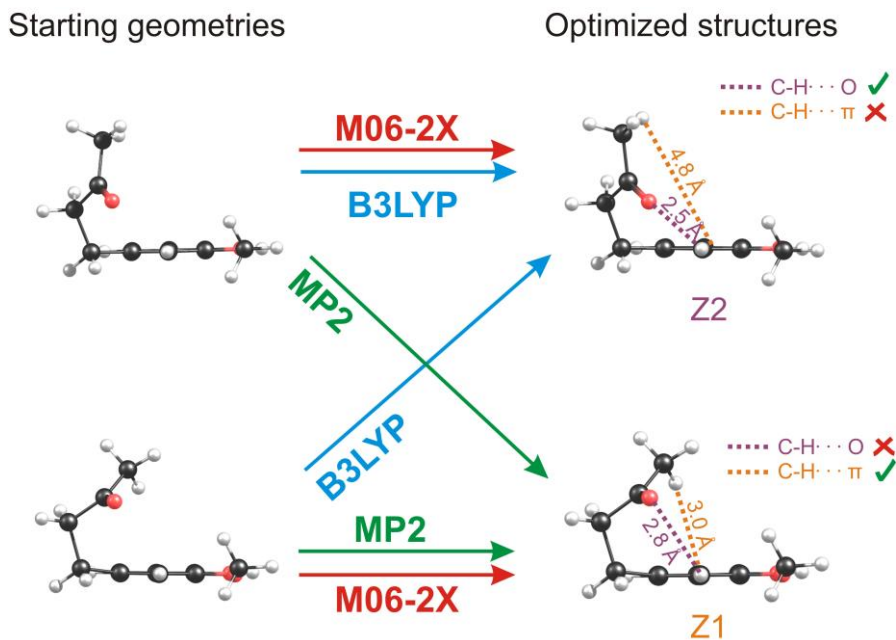

Figure VII.6 A schematic representation of the prototype behavior of theoretical methods in the casuistry of zingerone.

Table VII.6 Values of A_e, B_e and C_e based on experimental measurements are compared to theoretical values calculated with different methods (basis set: 6-311++G(d,p)) for Conf Z2 of zingerone. Note that the experimental values of B_e are calculated such that $B_e=B_0-B_{vib}$, and the anharmonic correction B_{vib} is estimated at the B97D3/def2-SVP level of theory.

	Exp.	B3LYP	TPSS	PBE	B2PLYP
A_e/MHz	1030.8436	1034.5	1021.8	1024.6	1021.2
%error A_e		-0.4	0.9	0.6	0.9
B_e/MHz	442.8122	421.4	423.0	422.7	433.2
%error B_e		4.8	4.5	4.6	2.2
C_e/MHz	357.79349	340.6	342.9	341.4	351.4
%error C_e		4.8	4.1	4.6	1.8
CPU time (h) /opt cycle		‹1	‹0.01	‹1	4.7

	Exp.	B3LYP -D3	B3LYP -D3BJ	B2PLYP -D3BJ	MP2	M06-2X	B97 -D3	B97 -D3BJ
A_e/MHz	1030.8436	1016.9	1017.8	1009.9	NA*	1028.5	1001.7	NA
%error A_e		1.4	1.3	2.0	NA	0.2	2.8	NA
B_e/MHz	442.8122	437.5	439.4	444.7	NA	441.7	436.9	NA
%error B_e		1.2	0.8	-0.4	NA	0.2	1.3	NA
C_e/MHz	357.79349	352.3	354.2	360.6	NA	357.6	351.7	NA
%error C_e		1.5	1.0	-0.8	NA	0.1	1.7	NA
CPU time (h) /opt cycle		‹1	‹1	4.7	NA	‹1	‹0.01	NA

*Not Applicable. The optimization leads to Conf. Z1.

Table VII.7 Theoretical values of A_e, B_e and C_e calculated with different theoretical methods (basis set: 6-311++G(d,p)) for Conf Z1 of zingerone.

	B3LYP	TPSS	PBE	B2PLYP			
A_e/MHz	NA*	NA	NA	NA			
B_e/MHz	NA	NA	NA	NA			
C_e/MHz	NA	NA	NA	NA			
CPU time (h) /opt cycle	NA	NA	NA	NA			

	B3LYP -D3	B3LYP -D3BJ	B2PLYP -D3BJ	MP2	M06-2X	B97 -D3	B97 -D3BJ
A_e/MHz	991.7	994.6	994.2	994.7	999.8	985.5	987.7
B_e/MHz	483.6	487.1	488.9	509.3	503.5	482.4	486.5
C_e/MHz	390.4	395.5	398.2	413.6	407.5	390.2	395.0
CPU time (h) /opt cycle	0.6	1.4	7.5	2.5	1.9	0.6	0.006

*Not Applicable. The optimization leads to Conf. Z2.

By comparing the experimental values of the rotational constants with the theoretical predictions, we can conclude that the experimental conformation of zingerone is Conf. Z2, which is stabilized by a CH···O interaction. This means that MP2/6-311++G(d,p), which is a very commonly used and most trusted method in the rotational spectroscopy community, fails to predict the experimentally observed conformation of zingerone. The observed conformer is not even predicted by this method. MP2 overestimates the CH···π interaction[37] and, as the balance between WHBs is so subtle, the real structure is not predicted by MP2 method. In order to visualize the subtlety of the competition between the two WHBs, we calculate the barrier between both structures by performing a relaxed scan of the 1-2-3-4 dihedral angle (see Scheme VII.1 for atom numbering). Moreover, we perform this scan using two different methods (M06-2X and B3LYP-D3BJ) to evaluate the response of both of them in the WHBs competition. Figure VII.7 displays the results.

We can observe the local minima corresponding to Conf. Z1 and Conf. Z2 in both scans. It is worth noting that these minima are almost isoenergetic. The energy difference between both of them is less than 0.5 kJ/mol (this value is probably within the error of the theoretical calculation). Moreover, M06-2X and B3LYP-D3BJ predict that the barrier between the two structures is very low (~1 kJ/mol), meaning that it can be easily overcome in the supersonic expansion and therefore, the system would relax to the most stable conformation. This behavior has been previously observed (in rotational spectra of amino acids) and it was referred to as the "missing conformer".[38] The most relevant difference between these theoretical methods is precisely the energetic order of the conformers. While M06-2X predicts that the most stable conformation is Conf. Z1 (CH···π interaction), B3LYP-GD3BJ predicts Conf. Z2 as the most stable structure (CH···O interaction). The small energy difference and the low barrier between both conformations proves the subtlety of the competition between the two interactions, with different theoretical methods tipping the balance in favor of one structure or the other.
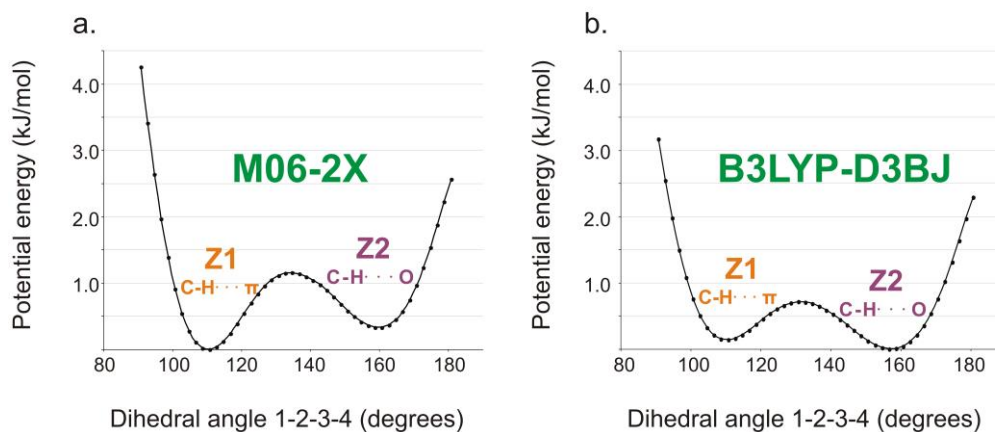
Figure VII.7 Potential energy scans of the 1-2-3-4 dihedral angle of zingerone to evaluate the energy barrier between Conf. Z1 (a., stabilized by a C-H⋯π interaction) and Conf. Z2 (b., stabilized by a C-H⋯O interaction).

This study confirms that rotational spectroscopy combined with theoretical methods is a powerful strategy, which can be broadly applied to flexible organic compounds. However, one must be cautious in the use of different theoretical methods. Using several distinct levels of theory allows one to get a good overview of the conformational scope. This work confirms that microwave spectroscopy is a perfect benchmark to develop new theoretical models so needed to support the experiments.

VII.5 References

[1] A. Lesarri, S. Mata, E. J. Cocinero, S. Blanco, J. C. López, J. L. Alonso, *Angew. Chem. Int. Ed.* **2002**, *41*, 4673-4676.

[2] A. Lesarri, R. Sánchez, E. J. Cocinero, J. C. López, J. L. Alonso, *J. Am. Chem. Soc.* **2005**, *127*, 12952-12956.

[3] E. J. Cocinero, P. Çarçabal, T. D. Vaden, J. P. Simons, B. G. Davis, *Nature* **2011**, *469*, 76-79.

[4] E. J. Cocinero, D. P. Gamblin, B. G. Davis, J. P. Simons, *J. Am. Chem. Soc.* **2009**, *131*, 11117-11123.

[5] E. J. Cocinero, A. Lesarri, P. Écija, F. J. Basterretxea, J. Grabow, J. A. Fernández, F. Castaño, *Angew. Chem. Int. Ed.* **2012**, *51*, 3119-3124.

[6] P. Écija, I. Uriarte, L. Spada, B. G. Davis, W. Caminati, F. J. Basterretxea, A. Lesarri, E. J. Cocinero, *Chem. Commun.* **2016**, *52*, 6241-6244.

[7] E. Nir, K. Kleinermanns, M. S. De Vries, *Nature* **2000**, *408*, 949-951.

[8] J. L. Alonso, I. Peña, J. C. López, V. Vaquero, *Angew. Chem. Int. Ed.* **2009**, *48*, 6141-6143.

[9] L. B. Favero, I. Uriarte, L. Spada, P. Écija, C. Calabrese, W. Caminati, E. J. Cocinero, *J. Phys. Chem. Lett.* **2016**, *7*, 1187-1191.

[10] H. Mouhib, W. Stahl, M. Lüthy, M. Büchel and P. Kraft, *Angew. Chem. Int. Ed.* **2011**, *50*, 5576-5580.

[11] H. V. L. Nguyen, H. Mouhib, S. Klahm, W. Stahl, I. Kleiner, *Phys.Chem. Chem. Phys.* **2013**, *15*, 10012-10018.

[12] D. Loru, M. M. Quesada-Moreno, J. R. Avilés-Moreno, N. Jarman, T. R. Huet, J. J. López-González, M. E. Sanz, *ChemPhysChem* **2017**, *18*, 274-280.

[13] I. León, J. Millán, E. J. Cocinero, A. Lesarri, J. A. Fernández, *Angew. Chem. Int. Ed.* **2014**, *53*, 12480-12483.

[14] I. León, J. Millán, E. J. Cocinero, A. Lesarri, J. A. Fernández, *Angew. Chem. Int. Ed.* **2013**, *52*, 7772-7775.

[15] A. Lesarri, A. Vega-Toribio, R. D. Suenram, D. J. Brugh, J.-U. Grabow, *Phys. Chem. Chem. Phys.* **2010**, *12*, 9624-9631.

[16] G. G. Brown, B. C. Dian, K. O. Douglass, S. M. Geyer, S. T. Shipman, B. H. Pate, *Rev. Sci. Instrum.* **2008**, *79*, 053103-1 – 053103-13.

[17] a) S. T. Shipman, B. H. Pate, in Handbook of High Resolution Spectroscopy (Ed.: M. Quack, F. Merkt), Wiley: New York, 2011, pp. 801-828. b) J. L. Neill, S. T. Shipman, L. Alvarez-Valtierra, A. Lesarri, Z. Kisiel, B. H. Pate, *J. Mol. Spectrosc.* **2011**, *269*, 21-29.

[18] a) C. Pérez, M. T. Muckle, D. Zaleski, N. A. Seifert, B. Temelso, G. C. Shields, Z. Kisiel, B. H. Pate, *Science* **2012**, *336*, 897-901. b) C. Pérez, S. Lobsiger, N. A. Seifert, D. P. Zaleski, B. Temelso, G. C. Shields, Z. Kisiel, B. H. Pate, *Chem. Phys. Lett.* **2013**, *571*, 1-15.

[19] I. Uriarte, C. Pérez, E. Caballero-Mancebo, F. J. Basterretxea, A. Lesarri, J. A. Fernandez, E. J. Cocinero, *Chem. Eur. J.* **2017**, *23*, 7238-7244.

[20] A. A. Fokin, T. S. Zhuk, S. Blomeyer, C. Pérez, L. V. Chernish, A. E. Pahenko, J. Antony, Y. V. Vishnevskiy, R. J. F. Berger, S. Grimme, C. Logemann, M. Schnell, N. W. Mitzel, P. R. Schreiner, *J. Am. Chem. Soc.* **2017**, *139*, 16696-16707.

[21] S. R. Domingos, A. Cnossen, W. J Buma, W. R. Browne, B. L. Feringa, M. Schnell, *Angew. Chem. Int. Ed.* **2017**, *56*, 11209-11212.

[22] N. A. Seifert, D. P. Zaleski, C. Pérez, J. L. Neill, B. H. Pate, M. Vallejo-López, A. Lesarri, E. J. Cocinero, F. Castaño, I. Kleiner, *Angew. Chem. Int. Ed.* **2014**, *53*, 3210-3213.

[23] A. L. Steber, C. Pérez, B. Temelso, G. C. Shields, A. M. Rijs, B. H. Pate, Z. Kisiel, M. Schnell, *J. Phys. Chem. Lett.* **2017**, *8*, 5744-5750.

[24] S. Ghosh, J. Thomas, W. Huang, Y. Xu, W. Jäger, *J. Phys. Chem. Lett.* **2015**, *6*, 3126-3131.

[25] A. D. Becke, *J. Chem. Phys.* **1993**, *98*, 5648-5652.

[26] C. T. Lee, W. T. Yang, R. G. Parr, *Phys. Rev. B* **1988**, *37*, 785-789.

[27] S. Grimme, *J. Comput. Chem.* **2006**, *27*, 1787-1799.

[28] S. Grimme, *J. Comput. Chem.* **2004**, *25*, 1463-1473.

[29] S. Grimme, S. Ehrlich, L. Goerigk, *J. Comput. Chem.* **2011**, *32*, 1456-1465.

[30] E. Caldeweyher, C. Bannwarth, S. Grimme, *J Chem Phys.* **2017**, *147*, 034112.

[31] Y. Zhao, D. G. Truhlar, *Theor. Chem. Acc.* **2008**, *120*, 215-241.

[32] C. Moller, M. S. Plesset, *Phys. Rev.* **1934**, *46*, 618-622.

[33] T. E. Acree, R. Nishida, H. Fukami, *J. Agric. Food Chem.* **1985**, *33*, 425-427; Y. Asamitsu, Y. Nakamura, M. Ueda, S. Kuwahara, H. Kiyota, *Chem. Biodivers.* **2006**, *3*, 654-659.

[34] a) J. J. Cheong, Y. D. Choi, *Trends Genet.* **2003**, *19*, 409–413. b) N.C. Avanci, D.D. Luche , G.H. Goldman, M.H.S. Goldman, *Genet. Mol. Res.* **2010**, *9*, 484-505.

[35] H. A. C. Fay, *Aust. J. Entomol.* **2012**, *51*, 189-197.

[36] N. Vogt, J. Demaison, E. J. Cocinero, P. Écija, A. Lesarri, H. D. Rudolph, J. Vogt, *Phys. Chem. Chem. Phys.* **2016**, *18*, 15555-15563.

[37] S. Tsuzuki, T. Uchimaru, K. Matsumura, M. Mikami, K. Tanabe, *Chem. Phys. Lett.* **2000**, *319*, 547-554.

[38] P. D. Godfrey, R. D. Brown, F. M. Rodgers, *J. Mol. Struct.* **1996**, *376*, 65-81.

Chapter VIII.

- -

Structural preferences of methyl 2-deoxy-D-ribofuranoside in the gas phase and in solution

Manuscript for publication in preparation.

VIII.1 Introduction

In this Chapter, we explore the potential of rotational spectroscopy as a tool to determine the conformations of biomolecular building blocks under isolation conditions, using the case of methyl 2-deoxy-D-ribofuranoside, the monosaccharide present in DNA. This project illustrates how microwave spectroscopy combines nicely with other techniques in order to extract structural information from a molecular system. We use chemical synthesis to prepare the sample, rotational spectroscopy to analyze the conformational space in the gas phase and a combination of NMR and Molecular Dynamics to explore the conformations in aqueous solution.

Sugars are one of the four major classes of biomolecules, along with proteins, lipids and nucleic acids. They are very versatile molecules that play many different roles in living organisms. One of their most well-known functions is as energy fuels, but sugars are also crucial as structural scaffolds, in cell signaling, molecular recognition and DNA/RNA, just to name a few.

The building blocks of sugars are monosaccharides. They display a very rich structural/conformational diversity, which we will briefly review in the next lines. The common formula of monosaccharides is $C_nH_{2n}O_n$. The most relevant ones in biological functions are pentoses (n=5) and hexoses (n=6). They can take on either linear or cyclic forms. The most common cyclic forms are five- or six-membered rings (furanoses or pyranoses, respectively). In the cyclic forms, monosaccharides appear as α or β anomers, depending on whether the cyclisation proceeded from one side of the molecule or the other. Moreover, each pyranose or furanose form may adopt different conformations. Pyranoses tend to adopt a chair (C) form of the ring (normally $^4C_1$ or $^1C_4$), whereas furanoses are more flexible and may take on envelope (E) or twist (T) shapes. Figure VIII.1 summarizes the conformational diversity of monosaccharides with the specific example of 2-deoxy-D-ribose. This figure is not meant as an exhaustive report of all the conformations of this molecule, but rather an exemplification of the conformational casuistry of the monosaccharide.
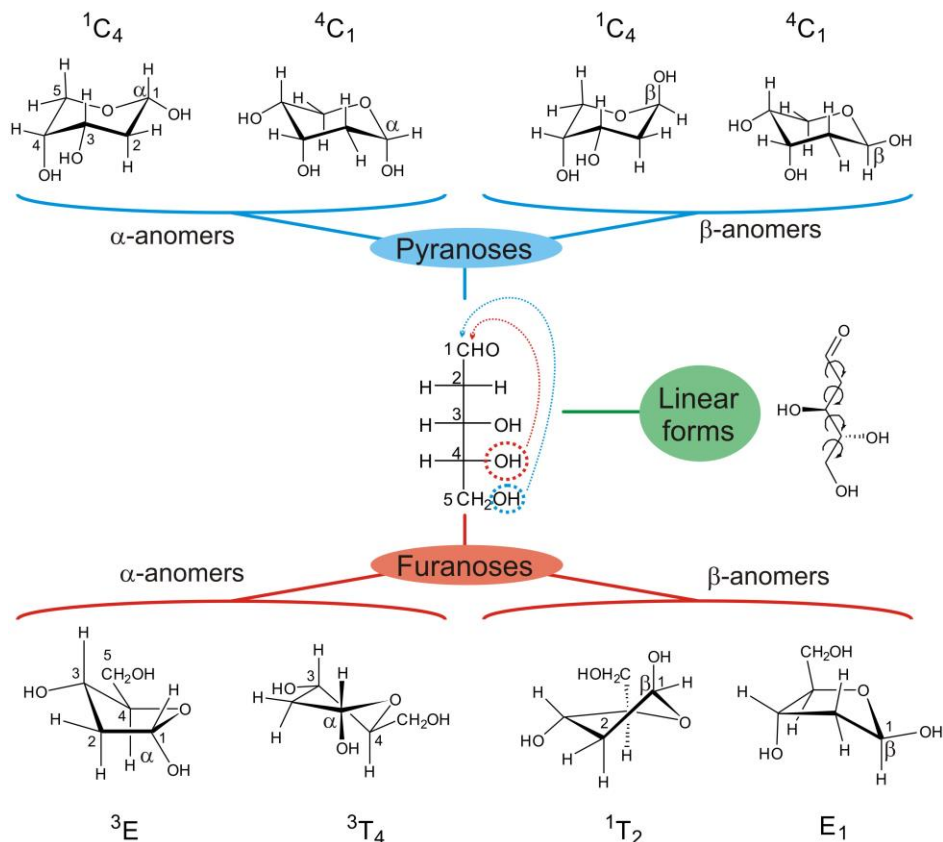
Figure VIII.1 Structural/conformational casuistry of 2-deoxy-D-ribose. Only a few of the possible ring conformations are displayed ($^1C_4$, $^4C_1$, ^3E, $^3T_4$, etc).

A lot of research is devoted to the structural determination of sugars, ranging from monosaccharides to large polysaccharides (with several hundred monomeric units). In general, those structural studies aim at a better understanding of the role that these biomolecules play in biological activity. Furthermore, many studies focus on the interactions of sugars with other molecules such as biological receptors or drugs, in order to identify the key interacting sites. In general, a profound knowledge of their mechanism of action at a molecular level is often sought in these structural studies. The field has been particularly active in solution phase, both in the past decades and nowadays. [1,2,3] On the contrary, high resolution structural studies in the gas phase are quite recent. It was not until the early 2000s that the group of Professor John P. Simons at Oxford pioneered the study of carbohydrates (and their hydrated clusters) in the gas phase [4,5,6] and introduced laser vaporization techniques to the structural studies of sugars.[7] They studied a myriad of monosaccharides and small oligosaccharides and their hydrated clusters using laser vibrational spectroscopy techniques.[8,9,10,11] In order to perform those experiment, the carbohydrates had to be tagged with a chromophore; normally, the OH group at position 1' was replaced by a OPh group. This served two purposes: on the one hand, the Ph group acted as a chromophore tag and, on the other hand, the α and β anomers could be

selectively isolated and probed with the spectroscopic techniques, because the presence of the Ph groups inhibits mutarotation.

Rotational spectroscopy studies on monosaccharides started a decade later than the pioneering work of Professor John P. Simons. The major issue with performing microwave studies on monosaccharides was the process of vaporization of the molecules. In some way, the chromophore tagging necessary to perform vibrational studies was also "protecting" the monosaccharide from breaking apart, and, hence, carbohydrates could be vaporized with conventional heating techniques in some cases. In pure (non-tagged) monosaccharides, on the other hand, conventional heating or IR nanosecond-pulsed lasers (similar to those used in vibrational spectroscopy) vaporization techniques resulted in decomposition products only. It was not until 2012 that the first rotational study on a monosaccharide (ribose) was published.[12] The work was performed by our group at the University of the Basque Country (UPV/EHU). In order to vaporize the sample, a picosecond (~40 ps) laser working on the UV region (355 nm) was used. Six different conformations of ribose were experimentally observed, all of them corresponding to pyranoside forms. This work opened the door to a series of rotational studies on monosaccharides in the following years, both by our group[13,14] and by other groups.[15,16,17] In all of those studies, pentoses (n=5) and hexoses (n=6) took on the shape of six-membered rings (pyranoses). Whereas pyranoses are the most common active forms in polysaccharides as energy storage units (for example, starch is a branched polymer of glucopyranose units) or structural scaffolds (cellulose is a β-1→4 linear polymer of glucopyranose units), in other cases, the active biological forms are furanoses. For instance, the active form of monosaccharides (in particular, 2-deoxyribose and ribose) in DNA/RNA are furanose forms. In 2016, our group presented the first rotational study of a monosaccharide in furanosic form, methyl β-D-ribofuranose, the active sugar in RNA.[18] That study was possible thanks to the combination of chemical synthesis and microwave spectroscopy. To be more specific, the OH group in position 1' was substituted with an OMe group. This step was crucial to stabilize the furanose ring. We observed two different conformers in the gas phase, both of them displaying a $^3T_2$ conformation of the ring.

In this chapter, we focus on the active form of the monosaccharide in the DNA, by performing the structural analysis of methyl 2-deoxy-D-ribofuranoside (see Figure **VIII**.2 for chemical structure). Although only the β anomer is present in DNA, we will perform the study of both anomers, with the aim of comparing both forms. Moreover, we will contrast the results obtained in the gas phase with NMR studies in solution performed by Dr. Francisco Corzana at the Universidad de La Rioja. This will allow us to assess the effect of the solvent on the structure of this important biomolecule. Finally, the comparison with the results reported in reference 18 enables us to evaluate the effect of removing the OH group in position 2' in 2-deoxy-ribofuranoside.
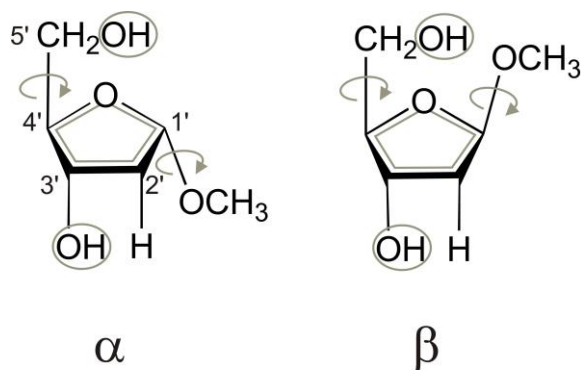
Figure VIII.2 Chemical structure of α and β anomers of methyl 2-deoxy-D-ribofuranoside, along with the main structural degrees of freedom (in gray, see text for further explanation).

VIII.2   Experimental section

The α and β anomers of methyl 2-deoxy-D-ribofuranoside were synthesized by the group of Professor Benjamin G. Davis at the University of Oxford, using similar synthetic strategies as used in previous studies.[18] Both samples (α and β) had a syrup-like consistency. In order to take them into the gas phase, they were heated in a customized heating nozzle. Table VIII.1 summarizes the experimental conditions used for the rotational study of both samples in the CP-FTMW spectrometer.

Table VIII.1 Experimental conditions for CP-FTMW spectra of the two anomers of methyl 2-deoxy-D-ribofuranoside.

Experimental conditions	α	β
Number of nozzles	2	3
Nozzle temperature	145ºC	145ºC
Carrier gas	He	He
Number of chirps/molecular pulse	30	30
Total number of cycles	~20 million	~40 million

VIII.3 Results

VIII.3.1 Theoretical calculations

a. Predicted conformations

Methyl 2-deoxy-D-ribofuranoside is a five-membered ring monosaccharide and, as such, it shares the conformational degrees of freedom of other furanosides previously studied.[18] In particular, the most important points to consider when describing the conformations of furanosides are (see Figure VIII.2):

- The hydroxymethyl group may adopt three different positions. In this chapter, we identify each position with two indices ("$X_1 X_2$"). X_1 refers to the O5'C5'C4'O4' dihedral angle while X_2 refers to O5'C5'C4'C3'. X_1 and X_2 can adopt two values: either G (Gauche, ±60°) or A (Anti, 180°). The three different positions of the hydroxymethyl group in this case are GG, GA and AG. See Figure VIII.3 for a graphical explanation using Newman's projections.

- Rotation along the bond connecting the methoxy group to the ring. In most of the conformations, the methyl group is pointing outwards from the molecule, in accordance with the exo-anomeric effect.

- The furanose ring may adopt different Twist (T) or envelope (E) conformations, preferably.

- Intramolecular interactions; in particular intramolecular hydrogen bonds arising from the two OH groups in the molecules.
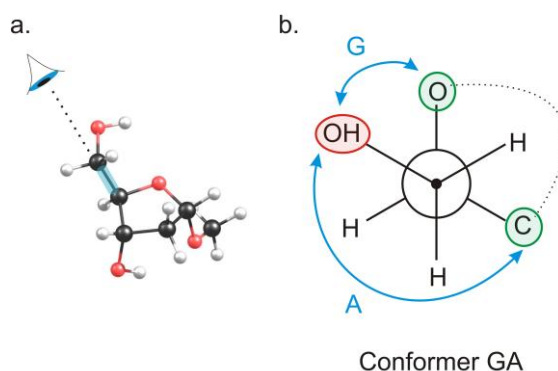

Conformer GA

Figure VIII.3 Visual representation of G and A nomenclature in methyl 2-deoxy-D-ribofuranoside. a. Highlighted in blue, chemical bond along which we will look at the molecule. b. Newman projection explaining Gauche (G) or Anti (A) dispositions of the OH group with respect to the two other groups. For the sake of simplicity, the rest of the molecule has been replaced by a dotted line.

The conformational search (using different force fields: MMFFs, OPLS and AMBER in a 20 kJ/mol energy window) followed by geometry optimizations at MP2 and B3LYP-D3/6-311++G(d,p) yielded 19 structures for the α anomer and 37 for the β. The high number of conformers predicted is proof of the flexibility of these systems, resulting from the interplay of the different degrees of freedom mentioned above. The predictions of the most relevant spectroscopic parameters of these conformations are summarized in Tables VIII.2 and VIII.3 for the ten lowest-lying structures. A full recollection of all conformers can be found in in the appendix.

Table VIII.2 Computed spectroscopic parameters for the lowest lying conformers of methyl 2-deoxy-α-D-ribofuranoside (MP2/B3LYP-D3 level of theory, with the 6-311++G(d,p) basis set)

			A	*B*	*C*	$|\mu_b|$	$|\mu_b|$	$|\mu_c|$	ΔE+ZPE	ΔG
α1	GG	$^2T_1$	2059/2050	1031/1011	871/854	1.8/1.7	2.3/2.2	0.0/0.0	0.0/0.0	0.0/0.0
α2	GA	$^2T_1$	1870/1873	1040/1014	817/799	2.0/1.9	1.1/1.0	1.9/2.0	3.3/2.6	2.8/2.0
α3	GG	^2E	2161/2149	1009/989	870/853	0.9/1.0	2.4/2.3	0.2/0.2	6.0/6.3	5.2/5.5
α4	AG	^2E	2335/2338	899/882	792/777	1.8/1.7	2.2/2.1	0.1/0.1	9.8/8.5	8.7/7.9
α5	AG	^2E	2360/2348	903/887	794/780	0.3/0.2	2.9/2.7	1.9/2.0	10.6/10.3	8.4/9.2
α6	GG	^2E	*/2147	*/979	*/845	*/0.1	*/0.3	*/0.1	*/11.4	*/10.7
α7	AG	$^2T_1$	2242/2268	909/886	800/780	2.2/2.0	0.6/0.5	1.8/1.9	12.7/10.7	11.2/9.2
α8	GG	E_1	1937/*	1028/*	844/*	1.1/*	0.0/*	1.0/*	13.0/*	9.9/*
α9	GG	E_4	1905/1899	984/964	753/739	1.3/1.3	0.4/0.5	1.2/1.3	13.9/12.4	9.7/8.3
α10	GG	E_4	1913/1911	977/956	738/725	0.7/0.6	0.8/0.8	0.4/0.5	14.0/12.4	10.6/8.9

*These conformers are not found as local minima with the given theoretical method. The optimization leads to another conformation

Table VIII.3 Computed spectroscopic parameters for the lowest lying conformers of methyl 2-deoxy-β-D-ribofuranoside (MP2/B3LYP-D3 level of theory, with the 6-311++G(d,p) basis set)

			A	B	C	$|\mu_b|$	$|\mu_b|$	$|\mu_c|$	$\Delta E+ZPE$	ΔG
β1	GG	^4E	1898/1892	1156/1137	924/907	1.8/1.7	1.6/1.6	1.3/1.4	0.0/0.0	2.4/0.0
β2	GG	^4E	1897/1898	1156/1134	920/902	0.0/0.1	0.1/0.1	1.4/1.1	1.5/1.7	3.0/0.9
β3	GG	^4E	1906/1907	1150/1128	918/901	0.4/0.3	1.6/1.6	0.5/0.6	1.8/2.1	3.3/1.1
β4	GG	$^3T_2$	1766/*	1166/*	854/*	1.2/*	1.7/*	0.1/*	2.4/*	0.0/*
β5	AG	E_2	1997/2019	1010/972	788/760	0.6/0.4	2.8/2.7	0.6/0.6	3.8/7.0	1.9/3.1
β6	GA	$^1T_2$	1481/1473	1274/1245	797/779	1.8/1.8	2.9/2.8	0.9/0.9	5.5/7.9	3.2/3.1
β7	GA	$^4T_3$	1664/1644	1207/1191	832/815	1.0/1.0	2.2/2.2	0.0/0.1	6.3/9.0	6.0/6.4
β8	GA	$^1T_2$	1474/1468	1283/1256	798/781	1.0/0.9	1.1/1.1	0.9/0.9	6.7/8.4	4.2/2.6
β9	GG	E_2	1754/*	1169/*	855/*	1.4/*	1.8/*	2.7/*	6.7/*	5.2/*
β10	AG	E_2	1979/2039	1003/952	781/748	0.4/0.3	1.5/1.5	1.1/1.1	6.9/8.8	3.6/4.7

*These conformers are not found as local minima with the given theoretical method. The optimization leads to another conformation

b. Barriers to internal rotation of the methyl top

Methyl 2-deoxy-D-ribofuranoside possesses a methyl top that is subject to produce splittings in its rotational spectrum due to coupling of the internal rotation with the overall rotation of the molecule. We estimate the barriers for internal rotation of the methyl top by performing a relaxed scan at MP2/6-311++G(d,p) in steps of 10° on the observed conformers of the α and β anomers of this species (see later). The results are shown in Tables VIII.4 and VIII.5.

Table VIII.4 Calculated methyl internal rotation barriers of the observed conformers of methyl 2-deoxy-α-D-ribofuranoside at MP2/6-311++G(d, p) level of theory.

	α1	α2
V_3/kJ mol^{-1}	7.6	7.7

Table VIII.5 Calculated methyl internal rotation barriers of the observed conformers of methyl 2-deoxy-β-D-ribofuranoside at MP2/6-311++G(d, p) level of theory.

	β1	β5	β6
V_3/kJ mol^{-1}	7.6	8.1	7.4

c. Cremer Pople analysis

In order to assess what kind of Twist (T) or Envelope (E) form the different conformations adopt, we performed a Cremer-Pople analysis on each one of them (see section III.5 for an explanation of Cremer-Pople analysis). Each predicted conformer was assigned to its corresponding T or E form (see Tables VIII.2 and VIII.3). For a detailed collection of the values of q and φ, see Tables VIII.A.3 and VIII.A.4 in the appendix.

VIII.3.2 Spectroscopic analysis

a. CP-FTMW spectrum

First, the rotational spectrum of methyl 2-deoxy-α-D-ribofuranoside in the 6-18 GHz region was collected by heating the sample at 145°C. Figure **VIII.**4 displays an overview of the rotational spectrum. There was around 600 rotational lines with a signal-to-noise ratio greater than 2/1. Two sets of independent rotational transitions were spotted and fitted to two semi-rigid rotor Hamiltonian in the S-reduction. These fits allowed for the determination of the A, B and C rotational constants as well as several centrifugal distortion constants. Table **VIII.**6 collects the experimental data. Tables VIII.A.5 and VIII.A.6 in the appendix show all measured rotational transitions. Comparison with theoretical calculations allow for the assignment of these two structures to conformers α1 and α2, the lowest lying predicted conformations. Figure **VIII.**4 also displays a zoom of the 9000 MHz region of the spectrum where lines from both conformations are observed. The rotational transitions of the methyl 2-deoxy-α-D-ribofuranoside do not display internal rotation splittings, which means that the barrier for internal rotation of the methyl top is too high to induce observable splittings. This might be consistent with the estimated barriers of 7.6 and 7.7 kJ/mol for α1 and α2, respectively (see Tables **VIII.**4 and **VIII.**5). The signal-to-noise ratio of the most intense transition in the spectrum (5 1 5 ← 4 1 4 for the α1 conformer) was 500/1. This encouraged us to look for rotational transitions arising from isotopologues of methyl 2-deoxy-α-D-ribofuranoside in natural abundance. In fact, we could observe the rotational spectra of isotopologues with ^{13}C monosubstitution in natural abundance for the most abundant conformer (α1). Six isotopologues were observed in the spectrum and Table **VIII.**7 summarizes the corresponding fits. Tables VIII.A.7 to VIII.A.12 in the appendix collect all experimental for transitions for the various isotopologue species.
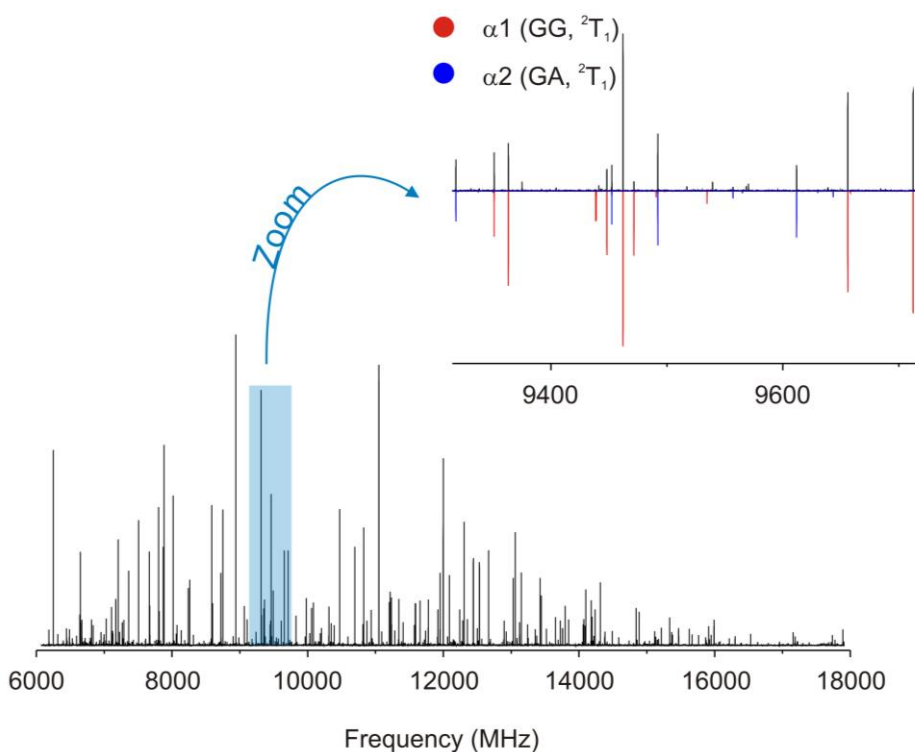
Figure VIII.4 Overview of the CP-FTMW rotational spectrum of methyl 2-deoxy-α-D-ribofuranoside in the 6-18 GHz region, with a zoomed view around the 9000 MHz region where lines arising from both observed conformers are visible.

Table VIII.6 Experimental spectroscopic parameters of methyl 2-deoxy-α-D-ribofuranoside and comparison with theoretical predictions at MP2/6-311++G(d,p) level.

	α1		α2	
	Exp.	MP2	Exp.	MP2
A/MHz	2056.39188 (60)	2059	1882.30839 (76)	1870
B/MHz	1019.67311 (21)	1031	1024.81006 (26)	1040
C/MHz	860.52781 (23)	871	804.74073 (31)	817
D_J/kHz	0.0797 (18)	0.0812	0.0728 (25)	0.1125
D_{JK}/kHz	0.0989 (92)	0.0721		
D_K/kHz	0.476 (17)	0.459	0.729 (43)	1.005
$\|\mu_a\|$/D	Observed	1.8	Observed	2.0
$\|\mu_b\|$/D	Observed	2.3	Observed	1.1
$\|\mu_c\|$/D	Not Observed	0.0	Observed	1.9
N	95		99	
σ/kHz	8.2		9.3	

Table VIII.7 Experimental rotational constants of all observed isotopologues of methyl 2-deoxy-α-D-ribofuranoside.

	¹³C1′	¹³C2′	¹³C3′
A/MHz	2049.2702 (13)	2037.8316 (15)	2043.8605 (19)
B/MHz	1016.90711 (86)	1015.84909 (51)	1019.06461 (99)
C/MHz	858.93148 (39)	859.89773 (24)	857.92522 (37)
N	16	15	13
σ/kHz	9.4	6.2	10.7
	¹³C4′	¹³C5′	¹³C1″
A/MHz	2051.7887 (11)	2049.3594 (11)	2045.3385 (17)
B/MHz	1017.27447 (89)	1008.34291 (44)	1002.97315 (75)
C/MHz	859.65333 (40)	852.99240 (24)	847.49558 (35)
N	16	18	16
σ/kHz	10.2	6.2	8.2

We followed a similar procedure for the rotational analysis of methyl 2-deoxy-β-D-ribofuranoside. Figure VIII.5 displays the rotational spectrum of this sample in the 6 to 18 GHz region, which has 1800 lines with a signal-to-noise ratio greater than 2/1. In this case, there are rotational transitions arising from three different conformations. Table VIII.8 collects the values of the experimental rotational and centrifugal distortion constants (see Tables VIII.A.13 to VIII.A.15 in the appendix for a complete list of the measured rotational lines). Comparison between theoretical and experimental values of A, B, C allow for the assignment of these three species to conformers β1, β5 and β6. In the Discussion section, we will give more details about the assignment of these three conformations. Similarly to the α anomer, rotational transitions do not possess hyperfine splittings, consistently with V_3 barriers of 7.6, 8.1 and 7.4 kJ/mol for β1, β5 and β6, respectively (see Table VIII.5). The signal-to-noise ratio of the most intense transition (5 1 5 ← 4 1 4 for the β1 conformer) was 1200/1 and, in this case, we were also able to observe ¹³C monoisotopologues in natural abundance of the most abundant species (β1). Experimental rotational constants of all observed isotopologues are summarized in Table VIII.9 and a full list of the observed rotational transitions of the isotopologues can be found in Tables VIII.A.16 to VIII.A.21 in the appendix.
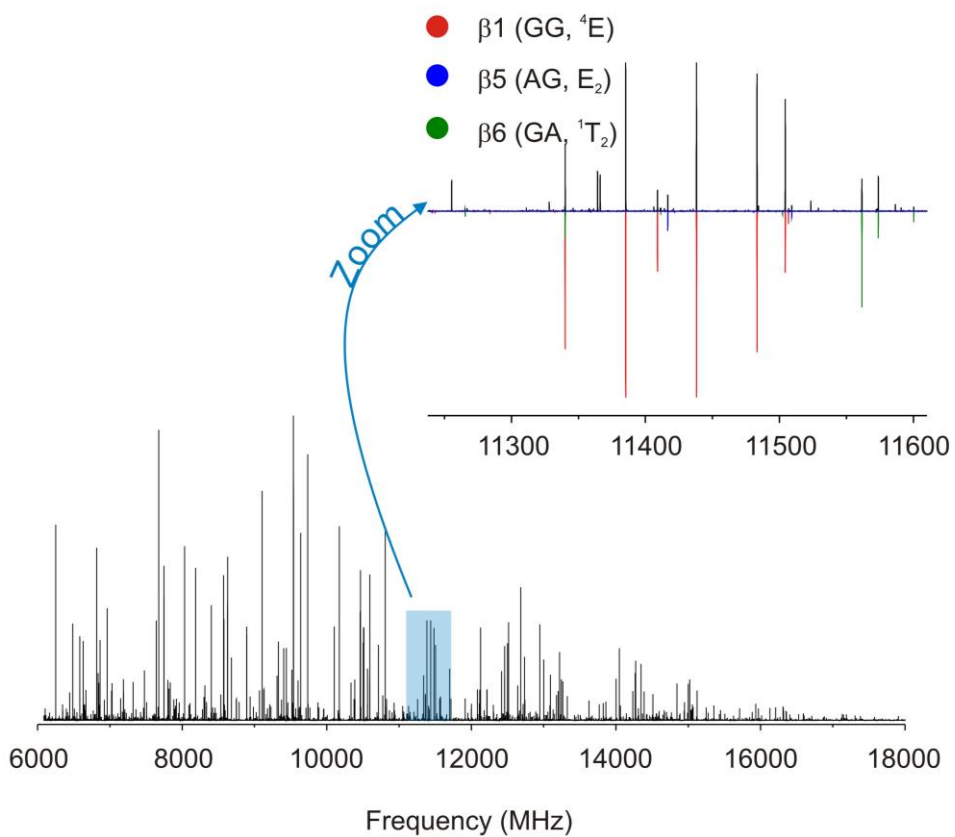
Figure VIII.5 Overview of the CP-FTMW rotational spectrum of methyl 2-deoxy-β-D-ribofuranoside in the 6-18 GHz region, with a zoomed view around the 11500 MHz region where lines arising from the three observed conformers are visible.

Table VIII.8 Experimental spectroscopic parameters of
methyl 2-deoxy-β-D-ribofuranoside and comparison with theoretical predictions at
MP2/6-311++G(d,p) level.

	β1		β5		β6	
	Exp.	MP2	Exp.	MP2	Exp.	MP2
A/MHz	1890.65747(49)	1898	1999.87647(81)	1997	1481.77004(72)	1481
B/MHz	1145.05589(21)	1156	991.81629(38)	1010	1256.10078(60)	1274
C/MHz	910.72056(22)	924	771.18931(31)	788	784.89436(42)	797
D_J/kHz	0.0563(21)	0.0603	0.3791(26)	0.3116	0.3203(78)	0.6722
D_{JK}/kHz	0.438(12)	0.372	-1.956(17)	-1.429	1.898(33)	0.5035
D_K/kHz			4.121(39)	2.976	-2.130(29)	-1.075
d_1/kHz			-0.1087(16)	-0.0892	-0.0972(37)	0.03035
d_2/MHz					-1.207(19)	0.2122
$|\mu_a|$/D	Observed	1.8	Observed	0.6	Observed	1.8
$|\mu_b|$/D	Observed	1.6	Observed	2.8	Observed	2.9
$|\mu_c|$/D	Observed	1.3	Observed	0.6	Observed	0.9
N	140		52		86	
σ/kHz	10.5		6.7		7.4	

Table VIII.9 Experimental rotational constants of all observed isotopologues of
methyl 2-deoxy-β-D-ribofuranoside.

	$^{13}C1'$	$^{13}C2'$	$^{13}C3'$
A/MHz	1882.83837(88)	1876.38801(88)	1889.4699(10)
B/MHz	1144.17523(27)	1141.43664(49)	1137.98292(63)
C/MHz	908.33842(31)	908.93586(32)	906.46917(36)
N	35	36	30
σ/kHz	8.9	9.9	10.6
	$^{13}C4'$	$^{13}C5'$	$^{13}C1''$
A/MHz	1884.4565(10)	1863.4550(10)	1887.27572(78)
B/MHz	1141.54673(52)	1144.31271(45)	1123.50991(36)
C/MHz	908.96044(30)	904.50980(24)	896.66275(26)
N	36	30	43
σ/kHz	10.4	7.5	9.7

b.   Molecular Dynamics (MD) simulations in water

In order to study the conformational preferences of methyl 2-deoxy-α-D-ribofuranoside and methyl 2-deoxy-β-D-ribofuranoside in water, these compounds were subjected to extensive 1 µs MD simulations in explicit water.

The protocol employed in this type of simulations was as follows. The starting structure (α- or β-anomer) was immersed in a water box with a 10 Å buffer of TIP3P[19] water molecules using the AMBER 16 package. [20] The simulations were performed using GLYCAM06 force field to properly reproduce the conformational behavior of these carbohydrates.[21] A two-stage geometry optimization approach was performed. The first stage minimizes only the positions of solvent molecules and the second stage is an unrestrained minimization of all the atoms in the simulation cell. The systems were then gently heated by incrementing the temperature from 0 to 300 K under a constant pressure of 1 atm and periodic boundary conditions. Harmonic restraints of 30 kcal·mol^{-1} were applied to the solute, and the Andersen temperature coupling scheme[22] was used to control and equalize the temperature. The time step was kept at 1 fs during the heating stages, allowing potential inhomogeneities to self-adjust. Water molecules are treated with the SHAKE algorithm such that the angle between the hydrogen atoms is kept fixed. Long-range electrostatic effects are modelled using the particle-mesh-Ewald method.[23] A cutoff of 8 Å was applied to Lennard-Jones and electrostatic interactions. Each system was equilibrated for 2 ns with a 2 fs time step at a constant volume and temperature of 300 K. Production trajectories were then run for additional 1 µs under the same simulation conditions.

VIII.4 Discussion

In this work, we probed the conformational landscape under isolation conditions of the monosaccharide present in the DNA: 2-deoxy-ribofuranoside. By performing a methylation on the OH group at position 1', the group of Professor Benjamin G. Davis achieved the chemical synthesis of both α and β anomers separately. This process of methylation is crucial in separating the anomers because, when the monosaccharide is in its "free" form (not methylated), mutarotation occurs, meaning that there is an interconversion between both anomers. Furthermore, mutarotation could also lead to pyranoside forms, which are not desirable in this case.

By means of rotational spectroscopy coupled with supersonic expansions, we have determined that methyl 2-deoxy-α-D-ribofuranoside adopts preferably two conformations in the gas phase, α1 and α2. According to the nomenclature summarized in Figure VIII.3, α1 and α2 correspond to GG and GA configurations of the methoxy group, respectively. The corresponding AG structure (α4) is not observed experimentally. It is predicted higher in energy ($\Delta(E+ZPE)=9.8$ kJ/mol) and the non-observation of this species could probably be explained by the lack of population of this conformation. It is worth noting that both observed conformers (α1 and α2) share the same configuration of the five-membered ring ($^2T_1$) and an intramolecular hydrogen bond O3'H3'···O1'. Figure VIII.6 summarizes interconversion paths between conformers that are directly related (through a rotation of the OH group at the methoxy moiety) to the observed species and to α4. We chose B3LYP-D3/6-311++G(d,p) level of theory for the estimation of interconversion barriers because it provides acceptable results at low computational cost. It is noteworthy that the next lowest-lying species after the two observed conformers is α3 and it is predicted at 6.3 kJ/mol ($\Delta(E+ZPE)$) above the global minimum. According to this energetic criterion, one could think that this species may be observed in the rotational spectrum. However, the interconversion barrier to the global minimum (α1) is estimated at 0.9 kJ/mol, and therefore, α3 can relax to α1 and it is not observed experimentally.
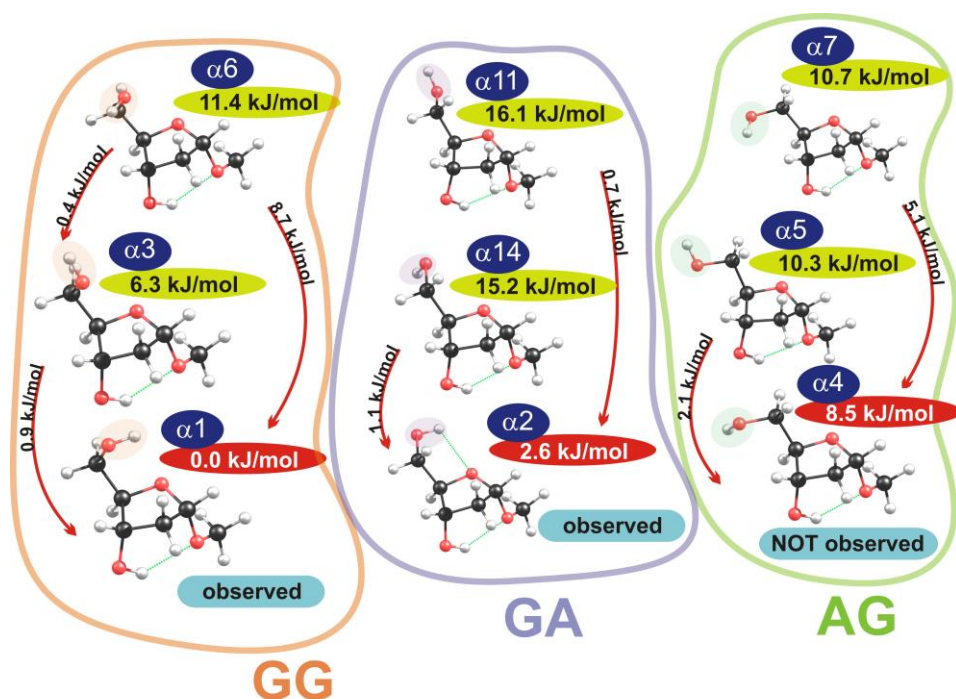
Figure VIII.6 Summary of interconversion paths between the lowest lying conformers of methyl 2-deoxy-α-D-ribofuranoside

Regarding methyl 2-deoxy-β-D-ribofuranoside, we have identified three different conformations in our rotational spectrum: β1, β5 and β6, which correspond to GG, AG and GA conformations, respectively. In the AG and GA conformations, the five-membered ring adopts similar configurations (distorted E_2 and $^1T_2$ forms, respectively). However, it is very interesting to note that in the GG conformations (β1), the furanose ring adopts a distorted ^4E form. This is probably due to the fact that in the GG form, there seems to be a strong O5'H5'···O1' interaction, that is not present in the other observed conformations. This hydrogen bond seems to pull atom C4' upwards and therefore, it stands above the plane formed by the other four atoms in the ring. In analogy to the α anomer, we have calculated some interconversion barriers that relate conformations related to the observed structures in a direct way. In the GG and GA configurations, the hydroxy group in the hydroxymethyl moiety is involved in an intramolecular interactions and its position is quite fixed. Therefore, the only degree of freedom available is the disposition of the hydroxyl group in position 3'. Figure VIII.7 displays all conformers arising from the rotation of the OH group at position 3' and the barriers to interconversion between them for conformers β1 and β6. This is particularly relevant in the case of the GG conformer (β1) because the two structures arising from OH3' rotation are quite low in energy (1.5 and 2.0 kJ/mol respectively) and their non-observation can only be explained by a relaxation to the global minimum. In conformer β5 (the one that is AG), on the other hand, the OH group in the hydroxymethyl moiety is not tightly involved in a hydrogen bond and, hence, there are

more possibilities available by varying the orientation of both OH groups in the molecule (see Figure VIII.7).
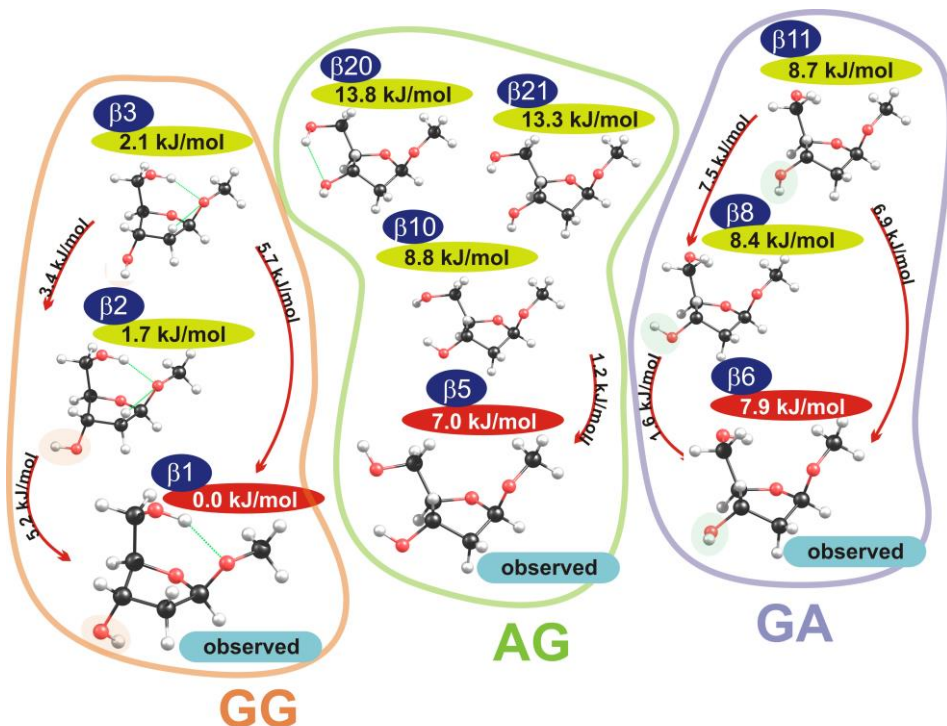

Figure VIII.7 Summary of interconversion paths between the lowest lying conformers of methyl 2-deoxy-β-D-ribofuranoside

Finally, there is one last point to consider about the observed conformers of the β anomer and the comparison with ab initio results. In MP2 calculations, there is one conformation (β4) that is predicted very low in energy (Δ(E+ZPE)=2.4 kJ/mol) but it is not observed experimentally. In fact, it is predicted to be the global minimum when considering ΔG estimations. β4 is a GG conformation but it does not possess a O5'H5'···O1' interaction like β1. Instead, the OH group in position 5' is pointing towards O4' (the oxygen in the ring). Therefore, the ring adopts a distorted $^3T_2$ form, instead of the ^4E form in β1 (where the intramolecular interaction pulls atom C4' up). Moreover, it is worth noting that B3LYP-D3 optimizations do not lead to this structure. When starting from this geometry, the optimization leads to the β1 conformer. This could mean that MP2 overestimates the strength of the O5'H5'···O4' interaction, and predicts β4 conformation more stable than it really is.

By analyzing relative intensities of rotational lines (taking into account the dipole moments), we could estimate the population ratio between the different observed conformers. Tables VIII.10 and VIII.11 compare experimental results for both α and β anomers with the theoretical values calculated with B3LYP-D3 method (based on ΔG at

418K). We do not choose MP2 as the reference method because the issue with the β4 structure that we have just mentioned may jeopardize the calculation of population ratios. Regarding the α anomer, we can observe that the experimental ratio α1/α2 is 4(2)/1. Theory predicts that this value is 1.8/1. This value increases to 2.1/1 if we consider conformer relaxation. In the case of the β anomer, our experimental estimations show that β1 is the global minimum. β5 and β6 are much less populated, the population ratios with respect to β1 being 26(13)/1 and 27(18)/1 respectively. This is in contrast with the calculated values with B3LYP-D3, which estimate population ratios for both conformers to be 2.4/1; this value being 3.2/1 and 2.0/1 for β5 and β6, respectively, when we consider conformer relaxation. While there is an agreement between theory and experiment in population ratios for the α anomer, it is clear that this is not the case for the β anomer. The conformational landscape of the β anomer is probably more complicated than the α, especially if we consider that there might be a competition in H-bonding between O5'H5'⋯O4' and O5'H5'⋯O1'. This might result in a struggle of the theoretical methods to predict relative energies of the different conformations and explain the difference between theory and experiment.

Table VIII.10 Experimental and predicted population ratios of the observed conformers of methyl 2-deoxy-α-D-ribofuranoside

Experimental	Predicted	Predicted
$\dfrac{N_{\alpha 1}}{N_{\alpha 2}}$	$\dfrac{N_{\alpha 1}}{N_{\alpha 2}}$	$\dfrac{N_{\alpha 1}+N_{\alpha 3}+N_{\alpha 6}}{N_{\alpha 2}+N_{\alpha 11}+N_{\alpha 14}}$
4(2)	1.8	2.1

Table VIII.11 Experimental and predicted population ratios of the observed conformers of methyl 2-deoxy-β-D-ribofuranoside

Experimental	Predicted	Predicted
$\dfrac{N_{\beta 1}}{N_{\beta 5}}$	$\dfrac{N_{\beta 1}}{N_{\beta 5}}$	$\dfrac{N_{\beta 1}+N_{\beta 2}+N_{\beta 3}}{N_{\beta 5}+N_{\beta 10}+N_{\beta 20}+N_{\beta 21}}$
26(13)	2.4	3.2
Experimental	Predicted	Predicted
$\dfrac{N_{\beta 1}}{N_{\beta 6}}$	$\dfrac{N_{\beta 1}}{N_{\beta 6}}$	$\dfrac{N_{\beta 1}+N_{\beta 2}+N_{\beta 3}}{N_{\beta 6}+N_{\beta 8}+N_{\beta 11}}$
27(18)	2.4	2.0

The results presented in this Chapter about methyl 2-deoxy-β-D-ribofuranoside are directly comparable to those obtained by our group about methyl β-D-ribofuranoside (active form in RNA) in 2016.[18] By comparing the conformations obtained in that study with those presented here about the β anomer, we can assess the effects of removal of the OH group in position 2'. In reference 18, the authors report the observation of two conformations of methyl β-D-ribofuranoside in the gas phase. The most stable one corresponds to a GG conformation, while the other one (lying 0.8 kJ/mol higher in energy) corresponds to an AG form (no GA structure was observed). Both of them display a $^3T_2$ configuration of the five-membered ring. Figure VIII.8 shows the two conformations, along with the observed conformations of methyl 2-deoxy-β-D-ribofuranoside (β1, β5 and β6) and β4. It is interesting to see that the AG conformations (both in the ribofuranoside and in the deoxyribofuranoside) are analogous; in both of them, the OH group in position 3' is pointing towards OH5'. However, the GG conformations observed in both cases (in this work and in reference 18) are not equivalent. As it has been mentioned earlier, in the case of methyl 2-deoxy-β-D-ribofuranoside (this work), the GG conformation is "dominated" by an O5'H5'···O1' that forces the ring to adopt a ^4E conformation. However, this is not the case in the ribofuranose form, where the GG conformation displays an O5'H5'···O4' hydrogen bond (that is, the OH group in position 5' is pointing towards the atom in the ring) and the ring adopt a distorted $^3T_2$ shape. In fact, this conformation is quite analogous to conformer β4 in this work, the one that was mentioned before. To sum up, there is a competition between two intramolecular hydrogen bonds (O5'H5'···O1' and O5'H5'···O4') and the removal of the OH group in position 2' tips the balance in favor of O5'H5'···O1'.
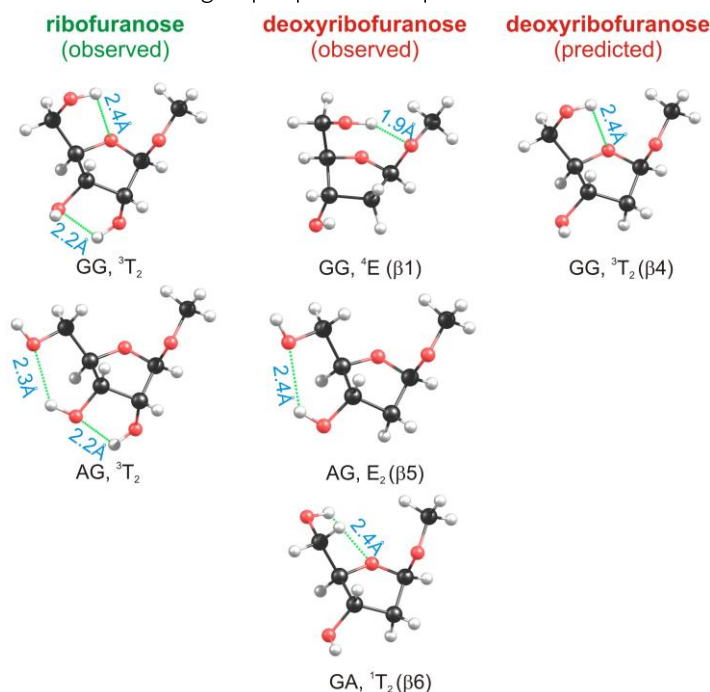

Figure VIII.8 Observed conformations of the β anomer of ribofuranose (reference 18) and 2-deoxy-ribofuranose (this work), along with the predicted β4 conformation

Furthermore, the work presented here offers the opportunity for comparing the conformations and intramolecular hydrogen bond patterns of the α and β anomers of methyl 2-deoxy-D-ribofuranoside. It is worth reminding that it is the β anomer the one that is present in the DNA. The most relevant difference between the observed conformations of the α and the β forms is that, in all the α conformations, there is a O3'H3'···O1' intramolecular hydrogen bond that is "locking" the OH3' group. This is not the case for the β conformations, where the OH3' group is "free", meaning that it is not taking part in any intramolecular hydrogen bond. The OH3' group in deoxyribose is very relevant in the DNA, since it is in that position that the next nucleotide is attached. The fact that, in the β anomer, the OH3' group is "free" (while it is "locked" in the α) could help explain why it is the β anomer the one present in DNA. Nevertheless, it is beyond doubt that this is a tentative hypothesis that needs further investigation.

Concerning the conformational preferences of these molecules in solution, the MD simulations indicate that they present a high degree of flexibility in water. Figure VIII.9 shows the theoretical ensembles derived from the MD simulations, together with the root-mean-square deviation (rmsd) values for the heavy atoms. 500000 structures were derived from these simulations for each anomer. As can be seen, the glycosidic linkage is rather rigid in both compounds, with values for the φ torsional angle (O4'-C1'-O1'-C1'') close to 60° or –60 for the α-or β-anomer, respectively, which is in accordance with the exoanomeric effect. [24] With regard to the conformational preferences of the hydroxymethyl group, the calculations indicate that this group is quite flexible in solution, adopting the three lowest energy staggered rotamers (GG, GA and AG, with GG and GA being more populated) in both anomers. Of note, no significant intramolecular hydrogen bonds are detected in solution, with a population ‹10% in all cases.
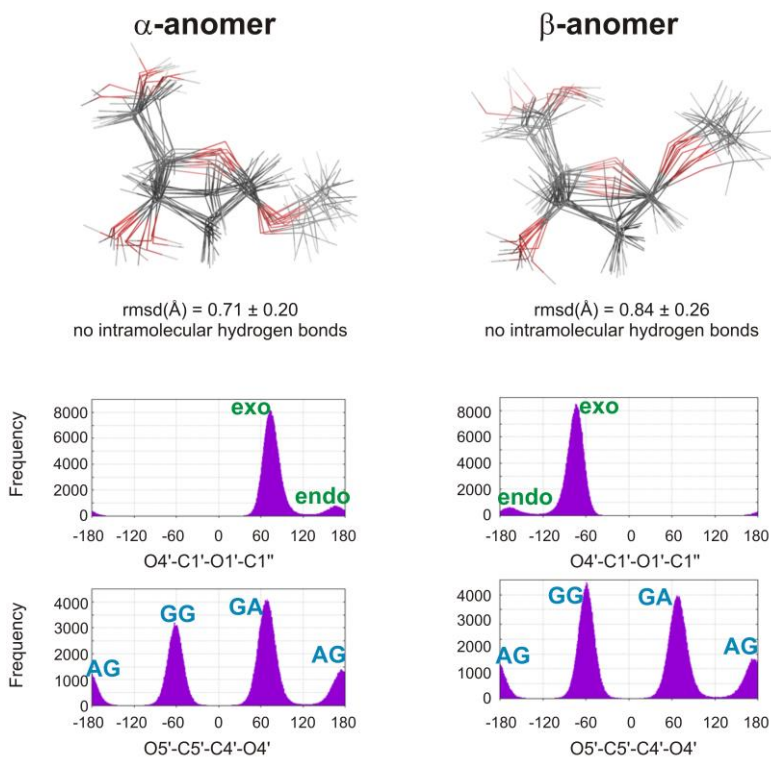
Figure VIII.9 Theoretical molecular ensembles from MD calculations. In the lower part, frequency counts as a function of the dihedral angles O4'-C1'-O1'-C1'' (conformations corresponding to exo- and endo-anomeric effect are labeled) and O5'-C5'-C4'-O4' (with conformations GG, GA and AG).

We then investigated the first hydration shell of both monosaccharides. Notably, the α-anomer can accommodate a higher number of water molecules around it (19 water molecules in comparison to 15 waters for the β-anomer). This different behavior can be visualized in the first hydration shell for both molecules derived from the MD simulations (see Figure VIII.10). As expected, the most hydrophobic parts of the molecules involve the C2' and the methyl group at the anomeric position.
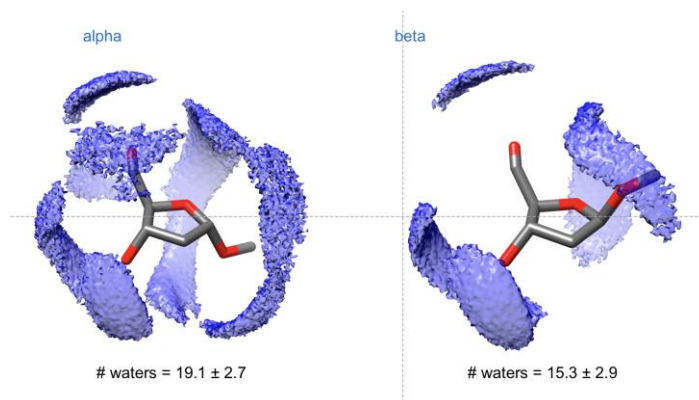
Figure VIII.10 Results of the first hydration shell calculations for both anomers of methyl 2-deoxy-D-ribofuranoside

Figure VIII.11 shows the Cremer–Pople distribution of all the structures calculated with MD simulations for both anomers. The puckering analysis indicates that while the $^2T_1$ and ^2E conformers are the most populated in water for the α-anomer, the E_2 and $^3T_2$ are the main conformer for the β-anomer. Figures VIII.12 and VIII.13 display the Cremer-Pople wheels for both anomers in the gas phase (observed and calculated structures). It is interesting to note the ^4E conformations of the β anomer (which was the global in our gas phase experiment) is irrelevant in solution. As it has been pointed out earlier, the ^4E conformation is driven by an intramolecular bond, which is inexistent in aqueous solution. Hence, this puckering conformation is not much populated in solution.
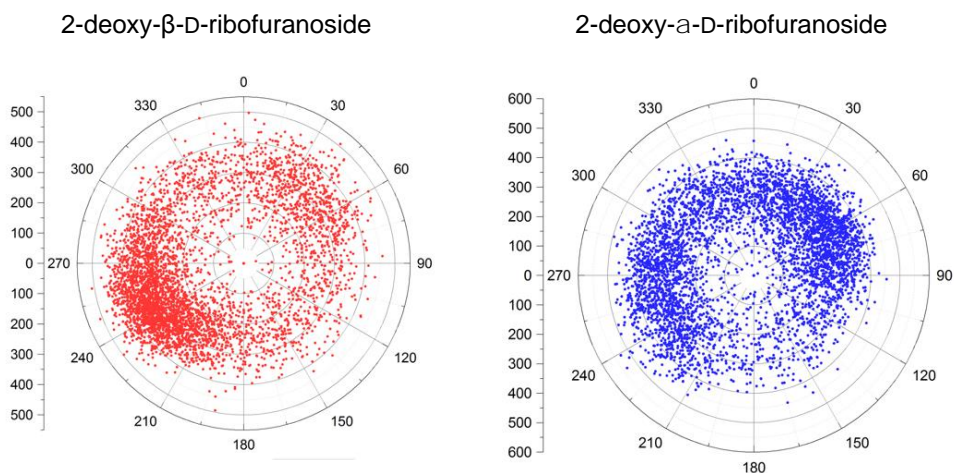
Figure VIII.11 Cremer-Pople wheels for both anomers of methyl 2-deoxy-D-ribofuranoside in aqueous solution.

Figure VIII.12 Cremer-Pople wheel for methyl 2-deoxy-α-D-ribofuranoside in the gas phase. Dark blue crosses represent predicted conformations (MP2) while light blue points are the observed conformers

Figure VIII.13 Cremer-Pople wheel for methyl 2-deoxy-β-D-ribofuranoside in the gas phase. Dark blue crosses represent predicted conformations (MP2) while light blue points are the observed conformers. Green points represent the two observed conformations of methyl β-D-ribofuranoside in reference 18.

This study in solution is somehow in good agreement with that previously reported by Dowd and co-workers,[25] which experimentally found by NMR a 71% of ^2E conformer in solution for the α-anomer and a 59% of $^3T_2$ puckering for the β derivative. The next step in our research, and out of the scope of this work, will involve the use of experiment-guided MD simulations, using as restraints the experimental coupling constant, previously determined by NMR.

VIII.5 References

[1] A. Canales, I. Boos, L. Perkams, L. Karst, T. Luber, T. Karagiannis, G. Domínguez, F. J. Cañada, J. Pérez-Castells, D. Häussinger, C. Unverzagt, J. Jiménez-Barbero, *Angew. Chem. Int. Edit.* **2017**, *56*, 14987-14991.

[2] K. Kato, T. Yamaguchi, *Glycoconjugate J.* **2015**, *32*, 505-513.

[3] J. O. Duus, C. H. Gotfredsen, K. Bock, *Chem. Rev.* **2000**, *100*, 4589-4614.

[4] F. O. Talbot, J. P. Simons, *Phys. Chem. Chem. Phys.* **2002**, *4*, 3562-3565.

[5] R. A. Jockusch, R. T. Kroemer, F. O. Talbot, J. P. Simons, *J. Chem. Phys. A* **2003**, *107*, 10725-10732.

[6] R. A. Jockusch, F. O. Talbot, J. P. Simons, *Phys. Chem. Chem. Phys.* **2003**, *5*, 1502-1507.

[7] E. J. Cocinero, E. C. Stanca-Kaposta, E. M. Scanlan, D. P. Gamblin, B. G. Davis, J. P. Simons, *Chem. Eur. J.* **2008**, *14*, 8947-8955.

[8] C. S. Barry, E. J. Cocinero, P. Çarçabal, D. P. Gamblin, E. C. Stanca-Kaposta, S. M. Remmert, M. C. Fernández-Alonso, S. Rudic, J. P. Simons, B. G. Davis, *J. Am. Chem. Soc.* **2013**, *135*, 16895-16903.

[9] E. C. Stanca-Kaposta, D. P. Gamblin, E. J. Cocinero, J. Frey, R. T. Kroemer, A. J. Fairbanks, B. J. Davis, J. P. Simons, *J. Am. Chem. Soc.* **2008**, *130*, 10691-10696.

[10] J. P. Simons, B. G. Davis, E. J. Cocinero, D. P. Gamblin, C. Stanca-Kaposta, *Tetrahedron-Asymmetr.* **2009**, *20*, 718-722.

[11] P. Çarçabal, T. Patsias, I. Hünig, B. Liu, C. Kaposta, L. C. Snoek, D. P. Gamblin, B. G. Davis, J. P. Simons, *Phys. Chem. Chem. Phys.* **2006**, *8*, 129-136.

[12] E. J. Cocinero, A. Lesarri, P. Écija, F. J. Basterretxea, J.-U. Grabow, J. A. Fernández, F. Castaño, *Angew. Chem. Int. Edit.* **2012**, *51*, 3119-3124.

[13] E. J. Cocinero, A. Lesarri, P. Écija, Á. Cimas, B. G. Davis, F. J. Basterretxea, J. A. Fernández, F. Castaño, *J. Am. Chem. Soc.* **2013**, *135*, 2845-2852.

[14] I. Peña, E. J. Cocinero, C. Cabezas, A. Lesarri, S. Mata, P. Écija, A. M. Daly, A. Cimas, C. Bermúdez, F. J. Basterretxea, S. Blanco, J. A. Fernández, J. C. López, F. Castaño, J. L. Alonso, *Angew. Chem. Int. Edit.* **2013**, *52*, 11840-11845.

[15] J. L. Alonso, M. A. Lozoya, I. Peña, J. C. López, C. Cabezas, S. Mata, S. Blanco, *Chem. Sci.* **2014**, *5*, 515-522.

[16] I. Peña, L. Kolesniková, C. Cabezas, C. Bermúdez, M. Berdakin, A. Simao, J. L. Alonso, *Phys. Chem. Chem. Phys.* **2014**, *16*, 23244-23250.

[17] I. Peña, C. Cabezas, J. L. Alonso, *Chem. Commun.* **2015**, *51*, 10115-10118.

[18] P. Écija, I. Uriarte, L. Spada, B. G. Davis, W. Caminati, F. J. Basterretxea, A. Lesarri, E. J. Cocinero, *Chem. Commun.* **2016**, *52*, 6241-6244.

[19] W. L. Jorgensen, J. Chandrasekhar, J. D. Madura, R.W. Impey, M. L. Klein, *J. Chem. Phys.* **1983**, 79, 926–935.

[20] D. A. Case, R. M. Betz, D. S. Cerutti, T. E. Cheatham, III, T. A. Darden, R. E. Duke, T. J. Giese, H. Gohlke, A. W. Goetz, N. Homeyer, S. Izadi, P. Janowski, J. Kaus, A. Kovalenko, T. S. Lee, S. LeGrand, P Li, C. Lin, T. Luchko, R. Luo, B. Madej, D. Mermelstein, K. M. Merz, G. Monard, H. Nguyen, H. T. Nguyen, I. Omelyan, A. Onufriev, D. R. Roe, A. Roitberg, C. Sagui, C. L. Simmerling, W. M. Botello-Smith, J. Swails, R. C. Walker, J. Wang, R. M. Wolf, X. Wu, L. Xiao, P. A. Kollman (2016), AMBER **2016**, University of California, San Francisco.

[21] K. N. Kirschner, A. B. Yongye, S. M. Tschampel, J. González-Outeiriño, C. R. Daniels, B. L. Foley, R. J. Woods, *J. Comput. Chem.* **2008**, *29*, 622–655.

[22] T. A. Andrea, W. C. Swope, H. C. J. Andersen, *Chem. Phys.* **1993**, 79, 4576–4584.

[23] T. Darden, D. York, L. J. Pedersen, *J. Chem. Phys.* **1993**, *98*, 10089–10092.

[24] G. R. J. Thatcher, 'The Anomeric Effect and Associated Stereoelectronic Effects', *American Chemical Society*, Washington, DC, **1993**.

[25] M. K. Dowd, A. D. French, P J. Reilly, *J. Carbohyd. Chem.* **2000**, *19*, 1091–1114.

Chapter IX.

Degradation mechanism of the CH$_3$NH$_3$PbI$_3$ perovskite in solar cell technology

Manuscript for publication in preparation

IX.1   Introduction

In this Chapter, we explore the potential of rotational spectroscopy as an analytical tool. In particular, this technique might be used for the unequivocal identification of gaseous products due to its ability to unambiguously identify chemical species. In fact, several research groups are working nowadays towards its implementation in the pharmaceutical industry and combustion-related processes, among others.[1,2] In this Thesis, we present the specific case of the identification of the degradation products of the perovskite CH$_3$NH$_3$PbI$_3$. This substance is being investigated for its use in solar cells and it is showing promising results in terms of power conversion efficiency. However, it has been shown that this material degrades at high temperatures and a deeper knowledge of the process of degradation is needed. The identification of the released gaseous products may provide insight into the mechanism of degradation.

With the rise of renewable energies in the last decades, a lot of research is devoted to the optimization of solar cells.[3,4,5,6] From the very beginning of the investigations, a major focus of interest has been the maximization of the rate of power conversion.[7,8] A lot of effort has been devoted in that respect, both in the past and nowadays. Solar cells based on perovskite compounds, and in particular, organic-inorganic hybrid perovskites, show promising results in that sense. There are reports in the literature of power conversion efficiencies slightly greater than 20% using this kind of materials.[9] Although perovskite solar cell technology has shown great results in terms of efficiency, one of the major issues for the future implementation of this kind of technology is long term operational stability.[10,11] Therefore, researchers are now turning their attention towards the understanding and prevention of the degradation process of this kind of materials. While initial signs of success on the long-term stability of perovskite solar cells are appealing lately,[12] operational device stability tests longer than 1000 hours at maximum power point are still scarce.[13] One of the most investigated light harvesting materials in organic-inorganic hybrid perovskites-based solar cells is CH$_3$NH$_3$PbI$_3$. However, one of the main issues with this substance is its low stability.[14,15,16] A profound understanding of the degradation paths of this material may help in the design of longer-lasting solar cells based on CH$_3$NH$_3$PbI$_3$. However, the details of the mechanism of degradation are not fully understood nowadays. It is known that CH$_3$NH$_3$PbI$_3$ degrades into a solid PbI$_2$ phase.[17] Nevertheless, the nature of the gas products released in the degradation process is a matter of debate. Two degradation mechanisms are considered the best candidates to explain the process:[18]

- Mechanism 1:

$$CH_3NH_3PbI_3(s) \longrightarrow PbI_2(s) + CH_3NH_2(g) + HI(g)$$

- Mechanism 2:

$$CH_3NH_3PbI_3(s) \longrightarrow PbI_2(s) + CH_3I(g) + NH_3(g)$$

The nature of the gases released with the two mechanisms is different. There are several attempts reported in the literature to identify which gases are released, in order to assess which one of the two mechanisms is responsible for the degradation of CH$_3$NH$_3$PbI$_3$. These studies consider different conditions (temperature, pressure,

presence of O_2 and/or H_2O) and provide confronting results as to the nature of the gases released. In order to study the intrinsic thermal instability of $CH_3NH_3PbI_3$, there are several reports in the literature that analyze the degradation of this sample under inert atmosphere conditions (noble gases, N_2, etc.) at high temperature. In 2014, a thermogravimetric analysis combined with FTIR spectroscopy (TGA-FTIR) suggested that NH_3 might be released upon thermal degradation of $CH_3NH_3PbI_3$ (Mechanism 2), although the results were not conclusive.[19] In 2016, two studies showed confronting results. First, a TGA analysis combined with Mass Spectrometry (TGA-MS) pointed to the detection of CH_3I and NH_3 (Mechanism 2) with no traces of CH_3NH_2 and HI.[20] Second, a Knudsen Effusion experiment coupled with MS (KEMS) suggested that the mechanism responsible for $CH_3NH_3PbI_3$ degradation is the one leading to CH_3NH_2 and HI as gas products (Mechanism 1).[21] Finally, in 2017, new KEMS experiments suggested that both mechanisms are possible: Mechanism 2 is found to be the thermodynamically favored process while Mechanism 1 would be predominant under kinetic control conditions.

It is obvious that there are confronting results in the literature regarding the nature of the gaseous products of degradation of $CH_3NH_3PbI_3$. In order for this material to develop in the solar cell technology, an unambiguous identification of the released gas products during degradation of this hybrid perovskite is absolutely needed. It would assist to alleviate the degradation problem of this well gifted light harvesting material and it could determine the best strategy for device encapsulation favoring long-term device stability.

In this work, we suggest the use of rotational spectroscopy in supersonic expansions to identify unambiguously the nature of the gases released in the thermal degradation of $CH_3NH_3PbI_3$. The main feature of microwave spectroscopy that makes it an ideal tool to fulfill this task is its inherent high spectral resolution, hardly achievable by other spectroscopic techniques. Lines separated by only a few kHz are resolvable and therefore, transitions arising from the different gas products are unambiguously identified. Although rotational spectroscopy has been traditionally devoted to the conformational analysis of molecules or intermolecular systems in the gas phase, some research groups are focusing nowadays on the use of rotational spectroscopy as an analytical tool.[1,2] For example, the ability of rotational spectroscopy to differentiate diastereaoisomers and even enantiomers may be a great advantage with respect to other techniques in the field of pharmaceutics.

IX.2   Experimental section

The $CH_3NH_3PbI_3$ sample was synthetized by the group of Dr. Juárez-Pérez at the Okinawa Institute of Science and Technology (OIST, Japan). It is a black powder. In order to perform the rotational spectroscopy experiment, we placed the sample in a customized heating nozzle (see Chapter III) and heated to the desired temperature thanks to a resistance heating wire. Table IX.1 summarizes the working conditions for this experiment.

Table IX.1 Experimental conditions for the recording of the CP-FTMW spectrum of the gases released by thermal decomposition of CH₃NH₃PbI₃.

Experimental conditions	CP-FTMW
Number of nozzles	1
Nozzle temperature	room temperature to 230ºC
Carrier gas	He
Number of chirps/molecular pulse	30
Total number of cycles	15 million

IX.3   Results and discussion

In this work, we use rotational spectroscopy to provide an unambiguous identification of the gas products released upon heating the CH₃NH₃PbI₃ sample.

In particular, we use rotational spectroscopy for the unambiguous determination of CH₃NH₂ (Mechanism 1) and CH₃I (Mechanism 2). Both species have been previously studied using rotational spectroscopy and the position (frequency) of their rotational transitions is well reported in the literature.[22,23] In our current set-up, it is not possible to detect the other plausible gaseous products (HI and NH₃) because they do not possess rotational transitions in the working frequency range of our spectrometer (6-18 GHz). In fact, the lowest transitions for these two species are located at 385 GHz for HI[24] and 572 GHz for NH₃,[25] well beyond the upper-frequency limit of our apparatus.

The proceeding in this work is to heat the CH₃NH₃PbI₃ progressively (in steps of 20ºC) and evaluate the appearance of transitions corresponding to CH₃I and CH₃NH₂. The results of this experiment can be found in Figure IX.1.
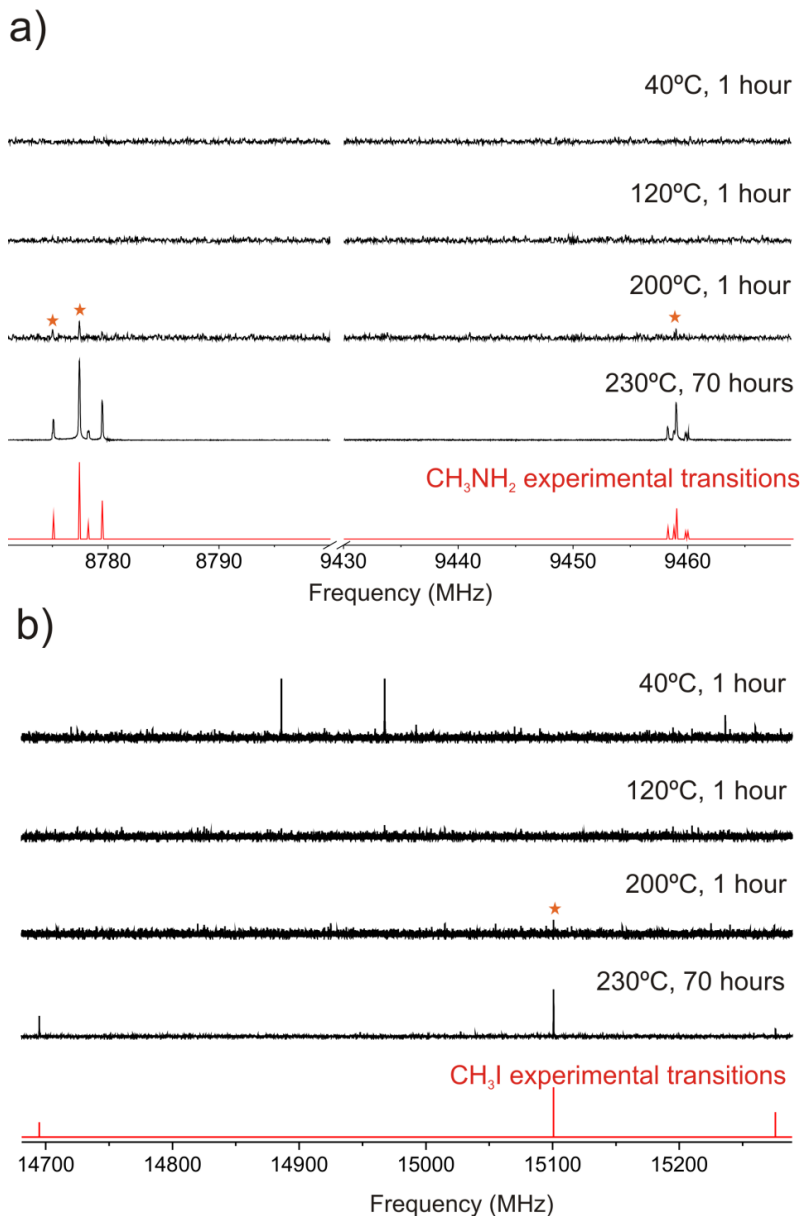
Figure IX.1 In black, two sections of the same experimental rotational spectrum obtained after heating $CH_3NH_3PbI_3$ as a function of temperature and time. Red stars mark the first appearance of lines corresponding to CH_3I or CH_3NH_2. In red, position of the rotational transitions of CH_3I and CH_3NH_2 reported in the literature. a) Frequency region corresponding to the transitions of CH_3NH_2 as reported in reference 23 b) Frequency region corresponding to the transitions of CH_3I as reported in reference 22 (the two peaks at 40ºC probably correspond to a volatile impurity that evaporates at higher temperatures).

We can see that the first traces of both CH_3I and CH_3NH_2 appear when the sample is heated at 200ºC. A further averaging of 70 hours at 230ºC improves the signal-to-noise ratio of these rotational transitions. Ten transitions of CH_3NH_2 and three transitions of CH_3I were unambiguously identified in the rotational spectrum, their frequencies matching within a few kHz the values reported in the literature. Tables IX.2 and IX.3 collect the full list of rotational transitions measured for both species, along with the experimental frequencies measured in this work and the values reported in the literature. Both molecules (CH_3I and CH_3NH_2) are quite small, their rotational constants are very large and therefore, the number of rotational transitions in our frequency range is much reduced. Most rotational transitions for these two species appear at higher frequencies. This is particularly so in the case of CH_3I. In fact, only the $J\,K_{-1}=1\,0 \leftarrow 0\,0$ rotational transition is visible in the 6-18 GHz region, which is split into 3 components due to nuclear quadrupole coupling splittings of the I atom. In the case of CH_3NH_2, only the $J\,K_{-1}=2\,0 \leftarrow 1\,1$ is intense enough to be observed in our frequency range. However, in this case, we can observe two components due to complicated tunneling splittings (internal rotation of the methyl top and inversion motion of the NH_2 group), each of them further split into several hyperfine components. By the end of the experiment, the sample had turned yellow because of the PbI_2 solid that is produced in the decomposition of $CH_3NH_3PbI_3$. Furthermore, there were no lines in the spectrum belonging to other species such as dimethylamine $(CH_3)_2NH$ or trimethylamine $(CH_3)_3N$. These two compounds could theoretically be products of degradation of $CH_3NH_3PbI_3$, but we did not find any trace of them in the microwave spectrum.

Table IX.2 Frequencies of the observed rotational transitions of CH_3I compared to the values reported in the literature.

J'	K_{-1}'	F'	J	K_a	F	Experimental frequency (this work)	Experimental frequency (ref 22)
1	0	5/2	0	0	5/2	14694.927	14694.93
1	0	7/2	0	0	5/2	15100.742	15100.74
1	0	3/2	0	0	5/2	15275.898	15275.89

Table IX.3 Frequencies of the observed rotational transitions of CH_3NH_2 compared to the values reported in the literature.

J'	K_{-1}'	Γ'	F'	J	K_a	Γ	F	Experimental frequency (this work)	Experimental frequency (ref 23)
2	0	B1	1	1	1	B2	0	8775.094	8775.096
2	0	B1	3	1	1	B2	2	8777.434	8777.440
2	0	B1	2	1	1	B2	2	8778.219	8778.226
2	0	B1	1	1	1	B2	1	8778.276	8778.275
2	0	B1	2	1	1	B2	1	8779.493	8779.498
2	0	E1+1	1	1	1	E1-1	0	9458.269	9458.292
2	0	E1+1	1	1	1	E1-1	1	9458.800	9458.805
2	0	E1+1	3	1	1	E1-1	2	9459.020	9459.037
2	0	E1+1	2	1	1	E1-1	2	9459.804	9459.823
2	0	E1+1	2	1	1	E1-1	1	9460.026	9460.028

The results presented in this Chapter unambiguously confirm the release of both CH_3NH_2 and CH_3I upon heating $CH_3NH_3PbI_3$ in the conditions of the experiment. This is definite proof that Mechanism 1 and Mechanism 2 can take place and that they may happen simultaneously. Further research seems necessary in order to investigate the conditions under which one or the other mechanism takes place. However, the feasibility of both routes is demonstrated without any doubt in this work thanks to rotational spectroscopy. Finally, we prove the potential of microwave spectroscopy for the unambiguous identification of gaseous products, as well as the possibilities of this spectroscopic technique as an analytical tool.

IX.4   References

[1] B. Harris, S. S. Fields, R. Pulliam, M. Muckle, J. L. Neill, 'Advances in molecular rotational spectroscopy for applied science' *72nd International Symposyum on Molecular Spectroscopy* **2017**, WE09.

[2] L. Evangelisti, W. Caminati, D. Patterson, J. Thomas, Y. Xu, C. West, B. H. Pate, 'A chiral tagging strategy for determining absolute configuration and enantiomeric excess by molecular rotational spectroscopy' *72nd International Symposyum on Molecular Spectroscopy* **2017**, RG03.

[3] E. Kabir, P. Kumar, S. Kumar, A. A. Adelodun, K. H. Kim, *Renew. Sust. Energ. Rev.* **2018**, *82*, 894-900.

[4] J. H. Hou, O. Inganas, R. H. Friend, F. Gao, *Nat. Mater.* **2018**, *17*, 119-128.

[5] F. Enrichi, A. Quandt, G. C. Righini, *Renew. Sust. Energ. Rev.* **2018**, *82*, 2433-2439.

[6] A. Fakharuddin, L. Schmidt-Mende, G. Garcia-Belmonte, R. Jose, I. Mora-Sero, *Adv. Energy Mater.* **2017**, *7*, 1700623.

[7] H. H. Tsai, W. Y. Nie, J. C. Blancon, C. C. S. Toumpos, R. Asadpour, B. Harutyunyan, A. J. Neukirch, R. Verduzco, J. J. Crochet, S. tretiak, L. Pedessau, J. Even, M. A. Alam, G. Gupta, J. Lou, P. M. Ajayan, M. J. Bedzyk, M. G. Kanatzidis, A. D. Mohite, *Nature* **2016**, *536*, 312-316.

[8] A. Swarnkar, A. R. Marshall, E. M. Sanehira, B. D. Chernomordik, D. T. Moore, J. A. Christians, T. Chakrabarti, J. M. Luther, *Science* **2016**, *354*, 92-95.

[9] W. S. Yang, B.-W. Park, E. H. Jung, N. J. Jeon, Y. C. Kim, D. U. Lee, S. S. Shin, J. Seo, E. K. Kim, J. H. Noh, S. I. Seok, *Science* **2017**, *356*, 1376-1379.

[10] Y. Yang, J. You, *Nature* **2017**, *544*, 155-156.

[11] J. P. Correa-Baena, M. Saliba, T. Buonassisi, M. Gratzel, A. Abate, W. Tress, A. Hagfeldt, *Science* **2017**, 739-744.

[12] S. G. Hashmi, A. Tiihonen, D. Martineau, M. Ozkan, P. Vivo, K. Kaunisto, V. Ulla, S. M. Zakeeruddin, M. Grätzel, *J. Mater. Chem. A* **2017**, *5*, 4797-4802.

[13] G. Grancini, C. Roldan-Carmona, I. Zimmerman, E. Mosconi, X. Lee, D. Martineau, S. Narbey, F. Oswald, F. De Angelis, M. Graetzel, M. K. Nazeeruddin, *Nat. Commun.* **2017**, *8*, 15684.

[14] T. A. Berhe, W.-N. Su, C.-H. Chen, C.-J. Pan, J.-H. Cheng, H.-M. Chen, M.-C. Tsai, L.-Y. Chen, A. A. Dubale, B.-J. Hwang, *Energ. Environ. Sci.* **2016**, *9*, 323-356.

[15] L. K. Ono, Y. Qi, *J. Phys. Chem. Lett.* **2016**, *7*, 4764-4794.

[16] H. Yuan, E. Debroye, K. Janssen, H. Naiki, C. Steuwe, G. Lu, M. Moris, E. Orgiu, H. Uji-i, F. De Schryver, P. Samorì, J. Hofkens, M. Roeffaers, *J. Phys. Chem. Lett.* **2016**, *7*, 561-566.

[17] B. Conings, J. Drijkoningen, N. Gauquelin, A. Babayigit, J. D'Haen, L. D'Olieslaeger, A. Ethirajan, J. Verbeeck, J. Manca, E. Mosconi, F. De Angelis, H.-G. Boyen, *Adv. Energy Mater.* **2015**, *5*, 1500477.

[18] A. Latini, G. Gigli, A. Ciccioli, *Sustain. Energy Fuels* **2017**, *1*, 1351-1357.

[19] A. E. Williams, P. J. Holliman, M. J. Carnie, M. L. Davies, D. A. Worsley, T. M. Watson, *J. Mater. Chem. A* **2014**, *2*, 19338-19346.

[20] E. J. Juárez-Pérez, Z. Hawash, S. R. Raga, L. K. Ono, Y. Qi, *Energy Environ. Sci.* **2016**, *9*, 3406-3410.

[21] B. Brunetti, C. Cavallo, A. Ciccioli, G. Gigli, A. Latini, *Sci. Rep.* **2016**, *6*, 31896.

[22] S. H. Young, S. G. Kukolich, *J. Mol. Spectrosc.* **1985**, *114*, 483-493.

[23] V. Ilyushin, F. J. Lovas, *J. Phys. Chem. Ref. Data* **2007**, *36*, 1141-1276.

[24] F. C. De Lucia, P. Helminger, W. Gordy, *Phys. Rev. A* **1971**, *3*, 1849-1857.

[25] P. Helminger, F. C. De Lucia, W. Gordy, *J. Mol. Spectrosc.* **1971**, *39*, 94-97.

Chapter X.

Conclusions

The field of rotational spectroscopy is undergoing a reawakening in the last decades, fueled by the advances in instrumentation, as well as the developments in theoretical methods and the availability of powerful computing resources. A large part of the work in this Thesis was devoted to building and implementing a CP-FTMW spectrometer at the Spectroscopy group at the University of the Basque Country (UPV/EHU) and, therefore, we have mostly focused on the possibilities of this device. Nevertheless, we have also analyzed the potential of the FTMW spectrometer and the ultrafast laser vaporization method. We have performed several rotational spectroscopy studies from which we can draw the following conclusions.

- Microwave studies are now opening up to larger and more flexible biomolecular systems, such as the cases of cotinine, α- and β-ionone and β-damascone that we have presented in this Thesis. The study of complex conformational landscapes is now possible, partly due to the speed of data acquisition enabled by CP-FTMW techniques.

- Rotational spectroscopy is a powerful tool in the analysis of tautomeric equilibria. It is possible to unambiguously identify the different tautomers and quantify the population ratio between them, as we have demonstrated with the analysis of two tautomers of purine. The very high spectral resolution allowed by microwave spectroscopy is the differentiating factor that makes this technique ideal for the analysis of tautomeric equilibria in the gas phase.

- Theoretical calculations are nowadays crucial in rotational spectroscopy studies. As the size and degrees of freedom of the molecular systems increase, so does the role played by theoretical calculations. The interplay between theory and experiment is two-fold: on the one hand, experimental studies are supported by reliable theoretical predictions and, on the other hand, the development of new theoretical models necessitates the benchmark of experimentally obtained molecular structures. We have seen this interaction between theory and experiment along this Thesis. Moreover, we have seen that one has to choose carefully the theoretical method to use, with the examples of methyl jasmonate and zingerone.

- Rotational spectroscopy offers the chance to perform structural studies of biomolecules in the gas phase. The results obtained with this technique can be combined with those resulting from other techniques and/or in other media in order to acquire a more general overview of the conformational possibilities of a given biomolecular system. We have experienced this by combining rotational spectroscopy with chemical synthesis, NMR in solution and Molecular Dynamics in the case of the monosaccharide methyl 2-deoxy-D-ribofuranoside.

- Finally, some research groups around the world are exploiting the possibility of using rotational spectroscopy as an analytical tool. The unambiguous discrimination of chemical species is one of the characteristics that makes this technique a potential candidate for analytical studies. In this Thesis, we have presented a specific example where rotational spectroscopy helps in the elucidation of the degradation mechanism of a hybrid perovskite that could be used in solar cells.

In general, we have seen that modern rotational spectroscopy is a powerful and versatile tool that can be used for a variety of applications (structural elucidation, investigation of tautomeric equilibria, as an analytical tool, etc). The next years will probably witness a full exploitation of the potential of this technique.

Chapter XI.

Other studies

Recollection of published material that is beyond the scope of this Thesis.

1,1′-Bi-2-naphtol

▍BINOL

Static and Dynamic Properties of 1,1′-Bi-2-naphthol and Its Conjugated Acids and Bases

Ibon Alkorta,*[a] Céline Cancedda,[b] Emilio José Cocinero,*[c] Juan Z. Dávalos,*[d] Patrica Écija,[c] José Elguero,[a] Javier González,[d] Alberto Lesarri,[e] Rocio Ramos,[d] Felipe Reviriego,[a] Christian Roussel,[b] Iciar Uriarte,[c] and Nicolas Vanthuyne*[b]

Abstract: Several convergent techniques were used to characterize 1,1′-bi-2-naphthol (BINOL) and some of its properties. Its acidity in the gas-phase, from neutral species to monoanion, was measured by mass spectrometry. The conformation and structure of BINOL in the gas phase was determined by microwave rotational spectroscopy. NMR experiments in fluorosulfonic acid established that BINOL was monoprotonated on one of the hydroxyl oxygen atoms. The enantiomerization barriers reported in the literature for BINOL under neutral, basic, and acid conditions were analyzed with regard to the species involved. Finally, DFT calculations allowed all of these results to be gathered in a coherent picture of the BINOL structure.

1. Introduction

1,1′-Bi-2-naphthol (BINOL) and its derivatives are one of the most widely used classes of ligands in asymmetric synthesis; they are utilized in a broad array of reactions, including Diels–Alder, carbonyl additions and reduction, Michael additions, epoxidations, and Henry reactions. BINOL has axial chirality and the two enantiomers can be separated because they are stable toward racemization. Their specific rotations are $\pm 35.5°$. Besides the great success obtained with the BINOL platform, other C_2-symmetric diol ligands have attracted considerable attention, for instance, BINAP, VAPOL, VANOL, and related compounds.[1]

The optical rotatory properties of (R or S) BINOL in various solvents have been reported.[2] The changes in the specific rotation and sign of optically active BINOL have been studied in polar/nonpolar solvents at different pH values. It is considered that these changes are determined by the equilibrium between cisoid and transoid conformations of BINOL with the same configuration (R or S), which is related to the change in dihedral angle between the two naphthalene ring planes of BINOL (Figure 1). This involves the orthogonal transition state, which is not relevant to the present work.

[a] Prof. I. Alkorta, Prof. J. Elguero, Dr. F. Reviriego
Instituto de Química Médica, CSIC
Juan de la Cierva, 3, 28006 Madrid (Spain)
Fax: (+ 34) 91-5644853
E-mail: ibon@iqm.csic.es

[b] C. Cancedda, Prof. C. Roussel, Dr. N. Vanthuyne
Aix-Marseille Université, Centrale Marseille
CNRS, iSm2 UMR 7313, 13397 Marseille (France)
E-mail: nicolas.vanthuyne@univ-amu.fr

[c] Dr. E. J. Cocinero, Dr. P. Écija, I. Uriarte
Departamento de Química Física, Facultad de Ciencia y Tecnología
Universidad del País Vasco (UPV-EHU)
Apartado 644, 48080 Bilbao (Spain)
Fax: (+ 34) 94-4608500
E-mail: emiliojose.cocinero@ehu.es

[d] Prof. J. Z. Dávalos, J. González, R. Ramos
Instituto de Química Física Rocasolano, CSIC. C/Serrano
119. 28006 Madrid (Spain)
Fax: (+ 34) 91-5642431
E-mail: jdavalos@iqfr.csic.es

[e] Prof. A. Lesarri
Departamento de Química Física y Química Inorgánica
Facultad de Ciencias
Universidad de Valladolid, 47011 Valladolid (Spain)

⌨ Supporting information for this article is available on the WWW under
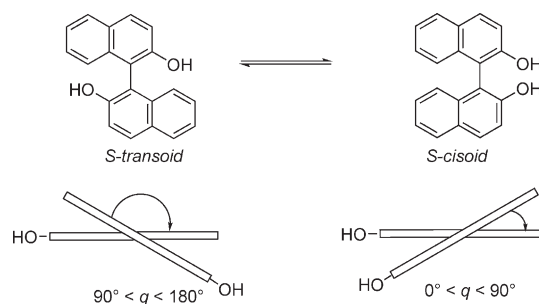http://dx.doi.org/10.1002/chem.201402686.

Figure 1. Cisoid and transoid conformations of BINOL.

The racemic and both pure enantiomers of BINOL are commercially available. The MS and microwave (MW) experiments were carried out with (±)-BINOL, and the dynamic experiments to determine the enantiomerization barriers with (R)-BINOL.
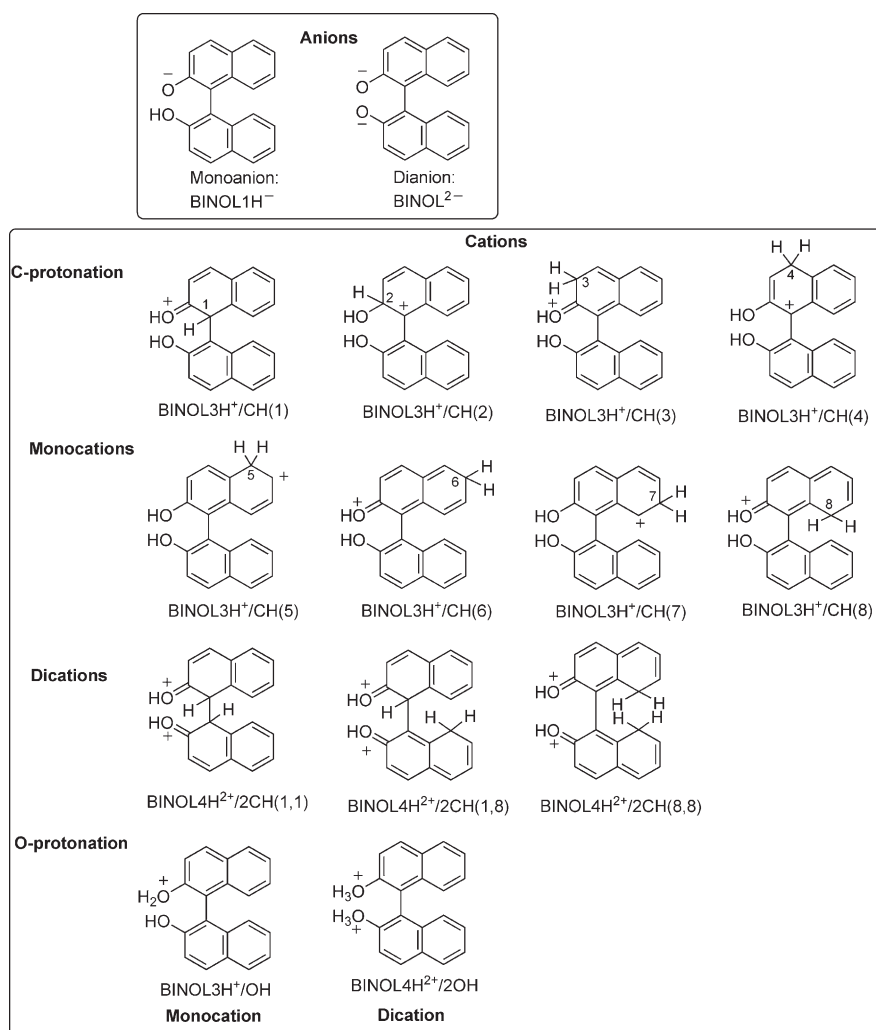
Figure 2. Deprotonated BINOL (anions) and protonated BINOL (cations).

sets for the optimized geometries and energetics revealed only small differences, that is, the geometrical structures and energies are not strongly basis set dependent. Therefore, the 6-31G(d) basis set was used to determine the potential-energy curve.

A more complete study was published in 2008.[5] The authors wrote "Recently, density functional theory (DFT) calculations of 2,2′-BINOL have been carried out to study its structural and spectroscopic properties."[6–10] The computational results were used to explain the measured vibrational circular dichroism and resonance Raman spectra.[6–8] The DFT calculations were also been utilized to investigate the isomerization/racemization mechanisms of 2,2′-BINOL, and various pathways for its racemization were proposed.[10]

2.1.1. Comparison of theoretical methods

We carried out calculations of the minima of neutral BINOL at four levels of theory (Table 1 and Figure 3). The relative energies

2. Results and Discussion

Figure 2 shows all of the structures (minima) studied in this work and their code names.

2.1. Theoretical calculations

The torsional barriers of substituted biphenyl are difficult to calculate.[3] The B3LYP-D, B97-D, and TPSS-D3 functionals were identified as the most promising methods, and were used to determine the torsional barriers of 33 other substituted biphenyls with known Gibbs energies of activation (25–190 kJ mol^{-1}).[3]

The mechanism of isomerization of BINOL has been investigated by means of DFT.[4] Three conformers exists for BINOL, each of which has two enantiomers. Geometry optimizations were carried out at the B3LYP level of theory, which consists of the hybrid Becke + Hartree–Fock exchange and the Lee–Yang–Parr correlation functional with nonlocal corrections, and two kind of basis sets were used for all atoms: 6-31G(d) and 6-31+G(d,p), as implemented in the Gaussian program package. Comparison between the results obtained with the two basis

Table 1. E_{rel} [kJ mol^{-1}] of the three conformations of BINOL (all of them minima).

	B3LYP/6-31G(d)	B3LYP/6-311++G(d,p)	M06-2x/6-311++G(d,p)	MP2/6-311++G(d,p)
EE	32.2	29.3	34.1	31.3
EZ	17.5	16.0	19.2	17.2
ZZ	0.0	0.0	0.0	0.0

are rather insensitive to the method used to calculate them. The ZZ isomer is always the most stable. Since the calculations of frequencies is essential for determining the nature of the transition state (TSs) (one imaginary frequency) and they depend on the size of the basis set and computational method, in the remainder of this work, the B3LYP/6-31G(d) level of theory is used with some exceptions.

2.1.2. Geometries

We will discuss only the angle θ between the naphthalene rings (C2-C1-C1′-C2′, about the C1—C1′ bond; C2 and C2′ are
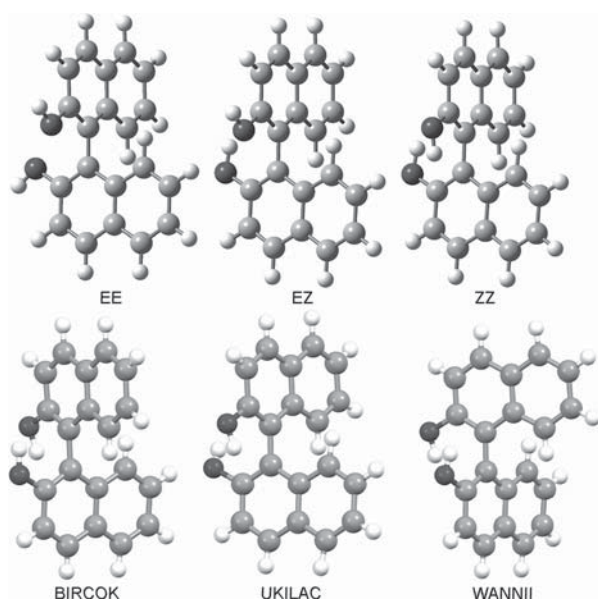
Figure 3. Top: The three minimum-energy conformations of BINOL. Bottom: the three kinds of X-ray structures reported with CSD codes (all of them ZZ).

Table 3. B3LYP/6-31G(d) calculations; in bold: minima for the three different families (same molecular formula). E in hartree; E_{rel} and ΔH in kJ mol^{-1}.

		E	E_{rel}	Acid–base ΔH
neutral	ZZ	−921.02799	**0.0**	–
	ZE	−921.02131	17.5	–
	EE	−921.01573	32.2	–
monoanion	BINOL1H$^-$ Z	−920.48460	**0.0**	1388.3
	BINOL1H$^-$ E	−920.45270	83.8	
dianion	BINOL^{2-}	−919.77830	–	1815.2
monocation	BINOL3H$^+$/OH	−921.35397	72.9	
	BINOL3H$^+$/CH(1)	−921.38173	**0.0**	894.4
	BINOL3H$^+$/CH(2)	−921.34907	85.8	
	BINOL3H$^+$/CH(3)	−921.36870	34.2	
	BINOL3H$^+$/CH(4)	−921.36979	31.4	
	BINOL3H$^+$/CH(5)	−921.36488	44.2	
	BINOL3H$^+$/CH(6)	−921.37503	17.6	
	BINOL3H$^+$/CH(7)	−921.36196	51.9	
	BINOL3H$^+$/CH(8)	−921.37868	8.0	
dication	BINOL4H^{2+}/2OH	−921.54942	173.4	
	BINOL4H^{2+}/2CH(1,1)	−921.61548	**0.0**	582.6
	BINOL4H^{2+}/2CH(1,8)	−921.61339	5.5	
	BINOL4H^{2+}/2CH(8,8)	−921.61078	12.3	

the atoms bearing OH substituents). The CSD contains three kinds of BINOL molecules:[11] racemic, R,S(±), BIRKOC, $\theta_{av} = 88.4°$; S(−) enantiomer UKILAC and R(+) enantiomer WANNII, $\theta_{av} = 76.8°$ (Figure 3). The difference is due to the different packing modes of enantiomers and racemate; thus, an average value of about 83° could be considered representative for the biaryl conformation of BINOL in the solid state. Since the value of (83 ± 5)° is less than 90°, the structure is of the *cisoid* type (Figure 1) but not far from orthogonal. The conformation of the hydroxyl groups in the solid state depends on the intermolecular hydrogen bonds and therefore cannot be used for comparison with the isolated molecule.

According to our calculations (Table 2) the θ values are very similar between B3LYP with two different basis sets on the one

Table 2. Calculated torsion angles θ of the three BINOL conformers calculated at four levels of theory.

	B3LYP/ 6-31G(d)	B3LYP/ 6-311++G(d,p)	M06-2x/ 6-311++G(d,p)	MP2/ 6-311++G(d,p)
EE	88.4	89.7	71.6	74.7
EZ	93.6	88.8	106.1	103.6
ZZ	97.2	93.6	105.6	104.8

hand, and M06-2x and MP2 with the same basis set on the other. The θ value in the crystal ($\approx 83°$) is closer to the B3LYP result for the ZZ isomer (94–97°) than to the M06-2x/MP2 value ($\approx 105°$). Since we are comparing gas- and solid-state geometries, it was considered necessary to determine the experimental gas-phase geometry.

2.1.3. Energies

The calculated energies of the minima of the compounds of Figure 2 are reported in Table 3. As reported in Table 1, neutral BINOL should exist as the ZZ isomer; the energy of the EZ isomer is intermediate between those of the EE and ZZ isomers. For the monocations, the most stable is that protonated in the 1-position [quaternary C, BINOL3H$^+$/CH(1)]; that protonated in the 8-position is slightly less stable (BINOL3H$^+$/CH(8), 8 kJ mol^{-1}); note that the cation resulting from protonation on an O atom is very unstable (BINOL3H$^+$/OH, ≈ 73 kJ mol^{-1}). The stability of dications is consistent with the results just discussed: 1,1 [BINOL4H^{2+}/2CH(1,1)] > 1,8 [BINOL4H^{2+}/2CH(1,8)] > 8,8 [BINOL4H^{2+}/2CH(8,8)] ≫ > O,O (BINOL4H^{2+}/2OH).

2.1.4. Acid–base equilibria

Although the acidity of BINOL is simple, since only two BINOL1H$^-$ monoanions and one BINOL^{2-} dianion are possible,[12] its basicity is a very complex problem because the possibility of protonation on the carbon atoms results in many cations (see Figure 2). Table 3 lists the values corresponding to the most stable conformations. The values for the dianion and the dication correspond to the mono-to-di transformations.

2.1.5. Chemical shifts

We calculated at the GIAO/B3LYP/6-311++G(d,p) level of theory the chemical shifts (^{1}H, ^{13}C, ^{17}O) of most molecules discussed in this paper with different conformations of the hydroxyl groups (neutral BINOL of most molecules, anions, and cations). They are reported in the Supporting Information (Tables S1–S3).

XI.7

2.1.6. Enantiomerization barriers

The energy hypersurfaces are very complex, since they include both rotation about the central C−C bond and the rotation of the OH groups (save in the case of the dianion). Consequently, Table 4 lists only the lower-energy barriers. All energies and ge-

Table 4. Enantiomerization transition barriers (corrected for zero-point energy) [kJ mol^{-1}]. All structures correspond to the relative minima in each class (Table 3).

Name	Structure	Isomer	Barrier
BINOL	neutral	ZZ	158.4
BINOL1H$^-$	anion	Z	167.0
BINOL^{2-}	dianion	–	113.4
BINOL3H$^+$/CH(1)	monocation	protonated on C1	147.5
BINOL4H^{2+}/2CH(1,1)	dication	diprotonated on C1, C1′	50.5

ometries of the stationary points located for these systems (23 minima and 30 TSs) are gathered in the Supporting Information (Tables S4–S9 and Figure S2). The geometries of the most stable minima (another view of ZZ BINOL is shown in Figure 3) and those of the lowest enantiomerization TSs are shown in Figure 4.

2.2. BINOL acidity: mass spectrometric measurements

The natural logarithms of the branching ratios ln([A$^-$]/[A$_{ref(i)}^-$]) were plotted against the values of $\Delta_{acid}H_{ref(i)}^0 - \Delta_{acid}H_{ref}^{avg}$ (first thermokinetic plot depicted in Figure 5), where $\Delta_{acid}H_{ref}^{avg} = (1384.7 \pm 8.4)$ kJ mol^{-1} is the average deprotonation enthalpy of reference acids. The data were fitted by a set of five regression lines, each of which corresponds to experiments done with different collision energies E_{cm}. The second thermokinetic plot (Figure 5), obtained from the results of the first plot, was generated by plotting the negative y-intercept values $-[(\Delta_{acid}H_{ref(i)}^0 - \Delta_{acid}H_{ref}^{avg})/RT_{eff} - \Delta(\Delta S^0)/R]$ versus the slopes $1/RT_{eff}$, where R is the universal gas constant and T_{eff} is the effective temperature of the activated system.[13] The thermochemical values for the deprotonation of BINOL were derived from the slope and negative y-intercept values of the linear fit of the second plot: $\Delta_{acid}H^0 = (1389.8 \pm 8.4)$ kJ mol^{-1}, $\Delta_{acid}S^0 = (107.1 \pm 8.4)$ J mol^{-1} K^{-1} and gas-phase acidity (GA) = (1357.9 ± 8.4) kJ mol^{-1}. The calculated value of $\Delta_{acid}H^0$ of Table 3 is 1388.3 kJ mol^{-1}.

Unfortunately, the gas-phase basicity of BINOL could not be measured by mass spectrometry because, under the conditions of the experiment, protonation of BINOL resulted in loss of a water molecule and fragmentation.

2.3. Rotational spectroscopy

The rotational spectrum of BINOL was investigated on the basis of initial theoretical models in Table 1, which predicted
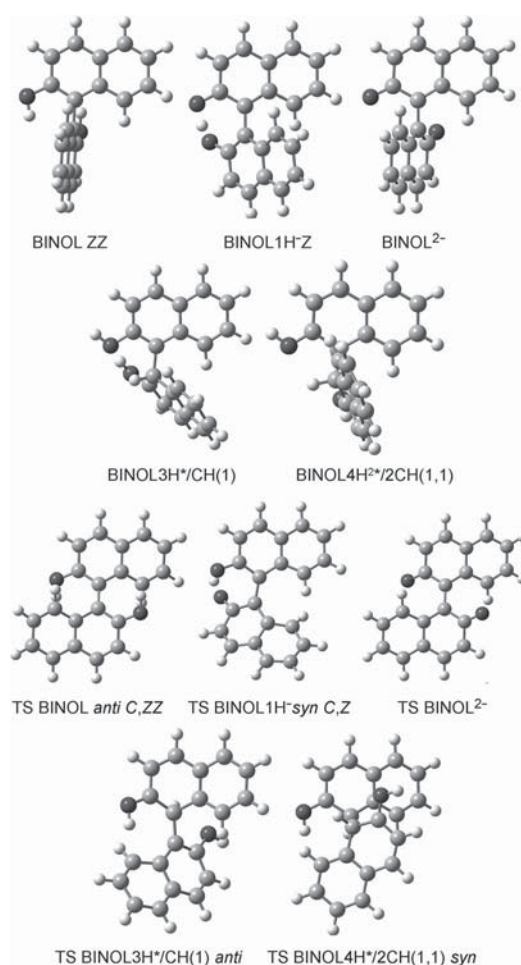
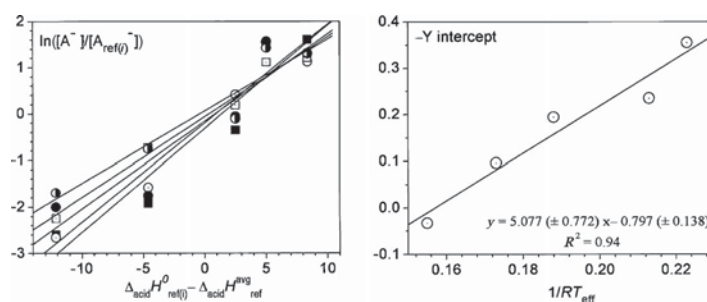**Figure 4.** Minimum-energy geometries of the five minima and the corresponding enantiomerization TSs.

Figure 5. First (left) and second (right) sets of thermokinetic plots of CID data of heterodimers [A···H···A$_{ref(i)}$]$^-$, where AH = BINOL and A$_{ref(i)}$H are the reference acids.

three skewed conformations as most stable. The labels ZZ, EZ, and EE in Table 1 correspond to conformations differing in the orientation of the hydrogen atoms in the hydroxyl groups. In the transoid global minimum ZZ (C_2), both hydroxyl groups point toward the second ring in the assembly, while they both point outwards in conformer EE (C_2). Finally, only one of the hydroxyl groups points to the second ring in conformer EZ (C_1). However, analysis of the spectrum yielded a single confor-
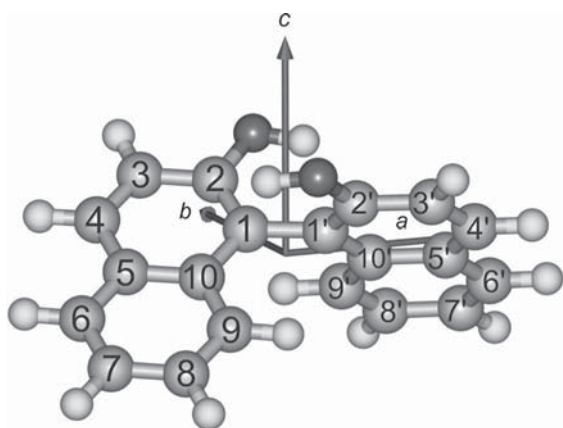
XI.8

Figure 6. Structure and atom labeling for the BINOL molecule showing the locations of the principal axes of inertia (*a*, *b*, *c*).

mation, which behaved as a semirigid asymmetric top with no hyperfine effects (Figure 6).

The frequency measurements (Table S10 in the Supporting Information) spanned angular momentum quantum numbers $J = 3–9$ were all identified as μ_c transitions. Other selection rules are zero by symmetry (since BINOL is very close to the limit of a prolate symmetric top, $k \approx -0.95$, the B3LYP predictions invert the *b* and *c* axes). Similarly to other biaryl compounds, conformer *ZZ* displays axial chirality (atropisomerism), but no evidence was found of inversion tunneling between the two chiral species, as in 2,2′-biphenol.[14] The rotational parameters are compared with the theoretical predictions in Table 5.

Despite the fact that no isotopologues could be detected, the most relevant structural parameters of BINOL were derived from the rotational spectrum. For this purpose the dihedral angle between the two naphthyl groups or the dihedral angle and the angle defining the orientation between the subunits of the assembly were fitted to the three experimental rotational constants of the parent species. The two fits were similar and satisfactorily reproduced the observed rotational constants (*B*, $C < 0.2$ MHz; $A < 2$ MHz) with a small adjustment of about 3° in the predicted dihedral angle [θ(C2-C1-C1′-C10′): $-81.1(4)°$ (r_0) versus -78.7 (MP2)]. The rest of the molecule was constrained to the ab initio (MP2) geometry. The ab initio and fitted values of the structure are listed in Table 6.

The agreement between experiment and theory (MP2) is excellent. In Table 2, it is now apparent that the MP2/6-311++G(d,p) (θ(C2-C1-C1′-C2′) = 104.8°) and the M06-2x/6-311++G(d,p) (θ = 105.6°) calculations give much better results than B3LYP with the same basis set (θ = 93.6°). In conclusion, BINOL in the gas phase has a *transoid* conformation while in the solid state (θ = 83°) it adopts a *cisoid* conformation due to crystal-field effects.

2.4. NMR studies: neutral BINOL and protonation experiments

Preliminary studies using different quantities of H_2SO_4 yield only sulfonated derivatives according to MS and NMR spectroscopy. This is related to the well-known sulfonation reaction of phenols with sulfuric acid.[15, 16] In view of this, we carried out experiments using the stronger and nonfluorosulfonating acid $HFSO_3$.

To test the quality of our calculations we started from BINOL itself. NMR data on this compound have been reported several times,[17, 18] even in a chiral nematic solvent (differentiation of the *R* and *S* enantiomers).[19] We measured its ^1H and ^{13}C spectra in [D_6]DMSO and carried out 2D experiments to assign the signals. Particularly useful to assign the ^1H NMR signals were the ^1H–^1H SSCC experiments. The results are reported in Table 7.

Using linear regressions, we compared the experimental and the three calculated values. For both ^1H and ^{13}C the best correlations correspond to the *ZZ* conformation, which was calculated to be the most stable. The correlations for the literature data in $CDCl_3$ are given by Equations (1) and (2)

Table 5. Rotational parameters of BINOL: experiment versus theory.

	Experiment	Theory[a] *ZZ*	Theory *EZ*	Theory *EE*
A [MHz]	465.7212(10)[b]	471.9/494.4/467.1	468.4/493.2/458.3	441.5/444.9/461.2
B [MHz]	219.026(64)	220.7/220.0/216.2	221.0/220.8/222.6	242.6/245.8/221.0
C [MHz]	214.380(67)	211.3/203.0/212.7	213.3/203.5/211.5	207.5/204.7/212.3
D_J [kHz]	0.391(37)			
D_{JK} [kHz]	−0.376(79)			
D_K [kHz]	0.684(47)			
d_1 [Hz]	5.21(51)			
d_2 [Hz]	−0.074(14)			
$|\mu_a|$ [D]		0.0/0.0/0.00	−2.0/2.0/2.0	0.0/0.0/0.0
$|\mu_b|$ [D]		0.0/0.0/1.2	2.1/0.5/2.1	1.4/1.6/1.4
$|\mu_c|$ [D]		1.3/1.12/0.0	−0.1/2.1/0.1	0.0/0.0/0.0
$|\mu_{TOT}|$ [D]		1.3/1.12/1.2	2.9/3.0/2.9	1.4/1.6/1.4
ΔE [kJ mol^{-1}]		0.0/0.0/0.0	17.2/19.2/16.0	31.3/34.1/29.3
N	32			
σ [kHz]	4.7			

[a] MP2, M06-2X, and B3LYP, respectively [basis set: 6-311++G(d,p)]. [b] Standard errors in parentheses in units of the last digit.

Table 6. Effective and ab initio structure of BINOL: distances [Å] and angles [°].[a]

Distances	r_e	Angles	r_0	r_e	Dihedral angles	r_0	r_e
r(C1–C2)	1.394	∡(C1-C2-C3)		120.9	θ(C1-C2-C3-C4)		−2.0
r(C2–C3)	1.416	∡(C2-C3-C4)		120.0	θ(C2-C3-C4-C5)		1.8
r(C3–C4)	1.381	∡(C3-C4-C5)		121.1	θ(C3-C4-C5-C6)		−178.7
r(C4–C5)	1.423	∡(C4-C5-C6)		122.0	θ(C4-C5-C6-C7)		178.3
r(C5–C6)	1.421	∡(C5-C6-C7)		120.7	θ(C5-C6-C7-C8)		−2.0
r(C6–C7)	1.385	∡(C6-C7-C8)		120.2	θ(C6-C7-C8-C9)		1.5
r(C7–C8)	1.416	∡(C7-C8-C9)		120.5	θ(C7-C8-C9-C10)		−1.5
r(C8–C9)	1.386	∡(C8-C9-C10)		120.5	θ(C8-C9-C10-C10)		179.4
r(C9–C10)	1.422	∡(C9-C10-C1)		121.5	θ(C1-C2-O-H)		3.2
r(C10–C1)	1.430	∡(C10-C1-C2)		119.6	θ(C2-C1-C1′-C10′)	−81.1(4)	−78.7
r(C1–C1′)	1.480	∡(C1-C2-O)		122.3	θ(C2-C1-C1′-C2′)	102.4(4)	104.8
r(C2–O)	1.362	∡(C2-O-H)		107.5			
r(O–H)	0.969	∡(C10-C1-C1′)		121.0			
		∡(C1-C1′-C10)	120.7(5)	121.0			

Table 7. Experimental and calculated chemical shifts of BINOL [ppm].

Atom	Exptl	Exptl (CDCl₃)[17] ¹H and ¹³C assigned	Exptl (CDCl₃)[18] ¹H assigned ¹³C unassigned[b]	Calcd EE ([D₆]DMSO) this work	Calcd ZZ	Calcd EZ average
OH	5.05	4.96	9.21	3.63	4.57	4.06
H3	7.12	7.28	7.32	6.76	7.31	7.04
H4	7.89[a]	7.88	7.84	7.75	7.89	7.84
H5	7.83[a]	7.80	7.83	7.24	7.80	7.74
H6	7.19–7.38	7.28	7.22	7.25	7.33	7.30
H7	7.19–7.38	7.21	7.15	7.18	7.32	7.23
H8	7.19–7.38	7.06	6.94	7.19	7.09	7.11
C1	110.9	110.8	115.9	118.2	111.2	115.0
C2	152.7	152.8	153.5	152.1	154.6	153.6
C3	117.7	117.8	119.0	114.4	116.4	115.3
C4	129.4	129.5	128.6	129.3	131.8	130.4
C4a	131.3	131.5	129.1	130.0	130.0	129.9
C5	128.3	128.4	128.3	127.4	128.1	127.8
C6	124.0	124.1	122.7	122.4	123.1	122.9
C7	127.4	127.5	126.3	125.9	127.1	126.6
C8	124.2	124.2	124.9	125.8	124.2	124.9
C8a	133.4	133.4	134.6	135.9	134.9	135.9

[a] Unassigned. [b] Assigned by analogy with the previous column.

$$^1H: \quad \delta_{exptl}^{[18]} = (0.97 \pm 0.19) + (0.87 \pm 0.03)\,\delta_{calcd}(ZZ)$$
$$n = 7, \; R^2 = 0.995 \tag{1}$$

$$^{13}C: \quad \delta_{exptl}^{[17]} = (8.0 \pm 4.3) + (0.94 \pm 0.03)\,\delta_{calcd}(ZZ)$$
$$n = 10, \; R^2 = 0.990 \tag{2}$$

and those for the data from this work in [D₆]DMSO by Equations (3) and (4)

$$^1H: \quad \delta_{exptl} = -(1.3 \pm 0.8) + (1.16 \pm 0.10)\,\delta_{calcd}(ZZ)$$
$$n = 7, \; R^2 = 0.968 \tag{3}$$

$$^{13}C: \quad \delta_{exptl} = (16.2 \pm 6.2) + (0.88 \pm 0.05)\,\delta_{calcd}(ZZ)$$
$$n = 10, \; R^2 = 0.976 \tag{4}$$

The agreement is worse in [D₆]DMSO than in CDCl₃ because of larger solvent effects.

We obtained the spectra depicted in Figure 7 from a solution of BINOL in FSO₃H (0.56 M) after waiting for stabilization (several days). Since there are neither ¹H nor ¹³C signals corresponding to an sp³ carbon atom, either CH₂ or CH (see Supporting Information, Figure S1), the problem is limited to mono- and diprotonation of the O atoms. To choose between BINOL3H⁺/OH and BINOL4H²⁺/2OH we compared the data of Figure 6 with the calculated chemical shifts (Section 2.1.5). The correlation coefficients R^2 are much better for the monocation than

for the dication. For BINOL3H⁺/OH we obtained the following regressions [Eqs. (5)–(7)].

$$\text{All signals}: \quad \delta_{exptl} = -(0.1 \pm 0.8) + (1.02 \pm 0.01)\,\delta_{calcd}$$
$$n = 32, \; R^2 = 0.998 \tag{5}$$

$$\text{Only } ^1H: \quad \delta_{exptl} = -(0.6 \pm 0.4) + (1.10 \pm 0.04)\,\delta_{calcd}$$
$$n = 12, \; R^2 = 0.983 \tag{6}$$

$$\text{Only } ^{13}C: \quad \delta_{exptl} = (5 \pm 10) + (0.99 \pm 0.08)\,\delta_{calcd},$$
$$n = 20, \; R^2 = 0.894 \tag{7}$$

For individual nuclei, the equations are not very good, probably because the quality of the spectra of Figure 6 is not excellent, partially due to some decomposition of the sample.

In the case of phenol[20,21] and 1-naphthol[22] different sites of protonation are observed that are acid- and time-dependent (Figure 8).

We were unable to C-protonate BINOL using FSO₃H. Olah and Mo[20] used superacid systems such as HSO₃F/SbF₅ and HSO₃F/SbF₅/SO₂ClF at low temperature and pointed out that O-protonation is favored in more weakly acidic media. Cerfontain et al.[21] showed that in concentrated aqueous sulfuric acid phenol is protonated predominantly on the O atom. In the case of naph-

Figure 7. Top: ¹H NMR spectrum (calculated values at the bottom). Bottom: ¹³C NMR spectrum (calculated values in the formula).

XI.10

Figure 8. Structure of the cations obtained by protonation of phenol and naphthol.

thol two *C*-protonated species were detected (HSO$_3$F/SbF$_5$/SO$_2$ClF at $-80\,°C$).[22] The ^{1}H and ^{13}C chemical shifts of the *C*-protonated cations reported in these papers are consistent with our calculated values (Supporting Information, Figure S1).

2.5. Enantiomerization barriers in solution

A careful distinction should be made between the kinetic constant of racemization and that of enantiomerization: $k_{racemization} = 2\,k_{enantiomerization}$. In several of the papers cited below, reported enantiomerization barriers are actually racemization barriers.

In his book "*Dynamic Stereochemistry of Chiral Compounds*", Christian Wolf discussed in several places the case of BINOL.[23] (see also ee ref. [24]). In particular, on page 91 he wrote, "Atropisomerization is an intramolecular process that is controlled by steric and electronic substituent effects. In some cases, the barrier to rotation can be altered by external factors. An important example is the acid-catalyzed racemization of BINOL. This biaryl does not show any sign of racemization on heating at 100° for 24 hours under neutral conditions but it racemizes at 100°C in 1.2 N hydrochloric acid within this period of time." The most important of the external factors are acid and basic conditions,[25] to the point that BINOL does not racemizes when heated during 24 h at 100°C while the same period of time and the same temperature lead to racemization in 1.2 HCl[9,10] (see, for related compounds; see references [26–28]). The same happens under basic conditions.[23,26] The explanation in the first case has been attributed to protonation leading to a C(sp^2)–C(sp^3) bond (Figure 9) and in the second case to deprotonation with formation of a naphthoxide.[23,26] On this case
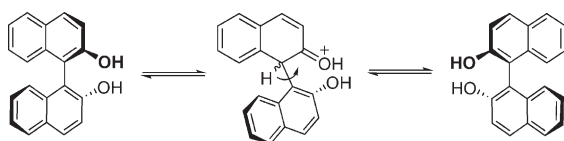
Figure 9. Acid-catalyzed atropisomerization of BINOL.

Wolf[23] comments "By analogy with the rationalization of electronic effects of electron-donating substituents on the energy barrier of biphenyls, it is believed that the increase in electron density at the central carbon atoms of the naphthoxide moieties facilitates rotation via out-of-plane bending in the transition state."[26] The experimental barrier of BINOL itself has been determined twice under rather different conditions with very consistent values (see Table 8).[10,29]

Before reporting our results, we have summarized those we obtained from the literature, either directly (BINOL itself) or

from the reported experiments. Taking into account that enantiomerization follows a first-order kinetics and using only the two points available (initial and final) we calculated the rates of

Table 8. Experimental enantiomerization barriers [kJ mol^{-1}] from the literature, directly reported or estimated.

Conditions	Species	Solvent	*T* [K]	Ref.	Barrier
–	neutral	naphthalene	468	–[10]	155.5[a]
–	neutral	diphenyl ether	493	–[10]	161
segmented flow	neutral	diglyme/*o*-xylene 97/3	553	–[29]	174
0.7 M KOH	anion	butan-1-ol	391	–[9]	135.3
5% NaOH$_{(aq.)}$, 1.25 M	anion	water	373	–[26]	122.3
1.2 M HCl	cation	dioxane/water	373	–[9]	129.1
13% HCl$_{(aq.)}$, 3.6 M	cation	THF	339	–[26]	115.4

[a] Since this value was determined with a polarimeter where the authors had to heat the cell to 195°C (naphthalene, m.p. 80°C) it should be considered less accurate than the other two (probably underestimated).

the four examples of Table 8, two for basic and two for acid conditions. We transformed the rates *k* into barriers using the Eyring equation [Eq. (8)].[30]

$$\Delta G_{T}/\text{kJ mol}^{-1} = 19.12\,T\,[10.32 + \lg(T/k)] \qquad (8)$$

Due to the importance of the subject and inherent imprecision of some of the barriers in Table 8, we determined all of them anew. The progress of the racemization was monitored by enantioselective chromatography.[31] The barriers reported in Table 9 are enantiomerization barriers in the solvent at the given temperature. Indeed, rotational barriers are solvent-dependent, and differences enantiomerization barriers of 4.5 kJ mol^{-1} for 3-*m*-tolyl-4-*tert*-butylthiazoline-2-thione between isooctane and ethanol at 65.5°C[32] and 12.5 kJ mol^{-1} for *N*-(1-naphthyl)-2(1*H*)-pyrimidinone between xylene and propan-1-ol at 90°C have been reported in the literature.[33] Rotational barriers also vary with temperature depending on the value of the rotational activation entropy ΔS^{+}. Experimental data and treatments of the first-order plots are reported in the Supporting Information.

Table 9 deserves the following comments:

1) The barrier of BINOL itself has been measured three times with values ranging from 155.5 to 174 kJ mol^{-1}, the first of which is probably underestimated. Our results lie in the range of 165.1–169.8 kJ mol^{-1}. Our calculated values (172.9–175.2 kJ mol^{-1}) are about 6.6 kJ mol^{-1} higher ($\Delta\Delta G$ column). As the entity involved in the enantiomerization is the diol, this difference of about 6.5 kJ mol^{-1} is due to the calculations having been carried out in the gas phase. Nevertheless, for the remaining discussion, this deviation is acceptable.

XI.11

Table 9. Experimental barriers determined in this work and calculated ones (all in kJ mol^{-1}).

Species	Solvent	Barrier (Table 8)	Solvent	T [K]	Barrier	Calcd ΔG_T (Table 4)	$\Delta\Delta G$	% pop. at T
neutral	naphthalene	155.5 at 468 K[a]	decan-1-ol	504.25	165.1±0.5	175.2 neutral	−7.8	100
neutral	diphenyl ether	161 at 493 K	1,2-dichlorobenzene	453.15	169.8±0.5	172.9 neutral	−5.4	100
neutral	diglyme/o-xylene (97/3)	174 at 553 K						100
anion	butan-1-ol	135.3 at 391 K	butan-1-ol	385.15	136.2±0.5	120.3 dianion[b]	+15.9	0.7[f]
anion	water	122.3 at 373 K	water	372.25	130–134	119.9 dianion[c]	+12.1	2.0[f]
cation	dioxane/water	129.1 at 373 K	dioxane/water	362.15	127.1±0.5	55.6 dication[d]	+71.5	4.9×10^{-9}
cation	THF	115.4 at 339 K	THF	339.15	125.2±0.5	55.2 dication[e]	+70.0	1.7×10^{-9}

[a] Probably underestimated (see Table 8, footnote [a]). [b] Calculated barrier for the monoanion at 385.15 K: 167.2 kJ mol^{-1}. [c] Calculated barrier for the monoanion at 372.25 K: 167.1 kJ mol^{-1}. [d] Calculated barrier for the monocation at 362.15 K: 149.1 kJ mol^{-1}. [e] Calculated barrier for the monocation at 339.15 K: 148.7 kJ mol^{-1}. [f] The largest population (2.0) corresponds to the most basic experimental conditions (1.25 M), and the lowest (0.7) to the least basic (0.7 M).

2) The new experimental barriers are consistent with those estimated from literature data (the maximum differences of 9.7 and 9.8 kJ mol^{-1} correspond to experiments 5 and 7).
3) The barrier under basic conditions involves the dianion.
4) The barrier under acidic conditions involves the diprotonated C1,C1′ cation. The mechanism of Figure 9 is correct concerning the protonation site (C1), but the rotation involves two sp^3 carbon atoms instead of only one. Experiments under more acidic conditions resulted only in decomposition of BINOL

On the basis of the Winstein–Holness equation,[34] we hypothesized that the difference between the experimental and calculated barriers is due to the presence of a very small amount of the doubly charged species in the solutions. The differences $\Delta\Delta G$ reported in Table 9 were transformed into populations through the equilibrium constants ($\Delta G = -RT\ln K$, where T is the experimental temperature and $R = 8.3145$ J K^{-1} mol^{-1}). They are reasonable for the experiments under basic conditions (2–5% of the dianion) but too low for those under acidic conditions (ca. 10^{-9}% of the dication). The calculations of Table 9 are approximate, but they at least reproduce the fact that more strongly basic conditions (0.7→1.25 M) correspond an increase in the population of the dianion from 0.7 to 2.0%. The error found for BINOL itself ($\approx$6.5 kJ mol^{-1}) cannot be used to correct the values under basic or acidic conditions, and this prevents a more elaborate estimation of the populations.

Conclusion

Intrinsic properties of BINOL such as its acidity ($\Delta_{acid}H^0 \approx 1390$ kJ mol^{-1}) and conformation ($\theta = 102.4°$) were determined in the gas phase by MS and MW spectroscopy, respectively. Solution NMR experiments (^{1}H and ^{13}C) in FSO$_3$H were rationalized as involving the cation monoprotonated on one of the hydroxyl groups. The enantiomerization barriers, which were known from the literature only for neutral BINOL, were determined here for neutral, basic, and acidic conditions. DFT and MP2 calculations were used to rationalize all of the discussed properties (acidity, conformation, protonation position),

especially the enantiomerization barriers, for which the species involved were ascertained (neutral species, dianion, and C21,C1′-diprotonated cation).

In summary: 1) BINOL is one of the largest molecules that has ever successfully been observed at high resolution in the gas phase; 2) The calculations showed that a contribution of the bis-protonated or bis-enolate (phenoxide) form is needed to account for the experimental barriers during acidic or basic catalysis. These forms are not highly populated, but they yielded very low barriers and their contribution, which was not expected, is an adjustable parameter to reproduce the experimental barriers. We hope that the present work will be useful to better understand the behavior not only of BINOL, but also that of the very large family of BINOL derivatives.

Experimental Section

Materials

(±)-BINOL (m.p. 214–217 °C, 99%) and (R)-BINOL (mp. 208–211 °C, 99%) are commercial products (Sigma-Aldrich 104655 and Strem Chemicals 08-1000) that were used without further purification.

Computational details

The geometry of neutral BINOL was optimized at the B3LYP/6-31G(d),[35,36] B3LYP/6-311++G(d,p),[37] M06-2X/6-311++G(d,p),[38] and MP2/6-311++G(d,p)[39] levels of theory. In all cases, frequencies were computed to confirm that the structures obtained correspond to energetic minima, save in the case of the EZ conformer at the MP2/6-311++G(d,p) level due to computational limitations. The exploration of the stationary points of the potential-energy surface of the five species considered here was carried out at the B3LYP/6-31G(d) level of theory and is detailed in the Supporting Information (a total of 23 minima and 30 TSs were located).

The absolute chemical shielding was obtained by using the GIAO method[40] at the B3LYP/6-311++G(d,p)//B3LYP/6-311++G(d,p) level of theory. Previously developed equations were used to obtain the corresponding chemical shifts.[41] All calculations were carried out with the Gaussian 09 package.[42]

XI.12

Determination of intrinsic (gas-phase) acidities by the Cooks extended kinetic method (EKM)

The gas-phase acidity of a protic acid AH, GA(AH), is defined as the Gibbs free-energy change for reaction (9). The corresponding enthalpy and entropy changes are referred to as gas-phase deprotonation enthalpy $\Delta_{acid}H^0$ and deprotonation entropy $\Delta_{acid}S^0$, respectively.

$$AH_{(g)} \rightarrow H^+_{(g)} + A^-_{(g)} \qquad \Delta_{acid}G^0(9) = GA, \Delta_{acid}H^0(9), \Delta_{acid}S^0(9)$$

(9)
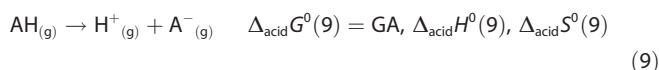
$\Delta_{acid}H^0$, GA, and $\Delta_{acid}S^0$ of BINOL were experimentally determined by means of the EKM[43,44,45,46] by using a triple-quadrupole mass spectrometer (Agilent/Varian MS-320) with an electrospray ionization source (ESI).

EKM takes into account entropic effects on the competitive dissociations of a mass-selected proton-bound heterodimer anions $[A\cdots H\cdots A_{ref(i)}]^-$ (in the gas phase) generated in the ESI source from a solution of a mixture of BINOL (AH) and a reference acid ($A_{ref(i)}H$) of well-known intrinsic GA and $\Delta_{acid}H^0_{ref}$ values. The heterodimers $[A\cdots H\cdots A_{ref(i)}]^-$ are fragmented by collision-induced dissociation (CID) in a collision cell of the spectrometer to yield the corresponding monomeric anions of BINOL (A^-) and the reference acid ($A_{ref(i)}^-$) via the two competitive dissociation channels with rate constants k and k_i, respectively (Figure 10). If secondary fragmentation is negli-
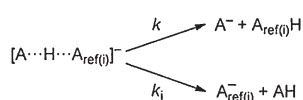
Figure 10. Fragmentation of the heterodimers.

gible, it is assumed that the abundance ratio of these fragment ions is equal to the ratio of the two dissociation rate constants k and k_i. Assuming no reverse activation energy, the acidities of AH and $A_{ref(i)}H$ are related by a linear equation for which a statistical procedure has been developed by Armentrout[44] (see Supporting Information).

Stock solutions ($\approx 10^{-3}$ M in methanol/water 1/1 v/v) of BINOL AH and reference acid $A_{ref(i)}H$ were mixed in appropriate volume ratios ($\approx 1/1$), and further diluted with methanol/water to achieve a final concentration of about 5×10^{-5} M for both BINOL and the reference acid (sample solution). All sample solutions were directly infused into the ESI ionization source in the negative mode at flow rates of 10 $\mu L\,min^{-1}$. ESI conditions, such as needle and capillary voltages, and compressed-air (nebulizing gas) and nitrogen (desolvation and drying gas) temperatures, were optimized to promote the formation of more intense signals of proton-bound heterodimeric anions $[A\cdots H\cdots A_{ref(i)}]^-$. These anions were isolated in the first quadrupole, underwent CID in the second quadrupole, and the resulting fragments analyzed in the third quadrupole. CID MS-MS experiments were performed with argon as collision gas (0.2 mTorr) at various ion kinetic energies in the collision cell. The center of mass energy E_{cm} was calculated as $E_{cm}=E_{lab}[m/(M+m)]$, where E_{lab} is the ion kinetic energy in the laboratory frame, m the mass of the collision gas, and M the mass of the heterodimeric anion.

Five compounds with known GA ranging from 1343.5 to 1364.4 $kJ\,mol^{-1}$ were chosen as reference acids $A_{ref(i)}H$: 4-nitrobenzoic acid, 3-methyl-4-nitrophenol, perfluoro-*tert*-butanol, *m*-trifluoromethylbenzoic acid, and 4-hydroxybenzaldehyde The CID branch-

ing ratios of the product ions were recorded at five collision energies E_{cm} from 2.25 to 3.5 eV. More details of the experimental data obtained using the EKM method for BINOL are described in the Supporting Information.

Rotational spectroscopy (MW)

Rotational spectroscopy was conducted with an FT microwave spectrometer[47] working in the 4–18 GHz frequency range. A BINOL sample was prepared as a solid rod with small addition of a commercial binder and vaporized with a UV picosecond Nd:YAG laser working at 355 nm.[48] The vapor was diluted in neon carrier gas at stagnation pressures of about 2 bar and expanded near-adiabatically in the vacuum chamber of the spectrometer to form a supersonic jet. The rotational transitions were detected in the time domain after short pulsed excitation, and later Fourier-transformed to the frequency domain. The accuracy of the frequency measurements is better than 3 kHz. Transitions separated by less than 6 kHz are resolvable.

NMR experiments

^{1}H and ^{13}C NMR spectra were recorded on a Varian System 500 NMR spectrometer equipped with a 5 mm HCN cold probe, operating at 499.81 and 125.69 MHz, respectively. Chemical shifts are expressed in parts per million (δ scale) downfield from TMS and are referenced to residual peaks of the deuterated NMR solvent or internal TMS. ^{1}H and ^{13}C assignments are based on g-COSY, gHSQC, and gHMBC correlation experiments. A sealed capillary tube (1.4 mm OD, Symta) containing [D$_6$]DMSO (50 mm height) was used as internal standard for experiments in FSO$_3$H. Both in [D$_6$]DMSO and in FSO$_3$H the concentration of ($\pm$)-2,2'-dihydroxy-1,1'-binaphthyl (BINOL) was 0.56 M.

Calculation of the barriers of Table 9

All the reported rotational barriers are the barriers to enantiomerization and not barriers to racemization.[49] An optically enriched sample was heated in the solvent at the chosen temperature. The *ee* variation as a function of time was monitored by chiral HPLC, and the rate constant for enantiomerization $k_{enantiomerisation}$ was determined by plotting the first-order kinetic line according to the equation $\ln(ee_t/ee_{t=0})=-2\,k_{enantiomerisation}t$. In all cases, R^2 was greater than 0.99. $\Delta G^{\ddagger}_{enantiomerization}$ was calculated from the k_{rot} and the Eyring equation.

Acknowledgements

XI.13

[1] a) H. Ishibashi, K. Ishihara, H. Yamamoto, *Chem. Rec.* **2002**, *2*, 177–188; b) K. Ishihara, D. Nakashima, Y. Hiraiwa, H. Yamamoto, *J. Am. Chem. Soc.* **2003**, *125*, 24–25; c) H. Yamamoto, K. Futatsugi, *Angew. Chem.* **2005**, *117*, 1958–1977; *Angew. Chem. Int. Ed.* **2005**, *44*, 1924–1942; d) C. H. Cheon, T. Imahori, H. Yamamoto, *Chem. Commun.* **2010**, *46*, 6980–6982; e) P. Christ, A. G. Lindsay, S. S. Vormittag, J.-M. Neudörfl, A. Berkessel, A. C. O'Donoghue, *Chem. Eur. J.* **2011**, *17*, 8524–8528; f) J. Mendizabal, P. de March, J. Recasens, A. Virgili, Á. Álvarez-Larena, J. Elguero, I. Alkorta, *Tetrahedron* **2012**, *68*, 9645–9651; g) F. Wang, R. Nandhakumar, Y. Hu, D. Kim, K. M. Kim, J. Yoon, *J. Org. Chem.* **2013**, *78*, 11571–11576; h) D. Carmona, M. P. Lamata, P. Pardo, R. Rodríguez, F. J. Lahoz, P. García-Orduña, I- Alkorta, J. Elguero, L. A. Oro, *Organometallics* **2014**, *33*, 616–619; i) X. Zhang, J. Yin, J. Yoon, *Chem. Rev.* **2014**, *114*, 4918–4959.

[2] C.-F. Chen, Z. Li, M. Ai, Y.-M. Chen, *Chin. J. Chem.* **2003**, *21*, 204–207.

[3] E. Masson, *Org. Biomol. Chem.* **2013**, *11*, 2859–2871.

[4] R. Sahnoun, S. Koseki, Y. Fujimura, *J. Mol. Struct.* **2005**, *735–736*, 315–324.

[5] L.-G. Da, T.-T. Lu, M. Xiang, T.-J. He, D.-M. Chen, *Chin. J. Chem. Phys.* **2008**, *21*, 367–375.

[6] V. Setnicka, M. Urbanová, P. Bour, V. Král, K. Volka, *J. Phys. Chem. A* **2001**, *105*, 8931–8938.

[7] R. H. Zheng, D. M. Chen, W. M. Wei, T. J. He, F. C. Liu, *J. Phys. Chem. B* **2006**, *110*, 4480–4486.

[8] Z. Y. Li, D. M. Chen, T. J. He, F. C. Liu, *J. Phys. Chem. A* **2007**, *111*, 4767–4775.

[9] E. P. Kyba, G. W. Gokel, F. de Jong, K. Koga, L. R. Sousa, M. G. Siegel, L. Kaplan, G. D. Y. Sogah, D. J. Cram, *J. Org. Chem.* **1977**, *42*, 4173–4184.

[10] L. Meca, D. Reha, Z. Havlas, *J. Org. Chem.* **2003**, *68*, 5677–5680.

[11] CSD database version 5.33, updates, 2008 (Nov. 2011). F. H. Allen, *Acta Crystallogr. Sect. B* **2002**, *58*, 380–388; F. H. Allen, W. D. S. Motherwell, *Acta Crystallogr. Sect. B* **2002**, *58*, 407–422.

[12] B. Paul, C. Näther, K. M. Fromm, C. Janiak, *CrystEngComm* **2005**, *7*, 309–319.

[13] K. M. Ervin, *J. Am. Soc. Mass Spectrom.* **2002**, *13*, 435–452.

[14] P. Ottaviani, A. Maris, W. Caminati, *J. Mol. Struct.* **2004**, *695–696*, 353–356.

[15] P. Rao, T. N. Pattabiraman, *Anal. Biochem.* **1989**, *181*, 18–22.

[16] A. Cisak, D. Kusztal, E. Brzezinska, *J. Chem. Soc. Perkin Trans. 2* **2001**, 538–544.

[17] Organisches Praktikum OCP II, **2009**, (http://www-oc.chemie.uni-regensburg.de/OCP/ch/chb/ocp2/ocp2/Hinweise_Binol.pdf).

[18] O. F. Aldosari, Synthesis of Some Novel Chiral Dendrimers 1,1-Binaphthyl Derivatives, MSc, School of Chemistry, University of Manchester, **2010**. (https://www.escholar.manchester.ac.uk/api/datastream).

[19] A. Meddour, P. Berdague, A. Hedli, J. Courtieu, P. Lesot, *J. Am. Chem. Soc.* **1997**, *119*, 4502–4508.

[20] G. A. Olah, Y. K. Mo, *J. Org. Chem.* **1973**, *38*, 353–366.

[21] A. Koeberg-Telder, H. J. A. Lambrechts, H. Cerfontain, *Rec. Trav. Chim. Pays-Bas* **1983**, *102*, 293–298.

[22] V. A. Koptyug, L. P. Kamshii, V. I. Mamatyuk, *Izv. Akad. Nauk SSSR Ser. Khim.* **1974**, 1440–1441.

[23] C. Wolf, *Dynamic Stereochemistry of Chiral Compounds: Principles and Applications*, RSC Publishing, The Royal Society of Chemistry, Cambridge, **2008**, p. 91 and 92.

[24] I. Alkorta, J. Elguero, C. Roussel, N. Vanthuyne, P. Piras, *Adv. Heterocycl. Chem.* **2012**, *105*, 1–188; see pages 69 and 70.

[25] D. J. Edwards, R. G. Pritchard, T. W. Wallace, *Tetrahedron Lett.* **2003**, *44*, 4665–4668.

[26] A. K. Yudin, L. J. P. Martyn, S. Pandiaraju, J. Zheng, A. Lough, *Org. Lett.* **2000**, *2*, 41–44.

[27] T. Shimada, A. Kina, T. Hayashi, *J. Org. Chem.* **2003**, *68*, 6329–6337.

[28] G. Bringmann, T. Gulder, T. A. M. Gulder, M. Breuning, *Chem. Rev.* **2011**, *111*, 563–639.

[29] J. E. Davoren, M. W. Bundesmann, Q. T. Yan, E. M. Collantes, S. Mente, D. M. Nason, D. L. Gray, *ACS Med. Chem. Lett.* **2012**, *3*, 433–435.

[30] a) H. Eyring, *J. Chem. Phys.* **1935**, *3*, 107–115; b) J. Sandström, *Dynamic NMR Spectroscopy*, Academic Press, London, **1982**; c) M. P. Sammes, K.-W. Ho, A. R. Katritzky, *Magn. Reson. Chem.* **1985**, *23*, 720–724; d) M. Pérez-Torralba, R. M. Claramunt, M. A. García, C. López, M. C. Torralba, M. R. Torres, I. Alkorta, J. Elguero, *Beilstein J. Org. Chem.* **2013**, *9*, 2156–2167.

[31] a) C. Roussel, N. Vanthuyne, M. Bouchekara, A. Djafri, J. Elguero, I. Alkorta, *J. Org. Chem.* **2008**, *73*, 403–411; b) E. Najahi, N. Vanthuyne, F. Nepveu, M. Jean, I. Alkorta, J. Elguero, C. Roussel, *J. Org. Chem.* **2013**, *78*, 12577–12584.

[32] C. Roussel, A. Djafri, *New J. Chem.* **1986**, *10*, 399–404.

[33] M. Sakamoto, F. Yagishita, M. Ando, Y. Sasahara, N. Kamataki, M. Ohta, T. Mino, Y. Kasashima, T. Fujita, *Org. Biomol. Chem.* **2010**, *8*, 5418–5422.

[34] a) S. Winstein, N. J. Holness, *J. Am. Chem. Soc.* **1955**, *77*, 5562–5578; b) J. I. Seeman, W. A. Farone, *J. Org. Chem.* **1978**, *43*, 1854–1864.

[35] A. D. Becke, *J. Chem. Phys.* **1993**, *98*, 5648–5652. C. Lee, W. Yang, R. G. Parr, *Phys. Rev. B* **1988**, *37*, 785–789.

[36] P. A. Hariharan, J. A. Pople, *Theor. Chim. Acta* **1973**, *28*, 213–222.

[37] M. J. Frisch, J. A. Pople, R. Krishnam, J. S. Binkley, *J. Chem. Phys.* **1984**, *80*, 3265–3269.

[38] Y. Zhao, D. G. Truhlar, *Theor. Chem. Acc.* **2008**, *120*, 215–241.

[39] C. Møller, M. S. Plesset, *Phys. Rev.* **1934**, *46*, 618–622.

[40] R. Ditchfield, *Mol. Phys.* **1974**, *27*, 789–807. F. London, *J. Phys. Radium* **1937**, *8*, 397–409.

[41] A. M. S. Silva, R. M. S. Sousa, M. L. Jimeno, F. Blanco, I. Alkorta, J. Elguero, *Magn. Reson. Chem.* **2008**, *46*, 859–864. F. Blanco, I. Alkorta, J. Elguero, *Magn. Reson. Chem.* **2007**, *45*, 797–800.

[42] Gaussian 09, M. J. Frisch, G. W. Trucks, H. B. Schlegel, G. E. Scuseria, M. A. Robb, J. R. Cheeseman, G. Scalmani, V. Barone, B. Mennucci, G. A. Petersson, H. Nakatsuji, M. Caricato, X. Li, H. P. Hratchian, A. F. Izmaylov, J. Bloino, G. Zheng, J. L. Sonnenberg, M. Hada, M. Ehara, K. Toyota, R. Fukuda, J. Hasegawa, M. Ishida, T. Nakajima, Y. Honda, O. Kitao, H. Nakai, T. Vreven, J. A. Montgomery, Jr., J. E. Peralta, F. Ogliaro, M. Bearpark, J. J. Heyd, E. Brothers, K. N. Kudin, V. N. Staroverov, R. Kobayashi, J. Normand, K. Raghavachari, A. Rendell, J. C. Burant, S. S. Iyengar, J. Tomasi, M. Cossi, N. Rega, J. M. Millam, M. Klene, J. E. Knox, J. B. Cross, V. Bakken, C. Adamo, J. Jaramillo, R. Gomperts, R. E. Stratmann, O. Yazyev, A. J. Austin, R. Cammi, C. Pomelli, J. W. Ochterski, R. L. Martin, K. Morokuma, V. G. Zakrzewski, G. A. Voth, P. Salvador, J. J. Dannenberg, S. Dapprich, A. D. Daniels, Ö. Farkas, J. B. Foresman, J. V. Ortiz, J. Cioslowski, and D. J. Fox, Gaussian, Inc., Wallingford CT, **2009**.

[43] X. H. Cheng, Z. C. Wu, C. Fenselau, *J. Am. Chem. Soc.* **1993**, *115*, 4844–4848.

[44] P. B. Armentrout, *J. Am. Soc. Mass Spectrom.* **2000**, *11*, 371–379.

[45] G. Bouchoux, *Mass Spectrom. Rev.* **2007**, *26*, 775–835.

[46] A. Guerrero, T. Baer, A. Chana, J. González, J. Z. Dávalos, *J. Am. Chem. Soc.* **2013**, *135*, 9681–9690.

[47] E. J. Cocinero, A. Lesarri, P. Écija, J.-U. Grabow, J. A. Fernández, F. Castaño, *Phys. Chem. Chem. Phys.* **2010**, *12*, 12486–12493.

[48] E. J. Cocinero, A. Lesarri, P. Écija, F. J. Basterretxea, J.-U. Grabow, J. A. Fernández, F. Castaño, *Angew. Chem.* **2012**, *124*, 3173–3178; *Angew. Chem. Int. Ed.* **2012**, *51*, 3119–3124.

[49] H. Maskill, *The Physical Basis of Organic Chemistry*, Oxford University Press, **1985**, pages 280–282.

XI.14

exo-2,3-Epoxynorbornane

Structural Distortion of the Epoxy Groups in Norbornanes: A Rotational Study of *exo*-2,3-Epoxynorbornane

Patricia Écija,[a] Iciar Uriarte,[a] Francisco J. Basterretxea,[a] Judith Millán,[b] Alberto Lesarri,[c] José A. Fernández,[a] and Emilio J. Cocinero*[a]

Exo-2,3-epoxynorbornane is studied in the gas phase by pulsed jet Fourier transform microwave spectroscopy in the 4–18 GHz region. Six isotopologues were observed and characterized in their natural abundance. The experimental substitution and effective structures were obtained. Comparison with the structure of norbornane shows significant differences in several bond lengths and valence angles upon introduction of the epoxy group. All the work is supported by quantum chemical calculations.

1. Introduction

Norbornane (bicyclo[2.2.1] heptane, see Figure 1) is a bridged bicyclic ring system with C_{2v} symmetry belonging to the category of strained organic molecules, and is a key compound in
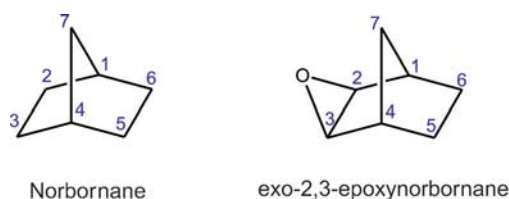
Figure 1. Molecular formula and atom numbering for norbornane and *exo*-2,3-epoxynorbornane.

structural and synthetic chemistry.[1, 2] In this compound, the cyclohexane ring is locked in an envelope configuration by the 7-methylene bridge, producing a strained geometry in which the carbon bond angles depart markedly from the standard $sp/sp^2/sp^3$ values. This distinctive structure is responsible for its high reactivity and unusually high thermochemical bond ener-

gies.[3] For these reasons strained molecules have been the subject of studies to explore the relationships between structure, strain, stability, and reactivity.[4] Moreover, norbornane compounds have been used in pharmaceutical research as synthetic intermediates, receptor agonists and antagonists, and analogues and inhibitors of enzymes.[5] From a structural point of view, this pivotal compound has been the subject of many studies. The crystalline structure[6] and some geometrical data of substituted derivatives have been obtained by X-ray[2] diffraction, but these data are affected by crystal-packing forces. Investigations of the free molecule have been carried out by gas-phase electron diffraction (GED),[7–10] although large correlations were found in its structural parameters. Microwave spectroscopy improved the scope of structure analysis methods;[11] finally, a consistent structure of the isolated molecule was evaluated by joint analysis of electron diffraction, microwave, Raman, and infrared spectroscopy in 1983,[12] which avoided interference from the solvent or crystal matrix.

There are many substituted norbornane derivatives that have key biological roles. However, in some cases their structures remain unknown. The effect of substituents on strained molecules has been investigated, as (de)stabilization of the molecule upon substitution by various types of common electron-withdrawing or -donating substituents can occur,[13, 14] and the substituents can affect the strain energy, heat of formation,[13, 15] or dissociation energies.[16] Since 2010, our group has been engaged in the accurate determination of the structure of systems with bridged bicyclic rings, and so far 2-aminonorbornane,[17] tropinone,[18] scopoline,[19] and even the hydrated complex tropinone···H$_2$O[20] have been studied. Some of these compounds are known for their neurostimulant and anticholinergic activity (i.e. cocaine, atropine). The goal of this work was to evaluate the influence of substituents on the geometry of bridged bicyclic rings. For example, in *exo*-2-aminonorbornane, we concluded that the carbon skeleton provides a rigid framework and the only conformational flexibility arises by rotation of the amino group around the C–N bond. These stud-

[a] Dr. P. Écija, I. Uriarte, Prof. F. J. Basterretxea, Dr. J. A. Fernández, Dr. E. J. Cocinero
Departamento de Química Física
Facultad de Ciencia y Tecnología
Universidad del País Vasco (UPV-EHU)
Apartado 644, 48080 Bilbao (Spain)http://grupodeespectroscopia.es/MW/
E-mail: emiliojose.cocinero@ehu.es

[b] Dr. J. Millán
Departamento de Química
Facultad de Ciencias, Estudios Agroalimentarios e Informática
Universidad de La Rioja
26006 Logroño (Spain)

[c] Prof. A. Lesarri
Departamento de Química Física y Química Inorgánica
Facultad de Ciencias
Universidad de Valladolid
47011 Valladolid (Spain)

XI.17

ies were performed under the isolated conditions of a cold su-
personic jet, which allowed us to elucidate the intrinsic confor-
mations of the free molecules, avoiding solvent and packing
effects. The structures of the most stable conformers were
characterized and determined by Fourier transform microwave
Spectroscopy (FTMW), which provides the most accurate view
of the molecular structure through the measurement of the
moments of inertia. Conformers,[21] tautomers,[22] isotopo-
logues,[23] and enantiomers[24] can be distinguished unambigu-
ously as independent species by using this spectroscopic tech-
nique. In the present paper, we increase the knowledge on the
structure and spectroscopy of molecules with bridged bicyclic
rings by studying *exo*-2,3-epoxynorbornane (Figure 1), which is
the simplest molecule in which the influence of the epoxy
group on the norbornane ring can be discerned. Norbornane
derivatives are known to adapt to induced strain by mecha-
nisms in which the entire skeleton takes part. However, exist-
ing studies have been carried out in the solid state,[25] or by
quantum mechanics calculations.[26,27]

2. Results and Discussion

2.1. Theoretical Calculations

Rotational spectroscopy in combination with quantum chemi-
cal theory provides a powerful strategy to investigate molecu-
lar structure and many examples can be found in the litera-
ture.[21,28–31] A single conformer has been predicted for *exo*-2,3-
epoxynorbornane, as expected from the steric constraints pres-
ent in the bridged bicycle motif. This conformer was optimized
with the Møller–Plesset perturbation (MP2) and density func-
tional theory (B3LYP and M06-2X functionals). The most rele-
vant spectroscopic parameters are shown in Table 1.

2.2. Rotational Spectrum

The theoretical calculations of Table 1 guided the experimental
study. According to these predictions, the analysis of the rota-
tional spectrum was started in the region 8–10 GHz. Inspection
of the rotational spectrum shown in Figure 2 suggests that the
predicted species was present in our supersonic expansion of
Ne. A frequency offset of approximately 60 MHz was observed
between the experimental and theoretical spectra for the first
observed transitions. The most intense lines were ascribed to
a series of μ_a and μ_c *R*-branch asymmetric rotor rotational tran-
sitions of the parent species. The absence of μ_b transitions is
due to the zero electric dipole component along this axis, im-
posed by the C_S symmetry of the molecule. A total of 25 rota-
tional transitions were measured, with 11 ^aR-type, 8 ^cR-type,
and 6 ^aQ-type components. The lower state rotational quan-
tum numbers (J) span the range $0 \leq J \leq 3$ (*R* branch) and $7 \leq J \leq 11$ (*Q* branch), with $0 \leq_{K-1} \leq 2$ (*R* and *Q* branches), $0 \leq_{K+1} \leq 2$ (*R* branch) and $6 \leq_{K+1} \leq 9$ (*Q* branch). The experimental tran-
sitions of the parent species were analyzed with a Watson
semirigid rotor Hamiltonian in the S reduction.[32]

The rotational constants (A, B, C) and four quartic centrifugal
distortion constants (D_J, D_{JK}, D_K, d_1) were determined. A com-

Table 1. Rotational parameters and electric dipole moment components[a] of *exo*-2,3-epoxynorbornane.

	Experiment[c]	Theory[b]		
		MP2	M06–2X	B3LYP
A [MHz]	3759.74628(28)	3772.9	3779.7	3760.6
B [MHz]	2324.90335(16)	2329.1	2341.9	2311.9
C [MHz]	2125.75513(18)	2127.4	2139.8	2113.3
D_J [kHz]	0.1258(78)	0.12	0.12	0.12
D_{JK} [kHz]	0.1042(66)	0.10	0.09	0.09
D_K [kHz]	0.135(53)	0.11	0.12	0.12
d_1 [Hz]	−5.27(45)	−4.14	−4.15	−4.65
d_2 [Hz]	[0.0][d]	−0.23	−0.18	−0.13
$|\mu_a|$/D	intense spectrum	2.06	2.06	2.11
$|\mu_b|$/D	nonobserved	0.00	0.00	0.00
$|\mu_c|$/D	weak spectrum	0.73	0.74	0.74
$|\mu_T|$/D		2.19	2.19	2.24
N[e]	25			
σ [kHz][e]	1.22			

[a] Rotational constants (A, B, C), Watson's quartic centrifugal distortion constants in the S reduction (D_J, D_{JK}, D_K, d_1, d_2), and electric dipole moment components (μ_α, $\alpha = a$, b, c; 1D $\approx 3.336 \times 10^{-30}$ C m) refer to the principal inertial axes. [b] In all the methods standard Pople's triple-ζ 6-311++G(d,p) basis functions were employed. [c] Standard error in pa-rentheses in units of the last digit. [d] Value set to zero in the fit. [e] Number of transitions (N) and root-mean-square deviation (σ) of the fit.
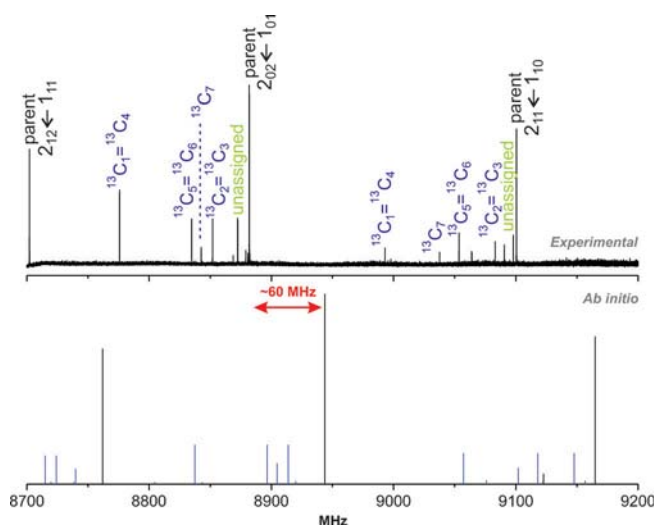
Figure 2. A section of the experimental microwave spectrum (upper trace) and the ab initio (MP2/6-311++G(d,p)) simulation (lower trace) of *exo*-2,3-epoxynorbornane around the 2←1 (J'←J'') rotational transition for the parent and its monosubstituted isotopologues. A shift of ≈60 MHz is ob-served between both spectra. Spectral assignment is shown in the experi-mental spectrum. In the upper spectrum the signal is saturated, so the in-tensity of isotopologues was enhanced 10 times in the ab intio simulation to aid comparison.

parison of experimental data (rotational and centrifugal distor-
tion constants) with the theoretical values is shown in Table 1.
These data unambiguously confirm that the assigned asym-
metric rotor corresponds to the predicted structure of *exo*-2,3-
epoxynorbornane, with discrepancies in the ranges 0.0–0.5 %
(MP2), 0.2–0.7 % (M06-2X), and 0.1–0.7 % (B3LYP), depending
on the theoretical method used to determine A, B, and C. The

XI.18

full list of rotational transitions observed for the parent species is given in the Supporting Information, Table S1. The rotational temperature of the molecules in the supersonic jet was estimated to be ~0.5–1 K from the observed relative intensities in the rotational spectrum.

2.3. Isotopic Species and Structure

Once the rotational transitions of the parent species were removed, a set of weaker lines remained in the rotational spectrum. Later, these were assigned to μ_a and μ_c transitions of the ^{13}C ($\approx 1.1\%$) and ^{18}O ($\approx 0.2\%$) monosubstituted isotopologue species. As evidence of the C_s symmetry of the molecule, the ^{13}C species has three equivalent positions (1/4, 2/3 and 5/6), which gave rise to a degenerate spectrum of double intensity. Detection of the ^{18}O species in natural abundance ($\approx 0.2\%$) demonstrates the good sensitivity of the instrument at the Universidad del País Vasco (UPV/EHU). A typical rotational transition is illustrated in Figure 3 for each of the isotopologues
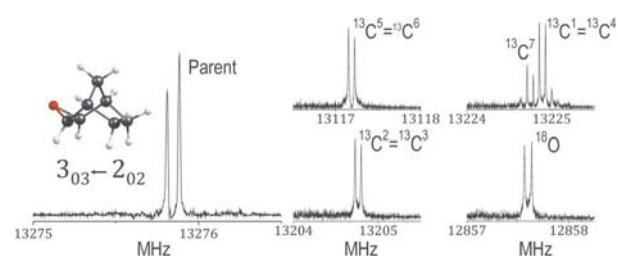
Figure 3. The $3_{0,3} \leftarrow 2_{0,2}$ rotational transition for the parent species and all possible monosubstituted isotopologues of *exo*-2,3-epoxynorbornane. The double intensity of $^{13}C^1 = {}^{13}C^4$ versus $^{13}C^7$, due to the C_s symmetry of the molecule can be noticed. All the transitions show the instrumental Doppler doublet.

observed. These minor species were analyzed with the same procedure used for the parent species. All the measured transitions are collected in the Supporting Information (Table S2), and the corresponding rotational constants are shown in Table 2. Some lines in the spectrum remain unassigned, but they were not identified as belonging to *exo*-2,3-epoxynorbornane.

The spectroscopic data of the isotopologues are consistent with the single structure observed of *exo*-2,3-epoxynorbornane and unambiguously confirm its assignment. A substitution structure (r_s) using Kraitchman's equations and ground-state

Figure 4. a) A comparison of the substitution and ab initio structures (Tables 3 and 4) of *exo*-2,3-epoxynorbornane. The full molecular structure is the MP2 structure. The smaller dark blue spheres are the experimental positions for the heavy atoms. b) A comparison of the substitution structure of *exo*-2,3-epoxynorbornane and ab initio structure of norbornane (Tables 3 and S6). c) Schematic drawing in which the changes in the heavy framework are shown from norbonane to *exo*-2,3-epoxynorbornane.

effective (r_0) coordinates through 27 rotational constants were determined, assuming C_s symmetry. The full heavy structure of *exo*-2,3-epoxynorbornane was resolved and is presented in Table 3. Both experimental structures are compared with the near-equilibrium (r_e) ab initio predictions of *exo*-2,3-epoxynorbornane in Table 3.

The experimental substitution and effective structures of *exo*-2,3-epoxynorbornane are consistent with MP2-predicted equilibrium structure, the largest discrepancy being lower than 1%. All the bond lengths, valence angles, and dihedral angles are shown in Table 3 and the corresponding Cartesian coordinates are given in Table 4. Cartesian coordinates of the MP2- and DFT-calculated structures appear in the Supporting Information (Tables S3–S5). A graphical comparison of r_s and MP2 r_e structures is presented in Figure 4a, where it can be observed that atom positions obtained by both methods are close.

2.4. Discussion

Rotational spectroscopy is the perfect benchmark to validate the theoretical electronic structure methods and to evaluate their predictive abilities. For *exo*-2,3-epoxynorbornane, all the

Table 2. Rotational constants of the monosubstituted isotopologues of *exo*-2,3-epoxynorbornane.[a]					
	$^{13}C^1 = {}^{13}C^4$	$^{13}C^2 = {}^{13}C^3$	$^{13}C^5 = {}^{13}C^6$	$^{13}C^7$	^{18}O
A [MHz]	3737.28998(34)	3721.17223(10)	3735.982720(56)	3707.56531(26)	3759.643(46)
B [MHz]	2297.75833(31)	2323.10102(10)	2313.164280(52)	2304.13527(24)	2246.86791(31)
C [MHz]	2099.68175(27)	2113.750760(86)	2113.997490(45)	2125.22183(95)	2060.34521(30)
N	8	8	8	8	6
σ [kHz]	1.11	0.36	0.19	0.87	0.96
[a] Parameter definition as in Table 1. Centrifugal distortion parameters fixed to the values of the parent species.					

XI.19

Table 3. Structure of *exo*-2,3-epoxynorbornane in the gas phase. The experimental and theoretical structures of norbornane are given for comparison. Bond lengths are in Å and angles in degrees.

	exo-2,3-Epoxynorbornane			Norbornane	
	r_s [a, b,c]	r_0	Ab initio r_e	Experimental[d]	Ab initio r_e
$r(C^1-C^6) = r(C^4-C^5)$	1.558(11)	1.556(5)	1.550	1.536(15)	1.541
$r(C^5-C^6)$	1.562(3)	1.568(4)	1.565	1.573(15)	1.561
$r(C^3-C^4) = r(C^1-C^2)$	1.509(11)	1.523(6)	1.522	1.536(15)	1.541
$r(C^1-C^7) = r(C^4-C^7)$	1.543(5)	1.541(3)	1.538	1.546(24)	1.539
$r(C^2-O) = r(C^3-O)$	1.438(20)	1.445(5)	1.444		
$r(C^2-C^3)$	1.465(4)	1.470(4)	1.471	1.573(15)	1.561
$\measuredangle(C^5-C^4-C^7) = \measuredangle(C^6-C^1-C^7)$	100.6(7)	100.8(3)	101.2	102.04(6)	101.5
$\measuredangle(C^1-C^6-C^5) = \measuredangle(C^4-C^5-C^6)$	103.1(5)	103.1(3)	103.2	102.71	103.1
$\measuredangle(C^1-C^7-C^4)$	94.8(4)	95.1(2)	95.2	93.41(9)	94.6
$\measuredangle(C^3-C^4-C^7) = \measuredangle(C^2-C^1-C^7)$	102.3(6)	102.3(4)	101.9	102.04(6)	101.5
$\measuredangle(C^1-C^2-C^3) = \measuredangle(C^2-C^3-C^4)$	105.5(5)	105.3(4)	105.3	102.71	103.1
$\measuredangle(C^2-O-C^3)$	61.3(11)	61.2(3)	61.2		
$\measuredangle(O-C^2-C^1) = \measuredangle(O-C^3-C^4)$	116.0(18)	115.4(4)	116.0		
$\measuredangle(C^1-C^2-H^2) = \measuredangle(C^4-C^3-H^3)$				121.9	111.7
$\tau(C^1-C^7-C^4-C^5) = -\tau(C^4-C^7-C^1-C^6)$	123.0(10)	123.4(5)	123.9		124.2
$\tau(C^5-C^4-C^3-O) = -\tau(C^6-C^1-C^2-O)$	−45.2(14)	−45.0(4)	−45.2		
$\tau(C^2-C^3-C^4-C^5) = \tau(C^3-C^2-C^1-C^6)$	−108.2(7)	−108.0(4)	−108.2		−108.8
$\tau(C^5-C^6-C^1-C^7) = -\tau(C^6-C^5-C^4-C^7)$	144.3(8)	144.6(4)	144.9		144.8
$\tau(C^2-C^1-C^6-C^5) = -\tau(C^3-C^4-C^5-C^6)$	−109.9(7)	−109.6(4)	−109.7		−108.8
$\tau(C^7-C^4-C^3-O) = -\tau(C^7-C^1-C^2-O)$	−149.6(18)	−149.6(5)	−149.9		
$\tau(O-C^2-C^3-C^4) = -\tau(O-C^3-C^2-C^1)$	−68.6(23)	−69.2(5)	−68.4		
$\tau(C^7-C^1-C^2-H^2) = -\tau(C^7-C^4-C^3-H^3)$				179.9	156.4
$\tau(C^1-C^2-C^3-C^4)$	[0.0]	[0.0]	0.0		0.0
$\tau(C^1-C^6-C^5-C^4)$	[0.0]	[0.0]	0.0		0.0
Θ [e]	104.1	103.8	104.0	113.1	108.3

[a] Substitution (r_s), effective (r_0), and ab initio [MP2/6-311++G(d,p)] equilibrium (r_e) structures. The rest of the parameters were fitted to ab initio values. Bond lengths, valence angle and dihedrals are denoted r, $\measuredangle$, and τ. [b] Errors in parentheses in units of the last digit. [c] In brackets, value set to zero by C_s symmetry. [d] Experimental structure from Ref. [12]. [e] Angle between the $C^1-C^2-C^3-C^4$ and $C^1-C^6-C^5-C^4$ planes.

Table 4. Cartesian coordinates (Å) of the *exo*-2,3-epoxynorbornane atoms for the different structural determinations.[a]

Atom	r_s a/b/c	r_0 a/b/c	r_e a/b/c
C^1	0.249(6)/−1.135(1)/0.337(4)	0.259(2)/−1.137(1)/0.342(3)	0.263/−1.136/0.341
C^2	−0.884(1)/−0.733(2)/−0.575(2)	−0.887(1)/−0.735(1)/−0.578(1)	−0.886/−0.735/−0.574
C^3	−0.884(1)/0.733(2)/−0.575(2)	-0.887(1)/0.735(2)/−0.578(3)	-0.886/0.735/−0.573
C^4	0.249(6)/1.135(1)/0.337(4)	0.259(2)/1.137(1)/0.342(2)	0.262/1.136/0.342
C^5	1.532(1)/0.781(2)/−0.473(3)	1.534(1)/0.784(2)/−0.476(2)	1.533/0.782/−0.474
C^6	1.532(1)/−0.781(2)/−0.473(3)	1.534(1)/−0.784(1)/−0.477(2)	1.533/−0.782/−0.474
C^7	0.251(6)/[0.000]/1.381(1)	0.260(2)/[0.000]/1.382(1)	0.253/0.000/1.378
O	−1.958(1)/[0.000]/0.040(6)	−1.959(1)/[0.000]/0.053(3)	−1.964/0.000/0.047

[a] Parameter definitions as in Table 3.

group. The experimental and theoretical structural parameters of norbornane are shown in Table 3 and Figure 4b and also in Figure 4c to aid the comparison. Cartesian coordinates of norbornane atoms calculated at MP2 level appear in Table S6 of the Supporting Information.

It is clear that the carbon framework is affected by the epoxy group; $r(C^2-C^3)$ and $r(C^1-C^2) = r(C^3-C^4)$ distances are shorter in *exo*-2,3-epoxynorbornane (7% and 2% respectively), whereas $r(C^4-C^5) = r(C^1-C^6)$ are larger (2%) and $r(C^5-C^6)$ and $r(C^4-C^7) = r(C^1-C^7)$ are practically not affected. The reduction in $r(C^2-C^3)$ by ≈ 0.1 Å is a drastic change, as this distance is closer to the value of a C−O bond rather than a C−C bond. Such readjustment is required to create the new three-membered ring in *exo*-2,3-epoxynorbornane and may be caused by the need to decrease the bond angle of the highly strained epoxy group. In addition, the presence of an oxygen atom removes electron density from C^2 and C^3. The distances $r(C^2-C^3)$ and $r(C^2-O) = r(C^3-O)$ are similar with values of 1.465(4) and 1.438(20) Å, respectively. The valence angles $\measuredangle C^2-O-C^3$ and $\measuredangle C^2-C^3-O$ are approximately two degrees apart (61.3° and 59.4°, respectively). These parameters indicate that the shape adopted by the epoxy group is close to an equilateral triangle. The angle between the $C^1-C^2-C^3-C^4$ and $C^1-C^6-C^5-C^4$ planes changed as well from 113.1° (norbonane) to 104.1° (*exo*-2,3-epoxynorbornane). Additionally, H^2 and H^3 atom positions drastically differ from one molecule to the other; valence angles $\measuredangle(C^1-C^2-H^2) = \measuredangle(C^4-C^3-H^3)$ vary from 111.7° (norbonane) to 121.9° (*exo*-2,3-epoxynorbornane) and dihedral angles $\tau(C^7-C^1-C^2-H^2) = -\tau(C^7-C^4-C^3-H^3)$ differ from 156.4° (norbonane) to 179.9° (*exo*-2,3-epoxynorbornane). The dihedral angles are MP2 theoretical values, owing to the lack of D-substitution experimental data. The change in the H^2 and H^3 atom positions can also be observed in Figure 5.

One question that arises is, whether any of the structural changes that result from the introduction of an epoxy group
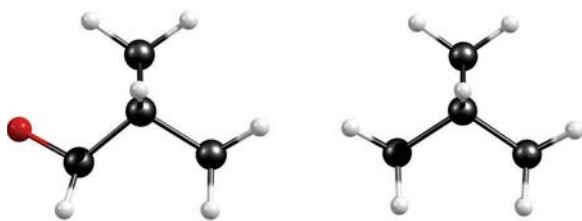
employed methods give satisfactory results with errors lower than 1% for the three rotational constants. MP2 provides the best rotational constants with discrepancies in the range 0.2–0.4%, whereas errors in B3LYP vary between 0.0 and 0.6% for *A*, *B*, and *C*. The M06-2X functional provides the worst results, with differences ranging between 0.5 and 0.7%. Method performance in predicting conformer relative energies cannot be assessed for *exo*-2,3-epoxynorbornane, because of the absence of observed higher energy structures.

In addition, the structure of *exo*-2,3-epoxynorbornane was compared with norbonane to evaluate the effect of the epoxy

XI.20

Figure 5. Top view of *exo*-2,3-epoxynorbornane (left) and norbonane (right). The shift in the positions of the H^2 and H^3 atoms can be noticed in *exo*-2,3-epoxynorbornane.

in norbornane will affect the reactivity of the molecule. Although some of the changes in bond lengths and angles could modify the reactivity of the molecule slightly, the reactivity in both molecules is largely determined by the nature of their functional groups; norbornane is an alkane with low reactivity, whereas the presence of an epoxy group in *exo*-2,3-epoxynorbornane makes it a highly strained and reactive molecule.

Our research group has investigated several bridged bicyclic rings, including 2-aminonorbornane,[17] tropinone,[18] scopoline,[19] but, due to their lack of an epoxy group, a direct structural comparison with *exo*-2,3-epoxynorbornane cannot be carried out. However, there is a reported study of a molecule with an epoxy group for which the structural parameters were obtained, that is 6-oxabiciclo[3.1.0]hexane (OBH);[33] this allows a direct comparison with the present investigation. All the bond lengths are practically equal [i.e. $r(C^2\text{–}C^3) = 1.465(4)$ Å versus 1.463(3) Å, $r(C^2\text{–}O) = r(C^3\text{–}O) = 1.438(20)$ versus 1.439(3) Å, $r(C^1\text{–}C^2) = r(C^3\text{–}C^4) = 1.509(11)$ Å versus 1.508(3) Å, and $r(C^1\text{–}C^6) = r(C^4\text{–}C^5) = 1.558(11)$ Å versus 1.545(4) Å] for *exo*-2,3-epoxynorbornane and OBH respectively. A similar result is observed for the valence angle involving the epoxy group, with $C^2\text{–}O\text{–}C^3 = 61.3(11)°$ versus 61.10(17)°. We can conclude that these are the typical structural parameters of an epoxy group, where the bridged bicyclo rings adapt to the epoxide and not vice versa.

3. Conclusions

To conclude, the use of rotational spectroscopy as a powerful tool to determine molecular structures in isolation conditions was demonstrated for *exo*-2,3-epoxynorbornane. By combining data for the parent species and six minor isotopologues, the experimental structure of the molecule has been obtained. Comparison with the norbonane structure evidences that the introduction of the epoxy group produces significant changes in bond lengths and valence angles. We have also tested the predictive performance of MP2, M06-2X, and B3LYP methods.

Experimental Section

The rotational spectrum of *exo*-2,3-epoxynorbornane was observed using the Fourier-transform microwave spectrometer at UPV/EHU,[34] covering the frequency region of 4–18 GHz. The experimental setup is based on the Balle–Flygare design.[35] In brief, excitation

pulses of 1 μs duration and powers below 150 mW were created by fast (ns) PIN-diode switches acting on a 2–20 GHz centimeter-wave (CW) microwave source. In this way, optimum π/2 polarization conditions were created on the sample, which expanded in a supersonic jet coaxially within a Fabry–Pérot microwave resonator.[36] The resulting transient spontaneous emission (free induction decay) originating from the expanding molecular ensemble was amplified at microwave frequencies and down-converted to the radiofrequency region, where it was digitized and Fourier transformed to yield the frequency-domain spectrum. All the transitions are split, owing to the Doppler effect resulting from the coaxial expansion of the jet. The accuracy of the frequency measurements was estimated to be below 3 kHz. Transitions separated by 7 kHz are resolvable.

A commercial sample of solid *exo*-2,3-epoxynorbornane (97%) was used without further purification. The sample was placed in a metallic reservoir built in a customized injection nozzle and transferred to the gas phase by heating the reservoir with a resistive wire (≈ 185 °C). The vaporized sample was carried to the spectrometer chamber by flowing Ne (99.997%) through the reservoir with stagnation pressures of ≈ 3 bar.

The experimental work was guided and supported by theoretical calculations. We performed ab initio (MP2) and density functional theory (DFT: B3LYP and M06–2X)[37–39] quantum chemical calculations. The most spectroscopically relevant features of the potential energy surface were predicted: equilibrium energies, rotational constants, and dipole moments. Standard Pople's triple-ζ 6–311++G(d,p) basis functions were employed in all the methods, as implemented in the Gaussian 09 software package.[40] The electronic energies were corrected for zero-point vibrational effects calculated within the harmonic approximation. From the experimental rotational constants and the obtained structure of the system we could test the predictive performance of the ab initio and DFT methods.

[1] P. Vollhardt, N. Schore in *Organic Chemistry: Structure and Function*, 6th ed., W. H. Freeman and Company, New York, **2011**.
[2] L. Doms, D. Van Hemerikj, W. Van de Mieroop, A. T. H. Lenbstra, H. J. Geise, *Acta Crys.* **1985**, *B41*, 270.
[3] P. V. R. Schleyer, J. E. Williams, K. R. Blanchard, *J. Am. Chem. Soc.* **1970**, *92*, 2377.
[4] C.-Y. Zhao, Y. Zhang, X.-Z. You, *J. Phys. Chem. A* **1997**, *101*, 5174.
[5] G. Buchbauer, I. Pauzenberger, *Die Pharmazie* **1999**, *54*, 5.
[6] A. N. Fitch, H. Jobic, *J. Chem. Soc. Chem. Commun.* **1993**, *1993*, 1516.
[7] A. Yokozeki, K. Kuchitsu, *Bull. Chem. Soc. Jpn.* **1971**, *44*, 2356.
[8] Y. Morino, K. Kuchitsu, A. Yokozeki, *Bull. Chem. Soc. Jpn.* **1967**, *40*, 1552.
[9] G. Dallinga, L. H. Toneman, *Trav. Chim. Pays-Bas.* **1968**, *87*, 795.

[10] J. F. Chiang, C. F., Jr. Wilcox, S. H. Bauer, *J. Chem. Soc.* **1968**, *90*, 3149.

[11] A. Choplin, *Chem. Phys. Lett.* **1980**, *71*, 503.

[12] L. Doms, L. Van den Enden, H. J. Geise, C. VanAlsenoy, *J. Am. Chem. Soc.* **1983**, *105*, 158.

[13] I. Novak, *Chem. Phys. Lett.* **2003**, *380*, 258.

[14] J. D. Dill, A. Greenberg, J. F. Liebman, *J. Am. Chem. Soc.* **1979**, *101*, 6814.

[15] R. Peverati, J. S. Siegel, K. K. Baldridge, *Phys. Chem. Chem. Phys.* **2009**, *11*, 2387.

[16] Y. Hosoi, T. Yatsuhashi, K. Ohtakeyama, S. Shimizu, Y. Sakata, N. Nakashima, *J. Phys. Chem. A* **2002**, *106*, 2014.

[17] P. Écija, E. J. Cocinero, A. Lesarri, J. Millán, F. Basterretxea, J. A. Fernández, F. Castaño, *J. Chem. Phys.* **2011**, *134*, 164311.

[18] E. J. Cocinero, A. Lesarri, P. Écija, J.-U. Grabow, J. A. Fernández, F. Castaño, *Phys. Chem. Chem. Phys.* **2010**, *12*, 6076.

[19] P. Écija, E. J. Cocinero, A. Lesarri, F. Basterretxea, J. A. Fernández, F. Castaño, *ChemPhysChem* **2013**, *14*, 1830.

[20] P. Écija, M. Vallejo-López, L. Evangelisti, J. A. Fernández, A. Lesarri, W. Caminati, E. J. Cocinero, *ChemPhysChem* **2014**, *15*, 918.

[21] E. J. Cocinero, A. Lesarri, P. Écija, F. J. Basterretxea, J.-U. Grabow, J. A. Fernández, F. Castaño, *Angew. Chem. Int. Ed.* **2012**, *51*, 3119; *Angew. Chem.* **2012**, *124*, 3173.

[22] J. L. Alonso, V. Vaquero, I. Peña, J. C. López, S. Mata, W. Caminati, *Angew. Chem. Int. Ed.* **2013**, *52*, 2331; *Angew. Chem.* **2013**, *125*, 2387.

[23] D. Banser, M. Schnell, J.-U. Grabow, E. J. Cocinero, A. Lesarri, J. L. Alonso, *Angew. Chem. Int. Ed.* **2005**, *44*, 6311; *Angew. Chem.* **2005**, *117*, 6469.

[24] D. Patterson, M. Schnell, J. M. Doyle, *Nature* **2013**, *497*, 475.

[25] C. Altona, M. Sundaralingam, *J. Am. Chem. Soc.* **1970**, *92*, 1995.

[26] J. W. de M. Carneiro, P. R. Seidl, J. G. R. Tostes, C. A. Taft, *J. Mol. Struct. (THEOCHEM)* **1987**, *37*, 281.

[27] P. R. Seidl, K. Z. Leal, J. G. R. Tostes, C. A. Taft, B. L. Hammond, W. A., Jr. Lester, *Chem. Phys. Lett.* **1988**, *147*, 373.

[28] C. Puzzarini, *Phys. Chem. Chem. Phys.* **2013**, *15*, 6595.

[29] H. Mouhib, W. Stahl, M. Luethy, M. Buechel, P. Kraft, *Angew. Chem. Int. Ed.* **2011**, *50*, 5576; *Angew. Chem.* **2011**, *123*, 5691.

[30] J. Thomas, F. X. Sunahori, N. Borho, Y. Xu, *Chem. Eur. J.* **2011**, *17*, 4582.

[31] N. A. Seifert, D. P. Zaleski, C. Pérez, J. L. Neill, B. H. Pate, M. Vallejo-López, A. Lesarri, E. J. Cocinero, *Angew. Chem. Int. Ed.* **2014**, *53*, 3210–3213; *Angew. Chem.* **2014**, *126*, 3274–3277.

[32] J. K. G. Watson in *Vibrational Spectra and Structure,* (Ed: J. R.Durig), Elsevier, Amsterdam, **1977**.

[33] S. Antolínez, A. Lesarri, J. C. López, J. L. Alonso, *Chem. Eur. J.* **2000**, *6*, 3345.

[34] E. J. Cocinero, A. Lesarri, P. Écija, J.-U. Grabow, J. A. Fernández, F. Castaño, *Phys. Chem. Chem. Phys.* **2010**, *12*, 12486.

[35] T. J. Balle, W. H. Flygare, *Rev. Sci. Instrumen.* **1981**, *52*, 33.

[36] J.-U. Grabow, W. Stahl, H. Dreizler, *Rev. Sci. Instrum.* **1996**, *67*, 4072.

[37] F. Jensen, in *Introduction to Computational Chemistry*, John Wiley & Sons, Chichester, UK, **2007**.

[38] Y. Zhao, D. G. Truhlar, *Theor. Chem. Acc.* **2008**, *120*, 215.

[39] Y. Zhao, D. G. Truhlar, *Acc. Chem. Res.* **2008**, *41*, 157.

[40] Gaussian 09 (Revision D.01), M. J. Frisch, G. W. Trucks, H. B. Schlegel, G. E. Scuseria, M. A. Robb, J. R. Cheeseman, G. Scalmani, V. Barone, B. Mennucci, G. A. Petersson, H. Nakatsuji, M. Caricato, X. Li, H. P. Hratchian, A. F. Izmaylov, J. Bloino, G. Zheng, J. L. Sonnenberg, M. Hada, M. Ehara, K. Toyota, R. Fukuda, J. Hasegawa, M. Ishida, T. Nakajima, Y. Honda, O. Kitao, H. Nakai, T. Vreven, J. A. Montgomery Jr., J. E. Peralta, F. Ogliaro, M. Bearpark, J. J. Heyd, E. Brothers, K. N. Kudin, V. N. Staroverov, T. Keith, R. Kobayashi, J. Normand, K. Raghavachari, A. Rendell, J. C. Burant, S. S. Iyengar, J. Tomasi, M. Cossi, N. Rega, J. M. Millam, M. Klene, J. E. Knox, J. B. Cross, V. Bakken, C. Adamo, J. Jaramillo, R. Gomperts, R. E. Stratmann, O. Yazyev, A. J. Austin, R. Cammi, C. Pomelli, J. W. Ochterski, R. L. Martin, K. Morokuma, V. G. Zakrzewski, G. A. Voth, P. Salvador, J. J. Dannenberg, S. Dapprich, A. D. Daniels, O. Farkas, J. B. Foresman, J. V. Ortiz, J. Cioslowski, D. J. Fox, Gaussian, Inc., Wallingford CT, **2009**.

XI.22

Fluoroxene

Potential energy surface of fluoroxene: experiment and theory†

Iciar Uriarte,[a] Patricia Écija,[a] Lorenzo Spada,[ab] Eneko Zabalza,[a] Alberto Lesarri,[c] Francisco J. Basterretxea,[a] José A. Fernández,[a] Walther Caminati[b] and Emilio J. Cocinero*[a]

The potential energy surface (PES) of the general anesthetic fluoroxene (2,2,2-trifluoroethyl vinyl ether) was probed in a supersonic jet expansion using broadband chirped-pulse Fourier transform microwave (CP-FTMW) spectroscopy and theoretical calculations. The PES is dominated by a single conformation, as other stable minima are shown to kinetically relax in the expansion to the global minimum. Consistently, the rotational spectrum reveals a single conformation. Fluoroxene adopts a C_S heavy-atom planar skeleton structure in the gas phase, with a *cis*–*trans* conformation (*cis* for the CH_2=CH–O–CH_2– and *trans* for the =CH–O–CH_2–CF_3 part). The sensitivity of a recently-built CP-FTMW spectrometer at the UPV/EHU is demonstrated by the detection of five isotopologues of fluoroxene in natural abundance, corresponding to the ^{13}C and ^{18}O monosubstituted species. The r_S and r_0 structures were determined and are in good agreement with theoretical predictions using the MP2, B3LYP and M06-2X methods.

Introduction

General anesthetics play a key role in modern medicine and are widely used inhalationally and intravenously in surgical operations nowadays. Despite the common use of these drugs, the details of their mechanism of action are still subject to debate. This controversy is fueled by the large variety of substances that can work as anesthetics, having different shapes, sizes and a large diversity of functional groups in their structures (*i.e.* di- or triatomic gases, ethers, alcohols, haloalkanes, *etc.*). Some of these general anesthetics (such as propofol) seem to work through an interaction with ligand-gated ion channels which would inhibit neuronal synapses.[1,2] However, this cannot be extended to all general anesthetics and further studies about their mechanism of action are needed. Understanding the structure and conformation of anesthetics as well as their preferences for specific intermolecular interactions may provide insight into the modeling of binding sites and docking mechanisms at the protein active sites.

In this sense, the gas phase provides a unique scenario to allow the investigation of the intrinsic molecular properties of anesthetics and their intermolecular binding forces. The lack of interferences from solvent interactions or crystal packing effects makes it possible to study the molecule under isolated conditions and gives access to its conformation and structure in the absence of "external" interactions. Moreover, the use of supersonic expansions allows one to isolate weakly-bound intermolecular complexes and, thus, study intermolecular interactions that govern the binding preferences of anesthetics.

Several spectroscopic techniques have been applied in the gas phase to the structural study of general anesthetics. Mass-resolved laser electronic spectroscopy has been used for the study of species such as propofol[3] and benzocaine,[4] for which several intermolecular complexes and clusters have been analyzed in supersonic expansions.[5,6] This kind of electronic spectroscopy technique allows one to study moderate–large size molecular systems in the gas phase (peptides,[7–10] carbohydrates,[11–14] nucleobase pairs,[15–17] *etc.*) but they require in most cases a chromophore and the conformational assignment is not always unambiguous.

On the other hand, microwave spectroscopy provides the most accurate structural description of molecular systems of small–medium size in the gas phase. Their inherent resolution (sub-Doppler) allows one to unambiguously identify conformers,[18] tautomers,[19] isotopologues[20] and enantiomers[21] as independent species. In addition, the validity of theoretical quantum chemistry methods can be evaluated. The conformational landscape of these molecules and their related intermolecular complexes can be extensively investigated, since the different conformations

[a] *Departamento de Química Física, Facultad de Ciencia y Tecnología, Universidad del País Vasco (UPV/EHU), Campus de Leioa, Ap. 644, E-48080, Bilbao, Spain. E-mail: emiliojose.cocinero@ehu.es; Web: http://www.grupodeespectroscopia.es/MW; Tel: +34 94 601 2529*

[b] *Department of Chemistry, University of Bologna, Via Selmi 2, I-40126, Bologna, Italy*

[c] *Departamento de Química Física y Química Inorgánica, Facultad de Ciencias, Universidad de Valladolid, E-47011, Valladolid, Spain*

† Electronic supplementary information (ESI) available. See DOI: 10.1039/c5cp06522d

3966 | *Phys. Chem. Chem. Phys.*, 2016, **18**, 3966–3974

This journal is © the Owner Societies 2016

XI.25

can be clearly distinguished in the rotational spectrum. In the last few decades, most microwave spectrometers have been based on the original design by Balle and Flygare (Fourier transform microwave, FTMW).[22] For example, the structural properties of the anesthetics sevoflurane[23] and isoflurane[24] were investigated in such spectrometers. The isoflurane–water complex[25] was also studied using FTMW spectroscopy in order to assess the effect of microsolvation on the conformational landscape of the anesthetic. In 2005, Pate introduced a new design for a microwave spectrometer based on chirped pulse (CP) microwave excitation (CP-FTMW).[26] This design overcomes the problem of the narrow bandwidth of conventional FTMW spectrometers and reduces significantly the spectral acquisition time. Thanks to this new instrument, the anesthetic propofol,[27] the sevoflurane dimer[28] and the sevoflurane–benzene complex[29] could be studied in a supersonic expansion; the latter study provides some insights into the molecular recognition properties of this anesthetic.
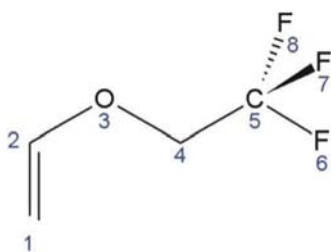
Scheme 1 Structure and atom numbering for the fluoroxene molecule.

Fluoroxene (2,2,2-trifluoroethyl vinyl ether, Scheme 1) exhibits general anesthetic properties and was used as an inhalational anesthetic. In the 1970s, it was removed from the market because of its flammability and toxicity. No further studies were performed to elucidate its mechanism of action, which remains unclear. In 1974, an infrared spectroscopic analysis in the vapor state[30] indicated that the skeleton of the molecule adopts a planar conformation although it was not possible to determine the specific configuration of the vinyl (CH_2=CH–O–CH_2–) and the trifluoroethoxy (=CH–O–CH_2–CF_3) groups (Fig. 1). A low resolution microwave (LRMW) rotational study in 1975[31] suggested a vinyl cis–trifluoroethoxy trans (cis–trans) planar conformation for fluoroxene in the gas phase, discarding any vinyl trans structure. An analysis of the Q branch band head of several μ_b transitions in the LRMW spectrum[32] was later found to be consistent with vinyl cis conformations but was unable to provide information about the trans or gauche conformations for the trifluoroethoxy group. None of these studies were conclusive so the conformation of fluoroxene has remained unclear so far.

The aim of the present work is to carry out an exhaustive exploration of the potential energy surface (PES) of fluoroxene and to unambiguously determine its conformation and structure in the gas phase by means of high resolution rotational spectroscopy in a supersonic expansion. The combination of both techniques allows the study of the isolated molecule and the assessment of its intrinsic conformational and structural preferences.
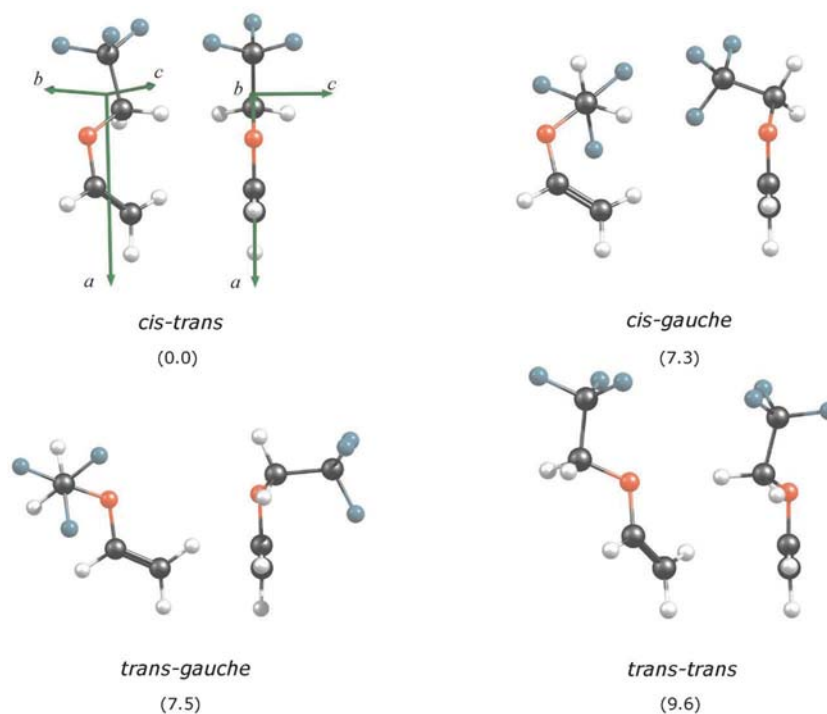
Fig. 1 Lowest-lying conformers of fluoroxene within an energy window in the 0–20 kJ mol^{-1} range (with relative energies (MP2/6-311++G(d,p)/ZPE corrected) in kJ mol^{-1} shown in brackets), front and side views are displayed. The conformers are named as follows: conformation vinyl-conformation trifluoroethoxy.

XI.26

Experimental and computational methods

The rotational spectrum of fluoroxene was measured in a recently built CP-FTMW spectrometer at the University of the Basque Country (UPV/EHU). This instrument is based on Pate's original design[26] and allows the acquisition of the rotational spectra in the 6.0–18 GHz frequency range in a single molecular pulse. Briefly, a 1 μs chirped pulse was generated in an arbitrary waveform generator, covering 11 GHz. This broadband pulse was frequency-upconverted with a broadband mixer and amplified in a travelling wave tube amplifier (250 W). It was later broadcast inside a high vacuum chamber (evacuable down to 10^{-6} mbar) by using a horn antenna. The excitation induces polarization, resulting in a spontaneous molecular emission signal. This emission was collected with the aid of a second horn antenna and sent to a digital oscilloscope with a 20 GHz bandwidth. For each chirped pulse, a 20 μs time domain signal was recorded in the scope. In the current set-up, 10 chirped pulses were used in each molecular pulse.

A commercial sample of fluoroxene (97%) was used without any further purification. The anesthetic is a very volatile liquid (vapour pressure of 381 mbar at 20 °C) with a low boiling point (43 °C). The sample was prepared as a gas mixture of about 0.5% of fluoroxene in Ne : He (80 : 20) and was expanded into the spectrometer vacuum chamber at a stagnation pressure of ∼2 bar.

Theoretical calculations supplemented the experimental work. First, a conformational search was accomplished using a fast molecular mechanics method (Merck Molecular Force Field: MMFFs[33]). Advanced Monte Carlo and large-scale low-mode conformational search algorithms were used to scan the conformational landscape of fluoroxene. Then, all structures within the 0–20 kJ mol^{-1} energy window were fully reoptimized using quantum chemical calculations. We compared the predictive capabilities of several molecular orbital methods, in particular *ab initio* (MP2) and density functional theory (B3LYP and M06-2X) models. In all cases a Pople's triple-ζ 6-311++G(d,p)

basis set was used, as implemented in the Gaussian 09 software package.[34] Relative energies, rotational and centrifugal distortion constants and dipole moments of the lowest lying conformers were predicted. In addition, the PES was evaluated with a grid of 169 calculations at MP2/6-311++G(d,p), varying the torsion angles C_1–C_2–O_3–C_4 and C_2–O_3–C_4–C_5 with a 15° step. Finally, we also estimated the isomerization barriers between different conformers at intervals of 10° at MP2/6-311++G(d,p).

Results

Theoretical calculations

The MP2, M06-2X and B3LYP methods predict that the conformational landscape of fluoroxene in the 0–20 kJ mol^{-1} range exhibits the four minima of Fig. 1. A bidimensional PES was created using the torsion angles C_1–C_2–O_3–C_4 and C_2–O_3–C_4–C_5, which were scanned every 15 degrees. All calculations agree that the C_S-symmetry *cis–trans* conformer is by far the most stable one and it is presumed to dominate the experimental rotational spectrum. The *cis–gauche* conformation suggested in previous works is predicted at an electronic energy of 7.3 kJ mol^{-1} (MP2). The *trans–gauche* and *trans–trans* structures are predicted at electronic energies of 7.5–9.6 kJ mol^{-1} (MP2). The dihedral angles of the three higher energy conformers show some distortion from the tetrahedral structure due to the fluorine atoms. The most relevant predicted spectroscopic parameters of the four conformers are shown in Table 1.

Rotational spectrum

An overview of the experimental spectrum of fluoroxene in the 6.0–18 GHz region is presented in Fig. 2 alongside the MP2 predicted spectra of the lowest-lying conformers. The experimental spectrum is the average of 1 675 600 accumulated spectra after an acquisition time of nearly 48 hours. The spectrum is very congested, consisting of nearly 2200 lines with a signal-to-noise ratio (SNR) ≥ 3/1. Visual inspection suggests

---

Table 1 Predicted rotational constants, dipole moment components and relative energies of the four lowest-lying conformers of fluoroxene at MP2, M06-2X and B3LYP respectively. In all cases the standard Pople's triple-ζ 6-311++G(d,p) basis set was used

	Conformer *cis–trans*	Conformer *cis–gauche*	Conformer *trans–gauche*	Conformer *trans–trans*
A^a/MHz	4393.5/4455.3/4403.1	3756.0/3781.0/3762.1	4178.4/4275.1/4301.9	4919.7/4961.1/4891.8
B/MHz	1121.3/1122.7/1098.9	1398.7/1414.6/1356.1	1226.0/1220.6/1159.0	1011.0/1016.4/1000.0
C/MHz	1067.5/1070.7/1048.9	1278.6/1292.6/1246.8	1189.4/1186.2/1133.9	994.0/997.8/982.5
D_J/kHz	0.067/0.069/0.068	0.27/0.23/0.35	0.55/0.55/0.45	0.052/0.066/0.060
D_{JK}/kHz	1.1/1.3/1.3	0.49/0.60/0.64	−1.4/−1.6/−1.1	2.0/2.0/2.6
D_K/kHz	−0.25/−0.37/−0.33	0.44/0.27/0.56	6.5/7.3/6.6	−0.80/−0.96/−1.5
d_1/Hz	−3.8/−3.4/−3.8	−37.1/−27.5/−55.1	−74.3/−66.2/−49.8	−0.50/0.65/0.54
d_2/Hz	3.7/4.9/3.6	3.9/3.2/5.7	−0.20/−0.66/0.27	0.96/5.7/1.5
P_c/amu Å^2	46.2/45.8/46.4	50.3/50.0/50.8	54.1/53.1/53.9	47.1/46.3/47.2
$|\mu_a|^b$/D	2.2/2.3/2.2	1.4/1.5/1.5	0.7/0.7/0.8	1.8/1.8/1.7
$|\mu_b|$/D	1.4/1.4/1.4	0.0/0.1/0.1	1.0/1.0/0.9	2.1/2.3/2.2
$|\mu_c|$/D	0.0/0.0/0.0	1.5/1.6/1.6	1.7/1.7/1.8	0.9/0,7/0.7
$|\mu_{tot}|$/D	2.6/2.7/2.6	2.1/2.2/2.2	2.1/2.1/2.9	2.9/3.0/2.9
ΔE + ZPE^c/kJ mol^{-1}	0.0/0.0/0.0	7.3/6.9/7.0	7.5/8.1/4.6	9.6/11.3/6.4
ΔG^d/kJ mol^{-1}	0.0/0.0/0.0	8.0/9.0/7.0	5.9/7.6/2.9	7.2/7.6/3.4

^{a} Rotational constants (A, B and C). ^{b} Electric dipole moment components ($|\mu_\alpha|$, α = a, b and c) referred to the principal inertial axis and total electric dipole moment; 1 D ≈ 3.336×10^{-30} C m. ^{c} Electronic energy with the inclusion of zero-point correction. ^{d} Gibbs free-energy at 298 K.
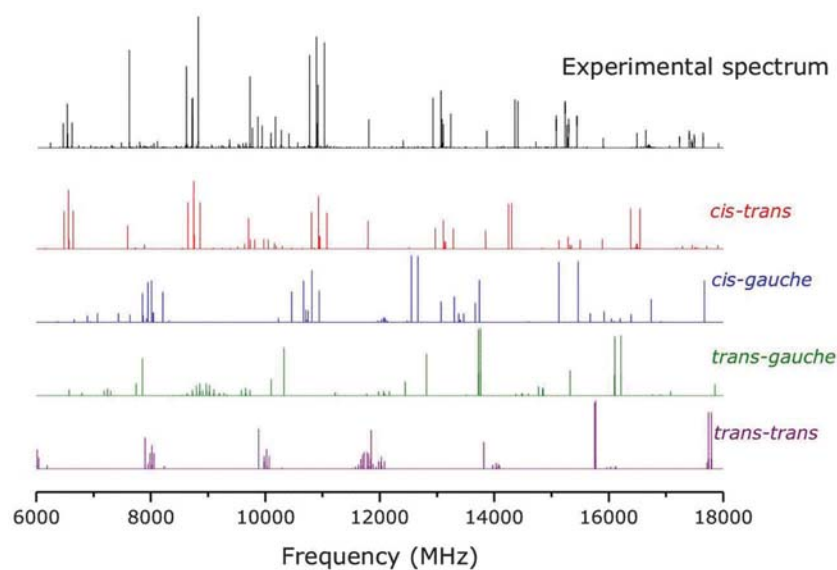

Fig. 2 Experimental rotational spectrum of fluoroxene and predicted MP2 spectra for the four lowest-lying conformers.

that it is dominated by the most stable *cis–trans* species. A total of 190 rotational transitions were fitted to a semirigid asymmetric rotor Hamiltonian in the Watson S-reduction.[35] The most intense transition ($J_{K_{-1},K_{+1}} = 4_{1,3} \leftarrow 3_{1,2}$) had a SNR $\approx$ 13 000/1. A preliminary assignment with a set of 26 ^aR transitions yielded precise values of the B and C rotational constants. A subsequent assignment of 43 μ_b transitions allowed the A rotational constant to be fitted. This permitted the assignment of further transitions, including ^aR, ^aQ, ^bR, ^bQ and ^bP branch lines. The determined rotational and centrifugal distortion constants are summarized in Table 2 alongside the LRMW constants.[32] A comparison between theory (Table 1) and experiment (Table 2) seems to indicate that the observed species is the *cis–trans* conformation of fluoroxene. Table 2 also displays the values of the rotational constants estimated in the LRMW study by Dennison *et al.*[32] with discrepancies >10 MHz for the three rotational constants. The present study clearly improves the accuracy of the previous

results. Relative errors are in the 0.5–0.9%, 0.4–1.6% and 0.2–1.5% ranges for A, B and C respectively depending on the theoretical method. The predicted rotational constants correspond to the equilibrium structure. The largest errors concern the B3LYP calculations, while M06-2X provides the most accurate data. The full list of rotational transitions observed for the parent species is given in the ESI† in Table S1. A comparison between the original spectrum and the result of removing the lines assigned to the parent species of fluoroxene is depicted in Fig. 3, showing that the spectrum is clearly dominated by the *cis–trans* conformer. However, the magnified spectrum presented in Fig. 3 shows that a large number of weaker lines (*ca.* 15 times weaker than the most intense transition of the *cis–trans* conformer) still remain unassigned.

Isotopic species and structure

Once the transitions assigned to the parent species were discarded, a set of approximately 2000 weaker lines (with a SNR $\geq$ 3/1) remained in the spectrum. Among these, a total of 354 transitions were assigned to the ^{13}C (natural abundance $\sim$ 1.1%) and ^{18}O ($\sim$0.2%) monosubstituted isotopologues of fluoroxene. Several μ_a and μ_b transitions of the four singly substituted ^{13}C species and the ^{18}O species could be fitted following the same procedure as in the parent species. Fig. 4 displays the region of the spectrum with the assignment of the $4_{0,4} \leftarrow 3_{0,3}$ transition for the five monosubstituted species. All the transitions assigned to the isotopologues of fluoroxene are shown in the ESI† in Tables S2–S6, and their rotational constants are summarized in Table 3. The isotopic data unambiguously confirm the C_S conformation of the molecule, with all carbons and the oxygen skeleton being contained in the C_S plane as observed in the constant value of the planar moment P_c in Table 3, giving mass extension out of the c axis. It may be noted that the A rotational constant of one of the isotopologues

Table 2 Experimental rotational parameters of the most abundant conformation of fluoroxene and a comparison with previous studies

	This work	Dennison *et al.*[32]
A^a/MHz	4431.82253(27)^d	4421.2(43)
B/MHz	1116.736849(75)	1128.3(196)
C/MHz	1065.058889(76)	1053.7(196)
$D_J{}^b$/kHz	0.06793(21)	
D_{JK}/kHz	1.0772(13)	
D_K/kHz	−0.1356(40)	
d_1/Hz	−3.612(46)	
d_2/Hz	3.028(14)	
P_c/amu Å^2	46.037925(36)	
N^c	190	
σ/kHz	5.8	

^{a} Rotational constants (A, B and C). ^{b} Watson's S-reduction quartic (D_J, D_{JK}, D_K, d_1 and d_2) centrifugal distortion constants and planar moment (P_c). ^{c} Number of transitions (N) and rms deviation of the fit (σ). ^{d} Standard errors in parentheses in units of the last digit.

This journal is © the Owner Societies 2016

Phys. Chem. Chem. Phys., 2016, **18**, 3966–3974 | **3969**

XI.28

Fig. 3 Comparison between the original spectrum of fluoroxene and the result of removing the lines assigned to the *cis–trans* conformer, showing that the most intense lines correspond to this conformer. In the normalized spectrum below it can be clearly seen that a large number of weak rotational transitions still remain.
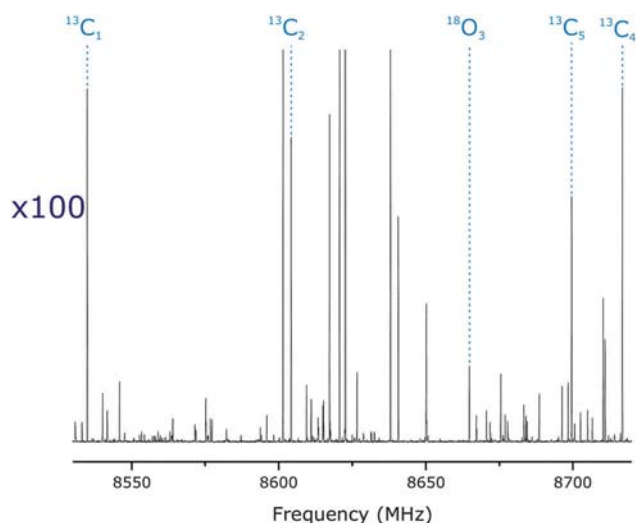
Fig. 4 Assignment of the $4_{0,4} \leftarrow 3_{0,3}$ transition for the different isotopologues of fluoroxene.

calculated from the rotational constants in Tables 2 and 3, assuming C_S symmetry. Both structures are compared to the near-equilibrium (r_e) *ab initio* predictions of fluoroxene in Table 4 (atomic coordinates in Table S7, ESI†). A visual comparison between the predicted (r_e, MP2) and the different meanings of the r_S (closer to the equilibrium values) and r_0 (vibrational ground state) experimental structures is depicted in Fig. 6. Fig. S1–S6 (ESI†, which provide a 3D interactive view) display the correspondence between the r_S and r_0 structures and the MP2, M06-2X and B3LYP predictions, although we are aware that these quantities must be compared with caution.

After removal of the lines assigned to the isotopologues of fluoroxene, a total of 1650 peaks with a SNR $\geq$ 3/1 remain unassigned in the spectrum. Attempts to assign these lines to the higher-energy conformers of fluoroxene proved unsuccessful. Several molecular species may be the cause of this spectrum, among them are the fluoroxene dimer, fluoroxene–water complexes,[37] van der Waals complexes with the carrier gas[38] or decomposition products. Another aspect that should not be overlooked is that the commercial sample contains 3% of impurities. As we were able to detect transitions due to the ^{18}O species ($\sim$0.2%), many observed lines will presumably arise from sample impurities.

(^{13}C$_5$) is slightly larger than that of the parent species due to the proximity of this atom to the *a* principal axis and vibrational effects. A substitution structure (r_S) (arising from Kraitchman's equations)[36] and ground-state effective (r_0) coordinates were

Table 3 Experimental rotational parameters of five isotopologues of fluoroxene detected in natural abundance

	$^{13}C_1$	$^{13}C_2$	$^{13}C_4$	$^{13}C_5$	$^{18}O_3$
A^a/MHz	4412.97690(32)^c	4423.94792(28)	4421.63911(18)	4432.01619(30)	4399.56060(57)
B/MHz	1092.87428(10)	1101.629349(73)	1116.491526(68)	1113.907802(83)	1110.37107(12)
C/MHz	1042.28334(10)	1050.865804(59)	1064.253774(64)	1062.474364(90)	1057.42050(12)
P_c/amu Å^2	46.037680(49)	46.038125(32)	46.039474(30)	46.032982(41)	46.039439(59)
N^b	83	81	67	72	51
σ/kHz	5.8	5.1	3.3	4.8	5.4

^{a} Rotational constants (A, B and C) and planar moment (P_c). Centrifugal distortion constants of the minor isotopologues are fixed to the values of the parent species. ^{b} Number of transitions (N) and rms deviation of the fit (σ). ^{c} Standard errors in parentheses in the units of the last digit.

Table 4 Substitution (r_S), effective (r_0) and calculated (r_e) structures of fluoroxene in the gas phase

	r_S	r_0	r_e (MP2)
$r(C_1–C_2)$/Å	1.335(5)^a	1.343(5)	1.343
$r(C_2–O_3)$/Å	1.365(3)	1.364(4)	1.362
$r(O_3–C_4)$/Å	1.432(8)	1.419(5)	1.407
$r(C_4–C_5)$/Å	1.482(7)	1.508(7)	1.512
$r(C_5–F_6)$/Å		1.343(12)	1.347
$r(C_5–F_7) = r(C_5–F_8)$/Å		1.334(3)	1.339
$\angle(C_1–C_2–O_3)$/deg	127.6(4)	127.2(3)	127.5
$\angle(C_2–O_3–C_4)$/deg	117.1(5)	116.0(3)	115.0
$\angle(O_3–C_4–C_5)$/deg	105.1(4)	106.8(4)	107.4
$\angle(C_4–C_5–F_6)$/deg		108.8(5)	109.0
$\angle(F_6–C_5–F_7) = \angle(F_6–C_5–F_8)$/deg		107.4(4)	107.8
$\tau_1 = \tau(C_1–C_2–O_3–C_4)$/deg	[180.0]^b	[180.0]	180.0
$\tau_2 = \tau(C_2–O_3–C_4–C_5)$/deg	[0.0]	[0.0]	0.0

^{a} Errors in parentheses in units of the last digit. ^{b} Values in brackets were fixed in the fitting.

Discussion

The combination of rotational data and theoretical calculations fully specified the molecular properties of the general anesthetic fluoroxene. A single dominant conformation was observed in the rotational spectrum, with no evidence of higher-energy conformers. We observed that under isolated conditions fluoroxene adopts a *cis–trans* planar conformation of C_S symmetry. This result is consistent with the conclusions of the infrared study by Charles *et al.*[30] which predicted a planar conformation and the low resolution microwave study by True and Bohn,[31] who proposed a *cis–trans* conformation. The present rotational study discards the observation of any *cis–gauche* conformation suggested previously.[32]

The structural observations can be rationalized based on the PES of Fig. 5. Molecular populations in a jet expansion are determined by the global topology of the PES, with the potential barriers between conformations determining whether collisional relaxation is effective in the expansion or individual minima are trapped within their potential wells. In the fluoroxene PES four minima are apparent. However, the most stable *cis–trans* nd *cis–gauche* conformations are connected by tiny potential barriers (3.9 kJ mol^{-1}, panel A in Fig. 5), thus transferring the population to the global minimum. Similarly, the two *trans–gauche* and *trans–trans* species again plausibly converge in a single conformation because of the low interconversion barrier (2.5 kJ mol^{-1}, panel D in Fig. 5). However, conformational relaxation by a torsion of the vinyl group like *trans–trans* to *cis–trans* or *trans–gauche* to *cis–gauche* exhibits larger barriers

(11.1–11.5 in panels B and C of Fig. 5). Previous information on collisional relaxation in jet expansions suggested that barriers between 5 to 12 kJ mol^{-1} may prevent conformational isomerization, depending on the complexity and degrees of freedom of the PES. In consequence, and from the potential energy barriers to conformational interconversion, we can state that *cis–gauche* relaxes to *cis–trans* and *trans–trans* relaxes to *trans–gauche* upon supersonic expansion. A second fluoroxene conformation could be expected, a *trans–gauche* conformer, but would be very depopulated. However, its small abundance and its small μ_a value make it difficult to detect its spectrum.[39]

The planarity of the *cis–trans* molecular skeleton can be explained in terms of a possible conjugation between the oxygen lone pairs and the vinyl group. This resonance effect is strongly favored in a planar conformation, like the one observed in our experiment. Such planarity was observed in other vinyl ethers such as methyl vinyl ether and was attributed to the same conjugation phenomenon.[40,41] Although the *cis* conformation of the vinyl group in fluoroxene may show larger steric hindrance than the *trans*, it is also the preferred form in several vinyl ethers such as methyl vinyl ether[40–42] or ethyl vinyl ether.[43,44] This effect was attributed to the smaller electrostatic repulsion between the lone pair electrons of the oxygen and the π electrons of the double bond in the *cis* configuration.[45]

Besides fluoroxene, other halogenated ethers that also display general anesthetic properties were investigated in the gas phase by rotational spectroscopy. Only one conformer was detected for sevoflurane,[23] whereas two conformers were observed for isoflurane in the gas phase.

The absence of internal rotation hyperfine effects in the spectrum of fluoroxene can be explained due to the large moment of inertia of the CF$_3$ internal rotor, for which the predicted internal rotation barrier is 19 kJ mol^{-1} at the MP2/6-311++G(d,p) level.

Furthermore, accurate values of the rotational and centrifugal distortion constants, together with the molecular structure, were determined in the present study for the first time, by analyzing the data of the parent species and five isotopologues in natural abundance. Assignments and measurements of the rotational spectra of the 5 isotopologues of fluoroxene arising from ^{13}C and ^{18}O substitution in natural abundance with good SNR proves the sensitivity of the CP-FTMW spectrometer. The determined substitution (r_S) and effective (r_0) structures of the molecular skeleton of fluoroxene, despite not being directly comparable with the equilibrium theoretical predictions, are in excellent agreement with the MP2 calculation, with the
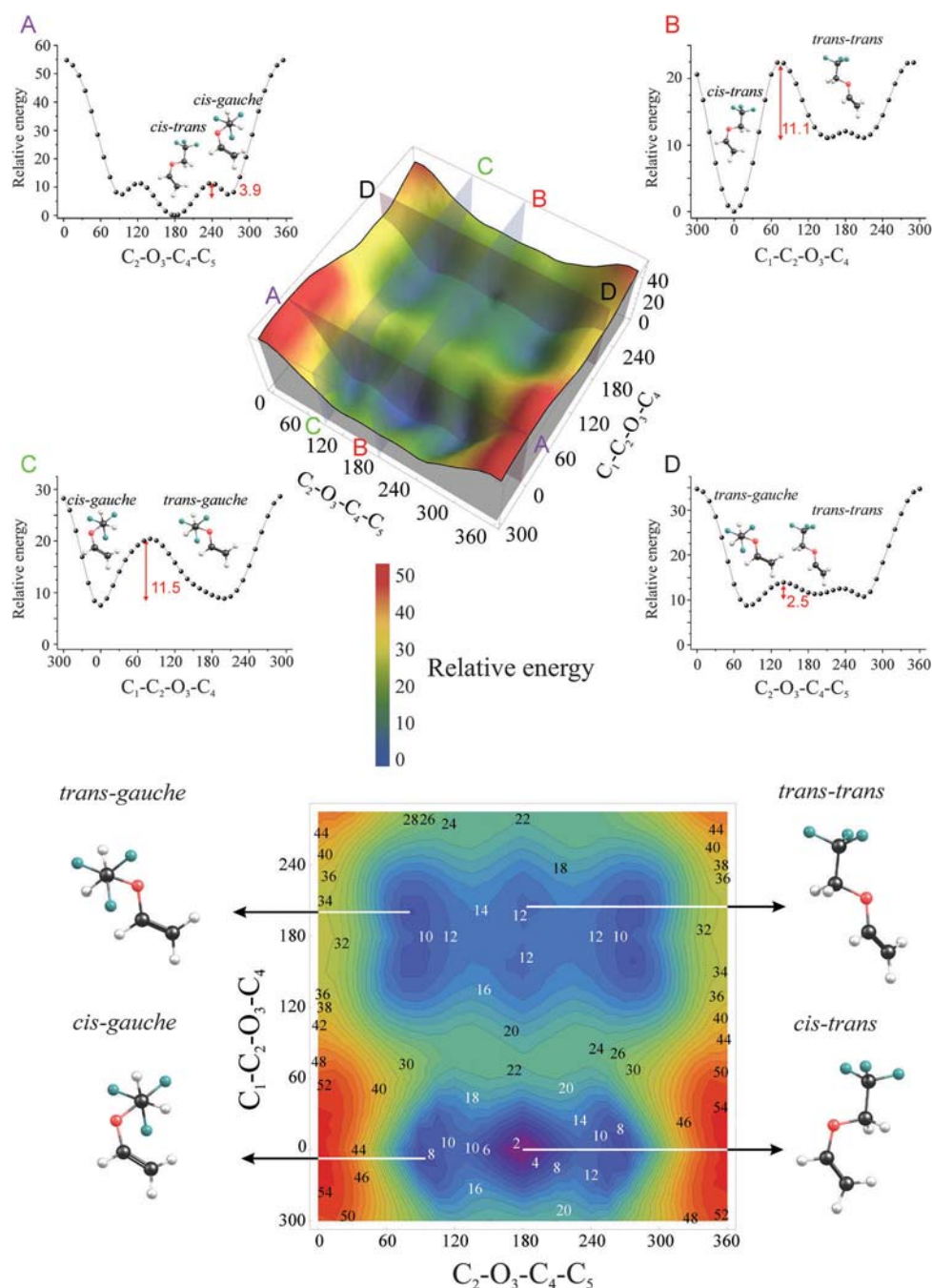
XI.30

Fig. 5 The *ab initio* (MP2/6-311++G(d,p)) PES of fluoroxene shows two wells and four distinct local minima. The independent variables correspond to the torsion angles $C_1-C_2-O_3-C_4$ and $C_2-O_3-C_4-C_5$ defined in Scheme 1 (energies in kJ mol^{-1}, angles in degrees).
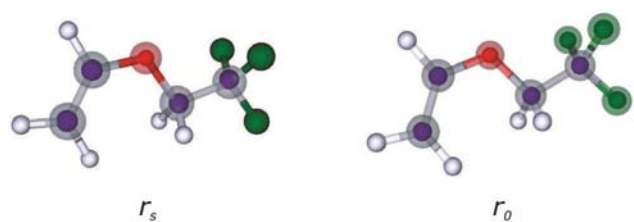

Fig. 6 Experimental structures (r_S and r_0) of fluoroxene compared to the *ab initio* structure (MP2/6-311++G(d,p) level). The larger spheres (transparent and/or solid) are the theoretical positions, while the smaller solid spheres represent the experimental structures.

discrepancies ranging between 0.0 and 2.2%. There are only two parameters with relative errors greater than 2%: the C_4-C_5 distance (2.0%) and the $O_3-C_4-C_5$ angle (2.2%) (MP2 predictions compared to r_S). These two parameters involve atoms (in particular, C_4 and C_5) lying close to one of the principal axes, which explains the larger uncertainties for these values.

Finally, the present structural study serves as a basis for future microsolvation and molecular recognition investigations about intermolecular complexes with the aim of shedding light on the structure–activity relationship of these kinds of drugs.

Acknowledgements

References

1 N. P. Franks and W. R. Lieb, *Nature*, 1994, **367**, 607–614.

2 P.-L. Chau, *Br. J. Pharmacol.*, 2010, **161**, 288–307.

3 I. Leon, E. J. Cocinero, J. Millán, A. M. Rijs, S. Jaeqx, A. Lesarri, F. Castaño and J. A. Fernández, *Phys. Chem. Chem. Phys.*, 2012, **14**, 4398–4409.

4 E. Aguado, A. Longarte, E. Alejandro, J. A. Fernández and F. Castaño, *J. Phys. Chem. A*, 2006, **110**, 6010–6015.

5 I. León, J. Millán, E. J. Cocinero, A. Lesarri and J. A. Fernández, *Angew. Chem., Int. Ed.*, 2013, **52**, 7772–7775.

6 E. Aguado, I. Leon, J. Millan, E. J. Cocinero, S. Jaeqx, A. M. Rijs, A. Lesarri and J. A. Fernandez, *J. Phys. Chem. B*, 2013, **117**, 13472–13480.

7 E. Gloaguen, B. de Courcy, J.-P. Piquemal, J. Pilmé, O. Parisel, R. Pollet, H. S. Biswal, F. Piuzzi, B. Tardivel, M. Broquier and M. Mons, *J. Am. Chem. Soc.*, 2010, **132**, 11860–11863.

8 J. A. Stearns, O. V. Boyarkin and T. H. Rizzo, *J. Am. Chem. Soc.*, 2007, **129**, 13820–13821.

9 E. J. Cocinero, E. Stanca-Kaposta, D. P. Gamblin, B. G. Davis and J. P. Simons, *J. Am. Chem. Soc.*, 2009, **131**, 1282–1287.

10 I. Compagnon, J. Oomens, G. Meijer and G. von Helden, *J. Am. Chem. Soc.*, 2006, **128**, 3592–3597.

11 E. J. Cocinero, E. C. Stanca-Kaposta, E. M. Scanlan, D. P. Gamblin, B. G. Davis and J. P. Simons, *Chem. – Eur. J.*, 2008, **14**, 8947–8955.

12 E. J. Cocinero, P. Çarçabal, T. D. Vaden, J. P. Simons and B. G. Davis, *Nature*, 2011, **469**, 76–79.

13 E. J. Cocinero, D. P. Gamblin, B. G. Davis and J. P. Simons, *J. Am. Chem. Soc.*, 2009, **131**, 11117–11123.

14 E. J. Cocinero, E. C. Stanca-Kaposta, M. Dethlefsen, B. Liu, D. Gamblin, B. Davis and J. Simons, *Chem. – Eur. J.*, 2009, **15**, 13427–13434.

15 D. Sivanesan, I. Sumathi and W. J. Welsh, *Chem. Phys. Lett.*, 2003, **367**, 351–360.

16 E. Nir, C. Janzen, P. Imhof, K. Kleinermanns and M. S. de Vries, *Phys. Chem. Chem. Phys.*, 2002, **4**, 732–739.

17 E. Nir, K. Kleinermanns and M. S. de Vries, *Nature*, 2000, **408**, 949–951.

18 E. J. Cocinero, A. Lesarri, P. Écija, F. J. Basterretxea, J.-U. Grabow, J. A. Fernández and F. Castaño, *Angew. Chem., Int. Ed.*, 2012, **51**, 3119–3124.

19 J. L. Alonso, V. Vaquero, I. Peña, J. C. López, S. Mata and W. Caminati, *Angew. Chem., Int. Ed.*, 2013, **52**, 2331–2334.

20 D. Banser, M. Schnell, J.-U. Grabow, E. J. Cocinero, A. Lesarri and J. L. Alonso, *Angew. Chem., Int. Ed.*, 2005, **44**, 6311–6315.

21 D. Patterson, M. Schell and J. M. Doyle, *Nature*, 2013, **497**, 475–477.

22 T. J. Balle and W. H. Flygare, *Rev. Sci. Instrum.*, 1981, **52**, 33–45.

23 A. Lesarri, A. Vega-Toribio, R. D. Suenram, D. J. Brugh and J.-U. Grabow, *Phys. Chem. Chem. Phys.*, 2010, **12**, 9624–9631.

24 A. Lesarri, A. Vega-Toribio, R. D. Suenram, D. J. Brugh, D. Nori-Shargh, J. E. Boggs and J.-U. Grabow, *Phys. Chem. Chem. Phys.*, 2011, **13**, 6610–6618.

25 Q. Gou, G. Feng, L. Evangelisti, M. Vallejo-López, L. Spada, A. Lesarri, E. J. Cocinero and W. Caminati, *Chem. – Eur. J.*, 2014, **20**, 1980–1984.

26 G. G. Brown, B. C. Dian, K. O. Douglass, S. M. Geyer, S. T. Shipman and B. H. Pate, *Rev. Sci. Instrum.*, 2008, **79**, 053103.

27 A. Lesarri, S. T. Shipman, J. L. Neill, G. G. Brown, R. D. Suenram, L. Kang, W. Caminati and B. H. Pate, *J. Am. Chem. Soc.*, 2010, **132**, 13417–13424.

28 N. A. Seifert, C. Pérez, J. L. Neill, B. H. Pate, M. Vallejo-López, A. Lesarri, E. J. Cocinero and F. Castaño, *Phys. Chem. Chem. Phys.*, 2015, **17**, 18282–18287.

29 N. A. Seifert, D. P. Zaleski, C. Pérez, J. L. Neill, B. H. Pate, M. Vallejo-López, A. Lesarri, E. J. Cocinero, F. Castaño and I. Kleiner, *Angew. Chem., Int. Ed.*, 2014, **53**, 3210–3213.

30 S. W. Charles, F. C. Cullen and N. L. Owen, *J. Chem. Soc., Faraday Trans. 2*, 1974, **70**, 483–491.

31 N. S. True and R. K. Bohn, *J. Chem. Phys.*, 1975, **62**, 3951–3954.

32 F. T. Dennison, C. W. Gillies and S. J. Borchert, *J. Chem. Phys.*, 1981, **75**, 3238–3251.

33 T. A. Halgren, *J. Comput. Chem.*, 1999, **20**, 730–748.

34 M. J. Frisch, G. W. Trucks, H. B. Schlegel, G. E. Scuseria, M. A. Robb, J. R. Cheeseman, G. Scalmani, V. Barone, B. Mennucci, G. A. Petersson, H. Nakatsuji, M. Caricato, X. Li, H. P. Hratchian, A. F. Izmaylov, J. Bloino, G. Zheng, J. L. Sonnenberg, M. Hada, M. Ehara, K. Toyota, R. Fukuda, J. Hasegawa, M. Ishida, T. Nakajima, Y. Honda, O. Kitao, H. Nakai, T. Vreven, J. A. Montgomery, Jr., J. E. Peralta, F. Ogliaro, M. Bearpark, J. J. Heyd, E. Brothers, K. N. Kudin, V. N. Staroverov, R. Kobayashi, J. Normand, K. Raghavachari, A. Rendell, J. C. Burant, S. S. Iyengar, J. Tomasi, M. Cossi, N. Rega, J. M. Millam, M. Klene, J. E. Knox, J. B. Cross, V. Bakken, C. Adamo, J. Jaramillo, R. Gomperts, R. E. Stratmann, O. Yazyev, A. J. Austin, R. Cammi, C. Pomelli, J. W. Ochterski, R. L. Martin, K. Morokuma, V. G. Zakrzewski, G. A. Voth, P. Salvador, J. J. Dannenberg, S. Dapprich, A. D. Daniels, Ö. Farkas, J. B. Foresman, J. V. Ortiz, J. Cioslowski and D. J. Fox, *Gaussian 09*, Gaussian, Inc., Wallingford CT, 2009.

35 J. K. Watson, in *Vibrational Spectra and Structure*, ed. J. R. Durig, Elsevier, Amsterdam, 1977, vol. 6, pp. 1–89.

36 H. D. Rudolph, in *Advances in Molecular Structure Research*, ed. M. Hargittai and I. Hargittai, JAI Press, Greenwich-Connecticut, 1995, vol. 1, pp. 63–114.

XI.32

37 C. Pérez, M. T. Muckle, D. P. Zaleski, N. A. Seifert, B. Temelso, G. C. Shields, Z. Kisiel and B. H. Pate, *Science*, 2012, **336**, 897–901.

38 A. Dell'Erba, S. Melandri, A. Millemaggi, W. Caminati and P. G. Favero, *J. Chem. Phys.*, 2000, **112**, 2204–2209.

39 T. Emilsson, T. C. Germann and H. S. Gutowsky, *J. Chem. Phys.*, 1992, **96**, 8830–8839.

40 N. L. Owen and N. Sheppard, *Trans. Faraday Soc.*, 1964, **60**, 634–645.

41 J. R. Durig and D. A. C. Compton, *J. Chem. Phys.*, 1978, **69**, 2028–2035.

42 A. C. Fantoni, W. Caminati and R. Meyer, *J. Chem. Phys.*, 1987, **86**, 1848–1857.

43 M. Hayashi and N. Inada, *J. Mol. Spectrosc.*, 1994, **165**, 195–204.

44 N. L. Owen and G. O. Sorensen, *J. Phys. Chem.*, 1979, **83**, 1483–1488.

45 J. Liu, S. Niwayama, Y. You and K. N. Houk, *J. Org. Chem.*, 1998, **63**, 1064–1073.

XI.33

Methyl β-D-ribofuranoside

COMMUNICATION

Furanosic forms of sugars: conformational equilibrium of methyl β-D-ribofuranoside†

Patricia Écija,[a] Iciar Uriarte,[a] Lorenzo Spada,[ab] Benjamin G. Davis,[c]
Walther Caminati,[b] Francisco J. Basterretxea,[a] Alberto Lesarri*[d] and
Emilio J. Cocinero*[a]

The investigation of an isolated ribofuranose unit in the gas phase reveals the intrinsic conformational landscape of the biologically active sugar form. We report the rotational spectra of two conformers of methyl β-D-ribofuranoside in a supersonic jet expansion. Both conformers adopt a near twisted ($^3T_2$) ring conformation with the methoxy and hydroxymethyl substituents involved in various intramolecular hydrogen bonds.

Sugars are flexible polymorphic species, exhibiting complex constitutional, configurational and conformational isomerism. The intramolecular reaction between carbonyl (typically reducing terminus) and hydroxyl groups gives rise to cyclic hemiacetal/ketals, particularly stable for five- or six-membered ring forms (furanose or pyranose, respectively, Scheme 1). Large amplitude motions, like ring puckering, inversion or pseudorotation, combine with the internal rotation of the hydroxyl groups to produce a rich conformational landscape, even in the most elementary monosaccharide units. A recent microwave spectroscopy study on ribose proved that this aldopentose is a pyranose (1) in the gas-phase, with six coexisting low-energy ($\Delta E < 6$ kJ mol^{-1}) conformers differing in ring conformation ($^1C_4$ or $^4C_1$) and epimerization (α/β).[1] Other rotational[2] and vibrational[3] studies of five- or six-carbon monosaccharides also confirmed the pyranose preference of free molecules, which had also been previously observed in the crystal[4,5] and liquid phases.[6] However, the preferred ribopyranose form starkly contrasts with the biological use of five-membered β-ribofuranose rings (2).

Ribofuranoside rings play different biochemical functions. In most species they appear as informational molecules and catalysts
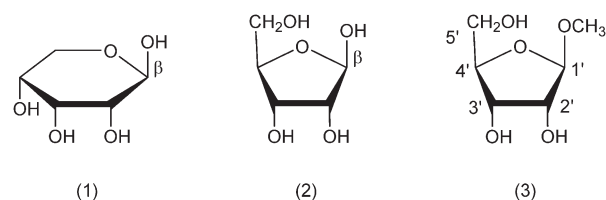
Scheme 1 The pyranose (1) and furanose (2) constitutional isomers of ribose, together with methyl-β-D-ribofuranoside (3), in Haworth projection.

(RNA), as substrates (ATP or sugar-diphospho-nucleosides), or as cofactors (NAD(P) or NAD(P)H).[7] Remarkably, their roles are often critical: DNA analogues in which the furanose rings are exchanged by pyranoses produce double helices with much stronger base pairing, but are unsuitable to replace DNA.[8] The biochemical functionality in ribose-based biomolecules probably relies on multiple related factors and functional optimization does not necessarily correlate with simple properties in the ground state. Changes in the furanose conformation can also critically modulate the ability of nucleosides to act as substrates with enzymes associated with disease processes, *e.g.* HIV-1 reverse transcriptase.[9] Furanosides also appear as part of oligosaccharides in plants and microbial organisms like bacteria, fungi and parasites, although not in humans or in mammals.[10]

Ultimately, the evolutionary preference for furanoses in RNA and other biomolecules may have a chemical origin, associated perhaps with the greater or differing flexibility of the five-membered ring. Saturated five-membered rings are structurally unique, as the small differences in energy between twisted and envelope forms give rise to pseudorotation, a quasi-monodimensional large-amplitude-motion in which the puckering rotates around the ring.[11] The furanose ring-puckered species thus may interconvert without passing through the planar species, making it difficult to specify conformational properties and pseudorotation pathways. The first pseudorotation model for nucleosides was developed by Altona and Sundaralingam (AS).[12] Cremer and Pople (CP) later solved the puckering problem using vibrational analysis and developed systematic curvilinear CP coordinates,[13] generally applicable to

[a] Departamento de Química Física, Facultad de Ciencia y Tecnología,
Universidad del País Vasco (UPV/EHU), Apartado 644, 48080 Bilbao, Spain.
E-mail: emiliojose.cocinero@ehu.eus

[b] Dipartimento di Chimica "G. Ciamician", Università di Bologna, Via Selmi 2,
1-40126 Bologna, Italy

[c] Department of Chemistry, University of Oxford, Mansfield Road, Oxford, OX1 3TA, UK

[d] Departamento de Química Física y Química Inorgánica, Universidad de
Valladolid, 47011 Valladolid, Spain. E-mail: lesarri@qf.uva.es

† Electronic supplementary information (ESI) available: Rotational transitions
and theoretical predictions. See DOI: 10.1039/c6cc01180b

any cycloalkane. Both models define furanoside puckering in terms of amplitude (q) and phase coordinates (φ_{AS} and φ_{CP} phase conventions are shifted by a constant angle). Noticeably, a first survey of crystal structures revealed that furanoside conformations in nucleosides display a bimodal distribution,[14] with two preferred puckering regions around $\varphi_{CP} = 288°$ ($\varphi_{AS} = 18°$, envelope $^3E \equiv C_3'\text{-}endo$)[15] $\varphi_{CP} = 72°$ ($\varphi_{AS} = 162°$, envelope $^2E \equiv C_2'\text{-}endo$). This two-state model has been instrumental for puckering determination in solution using NMR vicinal spin–spin coupling parameters.[16] More recent structural investigations on furanose glycosides showed a similar clustering in the conformational space, but they were heavily dependent on the pentose configuration.[10] In particular, β-ribofuranosides are located around the puckering phases of $\varphi_{CP} = 252°$ (envelope E_2) in the solid state. Recurrently, the question thus arises: does the furanose conformation in the crystal or solution reflect the intrinsic ring puckering properties, or is it imposed by the environment?

We answer this question by exploring the molecular structure of the five-membered ring unit of an isolated monosaccharide in the gas-phase. We analyzed methyl β-D-ribofuranoside (3) using a combination of chemical synthesis, microwave spectroscopy, supersonic jet expansion techniques, ultrafast laser vaporization and computational methods. The target pentose was specifically synthesized (see the ESI†) to lock the molecule as a five-membered ring, preventing the formation of the pyranose form dominant in the gas phase. Our main objectives include the observation of conformational preferences of furanose forms in C5 and C6 sugars, the determination of the number of coexisting species of the free molecule, and the comparison with the structural data in condensed phases. The conformational landscape was explored at different levels, including ring-puckering preferences, dynamics of the hydroxyl and hydroxymethyl groups, intramolecular hydrogen bonding and internal rotation of the methyl group. Our results give a valuable perspective on the intrinsic structural preferences of this biologically important aldopentofuranose, clarifying previous X-ray and neutron diffraction,[17] NMR[18] and *ab initio* data.[19]

The computational study included a comprehensive conformational search combining molecular mechanics (MMFFs) and special search algorithms based on stochastic and vibrational mode analysis,[20] together with *ab initio* (MP2) and density-functional-theory (M06-2X, B3LYP) molecular orbital reoptimizations, which refined the initial estimations. The final conformational energies and rotational constants are in Tables S1 and S2 (ESI†), while Table 1 gives the puckering properties, dipole moments and Gibbs energies for the six conformers with energies within 5 kJ mol⁻¹.

The calculated conformational stabilities were checked against the experimental microwave spectrum in the 6–14 GHz frequency region. The molecular jet was probed using a Fourier-transform microwave (FT-MW) spectrometer equipped with an UV ultrafast laser vaporization system[1] (experimental details in the ESI†). Two different sets of rotational transitions were independently assigned (Fig. 1). The first set was composed exclusively of R-branch ($J + 1 \leftarrow J$) μ_c-type transitions, with angular momentum quantum numbers spanning values $J = 2$–6. The second set included only R-branch μ_b-type rotational transitions ($J = 2$–7).

Table 1   Prediction of conformational energies for methyl β-D-ribofuranoside

Species[a]	ΔG^b/kJ mol⁻¹	q^c/Å	φ/deg	$\mu_a{}^d$/D	μ_b/D	μ_c/D
1 ($^3T_2$)	0.0/0.0/0.0	0.385	264.7	0.0	−0.3	−1.2
2 ($^3T_2$)	0.8/1.2/0.9	0.397	260.7	−0.9	−3.5	−0.9
3 ($^3T_2$)	2.9/0.4/2.2	0.397	266.4	−1.6	−3.5	1.7
4 (E_2)	3.5/4.6/2.9	0.400	252.3	1.3	−4.1	0.7
5 (^2E)	3.7/2.0/1.5	0.382	62.7	−2.1	−0.3	−0.5
6 (E_2)	4.9/5.0/3.6	0.391	247.8	−0.9	−1.4	2.9

[a] Conformational notation in ref. 15. [b] MP2/M06-2X/B3LYP calculations with a 6-311++G(d,p) basis set; relative Gibbs free energies at 298 K. [c] Cremer–Pole puckering parameters defined in ref. 13. [d] Electric dipole moment components (μ_a, μ_b, μ_c).
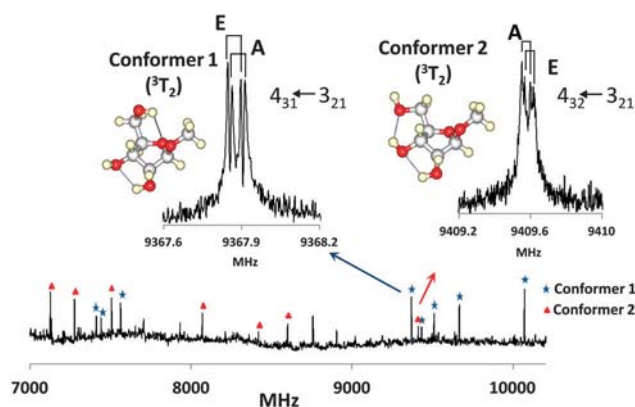

Fig. 1 A section of the experimental spectrum of methyl β-D-ribofuranoside in the region 7–10 GHz, with two typical rotational transitions split by internal rotation of the methyl group (each transition additionally split by Doppler effect).

Both datasets were mutually exclusive and they clearly corresponded to two different carrier species. Their similarity in rotational constants suggested that they are indeed isomers of the same molecule. Some of the observed lines showed small hyperfine effects for the two species, splitting some individual transitions into two close components separated by less than 20 kHz.

The hyperfine effects were attributed to the internal rotation of the *O*-1 methyl group in the ribofuranoside, detectable in the rotational spectra for small or moderate potential energy barriers.[21] The experimental observations were reproduced to experimental accuracy using a semirigid-rotor Watson Hamiltonian (S-reduction).[22] The internal rotation effects were analyzed using Wood's internal-axis-method (IAM).[23] Table 2 presents the results of least-squares fits of the experimental transitions of both conformers, which yielded accurate values of the rotational constants, the quartic centrifugal distortion constants and the internal rotation barrier height. The full set of transitions is collected in Tables S3 and S4 (ESI†). No lines attributable to other conformers were observed in the spectrum.

The conformational assignment of the two isomers of Fig. 2 relied on multiple arguments. An initial comparison of the rotational constants in Table 2 showed good agreement between the two lowest-lying conformations (relative errors below 1–2%). The prediction of (harmonic) centrifugal distortion constants was also consistent in magnitude and sign with the proposed

XI.38

Table 2 Experimental parameters for the two detected conformations of methyl β-D-ribofuranoside, and comparison with the MP2 predictions

	Conf. 1		Conf. 2	
	Experiment	Theory	Experiment	Theory
A/MHz	$1307.1463(55)^a$	1295.21	1443.5094(14)	1438.72
B/MHz	1095.47128(50)	1101.10	924.98477(53)	943.70
C/MHz	717.8046(49)	718.90	661.97710(32)	674.86
D_J/kHz	0.953(81)		0.2752(48)	
D_{JK}/kHz	−0.339(88)		−1.264(27)	
D_K/kHz			1.702(97)	
d_1/Hz	0.723(66)		−0.1004(31)	
d_2/Hz	−0.277(24)			
V_3^b/kJ mol^{-1}	7.304(13)	7.90	7.503(64)	8.23
σ^c/kHz	4.7	3.0		
N^d	46	32		

^{a} Uncertainties in units of the last digit. ^{b} Internal rotation barrier. The geometrical parameters I_α (=3.195 μÅ^2) and $<(i,a)$, $<(i,b)$, $<(i,c)$ (=23.1°, 81.3°, 68.8°, 51.4°, 43.9° and 72.3°, respectively, for conformers 1 and 2) have been fixed to the *ab initio* values. ^{c} Standard deviation of the fit. ^{d} Number of transitions.

Fig. 3 (a) Upper panel: Ring-puckering predictions (1–12) for methyl β-D-ribofuranoside in the gas phase (experimental conformers with green solid circles). (b) Lower panel: A survey of 30 fragment structures of furanose glycosides in the Cambridge Structural Database[10] (blue crosses), together with 2 neutron diffraction structures of methyl β-D-ribofuranoside[17] (red circles).

Fig. 2 Intramolecular hydrogen bonding distances (Å) and relative Gibbs energy (MP2) for the two observed conformers of methyl β-D-ribofuranoside.
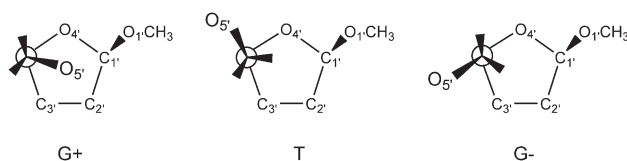
Scheme 2 Notation for staggered orientations around the $C_{4'}-C_{5'}$ bond.

assignment. Finally, the methyl group V_3 barrier increase for conformer 2 (V_3 = 7.3 *vs.* 7.5 kJ mol^{-1}) is in agreement with the *ab initio* predictions (7.9 *vs.* 8.2 kJ mol^{-1}). This evidence fully confirms the conformational assignments in Table 2 and Fig. 2 (interactive 3D model in Fig. S1 and S2, ESI†).

The ring-puckering properties were analyzed quantitatively, using the CP coordinates[13] in Fig. 3. The two detected isomers have similar puckering phases (φ_{CP} = 264.7° and 260.7°, respectively), intermediate between a twisted-$^3T_2$ and an envelope-E_2 ring conformation. Puckering amplitudes are also very similar (q = 0.385 and 0.397 Å, respectively). The hydroxymethyl side chain adopts the gauche staggered orientation of Scheme 2, either G$^+$ ($\tau_1(O_{5'}-C_{5'}-C_{4'}-C_{3'})$ = +56.2°) for the global minimum or G$^-$ (τ_1 = −58.1°) for the second conformer. Conversely, the methyl group is always *trans* with respect to $C_{2'}$ (T: $\tau_2(C_M-O_{1'}-C_{1'}-C_{2'})$ = 174.4° and 178.9°, respectively), so the observed conformations are denoted $^3T_2$ G$^+$T (global minimum) and $^3T_2$ G$^-$T.

The two ring hydroxyl groups, on opposite sides of the methoxy and hydroxymethyl substituents, are finally arranged to reach the highest possible number of internal hydrogen bonds. The global minimum exhibits two unconnected hydrogen bonds: a weak contact $O_{5'}-H\cdots O_{4'}$ with the hydroxymethyl group (MP2: $r(H\cdots O_{4'})$ = 2.4 Å) and a $O_{2'}-H\cdots O_{3'}$ link (MP2: $r(H\cdots O_{3'})$ = 2.17 Å). The second

conformer displays a network of two successive $O_{2'}-H\cdots O_{3'}-H\cdots O_{5'}$ hydrogen bonds involving three hydroxyl groups (MP2: $r(H\cdots O_{3'})$ = 2.17 Å, $r(H\cdots O_{5'})$ = 2.29 Å).

In conclusion, the combination of rotational data and *ab initio* calculations provides a direct comparison between β-ribofuranoside ring conformations in the gas phase and crystal structures. The isolated molecule preferably occupies three regions of the conformational space, represented by the $^3T_2-E_2$, ^2E and ^4E structures in Fig. 3 (*ab initio* structures in Tables S5–S7, ESI†).

The three most stable structures (<3 kJ mol^{-1}) share a twisted $^3T_2$ and envelope E_2 character, but most of the following conformations up to *ca.* 8 kJ mol^{-1} move toward the neighboring envelope E_2. The higher-energy forms of the isolated molecule also comprise envelopes ^2E and ^4E, which appear at relative energies above 3.7 and 7.3 kJ mol^{-1} (MP2), respectively, and become the most abundant in the upper range of the analyzed energy window. The two observed conformations for the isolated molecule simply represent alternative arrangements of the sugar hydroxymethyl side-chain (the third conformer being equivalent to the global minimum with reversed $O_{3'}-H\cdots O_{2'}$ hydrogen bond orientation). In previous rotational studies it was argued that

XI.39

intramolecular hydrogen bonding is the primarily stabilizing effect in isolated monosaccharides.[1,2] In methyl β-D-ribofuranoside the hydrogen bond pattern seems to favor conformer 2, predicted only 0.8 kJ mol^{-1} (MP2) to 1.2 kJ mol^{-1} (M06-2X) above the global minimum. However, the predicted stability could also reflect other contributions, like hyperconjugative effects, previously suggested in tetrahydrofuran[24] and other monosaccharides. Unfortunately, the small energy difference between both conformations cannot be verified experimentally, as the lack of common selection rules precludes the estimation of the intensity ratios. Noticeably, the neutron diffraction experiments of methyl β-D-ribofuranoside also identified two conformations with E_2 ring-puckering ($\varphi_{CP} = 258.6°$, 249.6°), relatively close to the $^3T_2$–E_2 structures observed here.[17] The two observed crystal structures mostly differ in the orientation of the ring substituents, which are both *trans* oriented to favor intermolecular hydrogen bonding, concomitant with this condensed phase. No intramolecular hydrogen bond is apparent in the crystal structures.

The comparison between the conformational behavior of an isolated unit of methyl β-D-ribofuranoside and that of the molecule embedded in a crystal matrix reveals features of the factors affecting the molecular structure. The ring puckering characteristics of the ribofuranose unit are very similar in the gas and crystal phases, and clearly suggest that the puckering forces associated with the minimization of the ring strain originate from the ring configuration and number and position of substituents, and not from crystal forces. This argument is reinforced by the comparison of the puckering characteristics of a set of 30 structural fragments in the Cambridge Structural Database (CSD), in Fig. 3, similarly centered around E_2. Furthermore, crystal data show that a change in the substituents' stereochemistry radically alters the ring puckering.[10] This view is confirmed by previous NMR studies, emphasizing the dominant influence of the anomeric substituent on the ring conformation in the liquid phase.[25] Natural Bond Orbital calculations in Table S8 (ESI†) are consistent with electronic hyperconjugation originated by the methoxy and ring oxygen atoms (*endo/exo* anomeric effects), but its contribution is relatively similar for the four lowest lying conformers. The molecular stability would thus primarily result from a combination of orbital effects reducing the ring strain, complemented with the effects of intramolecular hydrogen bonding. As a consequence, the presence of the heterocyclic bases found in nucleosides surely influences the conformational properties of the flexible ring, thereby determining its final biological properties.

The results for methyl β-D-ribofuranoside highlight the value of current crystal structures but also call for additional gas-phase experiments on related furanosides, nucleosides and nucleotides, both to assess the theoretical models and to compare with conventional data from condensed media. Considering the vital role of ribofuranosides in all life forms, it is remarkable that their structural properties free of any environmental effects have been unknown until now. These new results provide empirical data that may help to provide information about structural, predictive and enzymological RNA (and DNA) biology. In this sense, the emergence of new techniques in rotational spectroscopy is helping to provide a global view of the inherent structural properties of these biomolecular building blocks.

Notes and references

1 E. J. Cocinero, A. Lesarri, P. Écija, F. J. Basterretxea, J.-U. Grabow, J. A. Fernández and F. Castaño, *Angew. Chem., Int. Ed.*, 2012, **51**, 3119.
2 E. J. Cocinero, A. Lesarri, P. Écija, A. Cimas, B. G. Davis, F. J. Basterretxea, J. A. Fernández and F. Castaño, *J. Am. Chem. Soc.*, 2013, **135**, 2845; I. Peña, E. J. Cocinero, C. Cabezas, A. Lesarri, S. Mata, P. Écija, A. M. Daly, A. Cimas, C. Bermúdez, F. J. Basterretxea, S. Blanco, J. A. Fernández, J. C. Lopez, F. Castaño and J. L. Alonso, *Angew. Chem., Int. Ed.*, 2013, **52**, 11840; J. L. Alonso, M. A. Lozoya, I. Peña, J. C. López, C. Cabezas, S. Mata and S. Blanco, *Chem. Sci.*, 2014, **5**, 515; I. Peña, C. Cabezas and J. L. Alonso, *Angew. Chem., Int. Ed.*, 2015, **54**, 2991.
3 E. J. Cocinero and P. Çarçabal, in *Spectroscopy and Structure of Biological Molecules*, ed. A. M. Rijs and J. Oomens, Springer, New York, 2015, pp. 299–333; J. P. Simons, *Mol. Phys.*, 2009, **107**, 2435.
4 D. Šišak, L. B McCusker, G. Zandomeneghi, B. H. Meier, D. Bläser, R. Boese, W. B. Schweizer, R. Gilmour and J. D. Dunitz, *Angew. Chem., Int. Ed.*, 2010, **49**, 4503.
5 M. Sundaralingam, *Biopolymers*, 1969, **7**, 821.
6 E. Breitmaier and U. Hollstein, *Org. Magn. Reson.*, 1976, **8**, 573; S. J. Angyal, *Angew. Chem.*, 1969, **8**, 157; K. N. Drew, J. Zajicek, G. Bondo, B. Bose and A. Serianni, *Carbohydr. Res.*, 1998, **307**, 199.
7 W. Saenger, *Principles of Nucleic Acid Structure*, Springer-Verlag, New York, 1984.
8 A. Eschenmoser, *Science*, 1999, **284**, 2118.
9 H. Ford, Jr., F. Dai, L. Mu, M. A. Siddiqui, M. C. Nicklaus, L. Anderson, V. E. Marquez and J. J. Barchi, *Biochemistry*, 2000, **39**, 2581; V. E. Marquez, P. Wang, M. C. Nicklaus, M. Maiera, M. Manoharana, J. K. Christmanb, N. K. Banavalic and A. D. Mackerell, Jr., *Nucleosides, Nucleotides Nucleic Acids*, 2001, **20**, 451 and references therein.
10 H. A. Taha, M. R. Richards and T. L. Lowary, *Chem. Rev.*, 2013, **113**, 1851.
11 J. Laane, in *Vibrational Spectra and Structure*, ed. J. R. Durig, Marcel Dekker, Inc., New York, 1972, pp. 26–50.
12 C. Altona and M. Sundaralingam, *J. Am. Chem. Soc.*, 1972, **94**, 8205.
13 D. Cremer and J. A. Pople, *J. Am. Chem. Soc.*, 1975, **97**, 1354.
14 H. P. M. de Leeuw, C. A. G. Haasnoot and C. Altona, *Isr. J. Chem.*, 1980, **20**, 108.
15 IUPAC-IUB Joint Commission on Biochemical Nomenclature, *Eur. J. Biochem.*, 1980, **111**, 295. The primed atom notation used in nucleosides is adopted for simplicity.
16 F. de Leeuw and C. Altona, *J. Comput. Chem.*, 1983, **4**, 428; Z. Dzakula, M. DeRider and J. L. Markley, *J. Am. Chem. Soc.*, 1996, **118**, 12796.
17 A. G. Evdokimov, A. J. K. Gilboa, T. F. Koetzle, W. T. Klooster, A. J. Schultz, S. A. Mason, A. Albinati and F. Frolow, *Acta Crystallogr., Sect. B: Struct. Sci.*, 2001, **57**, 213; A. G. Evdokimov, A. J. K. Gilboa, T. F. Koetzle, W. T. Klooster and J. M. L. Martin, *J. Phys. Chem. A*, 1999, **103**, 744.
18 J. B. Houseknecht, C. M. Hadad, T. L. Lowary and I. Karplus, *J. Phys. Chem. A*, 2003, **107**, 372; C. A. Podlasek, W. A. Stripe, I. Carmichael, M. Shang, B. Basu and A. S. Serianni, *J. Am. Chem. Soc.*, 1996, **118**, 1413.
19 J. B. Houseknecht, T. L. Lowary and C. M. Hadad, *J. Phys. Chem. A*, 2003, **107**, 5763.
20 M. Saunders, K. N. Houk, Y.-D. Wu, W. C. Still, M. Lipton, G. Chang and W. C. Guida, *J. Am. Chem. Soc.*, 1990, **112**, 1419; G. M. Keresu and I. Kolossváry, *J. Am. Chem. Soc.*, 2001, **123**, 12708.
21 W. Gordy and R. L. Cook, *Microwave Molecular Spectra*, New York, Wiley, 1984; D. G. Lister, J. N. MacDonald and N. L. Owen, *Internal Rotation and Inversion: An Introduction to Large Amplitude Motions in Molecules*, New York, Academic Press, 1978.
22 J. K. G. Watson, in *Vibrational Spectra and Structure*, ed. J. R. Durig, Elsevier, Amsterdam, 1977, pp. 1–89.
23 R. C. Woods, *J. Mol. Spectrosc.*, 1967, **22**, 49; J. M. Vacherand, B. P. van Eijck, J. Burie and J. Demaison, *J. Mol. Spectrosc.*, 1986, **118**, 355.
24 R. Meyer, J. C. López, J. L. Alonso, S. Melandri, P. G. Favero and W. Caminati, *J. Chem. Phys.*, 1999, **111**, 7871.
25 J. Raap, J. H. van Boom, H. C. van Lieshout and C. A. G. Haasnoot, *J. Am. Chem. Soc.*, 1988, **110**, 2736.

XI.40

Scopine

Scopine Isolated in the Gas Phase

Patricia Écija,[a] Montserrat Vallejo-López,[a] Iciar Uriarte,[a] Francisco J. Basterretxea,*[a]
Alberto Lesarri,[b] José A. Fernández,[a] and Emilio J. Cocinero*[a]

The rotational spectrum of the tropane alkaloid scopine is detected by Fourier transform microwave spectroscopy in a pulsed supersonic jet. A nonconventional method for bringing the molecules intact into the gas phase is used in which scopine syrup is mixed with glycine powder and the solid mixture is vaporized with an ultrafast UV laser beam. Laser vaporization prevents the easy isomerization to scopoline previously observed with conventional heating methods. A single conformer is unambiguously observed in the supersonic jet and corresponds to the energetically most stable species according to quantum chemical calculations. Rotational and centrifugal distortion constants are accurately determined. The spectrum shows fine and hyperfine structure due to the hindered rotation of the methyl group and the presence of a quadrupolar nucleus (^{14}N), respectively. This additional information allows the angle of N-methyl inversion between the N—CH$_3$ bond and the bicyclic C-N-C plane to be determined (131.8–137.8°), as well as the internal rotation barrier of the methyl group (6.235(1) kJ mol^{-1}).

1. Introduction

Molecules derived from the tropane bicycle (N-methyl-8-azabicyclo[3.2.1]octane) are broadly used in the pharmaceutical industry.[1] These compounds find many applications as mydriatics, antiemetics, antispasmodics, anesthetics, and bronchodilators.[2–5] Of special importance are tropane alkaloids that can be found naturally in many plants of the Solanaceae family, such as atropine and cocaine.

Tropane derivatives having epoxy and hydroxyl groups in the two-carbon bridge are of considerable importance. For example, scopine (6,7-epoxytropine) is an *exo*-6,7-epoxytropane derivative on which several natural products such as scopolamine are based. Recent interest in 6-hydroxy-substituted tropanes has included valuable natural targets such as schizanthines, bao gong teng derivatives, and calystegines.[6] From the stereochemical point of view, epoxytropanes are interesting molecules, as the epoxy group can influence the reactivity, ring conformation, and N-methyl inversion.

Previously, we attempted to detect the rotational spectrum of scopine in the gas phase using microwave spectroscopy in a supersonic expansion.[7] In that experiment, the sample was heated to about 90 °C in the pulsed injector. As a result, the

detection of scopine was not possible, since at that temperature the structural isomerization of scopine to scopoline (oscine) by intramolecular cyclization is strongly favored. This behavior was explained by taking into account that the three-membered epoxide ring of scopine is considerably strained, and makes the molecule more reactive. Herein, we report the rotational spectrum of scopine for the first time. To this end, we employed an alternative method to bring scopine molecules into the gas phase, which consists of the vaporization of a solid sample of scopine mixed with a glycine matrix by using an ultrafast UV laser. This method avoids heating the sample and hence its structural isomerization (see Experimental Section). This study follows our previous work on the stereochemical properties of tropane derivatives by rotational spectroscopy in jet expansions, such as tropinone and its intermolecular complexes.[8, 9] Gas-phase rotational spectroscopy with microwave techniques offers the advantage that molecules are not affected by the solvent or crystal-packing effects that are present in condensed media, and it produces high-resolution (kilohertz) spectra that result in the most accurate structural description of the isolated molecule. This allows the conformational landscape of the isolated molecule to be described, which ultimately governs its stereochemical properties. The highly accurate data obtained by microwave techniques can also be used as a benchmark to test the performance of ab initio quantum chemical calculations, which are needed to provide adequate molecular models.

[a] Dr. P. Écija, Dr. M. Vallejo-López, I. Uriarte, Dr. F. J. Basterretxea,
    Dr. J. A. Fernández, Dr. E. J. Cocinero
    Departamento de Química Física
    Facultad de Ciencia y Tecnología
    Universidad del País Vasco (UPV/EHU)
    Apartado 644, 48080 Bilbao (Spain)
    E-mail: franciscojose.basterretxea@ehu.eus
            emiliojose.cocinero@ehu.es

[b] Prof. A. Lesarri
    Departamento de Química Física y Química Inorgánica
    Facultad de Ciencias
    Universidad de Valladolid (Spain)

    Supporting Information for this article can be found under:
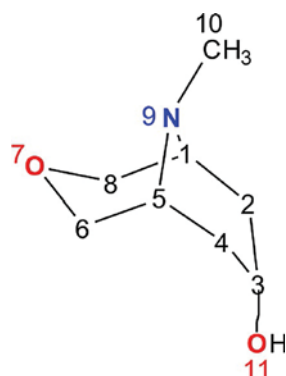   http://dx.doi.org/10.1002/cphc.201600368.

2. Results and Discussion

The starting point of the study was the analysis of the molecular potential-energy surface (PES). First, the six-membered ring of tropane (Scheme 1) can adopt chair, higher-energy twisted, and even boat conformations. Second, N-methyl equatorial/

XI.43

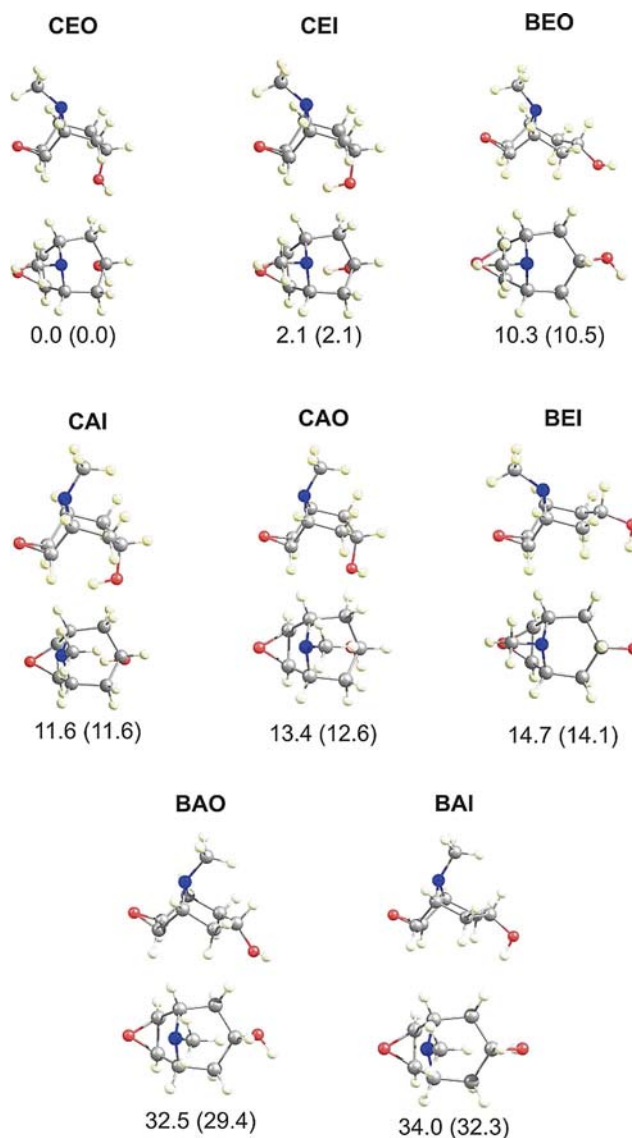Scheme 1. The structure of scopine with atom numbering.

Figure 1. MP2 computed structures of the eight lowest-lying conformers of scopine. We used the notation chair/boat (C/B), equatorial/axial (E/A), and inwards/outwards (I/O) to name the different conformers. Energies relative to the global minimum are indicated; values in parentheses are Gibbs free energies. Relative and free energies in kilojoules per mole.

axial isomerism characteristic of tropanes was predicted. Finally, the hydroxyl group can also adopt two different configurations: in one of them (doubled by symmetry) the OH group points outwards from the molecule, breaking the C_s symmetry, and in the other the OH group is directed inwards to the bicycle, retaining the C_s arrangement of tropane. Thus, according to these degrees of freedom, the molecule can adopt eight different structures. Figure 1 shows the MP2 computed structures of the lowest-lying conformers. Ab initio calculations showed that eight conformers of scopine are expected in the 0–34 kJ mol^{-1} energy range.[7] The most stable structure (conformer CEO) exhibits a chair configuration in the six-membered ring, an equatorial arrangement of the N-methyl substituent, and the hydroxyl group pointing out of the molecule.

The next conformer (CEI) lies 2.1 kJ mol^{-1} above the global minimum, and differs only in the orientation of the α-hydroxyl H atom, which points towards the bicycle. Conformer BEO, at 10.3 kJ mol^{-1} above the global energy minimum, is the most stable structure with the tropane ring in a boat conformation. The two lowest-energy conformers with an axial arrangement, in which the CH$_3$ internal rotor is oriented opposite to the epoxy group, have substantially higher energies (11.6 and 13.4 kJ mol^{-1}). The rest of the conformers are more than 14.0 kJ mol^{-1} from the global energy minimum, and cannot be populated at the low temperatures attained in the jet.

Initial scans showed several rotational transitions that could be assigned to the lowest-lying conformer and were used to obtain preliminary rotational constants. Rotational transitions were assigned in the 8200–12800 MHz range. All assigned transitions (J'', K''_{-1}, $K''_{+1} \rightarrow J'$, K'_{-1}, K'_{+1}) are listed in Table S1 (Supporting Information). An example of the observed transitions is shown in Figure 2. All transitions were of R type ($\Delta J = +1$) and obeyed μ_a- and μ_b-type selection rules. Although μ_c-type lines were also searched for, none could be detected. Each of them appeared to be split into a number of components (typically separated by less than 0.5 MHz) due to quadrupole hyperfine coupling arising from the ^{14}N nucleus, giving $F'' \rightarrow F'$ transitions (where the F quantum number can take the values $F = J + I$, $J + I - 1, \ldots, |J - I|$, and I is the quantum number for nuclear spin: $I(^{14}N) = 1$).[10] Another relevant feature of the spectrum was a small doubling detectable in some transitions (see Figure 2), different from the approximately 50–80 kHz line doubling

caused by the instrumental Doppler effect. This tunneling doubling was attributed to the hindered internal rotation of a single C_3-symmetric methyl group, which splits the torsional levels into species of A and E symmetry. All observed transitions were fitted to a semirigid Watson S-reduction Hamiltonian with centrifugal distortion.[11] This allowed us to obtain the rotational constants and two of the centrifugal distortion constants (D_J and D_{JK}). The fit also included the diagonal elements of the nuclear quadrupole coupling tensor χ_{aa} ($aa = aa$, bb, cc)[11, 12] and internal rotation terms expressed in the internal axis method (IAM) formalism[13] of Woods and van Eijck et al. The internal rotation analysis reveals additional structural information, since the experimental splittings depend both on the barrier height and the orientation of the internal CH$_3$ rotor with respect to the principal axes. The XIAM program devel-
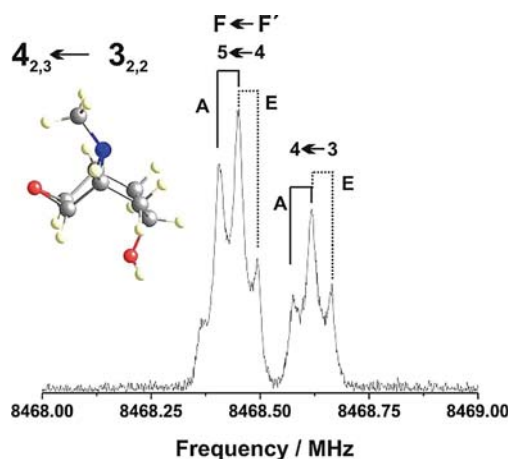
XI.44

Figure 2. Section of the rotational spectrum of scopine showing the $J(K_{-1}, K_{+1}) = 4(2,3) \leftarrow 3(2,2)$ transition of the CEO conformer. The transition splits into several components due to nuclear quadrupole coupling, of which the $F = 5 \leftarrow 4$ and $4 \leftarrow 3$ components are shown. Additionally, each component is split into A and E lines due to hindered internal rotation of the methyl internal rotor. Finally, all lines are doubled by the instrumental Doppler effect.

Table 1. Experimentally fitted and calculated parameters for the detected conformer of scopine.				
	Experiment	MP2	B3LYP	M06-2X
A [MHz] [a]	1866.6221(14)[b]	1866.1	1854.0	1873.5
B [MHz]	1110.09949(17)	1117.3	1094.3	1118.5
C [MHz]	1008.87184(19)	1014.3	994.5	1016.5
D_J [kHz]	0.0434(25)	0.047	0.056	0.049
D_{JK} [kHz]	0.099(13)	−0.009	−0.031	−0.016
D_K [kHz]	[0.082][c]	0.082	0.109	0.084
d_1 [Hz]	[6.175][c]	6.175	8.113	6.671
d_2 [Hz]	[−0.11][c]	−0.11	−0.27	−0.16
χ_{aa} [MHz]	1.5078(86)	1.50	1.51	1.50
χ_{bb} [MHz]	−4.236(12)	−4.27	−4.59	−4.27
χ_{cc} [MHz]	2.728(12)	2.77	3.07	2.77
$|\mu_a|$ [D]	–	1.82	1.81	1.86
$|\mu_b|$ [D]	–	1.32	1.44	1.34
$|\mu_c|$ [D]	–	1.06	1.05	1.07
μ_{TOT} [D]	–	2.5	2.5	2.5
$\angle(a,i)$ [°] [d]	174.01[c]	174.01	173.73	171.73
$\angle(b,i)$ [°]	95.98[c]	95.98	96.26	97.94
$\angle(c,i)$ [°]	90.35[c]	90.35	90.31	92.29
I_α [u Å²]	3.275[c]	3.275	3.251	3.250
V_3 [kJ mol⁻¹] [e]	6.235(1)	6.0	5.8	6.9
N [f]	112	–	–	–
σ [kHz]	3.8	–	–	–

[a] Rotational constants (A, B, C); centrifugal distortion constants (D_J, D_{JK}, D_K, d_1, d_2); nuclear quadrupole coupling elements (χ_{aa}, χ_{bb}, χ_{cc}), and dipole-moment components (μ_a, μ_b, μ_c, 1 D ≈ 3.336×10⁻³⁰ C m). [b] Standard errors in parentheses in units of the last digit. [c] Value cannot be experimentally determined and has been fixed in the fit to the MP2-calculated value. [d] $\angle(g,i)$: angles defining the orientation of the internal rotor axis (i) with respect to the principal inertial axes ($g = a$, b, c); moment of inertia I_α of the internal rotor with respect to its C_3 axis. [e] Threefold barrier height. [f] Number of transitions N and root mean square deviation σ of the fit.

oped by Hartwig and Dreizler was used for these fittings.[14] The height of the barrier to internal rotation of the methyl group was found to be 6.235(1) kJ mol⁻¹. All the fitted constants are listed in Table 1 and compared to ab initio predictions. The constants predicted for the other conformers and the computed Cartesian coordinates of the assigned conformer can be found in Tables S2 and S3, respectively.

Although the experimental rotational constants do not allow the full structure of the observed conformer of scopine to be obtained, the ¹⁴N nuclear quadrupole constants χ_{aa} exhibit a dependence on the position of the CH₃ rotor with respect to the bicyclic frame. This arises because the χ_{aa} constants are essentially dependent on the electronic environment around the ¹⁴N nucleus and the orientation of the principal inertial axes. Figure 3 shows the theoretical predictions and experimental values of the diagonal elements of the nuclear quadrupole coupling tensor for various inversion angles formed by the N—CH₃ bond and the C-N-C plane near the minimum-energy structure. The comparison between the experimental and computed plots allows estimation of the effective CH₃ rotor angle with respect to the bicyclic frame in the range 131.8–137.8°. This value is consistent with those of other tropane alkaloids, such as tropinone[8] (134.7–135.7°) and scopoline[7] (134.0–137.5°). The inversion angles corresponding to the computed minimum-energy structures also lie in this interval. The variation of the molecular energy with the inversion angle is also presented in Figure 3, and shows agreement with the χ_{aa} calculations.

In the observed conformer (CEO), the H atom of the hydroxyl group points out of the molecule, so this conformer is doubly degenerate, and the dihedral angle τ(H-O₁₁-C₃-H) can be about ±60°. The next conformer in energy (CEI) is only 2.1 kJ mol⁻¹ above the lowest-lying one, and differs in the orientation of the H atom, which points towards the bicyclic ring. In this case the dihedral angle τ(H-O₁₁-C₃-H) is 180°, giving a C_s

molecular symmetry. The nonobservation of this conformer could be explained by a conformational relaxation in the jet, since the CEO and CEI conformers are separated by a small barrier of 4.6 kJ mol⁻¹ (see Figure 4, top). Previous studies suggested that the carrier gas in the jet can relax the higher-energy conformers for barriers around 5–12 kJ mol⁻¹, whereby Ar and Kr are the most effective.[15]

The N-methyl group of conformer CEO adopts an equatorial position relative to the tropane ring. The corresponding axial conformer CAO lies about 13.4 kJ mol⁻¹ higher and was not observed due to the low population attained in the jet. The energy barrier for the CAO→CEO conversion was calculated (DFT) to be 22.6 kJ mol⁻¹ (Figure 4, bottom). The equatorial conformer CEO may be partially stabilized by the presence of a weak hydrogen bond with the epoxy group (C—H···O). The stabilization energy of this bond can be estimated from data of other tropane alkaloids that have also been studied by rotational spectroscopy (Figure 5). For tropinone,[8] both equatorial and axial conformers were observed, with an equatorial/axial population ratio in the jet close to 2/1, corresponding to a relative energy of about 2 kJ mol⁻¹ at 373 K, and an ab initio calculated inversion barrier of 40 kJ mol⁻¹. Assuming that the energy of N-methyl axial/equatorial inversion in tropinone is the same for scopine, and that the energies of N-methyl inver-
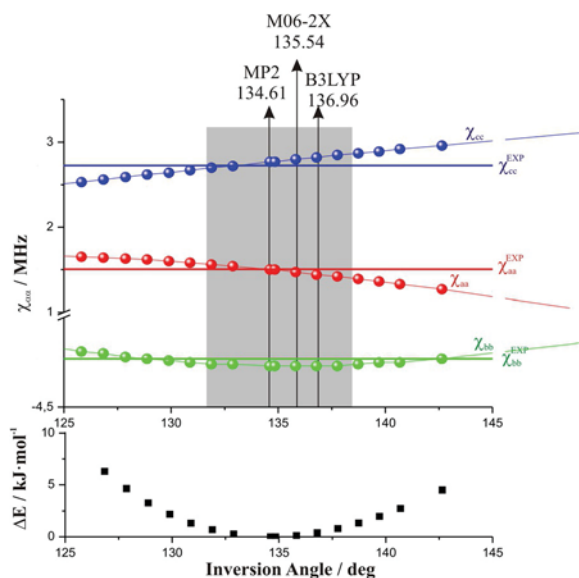
XI.45

Figure 3. Comparison between experimental and calculated values of the nuclear quadrupole coupling tensor diagonal elements χ_{aa}, χ_{bb}, and χ_{cc} for different values of the inversion angle (defined as the angle between the N—CH₃ bond and the C-N-C plane). The gray-shaded area between 131.8 and 137.8° gives the confidence interval for which the inversion angle can be specified, taking into account the experimental errors in the χ_{aa} diagonal elements. The inversion angles corresponding to the minimum-energy structures, as given by quantum chemical calculations, all lie within the proposed confidence interval. Also shown is the variation of the MP2 energy with the inversion angle and the predicted structure of the molecule.

sion and the hydrogen bond are simply additive, the stabilization energy of the weak C—H⋯O interaction in scopine can be estimated to be about 11 kJ mol⁻¹. On the other hand, in scopoline[7], the intramolecular O—H⋯N hydrogen bond forces the N-methyl group into the less stable axial position, so it cannot be compared directly with tropinone and scopine.

3. Conclusions

We have detected the scopine molecule in the gas phase for the first time. The most stable conformer of scopine was observed by rotational spectroscopy, and accurate rotational and centrifugal distortion constants were determined. Internal torsional splittings and quadrupole hyperfine structure in the spectra allowed us to determinate the angle of the methyl rotor with respect to the bicyclic frame and the height of the internal rotor barrier. Using ultrafast laser vaporization was crucial, since the samples react at moderately low temperatures, and thus the use of heating techniques for vaporization is precluded. No spectral lines originating from the reaction product of scopoline were detected, and this demonstrates that apparently the transfer of laser energy to the matrix is relatively clean and does not decompose or transform the sample appreciably. A new method of sample preparation in which the target in syrup form is mixed with a solid to obtain a solid sample vaporizable by a laser pulse could be a good alternative for gas-phase studies on samples that were previously un-
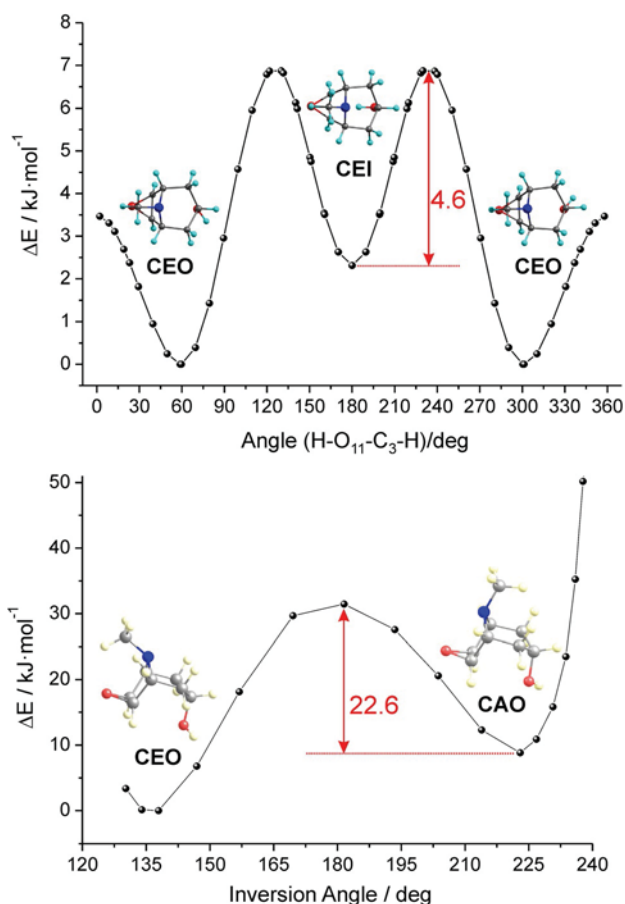
Figure 4. PES profiles (M06-2X) showing barriers for the interconversion between the two lowest-lying energy conformers (CEO and CEI, top) and N-methyl inversion (CEO and CAO, bottom).

observable or for which traditional heating methods lead to decomposition or other reactions.

Experimental Section

The experimental work was carried out with a 4–18 GHz Fourier transform microwave spectrometer based on the Balle–Flygare design,[16] constructed at the UPV/EHU and fully described elsewhere.[17] Commercial scopine (Sigma-Aldrich, 97%) is a sticky solid, and the conventional heating method results in an intramolecular reaction yielding scopoline. Therefore, a nonconventional method of vaporization was designed in which scopine (≈33%), finely powdered glycine (≈66%), and a commercial binder (minimum addition) were mixed and mechanically pressed to obtain cylinder-type solid samples. These were vaporized by the beam of a picosecond Nd:YAG laser operating at the third harmonic (355 nm) and giving approximately 5 mJ per pulse in a Smalley-type laser-ablation source.[18] The laser-vaporization system is described elsewhere.[19] The vaporized sample was mixed with 4–6 bar of neon carrier gas and adiabatically expanded by pulses of 200 µs duration in a vacuum chamber to achieve low temperatures ($T < 5$ K) that effectively depopulate excited rovibrational levels. After expansion, molecules in the jet absorb low power (0.1–100 mW) microwave pulses of 1 µs duration, which cause a spontaneous emission that is detected in the time domain and Fourier-transformed. The accuracy of the frequency measurements is
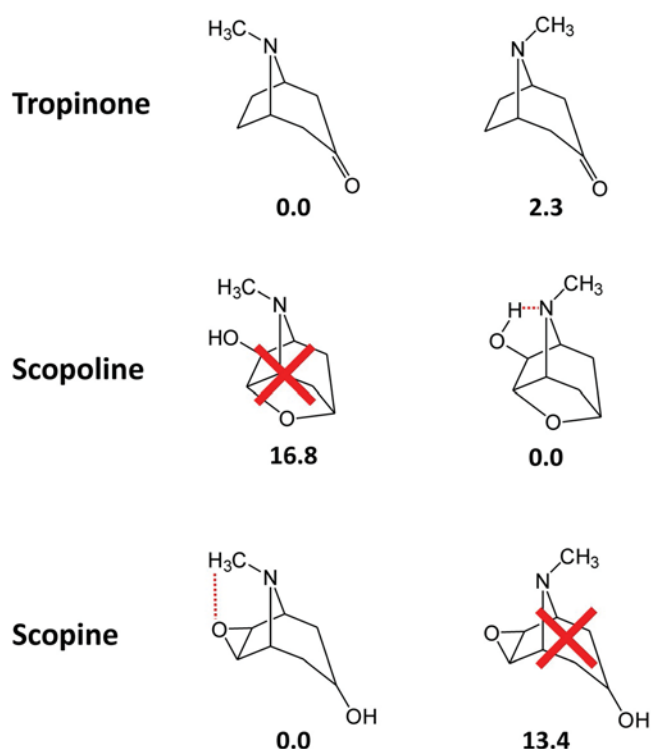
XI.46

Figure 5. MP2 predicted relative energies [kJ mol^{-1}] in equatorial/axial conformers of several alkaloids exhibiting *N*-methyl inversion. A red cross means that the conformer was not observed by rotational spectroscopy.

better than 3 kHz, and spectral lines separated by less than about 10 kHz can be resolved. Because the jet and resonator axis are coaxial, all transitions are split into two Doppler components.

The experimental work was supported by ab initio (MP2) and DFT methods. All the quantum chemical calculations were implemented in Gaussian 09.[20] Becke's B3LYP hybrid functional and Truhlar's dispersion-corrected M06-2X functional[21] were used in the DFT calculations. The Pople 6-311++G(d,p) basis set was used in all cases.

Acknowledgements

[1] a) G. Fodor, R. Dharanipragada, *Nat. Prod. Rep.* **1994**, *11*, 443–450; b) G. Fodor, R. Dharanipragada, *Nat. Prod. Rep.* **1993**, *10*, 199–206; c) G. Fodor, R. Dharanipragada, *Nat. Prod. Rep.* **1991**, *8*, 603–612; d) G. Fodor, R. Dharanipragada, *Nat. Prod. Rep.* **1990**, *7*, 539–548 for reviews of tropanes and related compounds.
[2] J. Jirschitzka, F. Dolke, J. C. D'Auria, *Adv. Bot. Res.* **2013**, *68*, 39–72.
[3] G. Grynkiewicz, M. Gadzikowska, *Pharmacol. Rep.* **2008**, *60*, 439–463.
[4] R. de Simone, L. Margarucci, V. de Feo, *Pharmacologyonline* **2008**, *1*, 70–89.
[5] G. Fodor in *Rodd's Chemistry of Carbon Compounds*, 2nd ed. (Ed.: M. Sainsbury), Elsevier, Amsterdam, **1997**, pp. 251–276.
[6] D. E. Justice, J. R. Malpass, *Tetrahedron Lett.* **1995**, *36*, 4689–4692.
[7] P. Écija, E. J. Cocinero, A. Lesarri, F. J. Basterretxea, J. A. Fernández, F. Castaño, *ChemPhysChem* **2013**, *14*, 1830–1835.
[8] E. J. Cocinero, A. Lesarri, P. Écija, J.-U. Grabow, J. A. Fernández, F. Castaño, *Phys. Chem. Chem. Phys.* **2010**, *12*, 6076–6083.
[9] P. Écija, M. Vallejo-Lopez, L. Evangelisti, J. A. Fernández, A. Lesarri, W. Caminati, E. J. Cocinero, *ChemPhysChem* **2014**, *15*, 918–923.
[10] W. Gordy, R. L. Cook in *Microwave Molecular Spectra*, Wiley, New York, **1984**.
[11] J. K. G. Watson in *Vibrational Spectra and Structure, Vol. 6* (Ed.: J. R. Durig), Elsevier, Amsterdam, **1977**, pp. 1–89.
[12] Y. Zhao, D. G. Truhlar, *Acc. Chem. Res.* **2008**, *41*, 157–167.
[13] a) R. C. Woods, *J. Mol. Spectrosc.* **1966**, *21*, 4–24; b) R. C. Woods, *J. Mol. Spectrosc.* **1967**, *22*, 49–59; c) J. M. Vacherand, B. P. Van Eijck, J. Burie, J. Demaison, *J. Mol. Spectrosc.* **1986**, *118*, 355–362; d) I. Kleiner, *J. Mol. Spectrosc.* **2010**, *260*, 1–18.
[14] H. Hartwig, H. Dreizler, *Z. Naturforsch. A* **1996**, *51*, 923–932.
[15] T. Emilsson, T. C. Germann, H. S. Gutowsky, *J. Chem. Phys.* **1992**, *96*, 8830–8839.
[16] J. Balle, W. H. Flygare, *Rev. Sci. Instrum.* **1981**, *52*, 33–45.
[17] E. J. Cocinero, A. Lesarri, P. Écija, J.-U. Grabow, J. A. Fernández, F. Castaño, *Phys. Chem. Chem. Phys.* **2010**, *12*, 12486–12493.
[18] D. E. Powers, S. G. Hansen, M. E. Geusic, A. C. Pulu, J. B. Hopkins, T. G. Dietz, M. A. Duncan, P. R. R. Langridged-Smith, R. E. Smalley, *J. Phys. Chem.* **1982**, *86*, 2556–2560.
[19] E. J. Cocinero, A. Lesarri, P. Écija, F. J. Basterretxea, J.-U. Grabow, J. A. Fernández, F. Castaño, *Angew. Chem. Int. Ed.* **2012**, *51*, 3119–3124; *Angew. Chem.* **2012**, *124*, 3173–3178.
[20] Gaussian 09, Revision A02, M. J. Frisch, G. W. Trucks, H. B. Schlegel, G. E. Scuseria, M. A. Robb, J. R. Cheeseman, G. Scalmani, V. Barone, B. Mennucci, G. A. Petersson, H. Nakatsuji, M. Caricato, X. Li, H. P. Hratchian, A. F. Izmaylov, J. Bloino, G. Zheng, J. L. Sonnenberg, M. Hada, M. Ehara, K. Toyota, R. Fukuda, J. Hasegawa, M. Ishida, T. Nakajima, Y. Honda, O. Kitao, H. Nakai, T. Vreven, J. A. Montgomery, Jr., J. E. Peralta, F. Ogliaro, M. Bearpark, J. J. Heyd, E. Brothers, K. N. Kudin, V. N. Staroverov, R. Kobayashi, J. Normand, K. Raghavachari, A. Rendell, J. C. Burant, S. S. Iyengar, J. Tomasi, M. Cossi, N. Rega, J. M. Millam, M. Klene, J. E. Knox, J. B. Cross, V. Bakken, C. Adamo, J. Jaramillo, R. Gomperts, R. E. Stratmann, O. Yazyev, A. J. Austin, R. Cammi, C. Pomelli, J. W. Ochterski, R. L. Martin, K. Morokuma, V. G. Zakrzewski, G. A. Voth, P. Salvador, J. J. Dannenberg, S. Dapprich, A. D. Daniels, Ö. Farkas, J. B. Foresman, J. V. Ortiz, J. Cioslowski, and D. J. Fox, Gaussian, Inc., Wallingford, CT, **2009**.
[21] Y. Zhao, D. G. Truhlar, *Theor. Chem. Acc.* **2008**, *120*, 215–241.

XI.47

Chloro-2-hydroxypyridine

▊ **Substituent Effects** |*Hot Paper*|

Effects of Chlorination on the Tautomeric Equilibrium of 2-Hydroxypyridine: Experiment and Theory

Camilla Calabrese,[a] Assimo Maris,[a] Iciar Uriarte,[b] Emilio J. Cocinero,*[b] and Sonia Melandri*[a]

Abstract: The effects of halogenation on the tautomeric and conformational equilibria of the model system 2-hydroxypyridine/2-pyridone have been investigated through chlorine substitution at positions 3, 4, 5, and 6. In the gas phase, the lactim *syn*-periplanar tautomer (OH$_s$) was the predominant species for all compounds over the lactam form (C=O) and the less abundant *anti*-periplanar lactim (OH$_a$). However, the population of the three species was shown to be dependent on the position of the chlorine substitution. Chlorination in position 5 or 6 strongly stabilizes the OH$_s$ tautomer, whereas the C=O form has a significant population when the ring is chlorinated in positions 3 or 4. Overall, the OH$_a$ form is the least favourable form, although the 3-substitution favours the population of this tautomer. In addition, the C=O tautomer is strongly stabilized in the solvent, which makes it the dominant form in some substituted species. This study has been performed by means of rotational spectroscopy in the gas phase and/or theoretical calculations in the isolated phase and in solution. Both the OH$_s$ and C=O forms of 5-chloro-2-hydroxypyridine and the OH$_s$ form of 6-chloro-2-hydroxypyridine were experimentally observed. All transitions displayed a complex nuclear hyperfine structure owing to the presence of the chlorine and nitrogen nuclei. For all species, a full quadrupolar hyperfine analysis has been performed. This has provided crucial information for the unambiguous identification of tautomers.

Introduction

Aromatic heterocycles play a key role in chemistry, biology, and pharmacology. To cite some examples, purines and pyrimidines are the building blocks of DNA and RNA, several aromatic heterocycles are essential components of proteins and enzymes, and the design and creation of mimetic scaffolds for new drugs are based on the combination of different heteroaromatic compounds.[1]

In particular, prototropic tautomerism in aromatic heterocycles is of great interest as it represents a model for intramolecular proton transfer and directly affects the function/biochemical behavior of this class of compounds.[2] For example, the existence of the rare lactim (enol) forms of DNA base pairs has been postulated to cause mismatches in the interstrand pairing of nucleobases, and the stability of its tautomeric forms is, thus, a theme of great interest and debate.[3]

The simplest model system with significant biological role is 2-hydroxypyridine/2-pyridone (2HP), and it has been the object of numerous studies.[4–13] Three tautomeric structures are plausible: two lactim forms (OH) and a lactam species (C=O). The lactim forms are named *syn*-periplanar (OH$_s$) and *anti*-periplanar (OH$_a$) with respect to the angle that is formed by the OH group with the C–N bond, which is 0 and 180°, respectively (Figure 1). We would like to note that this is the IUPAC recommended nomenclature; however, in the literature, it is still very common to indicate this particular tautomeric equilibrium as keto/enol instead of lactam/lactim. In 2HP, the OH$_s$ tautomer is strongly favoured over the OH$_a$ species by a weak hydrogen bond with the nitrogen atom. In this system, the C=O tautomer also has a notable contribution in the equilibrium. A great number of theoretical[4–7] and experimental[8–13] studies have highlighted that the tautomeric equilibrium strongly depends on the chemical environment selected and that its behavior

[a] Dr. C. Calabrese, Dr. A. Maris, Prof. S. Melandri
Dipartimento di Chimica "G. Ciamician"
Università degli Studi di Bologna
Via Selmi 2, 40126 Bologna (Italy)
E-mail: sonia.melandri@unibo.it
Homepage: http://www.ciam.unibo.it/freejet

[b] I. Uriarte, Dr. E. J. Cocinero
Dpto. Química Física
Universidad del País Vasco (UPV/EHU)
Apartado 644, 48080 Bilbao (Spain)
E-mail: emiliojose.cocinero@ehu.eus
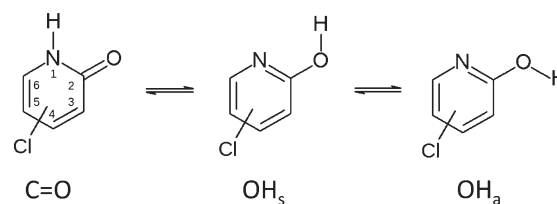Homepage: http://www.grupodeespectroscopia.es/MW/

Figure 1. Sketch of C=O, OH$_s$, and OH$_a$ forms of 2-hydroxypyridine/2-pyridone systems.

might differ in the solid state, in polar/apolar solutions, or in the gas phase. However, it is worth noting that computational studies have given contradictory results: either the OH$_s$ or the C=O tautomer has been determined to be the dominant species depending upon the method that was used. Nowadays, an accurate description of the tautomeric equilibrium of the 2HP system is a challenge from a theoretical point of view.

Actually, the experimental identification of tautomers is a keystone for the exploration of tautomeric equilibria. However, it is restricted by the fact that tautomers cannot be separated by simple chemical procedures;[14] furthermore, crystal, matrix, or solvent effects could mask or alter the tautomeric equilibrium. Rotationally resolved spectroscopy in the gas phase provides the most accurate vision of the molecular structure and undoubtedly allows identification of the different tautomers that are present as well as avoiding such masking interferences.

Rotational studies have been conducted previously on 2HP,[12] 3-hydroxypyridine (3HP),[15] and 4-hydroxypyridine (4HP)[16] to assess the effect that the position of the hydroxyl group has on the tautomeric equilibrium. In all cases, the equilibrium was shifted towards the OH$_s$ form, but some differences remained for the less abundant species; in 2HP, the C=O form was experimentally observed, whereas the OH$_a$ form was found to be predominant for 3HP. The equilibrium was strongly shifted towards the OH form for 4HP (OH$_s$ and OH$_a$ forms are equivalent by symmetry), and the C=O species was not detected; this behavior has been explained in terms of dipole–dipole interactions.[16]

The tautomeric equilibrium of hydroxypyridines can also be altered by any substitution on the ring by heteroatoms or electrophilic/nucleophilic groups. The nature of such groups is as important as the position of substitution. For example, in 2-mercaptopyridine (2MP), in which the oxygen atom is replaced by a sulfur atom, the SH$_s$ form is strongly stabilized. The C=S/SH$_s$ energy difference was calculated, from the experimental data, to be 9–11 kJ mol^{-1}, which is three times higher than the energy difference of its hydroxyl analogue 2HP, and the energy difference between the SH$_a$/SH$_s$ forms was determined to be 8 kJ mol^{-1}.[17]

The insertion of halogens, in particular chlorine atoms, into the 2HP model system strongly affects the tautomeric equilibrium, as shown for the 6-chloro-2-pyridone system by a 2D IR spectroscopic study performed in solution together with density functional theory calculations.[14] Regarding the consequences of halogen substitution, it has been demonstrated that such substrates show different biochemical properties. For example, it can influence the acidity and the leaving-group ability of nucleobases, particularly damaged ones, in relation to the mechanism of the enzymes that remove such bases from DNA.[11] There are several studies on chloro-2-hydroxypyridines reported in the literature that demonstrate the effect that substitution can have on the tautomeric equilibrium.[11,13,14,18–22] However, none of these studies is conclusive; some investigations designate the OH tautomer as the predominant species, whereas other works report that the C=O form dominates the tautomeric equilibrium. The polarity of the solvent or the dif-

ferent interactions that may take place in the solid, liquid, or gas phases are key factors in characterizing the tautomeric equilibrium.

Our goal is to explore the effects of ring chlorination on the tautomeric equilibrium of 2HP and give an exhaustive picture on this topic. Rotational studies in supersonic jets together with theoretical calculations are an excellent strategy for this task. For this purpose we considered the following systems: 3-chloro-2-hydroxypyridine/3-chloro-2-pyridone (3ClP), 4-chloro-2-hydroxypyridine/4-chloro-2-pyridone (4ClP), 5-chloro-2-hydroxypyridine/5-chloro-2-pyridone (5ClP), and 6-chloro-2-hydroxypyridine/6-chloro-2-pyridone (6ClP). The effect of different solvents on the tautomeric equilibria will also be discussed by means of theoretical calculations.

Results and Discussion

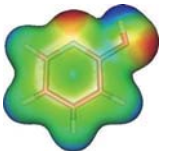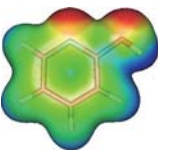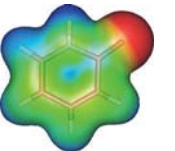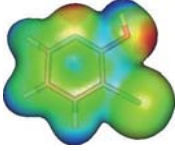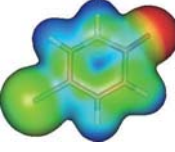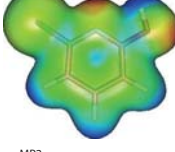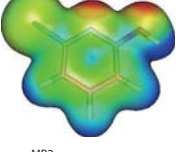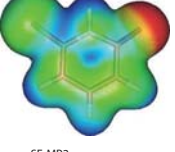### 5-Chloro-2-hydroxypyridine and 6-chloro-2-hydroxypyridine
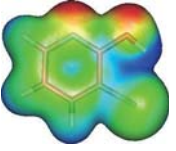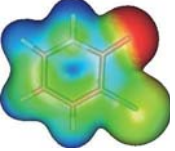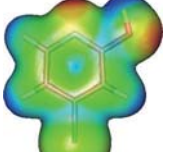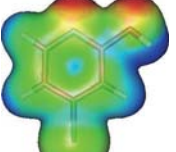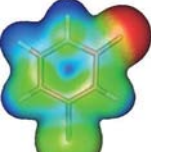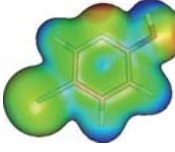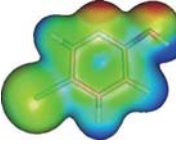
Rotational spectra

The conformational landscape of 2HP-like systems consists of three planar structures: the OH$_s$ and OH$_a$ lactim conformations and the C=O lactam form (Figure 1). A summary of the relative energy data is given in Table 1 and theoretical spectroscopic parameters are shown in Table 2 (see the computational methods in the Experimental Section).

First, the rotational spectra of 5ClP and 6ClP were recorded in the free-jet absorption millimetre-wave spectrometer (FJAMMW 59.6–74.4 GHz, see the Experimental Section) at the University of Bologna (Italy) by using argon as carrier gas. Based on theoretical predictions, the initial searches were aimed at the transitions of the OH$_s$ forms by using the ab initio spectroscopic parameters reported in Table 2. For both 5ClP and 6ClP, two sets of μ_b-type R-branch transition lines, which belong to the OH$_s$ form, were observed. Owing to the overall weakness of the spectra, it was not possible to observe the less intense μ_a-type rotational lines. All transitions displayed a complex hyperfine structure, which originates from the presence of both chlorine and nitrogen atoms. As well as the parent species (OH$_s$-6^{35}ClP and OH$_s$-5^{35}ClP), the corresponding ^{37}Cl isotopologues (OH$_s$-6^{37}ClP and OH$_s$-5^{37}ClP) were also observed in natural abundance (about 24.2%). Moreover, the hydroxyl-deuterated isotopologues (OD$_s$-6^{35}ClP, OD$_s$-6^{37}ClP, OD$_s$-5^{35}ClP, OD$_s$-5^{37}ClP) were obtained by fluxing D$_2$O over the sample and recording the spectra under the same conditions as for the normal species. The aforementioned spectra were also recorded by using helium as the carrier gas; the results were similar to those obtained when using argon, which indicates that there are no relaxation processes that strongly affect the equilibrium.[23]

A second experiment was performed with a pulsed-jet Fourier transform microwave spectrometer (FTMW) at Bilbao (Spain), which was equipped with a customized heating nozzle (see the Experimental Section). Initially, the measurements were extended to the 4–18 GHz frequency range for the previously assigned species (OH$_s$-6^{35}ClP, OH$_s$-6^{37}ClP, OH$_s$-5^{35}ClP, and OH$_s$-5^{37}ClP; Figure 2); then, a subsequent search for the C=O

XI.52

Table 1. Semiempirical and theoretical relative energy data ΔE_0 [kJ mol^{-1}] (both MP2/aug-cc-pVTZ and B3LYP/aug-cc-pVTZ) and potential energy barriers B [kJ mol^{-1}] are given for the C=O and OH forms of hydroxypyridine compounds. The electrostatic potential mapped onto the 0.01 a.u electron density isosurface, which was calculated at the MP2/aug-cc-pVTZ level, is also shown. The red areas signify the most electronegative regions and the blue ones the most electropositive areas.

	OH$_s$[a]	OH$_a$	C=O
2HP	$E_0^{MP2} = -322.829950$ $E_0^{B3LYP} = -323.552244$	$\Delta E_0^{MP2} = 20.2$ $\Delta E_0^{B3LYP} = 20.0$ $B_{OHa \to OHs}^{B3LYP} = 16.9$	$\Delta E_0^{EXP} = 3.2(4)$[12] $B_{C=O \to OHs}^{B3LYP} = 156$
3ClP	$E_0^{MP2} = -781.959352$ $E_0^{B3LYP} = -783.189410$	$\Delta E_0^{MP2} = 7.7$ $\Delta E_0^{B3LYP} = 7.6$ $B_{OHa \to OHs}^{B3LYP} = 26.6$	$\Delta E_0^{SE-MP2} = 1.4$ $\Delta E_0^{SE-B3LYP} = 2.2$ $B_{C=O \to OHs}^{B3LYP} = 158$
4ClP	$E_0^{MP2} = -781.963048$ $E_0^{B3LYP} = -783.193546$	$\Delta E_0^{MP2} = 20.1$ $\Delta E_0^{B3LYP} = 19.9$ $B_{OHa \to OHs}^{B3LYP} = 17.2$	$\Delta E_0^{SE-MP2} = 2.4$ $\Delta E_0^{SE-B3LYP} = 2.6$ $B_{C=O \to OHs}^{B3LYP} = 157$
5ClP	$E_0^{MP2} = -781.960678$ $E_0^{B3LYP} = -783.191389$	$\Delta E_0^{MP2} = 20.0$ $\Delta E_0^{B3LYP} = 19.7$ $B_{OHa \to OHs}^{B3LYP} = 16.0$	$\Delta E_0^{SE-MP2} = 10.4$ $\Delta E_0^{SE-B3LYP} = 10.3$ $B_{C=O \to OHs}^{B3LYP} = 155$
6ClP	$E_0^{MP2} = -781.965233$ $E_0^{B3LYP} = -783.196104$	$\Delta E_0^{MP2} = 19.6$ $\Delta E_0^{B3LYP} = 19.1$ $B_{OHa \to OHs}^{B3LYP} = 17.5$	$\Delta E_0^{SE-MP2} = 13.5$ $\Delta E_0^{SE-B3LYP} = 15.4$ $B_{C=O \to OHs}^{B3LYP} = 152$

[a] E_0^{MP2} and E_0^{B3LYP} in [a.u.].

R-branch rotational transitions, but none were detected. Actually, given the overall intensity of the spectrum, the predicted abundances were low enough to justify its absence. The higher resolving power of the FTMW spectrometer enabled good resolution of the most intense hyperfine components for each rotational transition related to both ^{35}Cl (or ^{37}Cl) and ^{14}N nuclei, whereas only the larger splittings that were due to the Cl nuclei could be resolved in the FJAMMW experiments.

The fitting procedure for the rotational transitions was performed by using Pickett's SPFIT program[24] in accordance with Watson's S-reduced Hamiltonian[25] in the I^r representation [Eq. (1)]:

$$H = H_R + H_{CD} + H_Q(Cl) + H_Q(N) \tag{1}$$

in which H_R represents the rigid rotational part of an asymmetric top Hamiltonian, H_{CD} represents the corresponding first-order centrifugal distortion contributions, and H_Q takes into account the interaction of the nuclear quadrupole moment of the Cl (^{35}Cl or ^{37}Cl) and ^{14}N nuclei with the electric field gradient at these nuclei.[26] For the nuclear hyperfine splittings, the sequential coupling of angular momenta was used ($F_1 = J + I_1$, $F = F_1 + I_2$), in which $I = 3/2$ for Cl and $I = 1$ for N. The transitions measured in the FJAMMW and FTMW spectra were weighted with an experimental uncertainty of 50 and 5 kHz, respectively, and analyzed together. The spectroscopic parameters of all observed species are shown in Tables 3 and 4, and the measured frequencies for all observed species are given in the Supporting Information.

Relative populations

As our goal is the unraveling of the tautomeric equilibrium of chlorinated 2HP species, it was crucial to gain information about the population ratio of the different tautomers. The rotational spectroscopy technique allows us to estimate the relative populations of different species, in this case the two tautomers. The intensity of rotational transitions is directly proportional to the population established in the jet expansion and the dipole moment components.[27] Having observed the transitions that originate from both OH$_s$ and C=O tautomers of 5ClP, we could estimate a OH$_s$/C=O population ratio of 19.0(5.7):1 and a tautomeric energy difference of 9.3(1.8) kJ mol^{-1} at 413 K. This datum is close to the semiempirical value of 10.4 kJ mol^{-1}, which was obtained by combining theoretical and experimental data, as explained in the subsequent gas phase section. Hence, the agreement between our experimental observations and the semiempirical values is satisfactory. A total of 29 μ_a-type rotational transitions were used for this analysis. For 6ClP, only the OH$_s$-6ClP species was experimentally observed, and a relative population analysis could not be performed. We can only report the semiempirical value of 13.5 kJ mol^{-1} for the energy difference between the OH$_s$ and C=O species.

species was performed. Regarding C=O-5ClP, the most intense μ_a-type R-branch lines were searched for, and finally, some weak lines that belonged to this species were observed; indeed, 76 new μ_a-type R-branch lines were measured. Because of the very low intensity of the lines, the spectrum of the C=O-5^{37}ClP isotopologue could not be observed. Regarding C=O-6ClP, the scans were aimed at observing some μ_a- and μ_b-type

XI.53

Table 2. Calculated MP2/aug-cc-pVTZ spectroscopic parameters (rotational constants, centrifugal distortion constants, dipole moment components, and quadrupole coupling constants) and relative abundances at the working temperatures for the three isomers of 6ClP and 5ClP.

		OH_s	OH_a	C=O
5ClP	A, B, C [MHz]	5811, 1007, 858	5832, 1003, 856	5680, 1007, 856
	$D_J, D_{JK}, D_K, d_1, d_2$ [Hz]	19.0, 74.8, 1161.7, −3.4, −0.4	18.7, 74.7, 1177.0, −3.3, −0.4	19.0, 72.6, 1251.0, −3.5, −0.5
	$\mu_a, \mu_b, \mu_c, \mu_{TOT}$ [D]	−0.33, 0.69, 0, 0.76	−0.48, 3.32, 0, 3.35	−2.49, 1.11, 0, 2.72
	$\chi_{aa}, \chi_{bb}, \chi_{cc}, \chi_{ab}$ Cl [MHz]	−68.74, 35.62, 33.13, 3.15	−68.69, 35.63, 33.06, 3.21	−70.23, 35.56, 34.68, 0.94
	$\chi_{aa}, \chi_{bb}, \chi_{cc}, \chi_{ab}$ N [MHz]	0.13, −2.68, 2.55, −2.48	0.08, −2.96, 2.88, −2.61	1.38, 0.96, −2.33, 0.02
	N_i/N_0 (413 K)	100	0.30 (0.32)[a]	0.57 (20.68)[a]
6ClP	A, B, C [MHz]	3432, 1285, 935	3443, 1281, 934	3436, 1280, 933
	$D_J, D_{JK}, D_K, d_1, d_2$ [Hz]	33.9, 63.9, 539.5, −12.1, −2.4	33.0, 61.5, 559.5, −11.7, −2.3	36.1, 47.2, 525.0, −12.9, −2.4
	$\mu_a, \mu_b, \mu_c, \mu_{TOT}$ [D]	−1.09, 1.70, 0, 2.02	3.06, −3.45, 0, 4.61	−2.46, 2.51, 0, 3.51
	$\chi_{aa}, \chi_{bb}, \chi_{cc}, \chi_{ab}$ Cl [MHz]	−56.22, 26.67, 29.55, 30.61	−56.02, 26.85, 29.17, 30.64	−56.72, 24.12, 32.59, −33.43
	$\chi_{aa}, \chi_{bb}, \chi_{cc}, \chi_{ab}$ N [MHz]	1.47, −3.62, 2.15, 1.35	1.47, −3.92, 2.46, 1.41	1.24, 1.31, −2.56, −0.37
	N_i/N_0 (373 K)	100	0.18 (0.21)[a]	0.12 (3.37)[a]

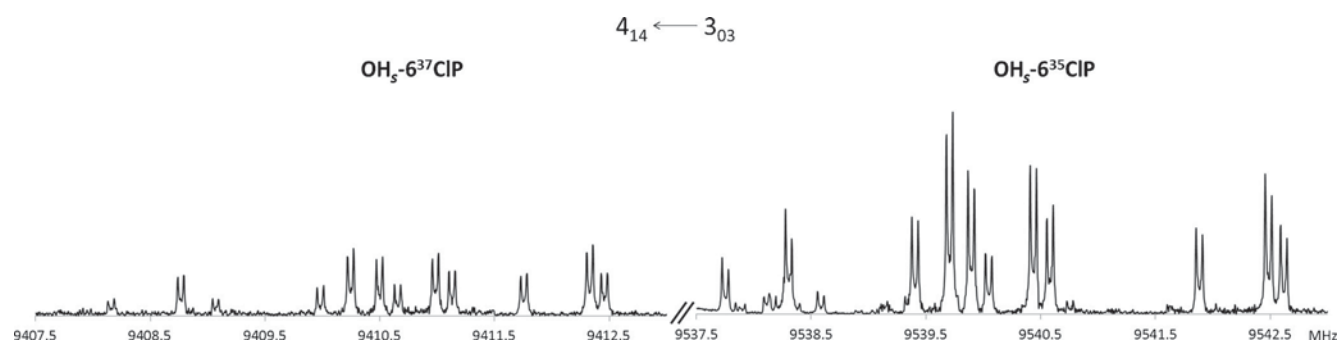[a] The data in parenthesis were obtained from B3LYP/aug-cc-pVTZ calculations.

$$4_{14} \longleftarrow 3_{03}$$

$OH_s\text{-}6^{37}ClP$

$OH_s\text{-}6^{35}ClP$

Figure 2. $4_{14} \leftarrow 3_{03}$ transition of the OH_s-6ClP tautomer recorded in the FTMW spectrometer. It shows that the hyperfine pattern between OH_s-6^{35}ClP and OH_s-6^{37}ClP is similar. The intensity ratio of 3:1 is typical of ^{35}Cl/^{37}Cl isotopologues observed in natural abundance.

Table 3. Experimental (S-reduction, I^r-representation) spectroscopic constants of all the 6ClP measured species.

	$OH_s\text{-}6^{35}ClP$	$OH_s\text{-}6^{37}ClP$	$OD_s\text{-}6^{35}ClP$	$OD_s\text{-}6^{37}ClP$
A [MHz]	3422.7097(1)[a]	3414.6413(3)	3308.949(7)	3300.523(8)
B [MHz]	1286.3294(1)	1251.0313(3)	1274.05(3)	1238.94(6)
C [MHz]	934.90405(7)	915.5363(1)	919.79(2)	901.11(6)
D_J [kHz]	0.037(1)	0.031(4)	(0.037)[b]	(0.031)[b]
D_{JK} [kHz]	0.045(6)	0.06(1)	(0.045)[b]	(0.06)[b]
D_K [kHz]	0.555(7)	0.54(1)	0.58(3)	0.63(4)
d_1 [kHz]	−0.0135(8)	−0.010(2)	(−0.0135)[b]	(−0.010)[b]
χ_{aa} Cl [MHz]	−60.227(4)	−47.8733(8)	−57.2(4)	−46.3(5)
χ_{bb} Cl [MHz]	29.149(4)	23.379(4)	(0)[c]	(0)[c]
χ_{cc} Cl [MHz]	31.077(4)	24.495(4)	(0)[c]	(0)[c]
χ_{ab} Cl [MHz]	32.83(4)	25.37(4)	(0)[c]	(0)[c]
χ_{aa} N [MHz]	1.628(4)	1.608(6)	–	–
χ_{bb} N [MHz]	−3.627(4)	−3.606(6)	–	–
χ_{cc} N [MHz]	1.999(4)	1.998(6)	–	–
χ_{ab} N [MHz]	1.37(6)	1.42(7)	–	–
N [d]	383	236	24	26
σ[e] [kHz]	22[f]	19[f]	34	44

[a] Errors are in parentheses in units of the last decimal digit. [b] Values fixed to the ones of the parent species. [c] Fixed to zero in the fit. [d] Number of lines in the fit. [e] Root-mean-square deviation of the fit. [f] Reduced deviation of the fit relative to measurement errors of 5 and 50 kHz for the FTMW and FJAMMW spectrometers.

Nuclear hyperfine structure

Structural information was also obtained from the analysis of the nuclear hyperfine structure. Accurate measurements of the nuclear quadrupole coupling can provide structural details on bonding geometry around a nucleus.

To relate the nuclear quadrupole coupling constants of different molecules measured in the Inertial Principal Axes System (IPAS: a, b, c), the nuclear quadrupole coupling tensors have to be transferred to the Quadrupole Principal Axes System of each nucleus (QPAS: x, y, z) (Figure 3). In the case of a planar molecule, the transformation between the two-coordinate systems was given by a rotation of the ab plane by an angle θ. The nuclear quadrupole coupling data are compared with a set of related molecules in Table 5.

First, it is worth noting that the angles θ achieved by the transformation were in excellent agreement with the ab initio data. Second, the OH or C=O tautomers of 5ClP and 6ClP were easily identified by simply observing the parameters of the quadrupole coupling constants of the ^{14}N nucleus, because pyridinic and pyrrolic nitrogen atoms have quite different values. Pyridine-like N atoms are associated with OH forms and pyrrole-like N atoms with the C=O tautomers. At a glance, this

XI.54

Table 4. Experimental (*S*-reduction, *I'*-representation) spectroscopic constants of all the 5ClP measured species.

	OH_s-5^{35}ClP	OH_s-5^{37}ClP	OD_s-5^{35}ClP	OD_s-5^{37}ClP	C=O-5^{35}ClP
A [MHz]	5785.0267(5)[a]	5784.848(1)	5728.720(1)	5728.45(1)	5612.110(1)
B [MHz]	1006.60906(7)	980.2862(4)	983.675(3)	958.22(9)	1009.4284(2)
C [MHz]	857.47814(9)	838.2986(2)	839.595(3)	820.62(8)	855.6732(2)
D_J [kHz]	0.018(1)	0.025(4)	0.020(5)	(0.025)[b]	0.021(3)
D_{JK} [kHz]	0.07(1)	0.05(2)	(0.07)[b]	(0.05)[b]	(0)[c]
D_K [kHz]	1.19(2)	1.19(3)	(1.19)[b]	1.6(2)	(0)[c]
d_1 [kHz]	−0.005(3)	−0.008(3)	(−0.005)[b]	(−0.008)[b]	(0) [c]
χ_{aa} Cl [MHz]	−72.772(4)	−57.363(4)	−73.5(3)	−58.0(4)	−74.30(2)
χ_{bb} Cl [MHz]	37.949(4)	29.916(5)	(0)[c]	(0)[c]	37.991(9)
χ_{cc} Cl [MHz]	34.823(4)	27.4478(5)	(0)[c]	(0)[c]	36.312(9)
χ_{aa} N [MHz]	0.282(5)	0.281(4)	–	–	1.636(5)
χ_{bb} N [MHz]	−2.635(4)	−2.637(5)	–	–	1.241(7)
χ_{cc} N [MHz]	2.352(4)	2.356(5)	–	–	−2.876(7)
N[d]	286	187	49	28	90
σ[e] [kHz]	20[f]	13[f]	39	54	3

[a] Errors are in parentheses in units of the last decimal digit. [b] Values fixed to the ones of the parent species. [c] Fixed to zero in the fit. [d] Number of lines in the fit. [e] Root-mean-square deviation of the fit. [f] Reduced deviation of the fit relative to measurement errors of 5 and 50 kHz for the FTMW and FJAMMW spectrometers.
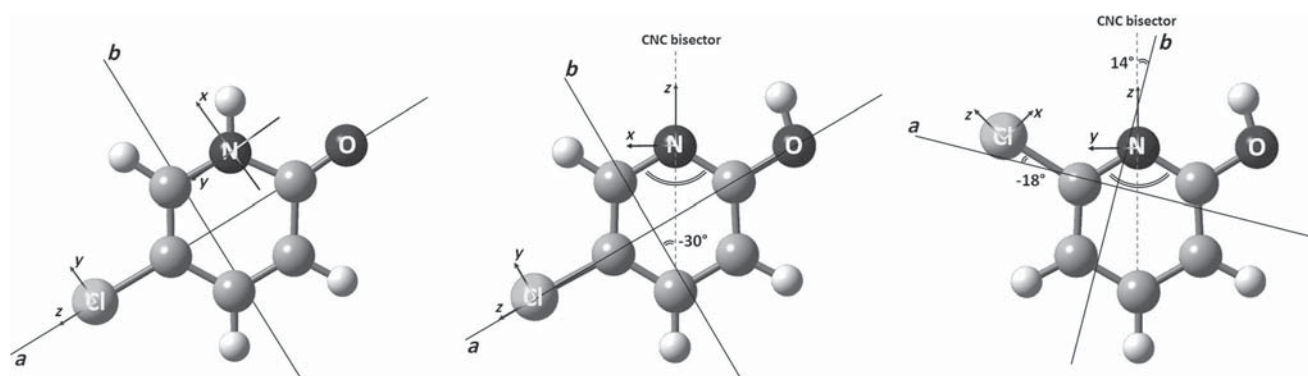

Figure 3. MP2/aug-cc-pVTZ calculated structures of C=O-5ClP, OH_s-5ClP (left side and center) and OH_s-6ClP (right side), which show the IPAS and the QPAS of the chlorine and nitrogen nuclei. The values of the angles between the C–Cl bond and the *a*-axis, the CNC bisector, and the *b*-axis are indicated. The sign is positive for the counter clockwise rotation. For OH_s-5ClP, $\theta_{a,C–Cl} = −2°$; for C=O-5ClP, $\theta_{a,C–Cl} = −0.5°$, $\theta_{a,C6–N} = 3°$.

provides irrefutable proof for the identification of the two tautomers.

In addition, comparison of the elements of the ^{35}Cl quadrupole tensors of the OH_s-6ClP, OH_s-5ClP, and C=O-5ClP conformers shows that χ_{zz} decreases across the series. As the *z* axis lies almost directly on the C–Cl bond (Figure 3), this term can be related to the density of the local electric field gradient at the Cl nucleus.

It can also be noted that, for the Cl nucleus, the χ_{xx} represents the term that is perpendicular to the *ab* plane ($=\chi_{cc}$), and its trend increased correspondingly to the one observed for the χ_{zz}. The experimental $\chi_{cc}(^{35}\text{Cl})/\chi_{cc}(^{37}\text{Cl})$ ratio was 1.2687(5), which is in excellent agreement with the ratio of the nuclear quadrupole moments $^{35}Q/^{37}Q = 1.26878$.[28]

Noticeably, the lowest value of χ_{zz} (highest value of χ_{xx}) belonged to C=O-5ClP and can be ascribed to the more electrophilic surroundings owing to the mesomeric effect. As will be discussed later, this effect may be relevant in explaining how chlorination affects the tautomeric equilibrium of 2HP.

Structural information

Microwave spectroscopy provides an inherently superior resolution of the molecular structure through the rotational constants, which critically depend on the mass distribution. Hence, it is an essential tool for the structural characterization of conformers,[29,30] tautomers,[31] isotopologues,[32] and even enantiomers.[33] In the present case, isotopic substitutions enabled the determination of the IPAS coordinates of the substituted atoms by using Kraitchman's equations.[34] To be more precise, the coordinates of the chlorine and the hydroxyl hydrogen atoms were determined. Furthermore, a partial r_0-structure was obtained through a least-squares structural refinement[35] by adjusting the C–Cl distance and the C-N-C bond angle to reproduce the experimental rotational constants of all the species with an accuracy of units of MHz. The parameters that were derived from both procedures (r_s and r_0) are given and compared in Table 6 together with the theoretical values (r_e).

XI.55

Table 5. Quadrupole coupling constants of the quadrupole coupling tensor for the chlorine and nitrogen nuclei in a representative set of molecules.

^{35}Cl	$\chi_{zz} = \chi_{bond}$	χ_{yy}	$\chi_{xx} = \chi_{cc}$	$\theta_{a,z} = \theta_{b,y}$	$\eta = (\chi_{xx} - \chi_{yy})/\chi_{zz}$
OH$_s$-6ClP	−70.99(3)[a] [−71.09][b]	39.91(3) [40.02]	31.077(4)	−18.15°(2){−18.22°}[c]	0.1245(4) [0.1257]
OH$_s$-5ClP	[−72.873]	[38.050]	34.823(4)	{−1.73°}	[0.044]
C=O-5ClP	[−74.309]	[38.000]	36.312(9)	{−0.51°}	[0.023]
Cl-benzene[36]	−71.241(7)	38.231	33.01(1)	0°	0.007
3-Cl-pyridine[37]	--	--	33.7(1)	--	--
2-Cl-pyridine[36]	--	--	30.73(4)	--	--
^{14}N	$\chi_{b,z} = \chi_{lone\,pair}$	$\chi_{yy} = \chi_{cc}$	χ_{xx}	$\theta_{b,z} = \theta_{a,x}$	$\eta = (\chi_{xx} - \chi_{yy})/\chi_{zz}$
OH$_s$-6ClP	−3.963(4) [−3.975]	1.999(4) [1.999]	1.964(3) [1.976]	13.8°(5) {14.0°}	0.009(7) [0.006]
OH$_s$-5ClP	[−4.138]	2.352(4)	[1.785]	{−30.25°}	[0.138]
OH$_s$-2HP[38]	[−4.131]	2.359(6)	[1.772]	{34.02°}	[0.142]
Pyridine[39]	−4.908(3)	3.474(3)	1.434(3)	0°	0.414
3-Cl-pyridine[37]	–	3.5(1)	–	–	–
2-Cl-pyridine[40]	–	3.03(3)	–	–	–
^{14}N	$\chi_{zz} = \chi_{cc} = \chi_{lone\,pair}$	χ_{yy}	χ_{xx}	$\theta_{b,x} = \theta_{a,y}$	$\eta = (\chi_{xx} - \chi_{yy})/\chi_{zz}$
C=O-5ClP	−2.876(7)	[1.637]	[1.240]	{3.06°}	[0.138]
C=O-2HP[f]	−2.765(4)	[1.501]	[1.265]	{7.98°}	[0.085]
Pyrrole[41]	−2.700(1)	1.406(1)	1.294(1)	0°	0.041

[a] Error are in parentheses in units of the last decimal digit. [b] The data in square brackets are derived combining the experimental χ_{aa}, χ_{bb}, and χ_{cc} values and the computed θ angle. [c] The data in curly brackets are the MP2/aug-cc-pVTZ values.

Table 6. Structural parameters and values of the IPAS coordinates for the chlorine atom and the hydrogen atom that is involved in the prototropic equilibrium relative to the isotopic substitution (r_s), relative to the effective structure (r_0), and obtained from calculations (r_e) of the observed conformers.

	OH$_s$-6ClP			OH$_s$-5ClP			C=O-5ClP	
	r_s	r_0	r_e (MP2/B3LYP)	r_s	r_0	r_e (MP2/B3LYP)	r_0	r_e (MP2/B3LYP)
a_{Cl} [Å]	±2.3725(6)[a]	2.3703(2)	2.3751/2.3862	±2.6182(3)	2.6169(1)	2.6175/2.6306	2.6129(3)	2.6207/2.6311
b_{Cl} [Å]	±0.431(3)	0.43213(4)	0.4311/0.4293	±0.04(4)	0.03482(7)	0.0362/0.0364	0.02030(6)	0.0186/0.0172
a_H [Å]	±1.927(3)	−1.9266(6)	−1.9379/−1.9420	±3.4204(5)	−3.4218(2)	−3.4246/−3.4404	−1.6794(8)	−1.6994/−1.6998
b_H [Å]	±2.2721(7)	2.2742(2)	2.2707/2.2850	±0.940(2)	0.9470(4)	0.9403/0.9401	1.9687(3)	1.9768/1.9827
C—Cl [Å]		1.7241(4)	1.7344/1.7540		1.7198(6)	1.7289/1.7475	1.694(1)	1.7270/1.7449
C-N-C [°]		117.74(3)	117.17/117.86		118.47(2)	118.02/118.48	127.43(5)	126.17/125.63

[a] Errors are in parentheses in units of the last decimal digit, the c coordinate is equal to zero for symmetry.

In general, there is a good agreement between experimental (r_s and r_0) and ab initio structural parameters, with errors ranging from 0.5 to −1.7% for OH$_s$ forms and 1.4 to −3% in C=O-5ClP.

Some useful information was obtained from the comparison of the structural parameters of OH$_s$ and C=O forms by inspecting the 5ClP species. Notably, the C—Cl distance is shortened in the C=O form (1.694(1) Å), with respect to OH$_s$-5ClP (1.7198(6) Å), whereas the C-N-C bond angle shows the reverse trend: 127.43(5) and 118.47(2)° for the C=O and OH$_s$ forms, respectively. This observation can be explained by considering the repulsive effect of the nitrogen lone pair on the adjacent N—C bonds in the OH$_s$ form (smaller angle), which is reduced (larger angle) when the hydrogen atom is covalently bonded to the nitrogen atom (C=O tautomer). The same trend in the C-N-C bond angle upon interconversion from the C=O to the OH$_s$ tautomer is also shown by 2HP. In fact, starting from the newly calculated MP2/aug-cc-pVTZ structure and adjusting the C-N-C bond angle to reproduce the experimental rotational constants measured by Hatherley et al.,[12] the obtained C-N-C bond angle values were 127.15(1) and 117.797(8)° for C=O-

2HP and OH$_s$-2HP, respectively. The same trend was found in a crystal structure study on 2HP and 6ClP.[42] These experimental findings assess and quantify the electronic repulsive role of the nitrogen lone pair.

3-Chloro-2-hydroxypyridine, 4-chloro-2-hydroxypyridine, 5-chloro-2-hydroxypyridine, and 6-chloro-2-hydroxypyridine

For a full picture of chlorination effects on the tautomeric and conformational equilibria, theoretical studies of 2HP itself and all its monosubstituted chlorinated isomers were undertaken in the gas phase and in solution.

Gas phase

A great number of computational studies (see refs. [4]–[7]) have dealt with this tautomeric equilibrium by using both DFT and ab initio methods, and as Stanovnik et al. summarized previously,[2] the results are greatly dependent on the method and the basis set used. In general, DFT methods overestimate the stability of the C=O tautomer, whereas ab initio (i.e., HF, MPn,

XI.56

and coupled-cluster) methods overestimate the stability of the OH_s form. Consequently, the predicted dominant species could change depending on the method used. The spreading of the computational results with respect to the experimental data indicates that the tautomeric equilibrium continues to represent a challenge from the theoretical point of view. To investigate how chlorination in different positions affects the tautomeric equilibrium of 2HP, we have explored the conformational spaces of 2HP, 3ClP, 4ClP, 5ClP, and 6ClP by means of both MP2 and B3LYP calculations combined with the aug-cc-pVTZ basis set (see the computational methods in the Experimental Section). The results are summarized in Table 1.

For the sake of clarity, Figure 4 shows the shifts of the relative energies of each tautomer upon chlorination, for which the reference value (fixed to zero) is the calculated energy difference between the OH_s and the C=O tautomers for the 2HP species (ΔE_0^{2HP}). From Figure 4, we can easily deduce that the shifts of the relative energies upon chlorination of the tautomers are consistent for the two methods (MP2 and B3LYP). It is also clear that the substitution in the 5 and 6 positions induces a different behavior compared with substitutions in positions 3 and 4. In 5ClP and 6ClP, the chlorination strongly stabilizes the OH_s tautomer, whereas in positions 3 and 4, the chlorination effects a slight stabilization of the C=O form.
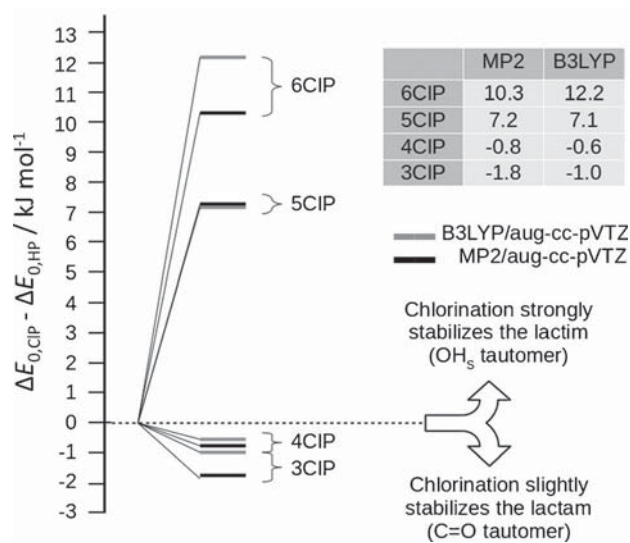

Figure 4. Calculated shifts of the C=O/OH_s relative zero-point-corrected electronic energies upon ring chlorination in the 2-Hydroxypyridine/2-Pyridone systems. $\Delta E_{0/ClP} - \Delta E_{0,ClP} - \Delta E_{0,HP} = (E_0^{C=O} - E_0^{OHs})_{ClP} - (E_0^{C=O} - E_0^{OHs})_{HP}$. The reference value, fixed to zero, corresponds to the calculated $\Delta E_{0,2HP}$ between the C=O and OH_s tautomers.

If we assume that such values are reliable, then by using the experimental energy difference for 2HP ($\Delta E_0^{EXP} = 3.2(4)$ kJ mol^{-1}),[12] we can estimate a semiempirical relative energy (ΔE_0^{SE}) by adding this value to each calculated energy shift upon chlorination. Our data, reported in Table 1, show that the OH_s tautomer represents the global minimum in all the chlorinated systems, followed by the C=O tautomer. In all cases, OH_a is the species that is least favoured. In 3ClP, the OH_a

form seems to undergo a slight stabilization, which is induced by a weak hydrogen bond between the hydroxyl hydrogen atom and the chlorine atom, as previously suggested by Michelson et al.[11] Concerning the tautomeric interconversion, a direct intramolecular proton-transfer mechanism that passes through a three-centre transition state was hypothesized. For all isomers, the geometries of the transition states, computed at the B3LYP/aug-cc-pVTZ level, are planar and the C=O→OH_s energy barrier values lie between 153 and 158 kJ mol^{-1} (Table 1). Regarding the OH conformational equilibrium, the hydroxyl bond internal rotation pathways that connect the OH_s and OH_a conformers were explored at the same level of calculation (B3LYP/aug-cc-pVTZ) (see the Supporting Information; Table 1). Except for 3ClP, the OH_a conformers for all the molecular systems lie ≈20 kJ mol^{-1} above the OH_s conformers, and the energy needed to overcome the OH_a→OH_s barrier ($B_{OHa \to OHs}$) is in the range 16–18 kJ mol^{-1}. Considering the aforementioned additional stabilization of the OH_a form for 3ClP, it is easily understood that the energy difference between the OH conformers halves and the OH_a→OH_s barrier increases. Because of the lack of experimental data, it was not possible to benchmark the theoretical results or to estimate semiempirical values, as was done for the tautomers. Nevertheless, as there is agreement between the B3LYP and MP2 methods in the relative energy values of the conformers (Table 1), we suggest that the computational description for the conformational equilibrium can be considered more reliable than that for the tautomeric equilibrium.

The molecular electrostatic potential (MEP) surfaces mapped onto the electronic density distribution were generated to provide a "chemical feeling" for the energetic behavior of these systems (Table 1). It is a hard task to rationalize these results in terms of simple chemical concepts; nevertheless, we have attempted to clarify our findings. By considering the chlorinated compounds, in which the OH_s form is stabilized with respect to 2HP (5ClP and 6ClP), we can see that this effect is greater for substitution in position 6. This can be explained by the fact that position 5 is a *para*-like position with respect to the hydroxyl group in position 2 and is activated by the mesomeric effect. For this reason the insertion of a chlorine atom at this electrophilic position seems to stabilize the C=O form with respect to chlorination in the nucleophilic position 6. The same rationale can be applied to the 3ClP–4ClP pair: chlorination in position 3 (*ortho*-like) stabilizes the C=O form with respect to chlorination in position 4.

To sum up, these tautomeric equilibria are the result of a balance between electronic and resonance effects and involve the acidity of the NH group of lactam forms and the OH group of lactim forms.[13] Thus, great care must be taken in rationalizing the results because of the different effects that are competing.

Solvent phase

Because of the importance of tautomeric equilibria in biological contexts, we extended the calculations to include the presence of the solvent by using the Polarizable Continuum Model (PCM, see the computational methods in the Experimental Sec-

XI.57

tion). As the tautomeric equilibria can occur both in hydrophilic and hydrophobic environments, three solvents that possessed different dielectric constants were considered, namely, cyclohexane, dimethyl sulfoxide (DMSO), and water.

For all three solvents, we have attempted to predict the most stable tautomer and explore the effect of solvation and chlorination on the tautomeric equilibrium for the different media. For that purpose, we first theoretically calculated the C=O/OH$_s$ energy shifts upon solvation ($\Delta E_{0,SOLV} - \Delta E_{0,BARE}$). Then, by adding this value to the experimental (2HP, ΔE_0^{EXP}) or semiempirical (3ClP, 4ClP, 5ClP, 6ClP, $\Delta E_0^{SE-B3LYP}$) C=O/OH$_s$ energy difference for the bare molecule, we estimated the C=O/OH$_s$ relative energy in the different solvents. These data are summarized in Figure 5. For all the species, we observed that the C=O tautomers are stabilized in solution with respect to the bare molecule. This effect increases with the polarity of the solvent, which is due to the fact that the most polar C=O tautomer tends to be stabilized in polar solvents.
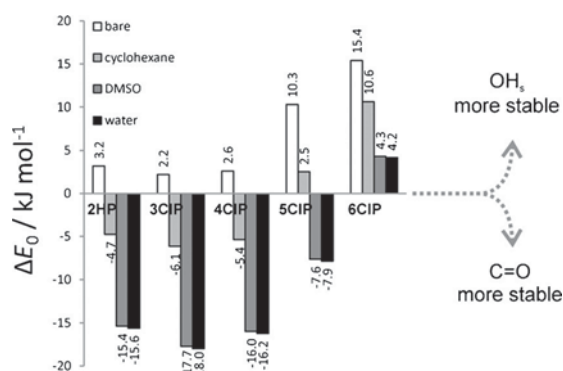

Figure 5. C=O/OH$_s$ relative zero-point-corrected vibrational electronic energies in the 2-hydroxypyridine/2-pyridone systems in gas and solvent phases. For all solvated systems, the $\Delta E_0 = \Delta E_0^{SE-B3LYP} + (\Delta E_{0,SOLV} - \Delta E_{0,BARE})$ is reported, whereas for 2HP, the value $\Delta E_0 = \Delta E_0^{EXP} + (\Delta E_{0,SOLV} - \Delta E_{0,BARE})$ is considered.

However, the magnitude of this stabilization depends on the position of the chlorine atom, and in general, the behaviour in solution was comparative to the gas phase. For 2HP, 3ClP, and 4ClP, the C=O tautomer was strongly stabilized, to the point that the tautomeric equilibrium was reversed, and this tautomer is predicted to be the most stable one for all three solvents. For 5ClP, only the most polar solvents (DMSO and water) reversed the equilibrium in favour of the C=O tautomer. For 6ClP, the OH$_s$ form was so energetically favoured that the effect of the solvent did not reverse the equilibrium, and the most stable species is predicted to be the OH$_s$.

A special point must be raised regarding the 6ClP species. Although our predictions estimated that the OH$_s$ form would be dominant in all solvents, experimental results reported by Forlani et al.[13] and Peng et al.[14] point to the C=O form as the major tautomer in various solvents. Nevertheless, they observed an important increase in the ratio of the OH forms. Qualitatively, our predictions agree with these experimental results, in that there is a significant increase in the population of the OH form with chlorination in position 6. However, our cal-

culations overestimated the population of the OH$_s$ form. When water was used as the solvent, this mismatch may be due to the fact that in our PCM calculations we did not take into account the protic nature of the solvent.

Finally, the OH$_a$/OH$_s$ conformational equilibrium shifts towards the OH$_a$ form, which is stabilized in the solvent; this is analogous to what happens to the C=O form. The trend is cyclohexane < DMSO ≈ water and the results are reported in Figure S2 (see the Supporting Information).

Conclusion

The present work shows the potential of a combined strategy of high-resolution rotational spectroscopy and theoretical calculations for the study of tautomeric equilibria. We systematically investigated the effects of chlorine substitution on the pyridine ring (in positions 3, 4, 5, and 6) on the tautomeric and conformational equilibria of the model system 2-hydroxypyridine/2-pyridone.

The combined experimental and theoretical results showed that the tautomeric equilibrium was greatly affected by substitution in different ring positions. The OH$_s$ tautomer, characterized by the O–H···N interaction, was found to be the dominant form, which is further stabilized by chlorination in positions 5 or 6. The C=O form, which is a high-energy compound, was observed to be stabilized by chlorination in positions 3 or 4. The OH$_a$ form was the least favourable in all cases, although the 3-substitution favoured this isomer owing to an O–H···Cl interaction. The accuracy of the theoretical calculations has been assessed by comparison with the results that were obtained from the microwave spectrum of the 5ClP and 6ClP species. Extension of the calculations for the solvated phase showed a qualitative agreement with previously reported experimental data, which enabled a discussion of the behavior of the tautomers in the solvent phase that our experiments do not cover.

Literature data and our own computations showed that, for these kind of equilibria, the results are greatly dependent on the theoretical method used, but the trend that is due to chlorination is similar for all of them. Moreover, it was possible to establish a semiempirical relative energy scale based on the experimentally observed tautomeric energy difference of 2HP.[12] The accuracy of these semiempirical data was tested and confirmed by experimental findings of 5ClP and 6ClP. Only the OH$_s$ tautomer was observed for 6ClP, whereas both the OH$_s$ and the C=O species were observed for 5ClP. This result is in accord with the higher energy difference between the OH$_s$ and C=O forms of 6ClP with respect to 5ClP; for the latter species, a relative energy value between the two forms was obtained from relative intensity measurements (9.3(1.8) kJ mol^{-1}), and it is in good agreement with the semiempirical result (10.4 kJ mol^{-1}).

The calculations that were extended to the solvated phase showed a stabilization of the C=O tautomer and the tautomeric equilibrium was reversed in some cases.

We have shown that rotational spectroscopy experiments were able to unambiguously identify different conformers and

XI.58

tautomers thanks to very precise structural data and the estimation of the relative energy difference. The strong synergy with theoretical calculations provides a solid strategy for a better understanding of this kind of equilibria.

Experimental Section

Computational methods: Quantum mechanical calculations were carried out by using the Gaussian09 package.[43] For each of the 2HP, 3ClP, 4ClP, 5ClP, and 6ClP compounds, the geometry of the three conformers (OH$_s$, OH$_a$, C=O) was fully optimized at the MP2/aug-cc-pVTZ and B3LYP/aug-cc-pVTZ levels of theory. Subsequent vibrational frequency calculations in the harmonic approximation confirmed that the stationary points were actual minima.

B3LYP/aug-cc-pVTZ calculations were used to characterize the transition state related to the lactam/lactim tautomeric equilibrium and to explore the hydroxyl internal rotation path. For this purpose, the HO-CN dihedral angle was varied in the 0–360° range by using a step of 10°.

Geometry optimizations and frequency calculations were also performed for all molecules in the presence of a solvent at the B3LYP/aug-cc-pVTZ level and by using the Polarizable Continuum Model (PCM) to mimic the solvents effect (cyclohexane $\varepsilon_r = 2.0165$, dimehylsolfoxide $\varepsilon_r = 46.826$, and water $\varepsilon_r = 78.3553$).[44]

Materials and methods: 6ClP (98%, m.p. 130°C, b.p. 327.5°C) and 5ClP (98%, m.p. 164°C, b.p. 319°C) were purchased from Alfa Aesar and used without further purification. The rotational spectra were recorded initially by using the free-jet absorption millimeter wave (FJAMMW) spectrometer at the University of Bologna (Italy) in the 59.6–74.4 GHz frequency region and later the Fourier transform microwave (FTMW) spectrometer at the UPV/EHU (Bilbao, Spain) in the 4–18 GHz spectral range.[31,45] It was necessary to heat both samples to obtain the vapour pressure suitable for the experiment in both spectrometers. In particular, the optimized temperatures for 6ClP and 5ClP were 100 and 140°C, respectively. Concerning the experiment with the FJAMMW instrument, at first the carrier gas was argon at a pressure of 25 kPa and the gas containing the vaporized sample was expanded to about 0.05 kPa through a 0.35 mm diameter nozzle, which was held 5°C above the vaporization temperature. For scans recorded with helium, a pressure of 50 kPa was used, and the mixture was expanded to about 0.1 kPa. Regarding the FTMW experiment, the carrier gas was neon at stagnation pressures of about 200–500 kPa and was expanded through a 0.8 mm nozzle to form a pulsed jet (≈ 200 μs). In this spectrometer, all transitions were observed to be split by the Doppler effect, so the rest frequencies were calculated as the average frequency of the two components. The estimated accuracy of the frequency measurements was better than 3 kHz. Lines separated by less than ≈ 10 kHz were resolvable, whereas for the FJAMMW, the accuracy of the frequency measurements was just under 50 kHz. In both cases, no decomposition products were observed.

Acknowledgements

[1] I. V. Magedov, L. Frolova, M. Manpadi, U. D. Bhoga, H. Tang, N. M. Evdokimov, O. George, K. Hadje Georgiou, S. Renner, M. Getlik, T. L. Kinnibrugh, M. A. Fernandes, S. Van Slambrouck, W. F. A. Steelant, C. B. Shuster S. Rogelj, W. A. L. van Otterlo, A. Kornienko, *J. Med. Chem.* **2011**, *54*, 4234–4246.

[2] B. Stanovnik, M. Tišler, A. R. Katritzky, O. V. Denisko, *Adv. Heterocycl. Chem.* **2006**, *91*, 1–134.

[3] A. Pérez, M. E. Tuckerman, H. P. Hjalmarson, A. O. von Lilienfeld, *J. Am. Chem. Soc.* **2010**, *132*, 11510–11515.

[4] P. Beak, J. B. Covington, J. M. White, *J. Org. Chem.* **1980**, *45*, 1347–1353.

[5] M. Ben Messaouda, M. Abderrabba, A. Mahjoub, G. Chambaud, M. Hochlaf, *Comput. Theor. Chem.* **2012**, *990*, 94–99.

[6] M. Piacenza, S. Grimme, T. O. Chemie, O. I. Der Universita, *J. Comput. Chem.* **2004**, *25*, 83–98.

[7] J. L. Sonnenberg, K. F. Wong, G. A. Voth, H. B. Schlegel, *J. Chem. Theory Comput.* **2009**, *5*, 949–961.

[8] P. Beak, F. S. Fry, Jr., J. Lee, F. Steele, *J. Am. Chem. Soc.* **1976**, *98*, 171–179.

[9] J. C. Poully, J. P. Schermann, N. Nieuwjaer, F. Lecomte, G. Gregoire, C. Desfrancois, G. A. Garcia, L. Nahon, D. Nandi, L. Poisson, M. Hochlaf, *Phys. Chem. Chem. Phys.* **2010**, *12*, 3566–3572.

[10] A. Maris, P. Ottaviani, W. Caminati, *Chem. Phys. Lett.* **2002**, *360*, 155–160.

[11] A. Z. Michelson, A. Petronico, J. K. Lee, *J. Org. Chem.* **2012**, *77*, 1623–1631.

[12] L. D. Hatherley, R. D. Brown, P. D. Godfrey, A. P. Pierlot, W. Caminati, D. Damiani, S. Melandri, L. B. Favero, *J. Phys. Chem.* **1993**, *97*, 46–51.

[13] L. Forlani, G. Cristoni, C. Boga, P. E. Todesco, E. Del Vecchio, S. Selva, M. Monari, *ARKIVOC* **2002**, *11*, 198–215.

[14] C. S. Peng, A. Tokmakoff, *J. Phys. Chem. Lett.* **2012**, *3*, 3302–3306.

[15] R. Sanchez, B. M. Giuliano, S. Melandri, W. Caminati, *Chem. Phys. Lett.* **2007**, *435*, 10–13.

[16] R. Sanchez, B. M. Giuliano, S. Melandri, W. Caminati, *Chem. Phys. Lett.* **2006**, *425*, 6–9.

[17] S. Melandri, L. Evangelisti, A. Maris, W. Caminati, B. M. Giuliano, V. Feyer, K. C. Prince, M. Coreno, *J. Am. Chem. Soc.* **2010**, *132*, 10269–10271.

[18] S. S. T. King, W. L. Dilling, N. B. Tefertiller, *Tetrahedron* **1972**, *28*, 5859–5863.

[19] P. Beak, *Acc. Chem. Res.* **1977**, *10*, 186–192.

[20] O. G. Parchment, I. H. Hillier, D. V. S. Green, *J. Chem. Soc. Perkin Trans. 2* **1991**, 799–802.

[21] M. Takasuka, T. Saito, H. Nakai, *Vib. Spectrosc.* **1996**, *13*, 65–74.

[22] E. Spinner, *Spectrochim. Acta Part A* **1986**, *42*, 1289–1293.

[23] R. S. Ruoff, T. D. Klots, T. Emilsson, H. S. Gutowsky, *J. Chem. Phys.* **1990**, *93*, 3142–3150.

[24] H. M. Pickett, *J. Mol. Spectrosc.* **1991**, *148*, 371–377.

[25] J. K. G. Watson, in *Vibrational Spectra and Structure* (Ed.: J. R. Durig), Elsevier Science Publishers, Amsterdam, **1977**, pp. 1–89.

[26] J. K. Bragg, *Phys. Rev.* **1948**, *74*, 533–538.

[27] G. T. Fraser, R. D. Suenram, C. L. Lugez, *J. Phys. Chem. A* **2000**, *104*, 1141–1146.

[28] P. Pyykkö, *Mol. Phys.* **2008**, *106*, 1965–1974.

[29] E. J. Cocinero, A. Lesarri, P. Écija, F. J. Basterretxea, J.-U. Grabow, J. A. Fernández, F. Castaño, *Angew. Chem. Int. Ed.* **2012**, *51*, 3119–3124; *Angew. Chem.* **2012**, *124*, 3173–3178.

[30] C. Calabrese, Q. Gou, A. Maris, S. Melandri, W. Caminati, *J. Phys. Chem. B* **2016**, *120*, 6587–6591.

[31] C. Calabrese, A. Maris, L. Evangelisti, L. B. Favero, S. Melandri, W. Caminati, *J. Phys. Chem. A* **2013**, *117*, 13712–13718.

XI.59

[32] J. Demaison, N. C. Craig, P. Groner, P. Écija, E. J. Cocinero, A. Lesarri, H. D. Rudolph, *J. Phys. Chem. A* **2015**, *119*, 1486–1493.

[33] V. A. Shubert, D. Schmitz, D. Patterson, J. M. Doyle, M. Schnell, *Angew. Chem. Int. Ed.* **2014**, *53*, 1152–1155; *Angew. Chem.* **2014**, *126*, 1171–1174.

[34] J. Kraitchman, *Am. J. Phys.* **1953**, *21*, 17–24.

[35] Z. Kisiel, *Spectroscopy from Space*, Kluwer Academic Publishers, Dordrecht, **2001**.

[36] I. Merke, C. Keussen, H. Dreizler, M. Onda, *Z. Naturforsch.* **1990**, *45a*, 1273–1280.

[37] R. D. Brown, J. Matouskova, *J. Mol. Struct.* **1975**, *29*, 33–37.

[38] C. Tanjaroon, R. Subramanian, C. Karunatilaka, S. G. Kukolich, *J. Phys. Chem.* **2004**, *108*, 9531–9539.

[39] N. Heineking, H. Dreizler, R. Schwarz, *Z. Naturforsch.* **1986**, *41a*, 1210–1213.

[40] M. Meyer, U. Andresen, H. Dreizler, *Z. Naturforsch.* **1986**, *42a*, 197–206.

[41] K. Bolton, R. D. Brown, *Aust. J. Phys.* **1974**, *27*, 143–146.

[42] J. Almlöf, Å. Kvick, I. Olovsson, *Acta Crystallogr. B* **1971**, *27*, 1201–1208.

[43] Gaussian 09, Revision D.01, M. J. Frisch, G. W. Trucks, H. B. Schlegel, G. E. Scuseria, M. A. Robb, J. R. Cheeseman, G. Scalmani, V. Barone, B. Mennucci, G. A. Petersson, H. Nakatsuji, M. Caricato, X. Li, H. P. Hratchian, A. F. Izmaylov, J. Bloino, G. Zheng, J. L. Sonnenberg, M. Hada, M. Ehara, K. Toyota, R. Fukuda, J. Hasegawa, M. Ishida, T. Nakajima, Y. Honda, O. Kitao, H. Nakai, T. Vreven, J. A. Montgomery, Jr., J. E. Peralta, F. Ogliaro, M. Bearpark, J. J. Heyd, E. Brothers, K. N. Kudin, V. N. Staroverov, R. Kobayashi, J. Normand, K. Raghavachari, A. Rendell, J. C. Burant, S. S. Iyengar, J. Tomasi, M. Cossi, N. Rega, J. M. Millam, M. Klene, J. E. Knox, J. B. Cross, V. Bakken, C. Adamo, J. Jaramillo, R. Gomperts, R. E. Stratmann, O. Yazyev, A. J. Austin, R. Cammi, C. Pomelli, J. W. Ochterski, R. L. Martin, K. Morokuma, V. G. Zakrzewski, G. A. Voth, P. Salvador, J. J. Dannenberg, S. Dapprich, A. D. Daniels, Ö. Farkas, J. B. Foresman, J. V. Ortiz, J. Cioslowski, D. J. Fox, Gaussian, Inc. Wallingford CT, **2009**.

[44] M. Cossi, N. Rega, G. Scalmani, V. Barone, *J. Comput. Chem.* **2003**, *24*, 669–681.

[45] E. J. Cocinero, A. Lesarri, P. Ecija, J.-U. Grabow, J. A. Fernández, F. Castaño, *Phys. Chem. Chem. Phys.* **2010**, *12*, 6076–6083.

XI.60
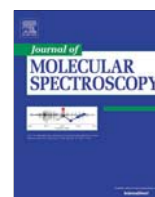
$$CF_3CH_2Cl$$

Comprehensive rotational spectroscopy of the newly identified atmospheric ozone depleter CF$_3$CH$_2$Cl

Iciar Uriarte [a], Zbigniew Kisiel [b,*], Ewa Białkowska-Jaworska [b], Lech Pszczółkowski [b], Patricia Ecija [a], Francisco J. Basterretxea [a], Emilio J. Cocinero [a]

[a] Departamento de Química Fisica, Universidad del País Vasco (UPV-EHU), Bilbao, Spain
[b] Institute of Physics, Polish Academy of Sciences, Al. Lotników 32/46, 02-668 Warszawa, Poland

ABSTRACT

The pure rotational spectrum of CF$_3$CH$_2$Cl (1-choro-2,2,2-trifluoroethane, HCFC-133a) was investigated at 8–18 GHz in supersonic expansion with chirped pulse and cavity rotational spectroscopy, and at 94–309 GHz with broadband millimetre wave spectroscopy. Spectroscopic constants for the two principal isotopic species have been considerably updated from global fits over extensive data sets, numbering close to 3000 lines for the ground state of CF$_3$CH$_2^{35}$Cl and 1800 lines for CF$_3$CH$_2^{37}$Cl. Four different ^{13}C containing isotopologues have been assigned, as well as several new low lying vibrational states. The new measurements have been augmented with anharmonic force field calculations in an evaluation of the semi-experimental equilibrium geometry for CF$_3$CH$_2$Cl.

© 2017 Elsevier Inc. All rights reserved.

1. Introduction

In a recent study [1] several previously unknown atmospheric ozone depleting compounds were identified by analysis of unpolluted air samples collected in Tasmania and extracted from deep firn snow in Greenland. Two of those compounds, CF$_3$CCl$_3$ and CF$_3$CH$_2$Cl, continue to accumulate in the atmosphere, and while their emissions are significantly smaller than for the compounds withdrawn under the Montreal Protocol, their origin is unclear. The greatest emissions appear to be for CF$_3$CH$_2$Cl. Some molecular properties of relevance to its atmospheric retrieval have already been investigated [2], while rotationally resolved data that could be used in such work have not yet been available. The only previous investigation of the rotational spectrum of CF$_3$CH$_2$Cl has been carried out by Ogata et al. [3] by means of Stark modulation spectroscopy, but it was limited to a small number of transitions at 8–26 GHz. The infrared and Raman spectrum has also been studied [4,5] and normal mode assignment has been carried out [4]. In the present work we combine several contemporary experimental techniques in order to provide a comprehensive update on the rotational spectroscopy of CF$_3$CH$_2$Cl.

2. Experimental details

Rotational spectra were measured with three spectrometers: at the low temperatures of supersonic expansion with two different Fourier-transform (FTMW) spectrometers, and at room temperature with a broadband millimetre wave (MMW) spectrometer. We first used the chirped pulse (CP-FTMW) spectrometer available at the University of the Basque Country (UPV/EHU). This instrument is based on Pate's original design [6] and has been described elsewhere [7]. The CF$_3$CH$_2$Cl sample was in the form of a 2% mixture in carrier gas (20% He, 80% Ne) at a pressure of 2.4 bar relative to vacuum. The supersonic expansion valve was opened for 700 μs and was pulsed at a rate of 1 Hz. For each chirped pulse, a 40 μs time domain signal was recorded, and 10 chirped pulses were used during each molecular pulse. A total of 800,000 time domain signals were coadded.

Additional, higher resolution measurements were carried out with the cavity, FTMW spectrometer in Warsaw [8]. This was constructed as a coaxial version of the original Balle, Flygare design [9] and was later modified to a single step downconversion mode [10]. The sample was a 1% mixture in Ar carrier gas at 1.2 bar, and was admitted into the spectrometer chamber as 1 ms long gas pulses repeated at a rate of 5 Hz. Room temperature measurements were carried out with the broadband MMW spectrometer in Warsaw, based on backward-wave oscillator sources [11,12]. Measurements in the 90–140 GHz region were made by using the same

* Corresponding author.
E-mail address: kisiel@ifpan.edu.pl (Z. Kisiel).

spectrometer but with a cascaded harmonic multiplication source [12]. The sample in this case was CF_3CH_2Cl vapour contained in a 3.5 m long absorption cell at a pressure of 5 mTorr.

All measurements were carried out on a commercially available sample. The AABS package [13,14] was used as a graphical front end for comparing spectra with predictions and for setting up the data sets for the fits. The fits and predictions were made by using the ASFIT/ASROT package from the PROSPE website [15,16] for the initial MMW assignments, and the SPFIT/SPCAT package [17,18] for hyperfine-resolved measurements and for the final
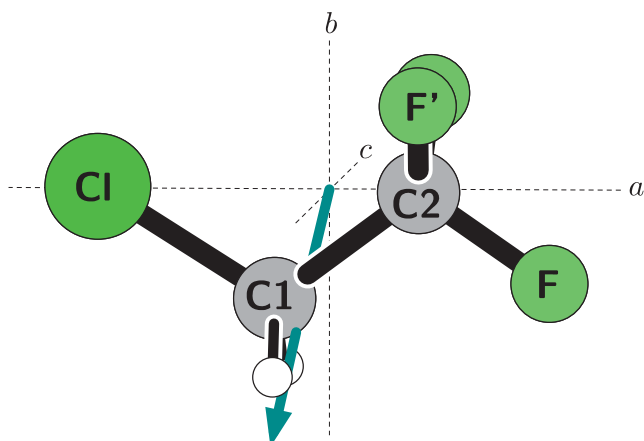
analysis. The measurements made in this work were used at assumed frequency uncertainties of 2 kHz for the cavity FTMW data, 5 kHz for the chirped pulse measurements and 50 kHz for the MMW spectrometer. The data from Ogata et al. [3] were also incorporated into the data sets at frequency uncertainty of 100 kHz.

3. Rotational spectrum

The electric dipole moment of CF_3CH_2Cl (see Fig. 1) has not been measured in the gas phase but is calculated to consist of a dominant $\mu_b = 1.87$ D component and a significantly smaller $\mu_a = 0.41$ D component (MP2/aug-cc-pVTZ level). This predicts the b-type transitions to be about 20 times stronger than the a-type transitions. Not surprisingly, only b-type transitions have hitherto been measured [3] and such transitions also dominated the chirped pulse spectrum. Nevertheless, the sensitivity of the chirped pulse experiment allowed the weaker ^aR-branch transitions to be observed at excellent signal to noise, as is apparent from Fig. 2.

Each rotational transition observed at the resolution of supersonic expansion is split into a number of components resulting from nuclear quadrupole hyperfine interaction with the chlorine nucleus. In Fig. 2 even the weaker, outlying $\Delta F = 0$ components are clearly visible. In addition, the use of the He/Ne expansion mixture leads to somewhat higher rotational temperatures (typically 5 K) than with Ar expansion (1 K or lower) so that transitions with higher values of rotational quantum numbers than is usual for supersonic expansion can be observed. The sequences of ^bQ-branch transitions for $CF_3CH_2^{35}Cl$ provide an opportunity to investigate this effect and Fig. 3 shows how transitions up to $J = 18$ are
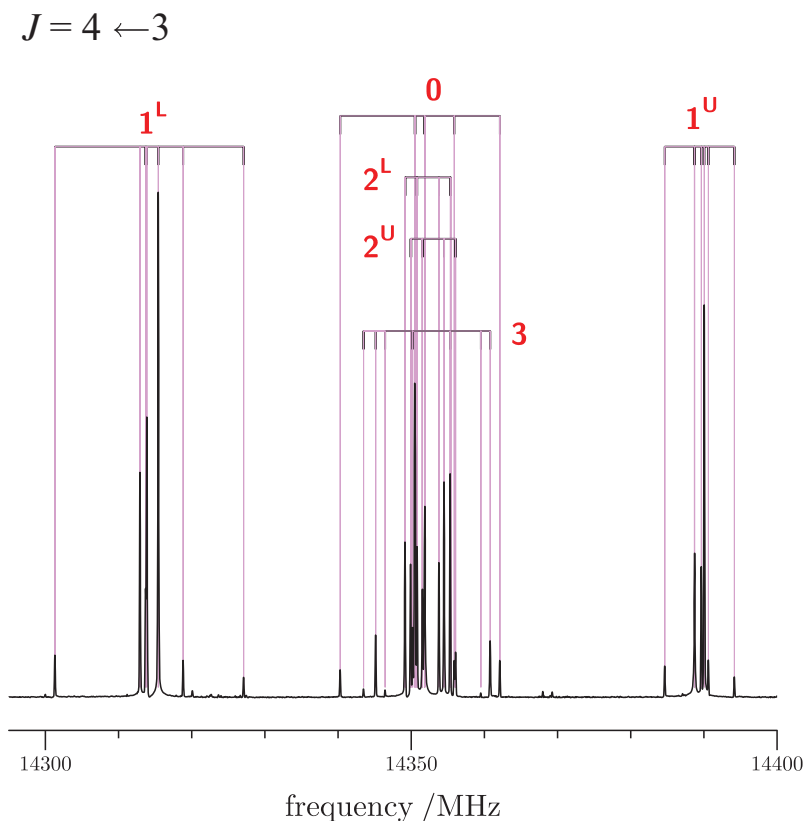

Fig. 1. The orientation of the CF_3CH_2Cl molecule in the inertial axes and atom numbering used in this work. The molecule is of C_s-symmetry where the ab inertial plane is the symmetry plane. The arrow indicates the direction of the electric dipole moment and is drawn from the notional negative to the notional positive charge.

Fig. 2. The complete $J = 4 \leftarrow 3$ ^aR-branch rotational transition of $CF_3CH_2^{35}Cl$ observed in the chirped pulse spectrum. The nuclear quadrupole splitting structure of each transition consists of a central clump of $\Delta F = +1$ lines, surrounded by weak $\Delta F = 0$ outliers. The values of the K_a quantum number are indicated, with L and U identifying the lower and upper frequency component, respectively.
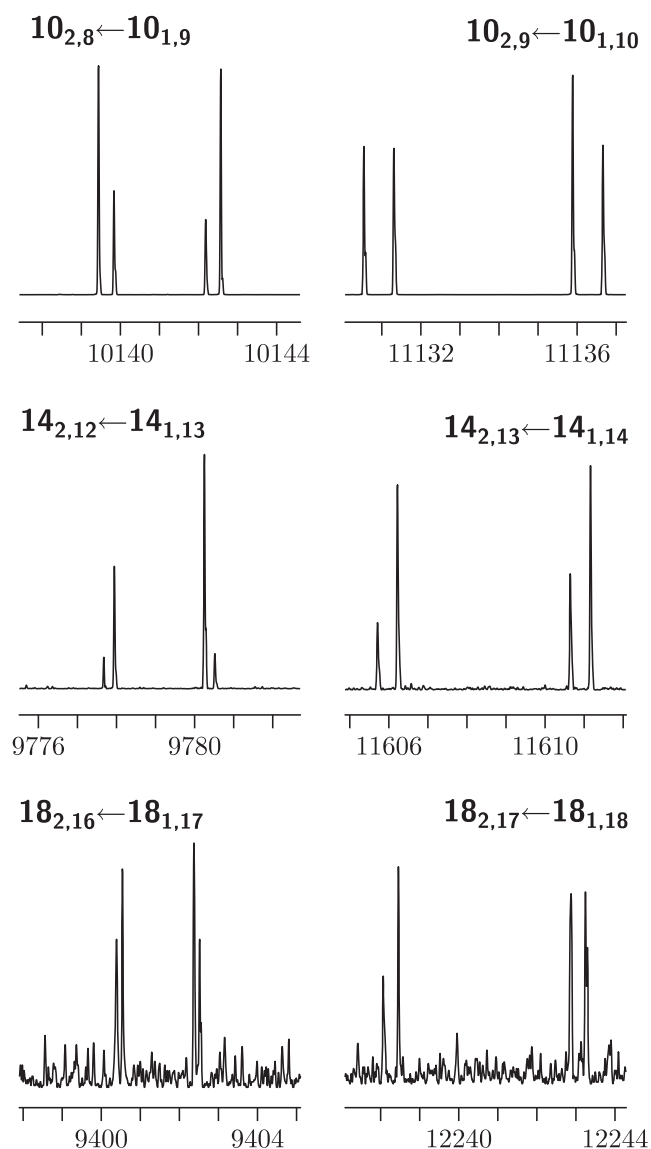
XI.64

Fig. 3. Illustration of the good visibility of ^bQ-branch transitions for $CF_3CH_2{}^{35}Cl$ for higher values of J observed in the chirped pulse spectrum recorded using supersonic expansion with predominantly Ne carrier gas.

visible in both lower and higher frequency parts of the $K_a = 2 \leftarrow 1$ band.

The analysis of the relatively low-J supersonic expansion spectrum allowed sufficiently accurate prediction of the much higher-J transitions expected in the room-temperature millimetre wave rotational spectrum, which was ultimately measured up to $J = 130$. This spectrum is not particularly dense and the strongest repetitive feature arises from $n = 3$ type-II$^-$ bands formed by ^bR-branch transitions, with general properties described in Refs. [19,20]. Examples of overlapped bands of this type for the ground and one of the excited states of $CF_3CH_2{}^{35}Cl$ are shown in Fig. 4. The bands are due to the fact that the rotational constant ratio $2A$ to $(B + C)$ is accidentally close to 3 (equal to 2.973 for $CF_3CH_2{}^{35}Cl$). This results in convergence into relatively compact bands of lines characterised by J changing in steps of 2 and K_a in steps of 1 between successive transitions in the band. Bands of this type have been observed for trichloroethylene [20], while $n = 4$, type-II$^-$ bands have been observed for $S(CN)_2$ [21].

Some MMW transitions showed a splitting ranging up to 3 MHz, presumably as an effect of the existence of the A and E internal

rotor substates due to the presence of the low frequency torsional motion [4]. The splitting showed only a weak dependence on K_a, J, and the vibrational state, and was averaged over in making frequency measurements. Some supersonic expansion lines showed Doppler doubling, which was averaged over when it was well defined. On the other hand, lines with malformed profiles were not measured due to the abundance of data. This included the highest-J lines shown in Fig. 3 since those were not critical to the determination of any of the spectroscopic constants.

In fitting the data we have taken advantage of the feature of the SPFIT program that allows hyperfine-resolved measurements to be combined with hyperfine-unresolved measurements in a single data set. In this way we have been able to carry out global fits of all of the available measurements and the resulting spectroscopic constants are reported in Table 1 for the ground states of the two principal isotopologues. The present results are also compared with previous values and with quantum chemistry calculations. The complete results of fits and the data files are in the electronic supplementary Tables S1 and S2. It is instructive to consider the subset statistics for the fits listed in Table 2. These are generated automatically with the PIFORM program from the PROSPE website and demonstrate that the frequency measurement uncertainty assumed for each spectrometer is reasonable. In fact, the result for the chirped pulse subset provides a calibration of the excellent performance of this spectrometer. It is noted, however, that we used a different FFT transformation of the time domain signal to the default one based on the Kaiser-Bessel windowing function [22]. While the latter has the advantage of removing the interference from lineshapes of very strong lines it has the disadvantage of broadening the line profiles. Instead, we used a standard Bartlett windowing function and a power mode display, as provided by the program FFTS written by one of the present authors (Z.K.). In this way full width, half height linewidths of 30–40 kHz were obtained leading to significant improvement in frequency measurement precision. Details of the program will be published elsewhere.

On inspecting the constants in Table 1 we were surprised at seeing extremely low values of the δ_J centrifugal distortion constant as determined from fitting Watson's A-reduced asymmetric rotor Hamiltonian [23]. In addition to the small values there was also a change in sign from the ^{35}Cl to the ^{37}Cl isotopologue. It turns out that this behaviour is relatively easy to rationalise since the value of δ_J arises from the difference between two underlying τ terms [24]. These terms, in the I^r representation used in the fits are τ_{bbbb} and τ_{cccc}. Evaluation from the *ab initio* harmonic force field (using the Firefly package [25]) and the FCONV and VIBCA programs [16] reveals that τ_{bbbb} and τ_{cccc} are practically identical and close to 1.05 kHz. Since $\delta_J = -(\tau_{bbbb} - \tau_{cccc})/16$ the self cancellation of the τ constants apparent in the experimental δ_J is to 0.06% of their values. It is impossible to achieve this level of precision with a quantum chemistry calculation of centrifugal distortion constants, even though Table 1 demonstrates satisfactory agreement with experiment. On the other hand, even though the calculated values of δ_J for the two isotopologues are both positive, their difference (0.057 Hz) is rather close to that between the experimental values (0.046 Hz).

4. Excited vibrational states

It is already apparent from Fig. 4 that rotational transitions in excited vibrational states play a significant role in the room-temperature MMW spectrum. Even though a complete normal mode analysis has been reported [4], the normal mode numbering has not yet been assigned. In the following we label the modes in standard manner, first the A' symmetry modes, from highest to lowest, then the A'' symmetry modes. The lowest frequency A''
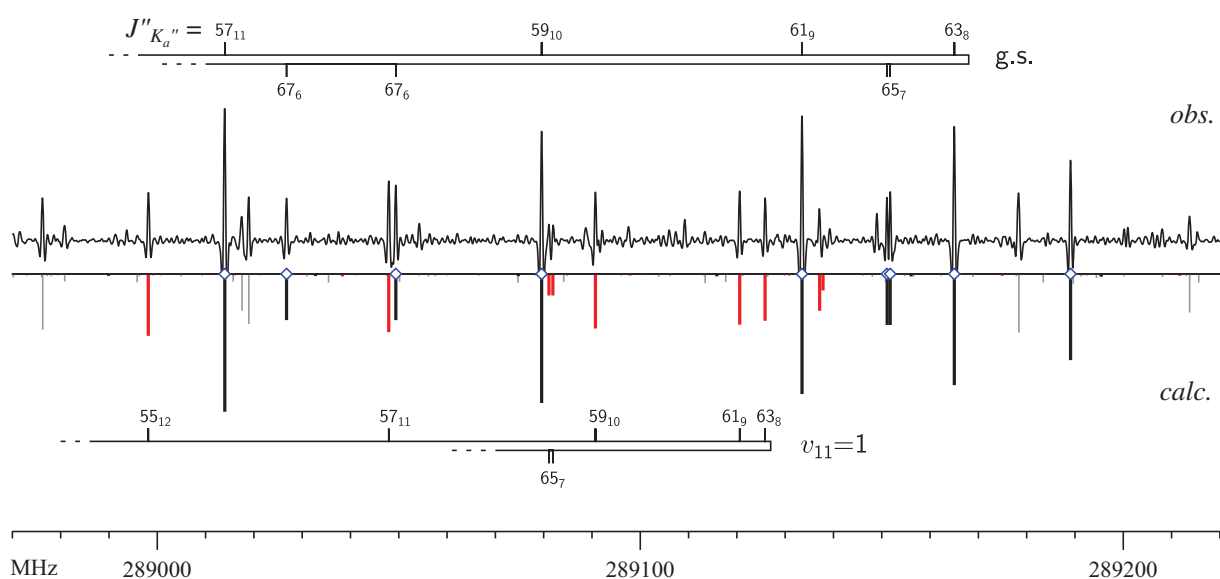
Fig. 4. Examples of the main repetitive features in the millimetre wave spectrum of CF_3CH_2Cl. These are $n = 3$, type-II$^-$ bands [20] arising from accidentally satisfied condition $2A = n(B + C)$. Successive lines in the band differ by 2 in J'' and 1 in K_a''. The lines of the ground state and $v_{11} = 1$ of $CF_3CH_2{}^{35}Cl$ are identified with heavier sticks in the prediction, while fainter sticks are for other assigned species. The open rhombus symbols mark lines in the ground state dataset for the parent species.

Table 1
Spectroscopic constants for the ground states of $CF_3CH_2{}^{35}Cl$ and $CF_3CH_2{}^{37}Cl$.

	$CF_3CH_2{}^{35}Cl$			$CF_3CH_2{}^{37}Cl$		
	Ref. [3]	This work	Calc.[a]	Ref. [3]	This work	Calc.[a]
A/MHz	5332.833(5)	5332.845695(46)[b]		5332.0829(6)	5332.821576(68)	
B/MHz	1803.400(3)	1803.398752(16)		1756.0200(2)	1756.199541(25)	
C/MHz	1784.671(3)	1784.676242(16)		1738.435(2)	1738.438412(24)	
Δ_J/kHz	0.271(12)	0.2788324(30)	0.2697	0.246(17)	0.2694044(53)	0.2604
Δ_{JK}/kHz	2.645(27)	2.709971(18)	2.6929	2.605(14)	2.633147(30)	2.6146
Δ_K/kHz	−1.66(20)	−1.611476(64)	−1.6015	−1.74(48)	−1.525020(93)	−1.5140
δ_J/kHz	0.49(19)	0.00004067(73)	0.000179	0.37(6)	−0.0000056(12)	0.000122
δ_K/kHz	0.89(13)	0.43716(73)	0.3367	0.59(7)	0.4080(13)	0.3129
H_J/Hz		0.00002194(16)			0.00002311(34)	
H_{JK}/Hz		0.0000103(11)			−0.0000138(24)	
H_{KJ}/Hz		−0.0014495(52)			−0.0015924(89)	
H_K/Hz		0.002297(22)			0.002453(33)	
$(3/2)\chi_{aa}$/MHz	−68.91(75)	−68.9477(15)		−54.31(59)[c]	−54.3987(24)	
$(1/4)(\chi_{bb}-\chi_{cc})$/MHz	−8.65(16)	−8.71437(48)		−6.81(13)[c]	−6.85925(85)	
χ_{ab}/MHz	51.95[d]	52.103(13)		40.94[c]	41.105(69)	
N_{lines}, N_{rot}[e]		2933,99			1803,86	
σ_{fit}/MHz		0.0317			0.0336	
σ_{rms}[f]		0.686			0.730	

[a] Evaluated from an unscaled B3LYP/6-311++G(d,p) harmonic force field.
[b] The quantities in round parentheses are standard errors in units of the least significant digit of the value of the constant.
[c] Estimated from the constants for the ^{35}Cl species by using the quadrupole moment ratio $^{35}Cl/^{37}Cl = 1.26874(4)$, Ref.[28].
[d] Calculated with the assumption that the hyperfine z-axis coincides with the C–Cl bond, which is at 31.79° to the z-axis.
[e] The number of different frequency lines in the global fit and the number of different rotational transitions for which hyperfine structure was measured.
[f] Unitless deviation of the weighted fit.

Table 2
Subset statistics for the global fit of rotational transitions for $CF_3CH_2{}^{35}Cl$.

	N_{lines}[a]	N_{rot}[b]	σ/kHz	J		K_a		Freq./GHz	
				Min	Max	Min	Max	Min	Max
Cavity	70	14	1.80	1	6	0	2	10.6	17.8
Chirped pulse	386	75	3.63	0	9	0	4	7.1	18.4
mmw	2448	2448	33.5	9	130	0	44	94.2	308.2
Ref.[3]	29	10	81.2	2	22	0	3	10.8	21.8

[a] The number of distinct measured frequencies.
[b] The number of different rotational transitions.

XI.66

mode, v_{18} (109 cm^{-1} [4]) and the lowest A' mode, v_{11} (191 cm^{-1} [4], 180 cm^{-1} [5]) are thus of greatest relevance to the room-temperature rotational spectrum. Some rotational transitions in the $v_{18} = 1$ state of the parent species have already been reported [3]. In this work, we extended those measurements to over 300 GHz and have also assigned $v_{18} = 1$ transitions in the CF$_3$CH$_2$-^{37}Cl isotopologue. The resulting spectroscopic constants are reported in Table 3, and the primary files are in Table S3.

In the parent isotopologue we found that, in addition to transitions in the $v_{18} = 1$ state, it was possible to assign rotational transitions in the two vibrational states immediately above it, $v_{11} = 1$ and $v_{18} = 2$. Transitions in these two states were initially identified on the basis of relative intensities, since both states are expected to be at vibrational energy of around 200 cm^{-1}, and the next higher vibrational state is expected to be 100 cm^{-1} higher. The vibrational assignment of these two states was also relatively straightforward since the rotational constants of the ground state, $v_{18} = 1$ and $v_{18} = 2$ are expected to be in a harmonic progression. The results for these two higher states are also reported in Tables 3 and S3. On inspecting the quartic centrifugal distortion constants obtained from single state fits for $v_{11} = 1$ and $v_{18} = 2$ we find some indication of effective behaviour resulting from possible perturbation between these states. In particular, the values of δ_J and δ_K have similar magnitude but opposed sign. We attempted to carry out a coupled fit for these two states based on the expected c-type Coriolis and Fermi interactions. This achieved moderate success in being able to encompass a somewhat larger numbers of measured lines and delivered values of quartic constants for $v_{11} = 1$ that were closer to those for the ground state, and for $v_{18} = 2$ that were closer to those estimated from $v_{18} = 1$ and the ground state. Nevertheless, such fits were ambiguous concerning the vibrational energy difference between the two states, possibly because we were not able to identify level-crossing type resonances that enabled the multiple successful coupled fits in our recent studies of 2,2-dichloropropane [26] or glycolic acid [27]. For this reason we prefer to report in Table 3 the effective single state constants, although in Table S4 we also provide a comparison of the performance of the single state fits and a specimen two-state coupled fit.

5. The ^{13}C isotopic species

The chirped pulse spectrum had a sufficiently high signal to noise ratio to allow assignment also of the ^{13}C species in natural abundance, as shown in Fig. 5. This was possible not only for the ^{13}C isotopologues of CF$_3$CH$_2$^{35}Cl, but also for those of CF$_3$CH$_2$^{37}Cl. The spectroscopic constants determined for the four newly assigned species are reported in Table 4 and the complete results and data files for the fits are in Table S5. The fits are based entirely on the chirped pulse data and their deviations are comparable to the deviation for the chirped pulse subset for the ground state of the parent species in Table 2. Since the range of quantum number values for the isotopic transitions is insufficient for determination of quartic centrifugal distortion constants we used assumed values as described in Table 4. We noted the considerable differences in the calculated values of δ_K for the ^{13}C1 and ^{13}C2 isotopologues, but those turned out to be rationalisable by similar arguments to those used above for δ_J. The almost identical values of the A rotational constant for CF$_3$CH$_2$^{35}Cl and CF$_3$CH$_2$^{37}Cl indicate that the chlorine atom has near zero b and c inertial coordinates. Furthermore, the values of A for the ^{13}C2 species are also very close to those for the parent species indicating that b and c coordinates of C2 are also near zero. Since symmetry dictates that the c coordinates are indeed zero this shows that the b coordinates of both Cl and C2 are very close to zero (as apparent in Fig. 1). Similar conclusions could also be made by considering the values of the planar moments P_b, and have significant repercussions for the structure determination, as discussed further below.

6. Nuclear quadrupole hyperfine coupling

The chlorine nuclear quadrupole coupling constants determined for the various isotopic species of CF$_3$CH$_2$Cl are a useful source of direct molecular information and a testing ground for calculations. In particular, the precision of the supersonic expansion measurements allowed accurate determination of χ_{ab}, the only off-diagonal nuclear quadrupole coupling constant. This, in turn,

Table 3
Spectroscopic constants for the excited vibrational states of CF$_3$CH$_2$Cl.

	CF$_3$CH$_2$^{35}Cl				CF$_3$CH$_2$^{37}Cl
	$v_{18} = 1$, Ref. [3]	$v_{18} = 1$	$v_{18} = 2$	$v_{11} = 1$	$v_{18} = 1$
A/MHz	5324.952(11)	5324.967909(90)	5317.19461(28)	5339.70650(38)	5325.03966(17)
B/MHz	1800.614(9)	1800.578351(34)	1796.323583(93)	1802.559862(72)	1753.469696(77)
C/MHz	1784.621(9)	1784.594882(35)	1783.153853(85)	1782.928818(73)	1738.327223(77)
Δ_J/kHz	[0.271][a]	0.2760335(58)	0.266202(17)	0.280573(16)	0.266630(15)
Δ_{JK}/kHz	[2.645]	2.823667(38)	2.94495(15)	2.68185(22)	2.743865(63)
Δ_K/kHz	[-1.66]	−1.765176(89)	−2.08903(32)	−1.40856(87)	−1.67486(20)
δ_J/kHz	[0.49]	−0.0002845(33)	−0.001475(10)	0.0011895(79)	−0.0003214(25)
δ_K/kHz	[0.89]	0.5567(28)	−2.0252(54)	2.0626(47)	0.5262(39)
H_J/Hz		0.00002920(49)	0.0000217(14)	0.0000170(14)	0.0000258(10)
H_{JK}/Hz		0.0002926(46)	0.003028(46)	−0.002841(48)	0.0002741(48)
H_{KJ}/Hz		−0.0024838(82)	0.009008(81)	−0.02608(51)	−0.002578(18)
H_K/Hz		0.002418(26)	−0.00701(15)	0.01410(64)	0.002682(78)
h_J/Hz		−0.00000327(31)	0.0000041(10)	−0.00001255(79)	[−0.00000327][b]
h_{JK}/Hz		0.00727(38)	−0.00556(95)	0.00100(71)	[0.00727][b]
h_K/Hz		[0.]	−0.1084(89)	−0.580(16)	[0.]
N_{lines}[c]		1994	946	1085	833
σ_{fit}/MHz		0.0314	0.0423	0.0454	0.0373
σ_{rms}[d]		0.621	0.846	0.905	0.747

[a] Fixed to the values in the ground state, determined in Ref. [3].
[b] Fixed to the value in the $v_{18} = 1$ state of the parent species.
[c] The number of lines in the global fit.
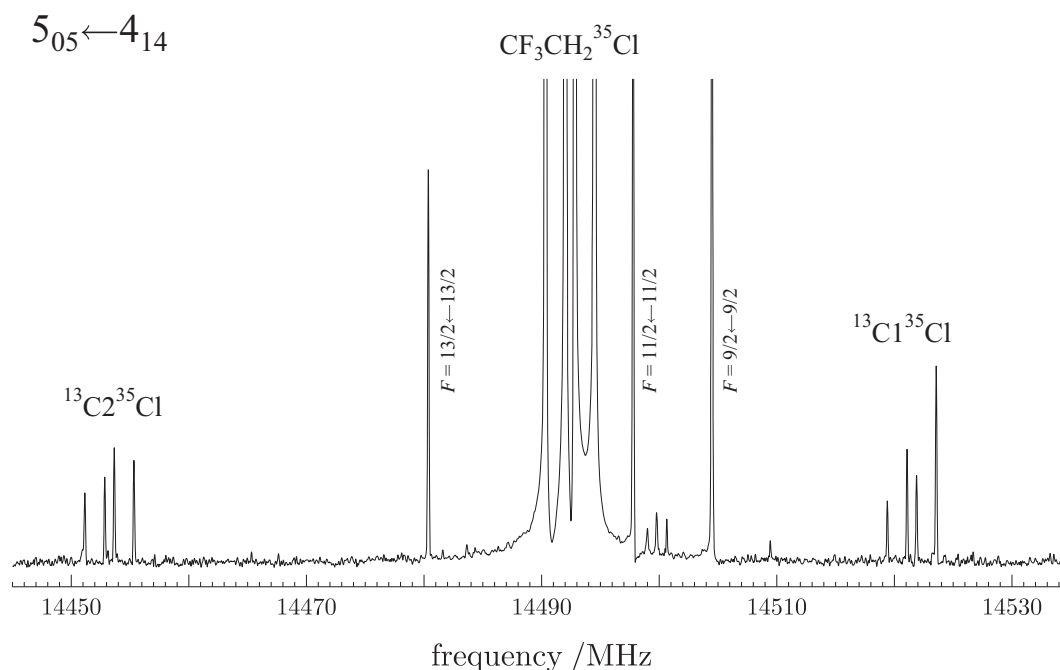[d] Unitless deviation of the weighted fit.

$5_{05} \leftarrow 4_{14}$

Fig. 5. Illustration of the good visibility in the chirped pulse spectrum of the natural abundance ^{13}C transitions of CF$_3$CH$_2$Cl. The three marked hyperfine patterns are all for the ^{b}R-branch $5_{05} \leftarrow 4_{14}$ transition.

allows diagonalisation of the nuclear quadrupole coupling tensor from the inertial principal axes *abc* to its own principal axes *xyz*. The components of the tensor in the two sets of axes are listed in Tables 5 and 6. The reliability of the evaluation of the principal nuclear quadrupole tensor elements is confirmed by the fact that the values for all three ^{35}Cl species are identical within 2–3 σ, and the same is the case for the three ^{37}Cl species.

We can use these results to test the performance of the methods used by spectroscopists to predict nuclear quadrupole splitting constants. The calculated values for CF$_3$CH$_2$^{35}Cl in Table 5 compare two different scaling approaches [28] with calculation based on a specially tailored basis set for chlorine advocated by Bailey [29]. All three approaches provide comparable (and good) accuracy concerning the values of the hyperfine constants, with the scaled DFT result being slightly more successful. On the other hand, the rotation angle θ_{za} between the principal inertial axes and the principal

quadrupole axes is, in this case, most accurately predicted by the Bailey approach.

Another quantity of interest is the difference δ between the quadrupole derived angle θ_{za} and the direction of the CCl bond. It has been shown [30] that the contribution to the nuclear field gradient at a given nucleus is dominated by the total electron density of the molecule scaled by cube of the distance from this nucleus. For a nucleus terminal to a chemical bond, significant asymmetry of such scaled electron density will be reflected by a deviation of the quadrupolar z axis from the internuclear axis of the bond. Supersonic expansion rotational spectra allow experimental determination of such differences, and their values also turn out to be easily calculable by *ab initio* [30]. Hence, even if only the quadrupolar angle θ_{za} is available, it still brings in useful structural information, when corrected by the calculated value of δ. In the present case we also find that the Bailey approach gives the closest

Table 4
Spectroscopic constants for the ground states of the ^{13}C isotopic species of CF$_3$CH$_2$Cl.

	^{13}C1^{35}Cl	^{13}C2^{35}Cl	^{13}C1^{37}Cl	^{13}C2^{37}Cl
A/MHz	5285.63733(17)	5333.39146(18)	5285.53961(29)	5333.36724(32)
B/MHz	1802.134983(77)	1799.883355(72)	1755.18690(10)	1752.56295(15)
C/MHz	1778.125852(96)	1781.231543(90)	1732.39521(13)	1734.87318(14)
Δ_J/kHz	[0.2759]^a	[0.2778]	[0.2667]	[0.2684]
Δ_{JK}/kHz	[2.6053]	[2.7063]	[2.5330]	[2.6291]
Δ_K/kHz	[−1.5562]	[−1.6073]	[−1.4704]	[−1.5204]
δ_J/kHz	[0.001491]	[0.00005067]	[0.00135]	[0.0000044]
δ_K/kHz	[0.1066]	[0.4360]	[0.0903]	[0.4068]
$(3/2)\chi_{aa}$/MHz	−68.6061(53)	−68.9701(58)	−54.1554(82)	−54.4161(76)
$(1/4)(\chi_{bb}-\chi_{cc})$/MHz	−8.7767(15)	−8.7104(14)	−6.9056(19)	−6.8577(20)
χ_{ab}/MHz	52.294(85)	52.159(30)	41.158(78)	40.77(18)
N_{lines}, N_{rot}^{b}	119,39	97,37	51,17	47,21
σ_{fit}/MHz	0.00405	0.00370	0.00343	0.00362
σ_{rms}^{c}	0.810	0.740	0.685	0.723

^{a} Values in square parentheses are assumed values estimated from the relevant ^{12}C species by adding the isotopic difference calculated at the B3LYP/6-311++G(d,p) level.
^{b} The number of lines in the fit and the number of different rotational transitions for which hyperfine structure was measured.
^{c} Unitless deviation of the weighted fit.

XI.68

Table 5
Nuclear quadrupole constants and derived parameters for CF$_3$CH$_2$^{35}Cl and CF$_3$CH$_2$^{37}Cl.

	^{35}Cl					^{37}Cl		
	Ref. [3]	Exp.	Calc.[a]	Calc.[b]	Calc.[c]	Ref. [3]	Exp.	Calc.[a]
χ_{aa}/MHz	−45.94(50)[d]	−45.9651(10)	−47.789	−46.653	−46.06	−36.21	−36.2658(16)	−37.632
χ_{bb}/MHz	5.68(40)	5.5538(11)	7.316	6.090	5.43	4.48	4.4144(19)	5.732
χ_{cc}/MHz	40.26(50)	40.4113(11)	40.472	40.563	40.63	31.73	31.8514(19)	31.898
χ_{ab}/MHz	[51.95][e]	52.103(13)	51.187	51.964	52.36		41.106(69)	40.362
χ_{zz}/MHz	−78.15	−78.329(12)	−78.368	−78.554	−78.66	−61.59	−61.789(62)	−61.767
χ_{xx}/MHz	37.89	37.917(12)	37.895	37.991	38.03	29.86	29.937(62)	29.867
$\chi_{yy} = \chi_{cc}$/MHz	40.26	40.4113(11)	40.472	40.563	40.63	31.73	31.8514(19)	31.898
θ_{za}/deg	31.79	31.8462(29)	30.853	31.546	31.90		31.836(19)	30.878
θ_{str}[f]/deg	31.79	32.241	31.763	32.197	32.32		32.218	31.739
δ[g]/deg	0.0	0.395	0.910	0.651	0.42		0.382	0.861
η[h]	0.0303	0.03184(15)	0.0329	0.0327	0.0331		0.0310(10)	0.0329

[a] Calculated at the B3LYP/aug-cc-pVDZ level scaled by the factor 1.0619 determined in Ref. [28].
[b] Calculated at the MP2/aug-cc-pVDZ level scaled by the factor 1.1451 determined in Ref. [28].
[c] W.C. Bailey, [29].
[d] The quantities in round parentheses are standard errors in units of the least significant digit of the value of the constant.
[e] Value corresponding to the assumptions made in Ref. [3] in order to evaluate χ_{zz} etc.
[f] The structural angle between the CCl bond and the a-axis from the r_e^{SE} geometry determined in this work.
[g] $\delta = \theta_{za} - \theta_{str}$.
[h] The nuclear quadrupole asymmetry parameter given by $\eta = (\chi_{xx} - \chi_{yy})/\chi_{zz}$).

Table 6
Nuclear quadrupole constants of the measured ^{13}C isotopologues of CF$_3$CH$_2$Cl.

	^{13}C1^{35}Cl	^{13}C2^{35}Cl	^{13}C1^{37}Cl	^{13}C2^{37}Cl
χ_{aa}/MHz	−45.7374(35)	−45.9801(39)	−36.1036(55)	−36.2774(51)
χ_{bb}/MHz	5.3153(35)	5.5692(34)	4.2406(47)	4.4233(47)
χ_{cc}/MHz	40.4221(35)	40.4108(34)	31.8630(47)	31.8541(47)
χ_{ab}/MHz	52.294(85)	52.159(30)	41.158(78)	40.77(18)
χ_{zz}/MHz	−78.403(76)	−78.385(27)	−61.767(70)	−61.494(161)
χ_{xx}/MHz	37.9819(76)	37.974(27)	29.904(70)	29.640(161)
$\chi_{yy} = \chi_{cc}$/MHz	40.4221(35)	40.4108(34)	31.8630(47)	31.8541(47)
θ_{za}/deg	31.991(18)	31.8517(66)	31.945(22)	31.737(51)
η	0.03114(98)	0.03108(35)	0.0317(11)	0.0360(26)

result to experiment, concerning the value of δ, presumably owing to the most faithful electron density representation at the chlorine nucleus.

7. Molecular geometry

Determination of molecular geometry for CF$_3$CH$_2$Cl poses multiple challenges. We have rotational constants for six different isotopic species, but only three out of the six symmetry distinct atoms have been substituted, and no fluorine and hydrogen substitution data is available. Furthermore, we find that for C2 and Cl the b coordinates from the standard Kraitchman analysis [31] are b(C2) = 0.07i Å and b(Cl) = 0.01(12) Å, and are thus not useful. The first is an imaginary quantity, while that for Cl is encumbered by an uncertainty considerably exceeding its value, once a realistic error estimate using the Costain criterion [32] is made.

It is still possible, however, to determine a plausible geometry by means of a least squares fit to all 18 available rotational constants. With four atoms in the symmetry plane and two symmetry-equivalent pairs of atoms out of this plane it turns out that a total of 11 internal coordinates completely describe the geometry of CF$_3$CH$_2$Cl. These coordinates need to comprise of five interatomic distances and six angles, two of which have to be either dihedral angles or angles defining the out-of-plane distance of atoms H and F′ in the two identical pairs. The adopted internal coordinate scheme is listed in the first column of Table 7. Early tests carried out with the STRFIT program [33] revealed that it is

actually possible to determine the parameters involving the fluorine atoms providing that the three parameters involving the hydrogen atoms are assumed. Those are r(CH), $\angle$(HCH), and the angle ψ between the bisector of $\angle$(HCH) and r(CC). The assumption of values for these parameters required some care and the most reliable estimates were expected to be possible from comparisons of *ab initio* calculations and equilibrium quality experimental geometries determined for related molecules. Since the assumptions concerned the equilibrium geometries we determined the least-squares r_e^{SE} semi-experimental equilibrium geometry [34,35] as reported in Table 7 and in detail in Table S6.

The values assumed for r(CH) and for $\angle$(HCH) were derived by comparing the r_e^{SE} geometry for CH$_2$ClF [36] with MP2/aug-cc-pVTZ values, and then adding the differences to the MP2/aug-cc-pVTZ values for CF$_3$CH$_2$Cl. Similarly, the r_m^ρ geometry for CH$_2$ClCH$_3$ [37] was used to correct the calculated $\angle$(HCC) for CF$_3$CH$_2$Cl. The value for ψ was then obtained by trigonometry using $\cos \psi = \cos \angle(\text{HCC})/\cos(\angle(\text{HCH})/2)$. We estimated the uncertainties in these assumptions to be ± 0.001 Å for r(CH) and $\pm 0.5°$ for $\angle$(HCC) and $\angle$(HCH), corresponding to $\pm 1.03°$ for ψ. These uncertainties have been accounted for in the uncertainties in the determined r_e^{SE} parameters cited in Table 7 and their determination is described at the bottom of Table S6. We found that many of the determined heavy atom structural parameters were relatively insensitive to the assumptions concerning the bonds and angles to the two hydrogen atoms. There were two exceptions: r(CCl) and ϕ, for which the standard deviations from the STRFIT fit

Table 7
The experimental and the calculated structural parameters for CF_3CH_2Cl.

	Exp.		Calc.	
	Ref. [3], set III	(r_e^{SE})[a]	MP2/aug-cc-pVTZ	B3LYP/6-311++G(d,p)
$r(CCl)$/Å	1.787	1.7637(4)[b]	1.7660	1.7920
$r(CC)$/Å	1.514	1.5099(10)	1.5107	1.5184
$r(CF)$/Å	1.335	1.3429(12)	1.3456	1.3554
$r(CF')$/Å	1.335	1.3294(11)	1.3363	1.3445
$r(CH)$/Å	1.095	[1.0856][c]	1.0855	1.0878
$\angle(CCCl)$/deg	111.58	111.28(6)	111.25	112.35
$\angle(CCF)$/deg	108.86	108.64(15)	108.73	108.48
$\angle(F'CF')$/deg	108.03	108.15(14)	108.00	107.90
$\angle(HCH)$/deg	108	[110.212][c]	110.44	110.33
ϕ[d]/deg		130.11(12)	130.08	130.34
ψ[e]/deg		[123.588][c]	123.88	124.04
N_{const}, N_{par}[f]		18,8		
σ_{fit}[g]/uÅ^2		0.000090		

[a] Semi-experimental equilibrium geometry based on an anharmonic force field evaluated at the MP2/aug-cc-pVDZ level.
[b] The quantities in round parentheses are standard errors in units of the least significant digit, accounting also for the estimated uncertainties in $r(CH)$, $\angle(HCC)$, $\angle(HCH)$, see text.
[c] Values estimated using the comparisons of r_e^{SE} and calculated values for CH_2ClF [36] and CH_2ClCH_3 [37], see text.
[d] Angle between the bisector of $\angle(F'CF')$ and $r(CC)$.
[e] Angle between the bisector of $\angle(HCH)$ and $r(CC)$, corresponding to the assumption of $\angle(HCC) = 108.450°$ and $\angle(HCH) = 110.212°$.
[f] The numbers of fitted rotational constants and of the parameters of fit.
[g] Deviation of fit.

Table 8
Comparison of the experimental and the calculated vibration–rotation contributions to rotational constants for the parent species of CF_3CH_2Cl.

		^{35}Cl	
		Exp.	Calc.[a]
$v_{18} = 1$	ΔA[b]	−7.8778(1)	−8.211
	ΔB	−2.82040(4)	−2.776
	ΔC	−0.08136(4)	−0.168
$v_{11} = 1$	ΔA	6.8619(5)	10.191
	ΔB	−0.83867(8)	−0.111
	ΔC	−1.74789(8)	−2.286
$v_{18} = 2$	ΔA	−15.6497(3)	−16.422[c]
	ΔB	−7.0751(1)	−5.552[c]
	ΔC	−1.52209(9)	−0.336[c]

[a] Anharmonic force field calculation made with CFOUR [38] at the MP2/aug-cc-pVDZ level.
[b] $\Delta A = (A_v − A_0)$, etc. where A_0 are the values for the ground state.
[c] Estimated as twice the value calculated for $v_{18} = 1$.

increased by a factor of four and two, respectively, primarily due to the uncertainty in $\angle(HCC)$. In deriving the r_e^{SE} geometry we also needed the B_e-B_0 corrections of the experimental rotational constants to equilibrium, which were carried out by means of an anharmonic force field calculation at the MP2/aug-cc-pVDZ level performed with CFOUR [38]. A check on the anharmonic calculation is provided by the comparison of the calculated vibrational changes in rotational constants against the experimental values determined above, as made in Table 8. This comparison is quite reasonable, as is the agreement between the current r_e^{SE} structural parameters and the calculated values listed in Table 7.

8. Conclusions

The rotational spectrum of CF_3CH_2Cl has been subjected to a comprehensive reinvestigation. Four new isotopic species have been assigned, as well as spectra of the two main chlorine species and four different excited vibrational states up to the submillimetre wave region. A plausible molecular geometry has been determined and complete nuclear quadrupole hyperfine tensors for the chlorine nucleus in all isotopologues have been obtained. The new analysis provides a complete data set for predicting the rotational spectrum of the title molecule for any foreseeable analytical applications using supersonic expansion or ambient temperature spectroscopy.

Acknowledgement

Appendix A. Supplementary material

Supplementary data associated with this article can be found, in the online version, at http://dx.doi.org/10.1016/j.jms.2017.02.011.

References

[1] J.C. Laube, M.J. Newland, C. Hogan, C.A.M. Brenninkmeijer, P.J. Fraser, P. Martinerie, D.E. Oram, C.E. Reeves, T. Röckmann, J. Schwander, E. Witrant, W.T. Sturges, Nature Geosci. 7 (2014) 266–269.
[2] M. Etminan, E.J. Highwood, J.C. Laube, R. McPheat, G. Marston, K.P. Shine, K.M. Smith, Atmosphere 5 (2014) 473–483.
[3] T. Ogata, K. Koike, H. Suzuki, J. Mol. Struct. 144 (1986) 1–9.
[4] J.R. Nielsen, C.Y. Liang, D.C. Smith, J. Chem. Phys. 21 (1953) 1060–1069.
[5] E. Cataland, K.S. Pitzer, J. Phys. Chem. 62 (1958) 838–840.
[6] G.G. Brown, B.C. Dian, K.O. Douglass, S.M. Geyer, S.T. Shipman, B.H. Pate, Rev. Sci. Instrum. 79 (2008) 053103.
[7] I. Uriarte, C. Pérez, E. Caballero-Mancebo, F.J. Basterretxea, A. Lesarri, J.A. Fernández, E.J. Cocinero, Chem.-Eur. J. (2017), http://dx.doi.org/10.1002/chem.201700023.
[8] Z. Kisiel, J. Kosarzewski, L. Pszczółkowski, Acta Phys. Pol. A 92 (1997) 507–516.
[9] T.J. Balle, W.H. Flygare, Rev. Sci. Instrum. 52 (1981) 33–45.
[10] A. Kraśnicki, L. Pszczółkowski, Z. Kisiel, J. Mol. Spectrosc. 260 (2010) 57–65.
[11] I. Medvedev, M. Winnewisser, F.C. De Lucia, E. Herbst, E. Białkowska-Jaworska, L. Pszczółkowski, Z. Kisiel, J. Mol. Spectrosc. 228 (2004) 314–328.
[12] Z. Kisiel, A. Kraśnicki, J. Mol. Spectrosc. 262 (2010) 82–88.
[13] Z. Kisiel, L. Pszczółkowski, I.R. Medvedev, M. Winnewisser, F.C. De Lucia, E. Herbst, J. Mol. Spectrosc. 233 (2005) 231–243.
[14] Z. Kisiel, L. Pszczółkowski, B.J. Drouin, C.S. Brauer, S. Yu, J.C. Pearson, I.R. Medvedev, S. Fortman, C. Neese, J. Mol. Spectrosc. 280 (2012) 134–144.

[15] Z. Kisiel, in: J. Demaison et al. (Eds.), Spectroscopy from Space, Kluwer Academic Publishers, Dordrecht, 2001, pp. 91–106.

[16] Z. Kisiel, PROSPE – Programs for ROtational SPEctroscopy, <http://info.ifpan.edu.pl/~kisiel/prospe.htm>.

[17] H.M. Pickett, J. Mol. Spectrosc. 148 (1991) 371–377.

[18] H.M. Pickett, SPFIT/SPCAT package, <http://spec.jpl.nasa.gov>.

[19] Z. Kisiel, E. Białkowska-Jaworska, L. Pszczółkowski, J. Mol. Spectrosc. 177 (1996) 240–250.

[20] Z. Kisiel, L. Pszczółkowski, J. Mol. Spectrosc. 178 (1996) 125–137.

[21] Z. Kisiel, O. Dorosh, M. Winnewisser, M. Behnke, I.R. Medvedev, F.C. De Lucia, J. Mol. Spectrosc. 246 (2007) 39–56.

[22] C. Pérez, S. Lobsiger, N.A. Seifert, D.P. Zaleski, B. Temelso, G.C. Shields, Z. Kisiel, B.H. Pate, Chem. Phys. Lett. 571 (2013) 1–15.

[23] J.K.G. Watson in J.R. Durig (Ed.), Vibrational Spectra and Structure, vol. 6, Elsevier, New York/Amsterdam, 1977, pp. 1–89.

[24] M.R. Aliev, J.K.G. Watson, J. Mol. Spectrosc. 61 (1976) 29–52.

[25] Alex A. Granovsky, Firefly version 8 computing package, <http://classic.chem.msu.su/gran/firefly/index.html> and based on the Gamess-US package.; M.W. Schmidt, K.K. Baldridge, J.A. Boatz, S.T. Elbert, M.S. Gordon, J.H. Jensen, S. Koseki, N. Matsunaga, K.A. Nguyen, S. Su, T.L. Windus, M. Dupuis, J.A. Montgomery, J. Comput. Chem. 14 (1993) 1347–1363.

[26] E. Białkowska-Jaworska, L. Pszczółkowski, Z. Kisiel, J. Mol. Spectrosc. 308–309 (2015) 20–27.

[27] Z. Kisiel, L. Pszczółkowski, E. Białkowska-Jaworska, S.B. Charnley, J. Mol. Spectrosc. 321 (2016) 13–22.

[28] E. Białkowska-Jaworska, Z. Kisiel, L. Pszczółkowski, J. Mol. Spectrosc. 238 (2006) 72–78.

[29] W.C. Bailey, Calculation of Nuclear Quadrupole Coupling Constants in Gaseous State Molecules, 2004. <nqcc.wcbailey.net>.

[30] Z. Kisiel, E. Białkowska-Jaworska, L. Pszczółkowski, J. Chem. Phys. 109 (1998) 10263–10272.

[31] J. Kraitchman, Am. J. Phys. 21 (1953) 17–24.

[32] C.C. Costain, Trans. Am. Crystallogr. Assoc. 2 (1966) 157–164.

[33] Z. Kisiel, J. Mol. Spectrosc. 218 (2003) 58–67.

[34] J. Demaison, Molec. Phys. 105 (2007) 3109–3138.

[35] C. Puzzarini, J.F. Stanton, J. Gauss, Int. Rev. Phys. Chem. 29 (2010) 273–367.

[36] N. Vogt, J. Demaison, H.D. Rudolph, Molec. Phys. 112 (2014) 2873–2883.

[37] H.S. Tam, J.-I. Choe, M.D. Harmony, J. Phys. Chem. 95 (1991) 9267–9272.

[38] CFOUR, a quantum chemical program package written by J.F. Stanton, J. Gauss, M.E. Harding, P.G. Szalay with contributions from A.A. Auer, R.J. Bartlett, U. Benedikt, C. Berger, D.E. Bernholdt, Y.J. Bomble, O. Christiansen, M. Heckert, O. Heun, C. Huber, T.-C. Jagau, D. Jonsson, J. Jusélius, K. Klein, W.J. Lauderdale, D.A. Matthews, T. Metzroth, D.P. O'Neill, D.R. Price, E. Prochnow, K. Ruud, F. Schiffmann, S. Stopkowicz, J. Vázquez, F. Wang, J.D. Watts and the integral packages MOLECULE (J. Almlöf and P.R. Taylor), PROPS (P.R. Taylor), ABACUS (T. Helgaker, H.J. Aa. Jensen, P. Jørgensen, and J. Olsen), and ECP routines by A.V. Mitin and C. van Wüllen. For the current version, see <http://www.cfour.de>.

Levoglucosan

CHEM**PHYS**CHEM
Articles

Investigating the Conformation of the Bridged Monosaccharide Levoglucosan

Iciar Uriarte,[a] Patricia Écija,[a] Rolando Lozada-Garcia,[b] Pierre Çarçabal,[b] and Emilio J. Cocinero*[a]

Levoglucosan is one of the main products of the thermal degradation of glucose and cellulose and is commonly used as a tracer for biomass burning. Herein we report a conformational analysis of levoglucosan under isolation conditions, by means of microwave spectroscopy coupled with ultrafast laser vaporization in supersonic expansions. We observed three different conformations of levoglucosan in the gas phase. They all share a common heavy atom rigid bicyclic structure. The difference between the three of them lies in the network of intramolecular hydrogen bonds that arises from the OH groups at positions 2, 3 and 4. The different combinations of H-bonds give richness to the conformational landscape of levoglucosan. The gas phase conformers obtained in this work are compared to the crystal structure of levoglucosan previously reported. Although the heavy atom frame remains unchanged, there are significant differences in the positions of the H-atoms. In addition, the levoglucosan structure can be compared to the related glucose, for which gas phase conformational studies exist in the literature. In this case, in going from glucose to levoglucosan, there is an inversion in the chair conformation of the pyranose ring. This forces the OH groups to adopt axial positions (instead of the more favorable equatorial positions in glucose) and completely changes the pattern of intramolecular H-bonds.

1. Introduction

Levoglucosan (1,6-anhydro-β-D-glucose) is one of the main products of the thermal degradation of glucose and cellulose (β(1→4) linked glucose units). It is commonly used as a tracer for cellulose in biomass burning.[1–3] From a chemical point of view, levoglucosan arises from the intramolecular cyclization of a glucopyranose unit resulting in a bicyclic form structurally similar to glucose, with a bridge between positions 1 and 5 (see Figure 1). The mechanism of glucose pyrolysis to levoglucosan (and other substances) has been widely investigated both experimentally[4–6] and with theoretical methods.[7–10] This mechanism necessarily involves an intramolecular cyclization and a dehydration process. In reference [11], the authors use computational methods to prove that it is the OH group at position 1 that leaves the molecule (rather than OH6).

Since levoglucosan is an important product in the degradation process of glucose and cellulose, a lot of research has been devoted to different aspects of this molecule. In particular, several studies can be found in the literature about the
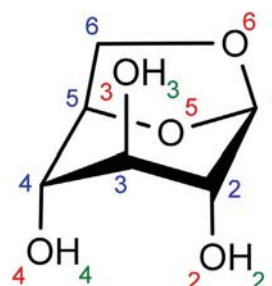

Figure 1. Chemical structure and atom numbering of levoglucosan. Atoms have been numbered according to the standards of monosaccharides. Blue corresponds to carbon atoms, red to oxygen and green to hydrogen. To number the atoms in the bridge, we have followed the results in ref. [11].

conformation and structure of this molecular system. First, theoretical methods have been used to predict the 3-dimensional conformation of levoglucosan in vacuo.[12, 13] In 1971, the crystal structure of levoglucosan was first studied by X-ray diffraction,[14] and only the positions of the non-H atoms were obtained. This study was later complemented with a neutron diffraction analysis[15] that focused on obtaining the positions of the H atoms. This kind of solid-state studies provides important structural information. However, the hydrogen-bond distribution is affected by the presence of neighboring units of the molecule. In fact, in this particular case, strong O—H···O interactions were characterized between units of levoglucosan.

A different approach to structural analysis is to perform conformational analysis in the gas phase. By isolating the molecule from external interactions such as solvent or crystal packing

[a] I. Uriarte, Dr. P. Écija, Dr. E. J. Cocinero
Departamento Química Física
Universidad del País Vasco (UPV/EHU)
Apartado 644, 48080 Bilbao (Spain)
E-mail: emiliojose.cocinero@ehu.eus
Homepage: http://www.grupodeespectroscopia.es/MW/

[b] Dr. R. Lozada-Garcia, Dr. P. Çarçabal
Institut des Sciences Moléculaires d'Orsay
UMR 8214, Université Paris-Sud, bat 210
F-91405 Orsay cedex (France)

Supporting Information and the ORCID identification number(s) for the author(s) of this article can be found under:
https://doi.org/10.1002/cphc.201701242.

XI.75

forces, we can access its preferred conformations. The intrinsic molecular properties of the molecule can thus be obtained. Several spectroscopic techniques are used to monitor the structure of this kind of molecule in the gas phase. Mass-resolved laser electronic spectroscopy can be applied for the study of moderate to large size molecular systems such as peptides,[16–19] carbohydrates[20–23] or nucleo-base pairs.[24–26] For small to medium size molecules on the other hand, microwave spectroscopy provides the most accurate structural description in the gas phase. The inherent high resolution of this spectroscopic technique allows one to distinguish and unambiguously identify different conformers, tautomers and isotopologues as independent species. Even enantiomers have been identified using rotational spectroscopy[27] with the recent advances in three-wave mixing techniques.[28–29] Microwave spectroscopy has been successfully used in the past to evaluate the gas phase conformations of several monosaccharides,[30–32] which are structurally similar to levoglucosan. In particular, up to seven conformations of glucose were detected in the gas phase.[33] Regardless of the spectroscopic technique, the vaporization method is a key point in these studies. There are numerous examples in the literature where conventional heating techniques have been used to bring biomolecules intact into the gas phase.[34–37] However, in many other cases, biological molecules are thermolabile and decompose upon heating. So, conventional heating techniques cannot be used in those cases. An alternative approach is to use ultrafast laser vaporization. In this case, a short laser pulse hits the sample and a fraction of the molecule is brought intact into the gas phase without degradation.

The goal of this work is to probe the intrinsic conformational preferences of levoglucosan in the interaction-free environment of a supersonic expansion by means of microwave spectroscopy. By comparing the results obtained here with the crystal structure, it is possible to evaluate the effect of crystal packing on the conformation of this substance. In addition, we can compare the gas phase structures of levoglucosan and glucose to assess the impact of the internal bridge. To the best of our knowledge, this is the first high resolution structural study of a bridged monosaccharide.

2. Results and Discussion

First, a conformational search followed by ab initio calculations was performed to survey the conformational landscape of levoglucosan in vacuo. Details about these theoretical calculations can be found in the Experimental Section. The predicted conformations of levoglucosan under isolation conditions can be rationalized according to the following two criteria. First, the pyranose ring can adopt two conformations: inverted chair ($^1C_4$) and boat-type configuration. The inverted chair (IC) shape is so called because it is the opposite ring structure of the related molecule glucose ($^4C_1$). The second criterion is the interplay of intramolecular hydrogen bonds that arises from the three OH groups in the molecule. Several combinations are possible and give richness to the conformational landscape of levoglucosan.

The conformational search and the ab initio calculations result in 24 different conformations in an energy window of 30 kJ mol^{-1}, see table S1. The most stable predicted conformations correspond to inverted chair structures, the first boat conformation (B1) lying 11.1 kJ mol^{-1} above the global minimum ($\Delta(E+ZPE)$ at MP2/6-311++G(d,p)). Among the inverted chair conformers, the most stable ones display an intramolecular hydrogen bond O3H3···O6 on the top face of the molecule, with the H3 atom pointing towards O6. The first structure that does not possess this intramolecular interaction (IC5) is located at 4.2 kJ mol^{-1} ($\Delta(E+ZPE)$ at MP2/6-311++G(d,p)). In general, our calculations are in good agreement with previous theoretical studies about levoglucosan,[12,13] although small differences arise mainly from the use of different methods/basis sets. For example, in ref. [12], the authors only consider five different conformations of levoglucosan at MP2(full)/6-31G(d) level of theory. Among these five conformations, there are differences in the energetic order of some of the conformers (IC2 and IC3, for instance, are in the inverse order as in our results).

So, as a summary, the four lowest lying conformers share a common rigid bicyclic frame with a $^1C_4$ ring conformation of the six-membered ring and an intramolecular O3H3···O6 hydrogen bond. Starting from this disposition, we performed a Potential Energy Surface by scanning the dihedral angles H2—O2—C2—C1 and H4—O4—C4—C3 in order to consider all possible positions of the OH groups and the corresponding interactions. Figure 2 shows this potential energy surface. We can clearly distinguish five minima which correspond to conformers IC1, IC2, IC3, IC4 and IC8. It is worth mentioning that these conformers were also predicted in the conformational search. This validates the performance of the conformational search. Finally, a high energy plateau resembling region can be observed in the PES (H2—O2—C2—C1 and H4—O4—C4—C3 between 0° and 200°, approximately). This region corresponds to conformations where either the OH groups at positions 2 and 4 are pointing out of the molecule and hence do not give rise to intramolecular hydrogen bonds or there are strong repulsions between the two hydrogen atoms (for example, the region with H2—O2—C2—C1 ≈ 200° and H4—O4—C4—C3 ≈ 0°).

The first attempt to record the rotational spectrum of levoglucosan was done using a Chirp-Pulse Fourier Transform Microwave (CP-FTMW) spectrometer available at the University of the Basque Country (UPV/EHU).[38] The main advantage of this spectrometer is that it allows one to record the whole rotational spectrum (in our case, 6–18 GHz region) in a single molecular pulse, resulting in short spectral acquisition times. In our current set-up, the vaporization system for getting the sample in the gas phase in the CP-FTMW consists of conventional heating techniques. Levoglucosan was heated to 220 °C in a customized heating nozzle, but no lines attributable to this molecule were found in the rotational spectrum. This may be due to the low vapor pressure of levoglucosan, meaning that there is not enough amount of molecules in the gas phase or it is a thermolabile sample and degrade. An alternative approach to vaporization of low vapor pressure or thermolabile samples consists in the use of ultrafast laser sources.[30] Therefore, we performed the rotational study of levoglucosan in the
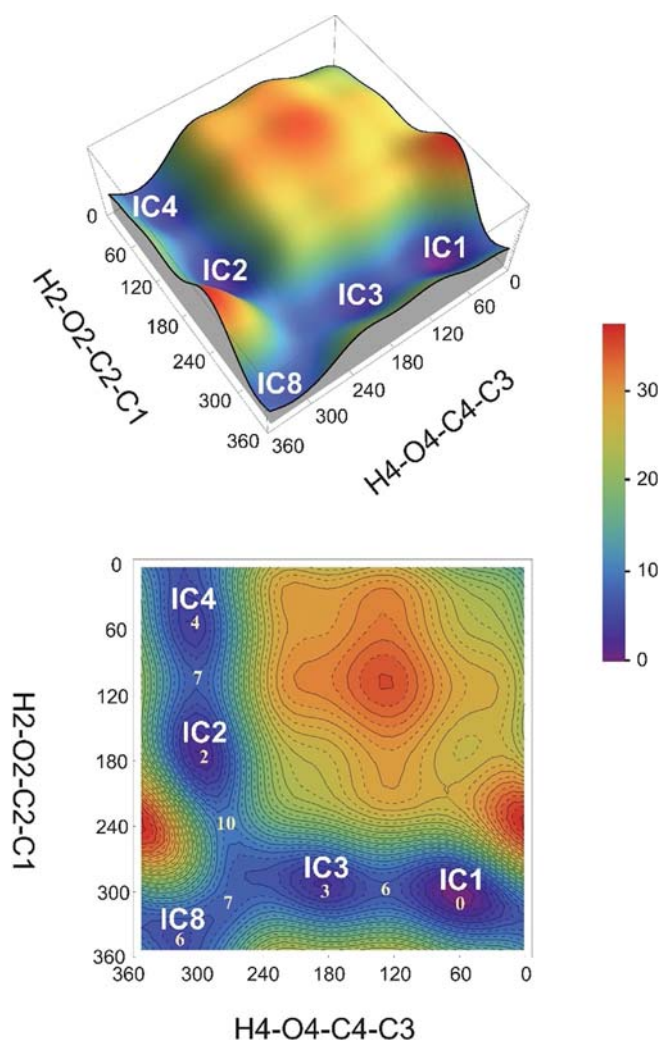
XI.76

Figure 2. Potential energy surface of levoglucosan and two-dimensional contour plot computed at B3LYP-D3/6-311++G(d,p). The heavy atom frame is fixed at an inverted chair configuration displaying an intramolecular O3H3···O6 hydrogen bond. The independent variables correspond to the torsion angles H2—O2—C2—C1 and H4—O4—C4—C3 (energies in kJ mol^{-1}, angles in degrees). The positions of the minima are highlighted as well as some relevant energy values.

FTMW spectrometer available in our group, which is coupled to an UV ultrafast laser vaporization system.

The theoretical calculations mentioned before guided the experimental work. The rotational spectra of the most stable conformations of levoglucosan were predicted based on calculated rotational constants. Following these predictions, the 9–12 GHz region was first scanned to look for $J = 4$ and $J = 5$ μ_a, μ_b and μ_c-type lines of the most stable conformations. Different sets of lines were spotted which corresponded to three different conformations of levoglucosan. The rotational transitions were fitted to a Watson semi-rigid rotor Hamiltonian and the experimental values of the A, B and C rotational constants and some of the centrifugal distortion constants were obtained. The results are summarized in Table 1 for the three conformations and a portion of the rotational spectrum in the 9600–9700 MHz region is depicted in Figure 3.

The three sets of constants obtained (Conf1, Conf2 and Conf3) seem to correspond to IC1, IC2 and IC3, which are the lowest lying conformations predicted for levoglucosan. However, the values of the rotational constants are very similar between the three conformations, and this is particularly so for Conf1 and Conf2. In order to have an unambiguous assignment, we look at the difference error defined as $\Delta X = X_{theor} - X_{exp}$, where X refers to the rotational constants (A, B or C). This difference error should be almost identical for the two conformations. By assigning Conf1 to IC1 we obtain $\Delta A = 7.9$ MHz, $\Delta B = 3.7$ MHz and $\Delta C = 7.6$ MHz. The values for Conf2 and IC2 are $\Delta A = 9.2$ MHz, $\Delta B = 3.9$ MHz and $\Delta C = 7.6$ MHz. So, the difference errors are almost identical in both cases and the correct assignment is therefore Conf1 = IC1, Conf2 = IC2 and Conf3 = IC3. Moreover, this is corroborated by the observation of transitions of c-type in Conf1 excluding the possibility that this rotamer is IC2 ($\mu_c = 0$). Figure 4 displays the three-dimensional dispositions of these three conformers. As mentioned previously, these three species correspond to structures where the heavy atom frame is fixed and the six-membered ring adopts an inverted chair conformation. Also, the strong O3H3···O6 bond is present in the three observed conformers. The differences between the observed structures lie in the net-

Table 1. Experimental and ab initio (MP2/6-311++G(d,p)) rotational constants, centrifugal distortion constants and dipole moment components of the three observed conformers of levoglucosan.

	Conf1	Conf2	Conf3	IC1	IC2	IC3
$A^{[a]}$ [MHz]	1426.65036(49)[e]	1428.92424(52)	1436.44859(58)	1434.6	1438.1	1449.5
B [MHz]	1224.20654(42)	1222.98567(32)	1219.67041(31)	1227.9	1226.9	1222.1
C [MHz]	1189.03274(42)	1188.36258(36)	1187.75585(31)	1196.6	1196.1	1196.0
$\Delta_J^{[b]}$ [kHz]	0.0500(96)	0.0375(77)	0.0495(65)	0.043	0.043	0.042
Δ_{JK} [kHz]	0.079(20)	0.113(15)	0.093(15)	0.079	0.092	0.084
Δ_K [kHz]	0.030(18)			0.017	−0.005	0.015
$|\mu_a|^{[c]}$ [D]	Observed	Observed	Observed	1.1	0.9	2.2
$|\mu_b|$ [D]	Observed	Observed	Observed	1.9	0.9	3.3
$|\mu_c|$ [D]	Observed	Not observed	Observed	0.8	0.0	0.4
$N^{[d]}$	51	26	24			
σ [kHz]	4.3	2.5	2.1			

[a] Rotational constants (A, B and C). [b] Centrifugal distortion constants (Δ_J, Δ_{JK} and Δ_K). [c] Electric dipole moment components ($|\mu_\alpha|$, $\alpha =$a, b and c) referred to the principal axis; 1 D $\approx$ 3.336$\times$10^{-30} C m. [d] Number of transitions (N) and rms deviation of the fit (σ). [e] Standard errors in parentheses in units of the last digit.
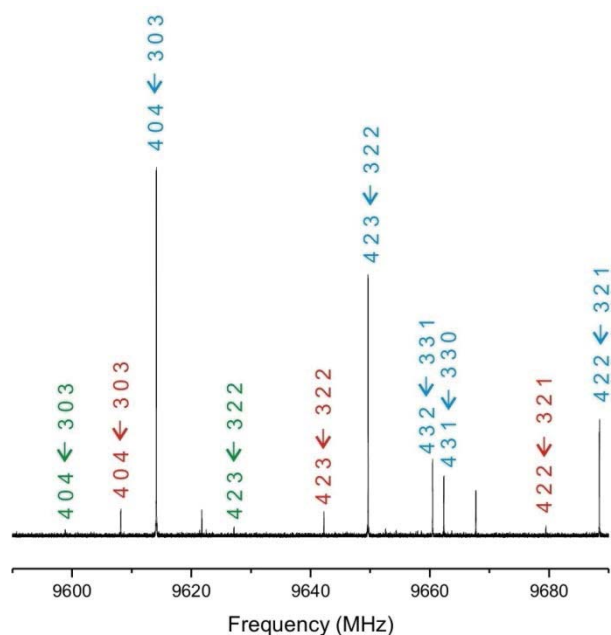
XI.77

Figure 3. Section of the experimental rotational spectrum of levoglucosan in the 9590 to 9690 MHz region. Rotational transitions (J K'_{-1} K'_{+1}←J'' K''_{-1} K''_{+1}) corresponding to the three different observed conformations are labeled (blue: IC1, red: IC2, green: IC3). The two non-labeled rotational lines may arise from decomposition products due to laser desorption. All rotational transitions are split ($\approx$20–30 kHz) due to Doppler effect (not observable in the figure).

work of hydrogen bonding arising from the OH groups at positions 2 and 4. Although some unassigned lines remained in the rotational spectrum, they could not be identified as higher energy conformers of levoglucosan or decomposition products.

In order to study the patterns for hydrogen bonding in IC1, IC2 and IC3 we use three different methods to characterize intramolecular interactions. First, we carried out NBO calculations to evaluate hyperconjugation energies between the lone pairs of the oxygen atoms and the vicinal σ*(O—H) orbitals. We consider that hyperconjugation energies greater than 0.5 kcal

mol^{-1} are indicators of some kind of interaction. Also, we use Bader's QTAIM theory to evaluate the presence of Bond Critical Points (BCPs) and to estimate the bond strength of H-bonds. In this case, an intramolecular interaction is confirmed by the mere presence of a BCP. Finally, an analysis of the H⋯O distances and the O—H⋯O angles may help us identify H-bonds. The distance and angle cut-off values for H-bonds are a matter of debate and it is not the objective of this work to discuss the issue. However, for the present work, we will follow the considerations about weak hydrogen bonds in ref. [39]. We consider that distances shorter than 3.2 Å and angles in the range 90°–150° may be indicative of weak intramolecular interactions.[39] The results of these three methods for IC1, IC2 and IC3 are summarized in Table 2. First, we can see that the three methods confirm an O3H3⋯O6 interaction for the three conformers. For IC2, an additional O4H4⋯O2 H-bond contributes to stabilizing the system, as is confirmed by QTAIM, NBO and structural analysis. IC3 on the other hand displays an O2H2⋯O4 interaction, also confirmed by the three methods. Finally, for IC1, QTAIM, NBO and structural analysis confirm an O2H2⋯O4 interaction. However, there is a slight disagreement between the three methods concerning a possible O2H2⋯O5 contact in conformers IC1 and IC3. In IC1, while QTAIM does not find a BCP which would support O2H2⋯O5, the hyperconjugation energy according to NBO is 0.6 kcal mol^{-1}, which would indicate a slight interaction. Also, the structural analysis would confirm an intramolecular interaction, with the distance being 2.3 Å and the angle 107.0°. For IC3, QTAIM and NBO do not support an interaction while the structural consideration does (2.5 Å and 98.4°).

An interesting feature of microwave studies is that they allow the determination of the relative conformational populations in the gas phase, since the intensity of rotational transitions in the jet is proportional to the population and the molecular dipole moment.[40] However, these measurements are affected by several non-quantified uncertainties like the ab initio dipole moments, and should be taken as an approximation. In levoglucosan, we have determined that the population ratio IC1/IC2 is 8(1)/1 and IC1/IC3 is 39(9)/1. This means that
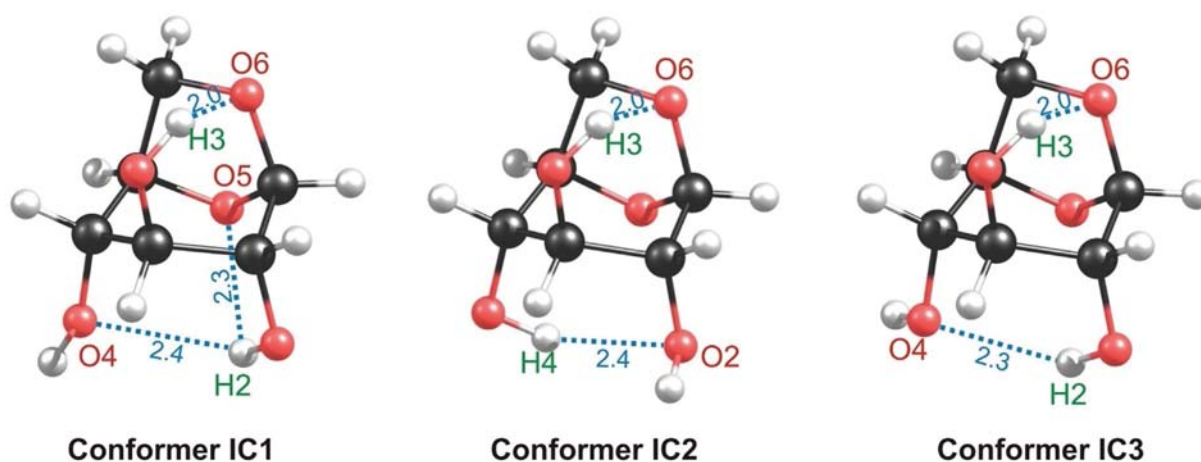

Figure 4. The three observed conformers of levoglucosan. Intramolecular hydrogen bonds are shown with blue dotted lines, distances in Å.

XI.78

	O3H3···O6 QTAIM[a]	NBO[b]	r [Å]	∡ [°][c]	O2H2···O4 QTAIM	NBO	r [Å]	∡ [°]
IC1	−6.5	3.6	2.0	132.1	−2.6	0.7	2.4	124.1
IC2	−6.3	3.6	2.0	132.0			3.4	62.5
IC3	−6.2	3.5	2.1	131.2	−3.4	1.3	2.3	132.6
	O2H2···O5 QTAIM	NBO	r [Å]	∡ [°]	O4H4···O2 QTAIM	NBO	r [Å]	∡ [°]
IC1		0.6	2.3	107.0			3.3	68.5
IC2			3.6	17.3	−2.8	0.9	2.4	127.3
IC3			2.5	98.4			3.7	33.9

[a] Bond strength (*E*, kcal mol^{-1}) according to Bader's quantum theory of atoms in molecules (QTAIM). *E* values are shown for those intramolecular interactions where BCPs have been found. [b] Hyperconjugation energies (kcal mol^{-1}) between the lone pairs of the oxygen atoms and the vicinal σ*(O-H) orbitals. Only values greater than 0.5 kcal mol^{-1} are shown. [c] Structural parameters referring to the H-bonds. *r* [Å] is the distance H···O and ∡ [°] is the angle O—H···O.

the relative energies (ΔG) of conformers IC2 and IC3 are 5.2(4) and 9.0(9) kJ mol^{-1} above the global minimum (IC1). These values are quite different from the ab initio (MP2/6-311++(d,p)) values (1.4 and 2.8 kJ mol^{-1}, respectively). However, the energetic order of the conformers is maintained.

Crystal-phase studies of levoglucosan have been reported previously in the literature. In particular, in ref. [15], X-ray and neutron diffraction studies were carried out so that the positions of the heavy atoms and the hydrogen atoms could be obtained. We can then easily compare the structure of levoglucosan in the gas phase (this work) and in crystal (ref. [15]) and evaluate how the crystal packing in the solid phase affects the structure of this molecule. The heavy atom frame does not change when going from gas to crystalline phase. However, the disposition of the hydrogen atoms is different in the two situations. Figure 5 displays the gas phase structure of levoglu-
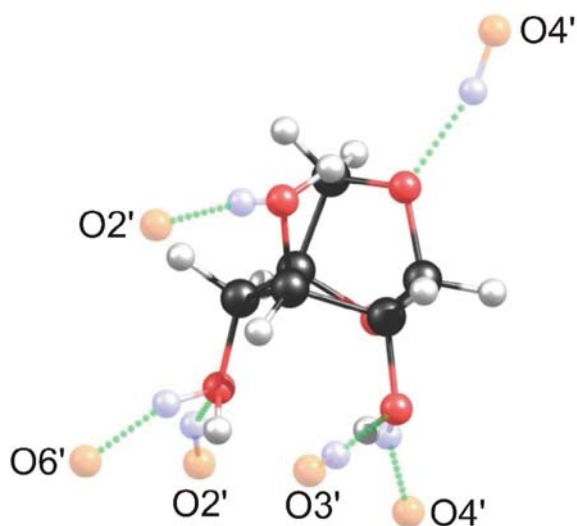
cosan, along with the position of H2, H3 and H4 in the crystal.[15] Also, some atoms (O and H) of the neighboring units of levoglucosan in the crystal are shown. As mentioned before, in the gas phase the hydrogen atoms are arranged so that intramolecular H-bonds can be formed. However, in the crystal phase, intermolecular H-bonds with neighboring units of levoglucosan are preferred and the hydrogen atoms point "out" of the molecule. This is particularly clear for H3, whose position is shifted ≈180° from the gas phase to form an intermolecular bond with an O2′ atom from a neighboring levoglucosan unit. This is the main difference that arises from the comparison of the structures of levoglucosan in the gas phase and in crystal.

It is also interesting to compare the structures in the gas phase of levoglucosan and glucose. The former is a degradation product of the latter and results from an intramolecular cyclization, meaning that the structures of the two molecules are intimately related. Glucose was studied under isolation conditions by means of FTMW spectroscopy.[33] Several conformations were observed for α-glucose (four conformations) and β-glucose (three). All of them possess a $^4C_1$ chair conformation of the six-membered ring. In contrast, the observed conformations of levoglucosan display a $^1C_4$ chair conformation. This means that there is an inversion of the chair conformation when the cyclization occurs. We have performed a Cremer–Pople (CP) analysis to visualize this inversion in the configuration of the pyranose ring. CP allows one to describe quantitatively the puckering of a six-membered using three polar coordinates (an amplitude (q) and two phases (θ and ϕ)). The graphical result is a sphere in which the different conformations occupy a given position defined by the three polar coordinates. In Figure 6, we present the results of the CP analysis of levoglucosan, β-glucose and β-ribose. It is very easy to see in this Figure the ring inversion from glucose to levoglucosan. The conformations corresponding to glucose are on the north pole of the sphere ($^4C_1$ chair) while the levoglucosan conformations are on the opposite side, on the south pole (near the $^1C_4$ chair). It is also interesting to compare with the results from ribose. In a previous study of β-ribose in the gas phase,[30] the authors found one conformer with a $^4C_1$ chair and two with a

Figure 5. Comparison of the H-bond network of levoglucosan in the gas phase (global minimum structure, IC1) and in the crystal. The positions of relevant atoms in the crystal (from ref. [15]) are displayed with transparent spheres.
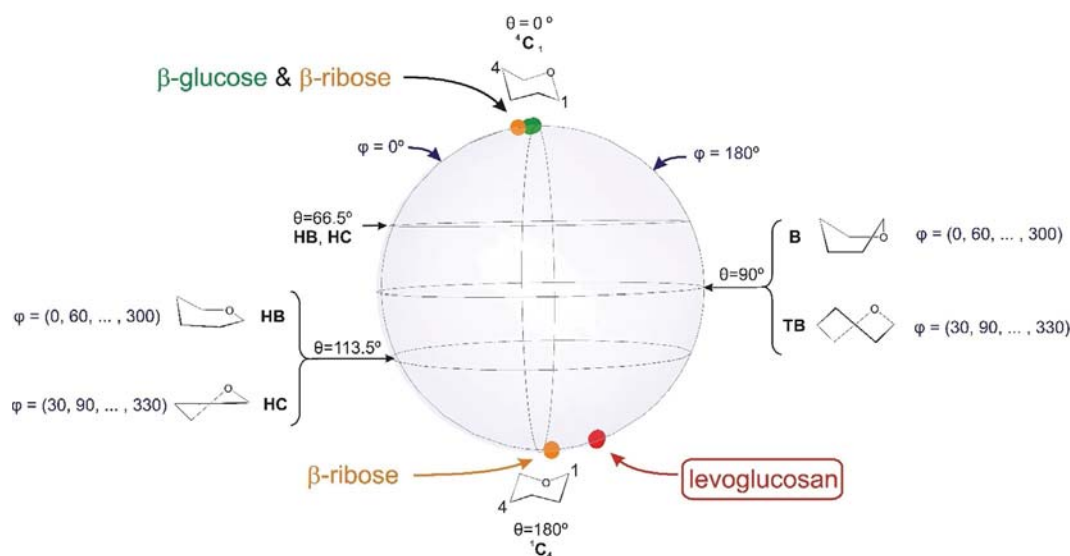
XI.79

Figure 6. Cremer–Pople sphere with the observed conformers of levoglucosan (this work, red dots), β-glucose (ref. [32], green) and β-ribose (ref. [29], orange). All amplitudes have been given the same value for the sake of clarity in the Figure. The positions of some ideal structures are shown in the sphere: Chair (C), Boat (B), Twist-Boat (TB), Half-Boat (HB) and Half-Chair (HC).

$^1C_4$ chair. They are shown in Figure 6, lying in opposite poles of the sphere. If we compare the position of the $^1C_4$ chairs of ribose with levoglucosan, it is clear that there is a distortion in levoglucosan from the $^1C_4$ chair of ribose, which lies almost ideally in the southernmost point of the sphere. Levoglucosan does not occupy the ideal position for a perfect $^1C_4$ chair, it is distorted from this ideal position, adopting some Half-Boat character.

This inversion in the chair results in the OH groups adopting axial positions in levoglucosan, while they have equatorial positions in glucose. This also implies that the network of intramolecular hydrogen bonds changes drastically from glucose. For example, in the most stable conformer of β-glucose reported in reference 33, there is a cooperative network of hydrogen bonding that the authors describe in the following way: O4H4···O3H3···O2H2···O1H1···O5. Nevertheless, for the observed conformers of levoglucosan, such cooperative network cannot take place and, instead, the possible H-bond contacts for the global minimum are: O2H2···O4 and O2H2···O5. In summary, in glucose the H-bond contacts take place between vicinal units of equatorial OH groups in a cooperative way while in levoglucosan the H-bonds involve "alternated" axial OH groups.

3. Conclusions

The conformation of levoglucosan was probed under isolation conditions by means of FTMW rotational spectroscopy coupled with UV ultrafast laser vaporization. Three conformers were observed in the gas phase. They all share a heavy atom bicyclic frame, with the six-membered ring displaying a $^1C_4$ chair conformation, which is the opposite conformation of the glucose chair ($^4C_1$). This forces the OH groups to adopt axial positions and creates an unusual pattern of intramolecular H-bonds. In particular, all observed conformers of levoglucosan display contacts between alternate OH groups, while previous studies

prove that in glucose cooperative H-bonds exist between vicinal OH groups.

Experimental Section

Experimental Methods

Levoglucosan was purchased from Sigma Aldrich and used without further purification. It is a white powder with high melting point (182–184 °C). Conventional heating techniques proved unsuccessful to vaporize the sample. Therefore, UV ultrafast laser vaporization was used to get levoglucosan in the gas phase. For that purpose, levoglucosan and a commercial binder were mixed and then mechanically pressed to get cylinder-type solid samples ("rods").

The rotational spectrum of levoglucosan was recorded in a FTMW spectrometer coupled with ultrafast laser vaporization available at the University of the Basque Country (UPV/EHU) and described elsewhere.[30,41] The ultrafast vaporization system consists of a picosecond-pulsed Nd:YAG laser operating in the third harmonic (355 nm). Briefly, the picosecond laser pulse vaporized the rod in the presence of a carrier gas (Ne) at a stagnation pressure of ≈ 6 bar. Then, through a 1.0 mm ablation nozzle, the sample was supersonically expanded into the FTMW cavity. The rotational spectrum was recorded in the 9–14 GHz region. The accuracy of the frequency measurements is below 3 kHz and rotational transitions separated less than 7 kHz are resolvable. All transitions appear as Doppler doublets.

Computational Methods

We used computational methods in order to predict the most stable conformations of levoglucosan under isolation conditions and guide the experimental work. We followed the ensuing methodology, which we have previously used with excellent results. First, a fast conformational search was performed using Molecular Mechanics. The force field MMFFs (Merck Molecular Force Field[42]) was used to sample the conformational space using a combination of Advanced Monte Carlo and large-scale low-mode algorithms.

XI.80

This conformational search was done within an energy window of 30 kJ mol^{-1}. The structures resulting from this procedure were later re-optimized using ab initio methods. In particular, MP2 calculations were carried out using the Pople's triple-ζ 6–311++G(d,p) basis set.

Alternatively, the lowest lying conformations of levoglucosan were predicted by performing a Potential Energy Surface (PES). Levoglucosan displays a rigid bicyclic frame with a strong intramolecular interaction O3H3⋯O6. Starting from this structure, the lowest lying conformations arise from the different configurations that the OH groups at positions 2 and 4 may adopt. Hence, the two dihedral angles H2—O2—C2—C1 and H4—O4—C4—C3 were scanned in steps of 10 degrees, using B3LYP-D3/6-311++G(d,p) method. In this way, all possible orientations of the OH groups at positions 2 and 4 were considered. The most stable conformations of levoglucosan are accounted for in this PES and the barriers connecting them can be easily visualized.

In order to analyze the possible patterns of intramolecular interactions, NBO calculations were carried out. Density Functional Theory methods were applied (in particular B3LYP) at the 6-311++G(d,p). We also used Bader's quantum theory of atoms in molecules[43] (QTAIM) as an alternative approach to study intramolecular interactions. In particular, we predicted Bond Critical Points (BCPs) and bond paths and estimated the bond strength. We used the Multiwfn program[44] for the QTAIM analysis.

All ab initio calculations were run in the Gaussian 09 software package.[45]

Acknowledgements

Conflict of interest

The authors declare no conflict of interest.

Keywords: conformational analysis · intramolecular hydrogen bonding · monosaccharide derivatives · rotational spectroscopy · supersonic expansion

[1] B. R. T. Simoneit, J. J. Schauer, C. G. Nolte, D. R. Oros, V. O. Elias, M. P. Fraser, W. F. Rogge, G. R. Cass, *Atmos. Environ.* 1999, 33, 173–182.
[2] P. M. Fine, G. R. Cass, B. R. T. Simoneit, *Environ. Eng. Sci.* 2004, 21, 387–409.
[3] C. You, T. Yao, C. Xu, L. Song, *Atmos. Environ.* 2017, 152, 1–5.
[4] H. B. Mayes, M. W. Nolte, G. T. Beckham, B. H. Shanks, L. J. Broadbelt, *ACS Sustainable Chem. Eng.* 2014, 2, 1461–1473.
[5] Y. Long, Y. Yu, Y. W. Chua, H. Wu, *Fuel* 2017, 193, 460–466.
[6] S. Wu, D. Shen, J. Hu, H. Zhang, R. Xiao, *J. Anal. Appl. Pyrolysis* 2016, 119, 147–156.
[7] V. Seshadri, P. R. Westmoreland, *Catal. Today* 2016, 269, 110–121.
[8] W. Lan, J. Huang, *Asian J. Chem.* 2014, 26, 4227–4231.
[9] Y. Zhang, C. Liu, X. Chen, *J. Anal. Appl. Pyrolysis* 2015, 113, 621–629.
[10] T. Hosoya, Y. Nakao, H. Sato, H. Kawamoto, S. Sakaki, *J. Org. Chem.* 2009, 74, 6891–6894.
[11] V. Seshadri, P. R. Westmoreland, *J. Phys. Chem. A* 2012, 116, 11997–12013.
[12] I. M. Rocha, T. L. P. Galvão, E. Sapei, M. D. M. C. Ribeiro da Silva, M. A. V. Ribeiro da Silva, *J. Chem. Eng. Data* 2013, 58, 1813–1821.
[13] M. Sládkovičová, P. Mach, L. Smrčok, H. Rundlöf, *Cent. Eur. J. Chem.* 2007, 5, 55–70.
[14] Y. J. Park, H. S. Kim, G. A. Jeffrey, *Acta Crystallogr. Sect. B* 1971, 27, 220–227.
[15] L. Smrčok, M. Sládkovičová, V. Langer, C. C. Wilson, M. Koóš, *Acta Crystallogr. Sect. B* 2006, 62, 912–918.
[16] E. Gloaguen, B. de Courcy, J.-P. Piquemal, J. Pilmé, O. Parisel, R. Pollet, H. S. Biswal, F. Piuzzi, B. Tardivel, M. Broquier, M. Mons, *J. Am. Chem. Soc.* 2010, 132, 11860–11863.
[17] J. A. Stearns, O. V. Boyarkin, T. H. Rizzo, *J. Am. Chem. Soc.* 2007, 129, 13820–13821.
[18] E. J. Cocinero, E. Stanca-Kaposta, D. P. Gamblin, B. G. Davis, J. P. Simons, *J. Am. Chem. Soc.* 2009, 131, 1282–1287.
[19] I. Compagnon, J. Oomens, G. Meijer, G. von Helden, *J. Am. Chem. Soc.* 2006, 128, 3592–3597.
[20] E. J. Cocinero, E. C. Stanca-Kaposta, E. M. Scanlan, D. P. Gamblin, B. G. Davis, J. P. Simons, *Chem. Eur. J.* 2008, 14, 8947–8955.
[21] E. J. Cocinero, P. Çarçabal, T. D. Vaden, J. P. Simons, B. G. Davis, *Nature* 2011, 469, 76–79.
[22] E. J. Cocinero, D. P. Gamblin, B. G. Davis, J. P. Simons, *J. Am. Chem. Soc.* 2009, 131, 11117–11123.
[23] E. J. Cocinero, E. C. Stanca-Kaposta, M. Dethlefsen, B. Liu, D. Gamblin, B. Davis, J. Simons, *Chem. Eur. J.* 2009, 15, 13427–13434.
[24] D. Sivanesan, I. Sumathi, W. J. Welsh, *Chem. Phys. Lett.* 2003, 367, 351–360.
[25] E. Nir, C. Janzen, P. Imhof, K. Kleinermanns, M. S. de Vries, *Phys. Chem. Chem. Phys.* 2002, 4, 732–739.
[26] E. Nir, K. Kleinermanns, M. S. de Vries, *Nature* 2000, 408, 949–951.
[27] D. Patterson, M. Schnell, J. M. Doyle, *Nature* 2013, 497, 475–477.
[28] D. Patterson, J. M. Doyle, *Phys. Rev. Lett.* 2013, 111, 023008.
[29] S. Lobsiger, C. Pérez, L. Evangelisti, K. K. Lehmann, B. H. Pate, *J. Phys. Chem. Lett.* 2015, 6, 196–200.
[30] E. J. Cocinero, A. Lesarri, P. Écija, F. J. Basterretxea, J. Grabow, J. A. Fernández, F. Castaño, *Angew. Chem. Int. Ed.* 2012, 51, 3119–3124; *Angew. Chem.* 2012, 124, 3173–3178.
[31] I. Peña, E. J. Cocinero, C. Cabezas, A. Lesarri, S. Mata, P. Écija, A. M. Daly, Á. Cimas, C. Bermúdez, F. J. Basterretxea, S. Blanco, J. A. Fernández, J. C. López, F. Castaño, J. L. Alonso, *Angew. Chem. Int. Ed.* 2013, 52, 11840–11845; *Angew. Chem.* 2013, 125, 12056–12061.
[32] P. Écija, I. Uriarte, L. Spada, B. G. Davis, W. Caminati, F. J. Basterretxea, A. Lesarri, E. J. Cocinero, *Chem. Commun.* 2016, 52, 6241–6244.
[33] J. L. Alonso, M. A. Lozoya, I. Peña, J. C. López, C. Cabezas, S. Mata, S. Blanco, *Chem. Sci.* 2014, 5, 515–522.
[34] R. D. Brown, P. D. Godfrey, D. McNaughton, A. P. Pierlot, *J. Am. Chem. Soc.* 1988, 110, 2329–2330.
[35] F. J. Lovas, Y. Kawashima, J.-U. Grabow, R. D. Suenram, G. T. Fraser, E. Hirota, *Astrophys. J.* 1995, 455, L201–L204.
[36] B. C. Dian, A. Longarte, T. S. Zwier, *Science* 2002, 296, 2369–2373.
[37] J. L. Alonso, M. E. Sanz, J. C. López, V. Cortijo, *J. Am. Chem. Soc.* 2009, 131, 4320–4326.
[38] I. Uriarte, P. Écija, L. Spada, E. Zabalza, A. Lesarri, F. J. Basterretxea, J. A. Fernández, W. Caminati, E. J. Cocinero, *Phys. Chem. Chem. Phys.* 2016, 18, 3966–3974.
[39] G. A. Jeffrey in *An Introduction to Hydrogen Bonding*, Oxford University Press, New York, Oxford, 1997, pp. 11–12.
[40] W. Caminati, J.-U. Grabow, in *Frontiers in Molecular Spectroscopy* (Ed.: J. Laane), Elsevier, Amsterdam, 2009, chap. 15, pp. 455–552.
[41] E. J. Cocinero, A. Lesarri, P. Écija, J.-U. Grabow, J. A. Fernández, F. Castaño, *Phys. Chem. Chem. Phys.* 2010, 12, 12486–12493.
[42] T. A. Halgren, *J. Comput. Chem.* 1999, 20, 730–748.
[43] R. F. W. Bader, *Chem. Rev.* 1991, 91, 893–928.
[44] T. Lu, F. Chen, *J. Comput. Chem.* 2012, 33, 580–592.

[45] M. J. Frisch, G. W. Trucks, H. B. Schlegel, G. E. Scuseria, M. A. Robb, J. R. Cheeseman, G. Scalmani, V. Barone, B. Mennucci, G. A. Petersson, H. Nakatsuji, M. Caricato, X. Li, H. P. Hratchian, A. F. Izmaylov, J. Bloino, G. Zheng, J. L. Sonnenberg, M. Hada, M. Ehara, K. Toyota, R. Fukuda, J. Hasegawa, M. Ishida, T. Nakajima, Y. Honda, O. Kitao, H. Nakai, T. Vreven, J. A. Montgomery, Jr., J. E. Peralta, F. Ogliaro, M. Bearpark, J. J. Heyd, E. Brothers, K. N. Kudin, V. N. Staroverov, R. Kobayashi, J. Normand, K. Raghavachari, A. Rendell, J. C. Burant, S. S. Iyengar, J. Tomasi, M. Cossi, N. Rega, J. M. Millam, M. Klene, J. E. Knox, J. B. Cross, V. Bakken, C. Adamo, J. Jaramillo, R. Gomperts, R. E. Stratmann, O. Yazyev, A. J. Austin, R. Cammi, C. Pomelli, J. W. Ochterski, R. L. Martin, K. Morokuma, V. G. Zakrzewski, G. A. Voth, P. Salvador, J. J. Dannenberg, S. Dapprich, A. D. Daniels, Ö. Farkas, J. B. Foresman, J. V. Ortiz, J. Cioslowski, D. J. Fox, Gaussian 09, Revision A.02 Gaussian, Inc., Wallingford CT, 2009.

XI.82